NANOEMULSION-LOADED HYDROGELS FOR ADVANCED PHARMACEUTICAL FORMULATIONS

by

Liang-Hsun Chen

B.S. in Chemical Engineering, National Taiwan University

M.S. in Chemical Engineering Practice, Massachusetts Institute of Technology

Submitted to the Department of Chemical Engineering

in partial fulfillment of the requirements for the degree of

Doctor of Philosophy in Chemical Engineering

at the

MASSACHUSETTS INSTITUTE OF TECHNOLOGY

September 2022

Author_____

Department of Chemical Engineering

May 24, 2022

Certified by_____

Patrick S. Doyle

Robert T. Haslam (1911) Professor of Chemical Engineering

Thesis Supervisor

Accepted by_____

Patrick S. Doyle

Chairman, Department Committee on Graduate Students

Nanoemulsion-Loaded Hydrogels for Advanced Pharmaceutical Formulations

by

Liang-Hsun Chen

Submitted to the Department of Chemical Engineering on May 27, 2022

in partial fulfillment of the requirements for the degree of

Doctor of Philosophy in Chemical Engineering

ABSTRACT

Pharmaceutical formulation plays an important role in transforming a drug substance into the final drug product taken by a patient. It involves processes that combine an active pharmaceutical ingredient (API) and a mixture of inactive excipients into a final drug product with desired therapeutic effects and physical properties. Among various drug products, oral solid dosage forms are the most preferred product forms dominating the market because of their high patient compliance and wide acceptance. However, conventional oral drug formulations typically require costly multistep manufacturing, and poor bioavailability of hydrophobic APIs still remains a persistent challenge in many formulations. To address the limitations, we utilize two promising building blocks, nanoemulsions and hydrogels, to design new materials that enable more efficient and effective formulations of oral drug products with high quality and versatile release.

First, we present a method to encapsulate functional nanoemulsions in alginate capsules for more versatile delivery of lipophilic active ingredients. The nanoemulsions are intrinsically viscous, ensuring the formation of spherical capsules and large encapsulation efficiency. Quantitative release analyses show that the capsule systems possess a tunable, delayed-burst release. The proposed encapsulation methodology can be further generalized to other functional nanoemulsions with various active ingredients, oil phases, nanodroplet sizes, and chemically crosslinked inner hydrogel cores.

Second, we design a new thermogelling methylcellulose (MC) nanoemulsion that can be efficiently formulated into composite solid dosage drug products with well-controlled API nanocrystals embedded in a MC matrix. The composite drug products possess a fast and

tunable release performance because of the fast-eroding MC matrix and successful formation of API nanocrystals. Using the versatile thermal processing approach, we formulate the nanoemulsion into various dosage forms (nanoparticle suspension, drug tablet, and oral thin film) in a manner that avoids nanomilling.

Finally, we develop thermogelling hydroxypropyl methylcellulose (HPMC) nanoemulsions as robust templates to formulate oral films loaded with poorly water-soluble drug nanoparticles. The thermally gelled network effectively immobilizes the oil nanodroplets for confined nanoparticle crystallization and avoids potential irreversible nanoparticle aggregation. The oral films possess a tunable immediate release, and a scaling rule is developed for designing the release profiles of oral films.

Thesis Supervisor: Patrick S. Doyle
Robert T. Haslam (1911) Professor of Chemical Engineering

Acknowledgements

First and foremost, I am extremely grateful to my thesis advisor, Prof. Patrick S. Doyle for his invaluable guidance and continuous support. I came to the lab with a huge language barrier, but he has always guided me with a lot of patience. His guidance and patience are important nutrients for my academic growth. I appreciate the way he approaches and analyzes research problems. Whenever I feel lost in my research, he can always guide me to the right track and converge my thoughts. I am very fortunate to have him as my advisor during my PhD journey.

I would also like to thank my thesis committee members, Prof. Allan S. Myerson and Prof. Muhammad H. Zaman. I enjoy sharing my research progress to them during the committee meetings. They can always ask me important questions to think and provide insightful suggestions. I greatly appreciate their encouragement and support to my research.

I would like to thank my friends that I met in our year, Chun Man, Emily, Charles, Ge, Smiley, Soonhyoung, Jingfan, Srinu, Xiaorui. I enjoy the time we spent together studying and playing at MIT. Moreover, I would like to thank Tzyy-Shyang for many informative research discussions.

I am grateful to many wonderful labmates in the Doyle group. I enjoy working with these people, and I always learn a lot from them. I want to thank Beatrice and Li-Chiun for being friendly to me when I first joined the lab, so I could blend into the lab quickly. I would like to thank Abu and Trystan for teaching me skills that are useful in my research. I would like to thank Jae Jung for kindly teaching me contact flow lithography. I would like to thank Devashish for sharing his extensive knowledge about MD simulation with me. I would like to thank Lucas for being a productive collaborator during the final year of my PhD. I also want to thank Nidhi, Yuan, Nitesh, Jeremy, Amir, Arif, Jennifer, Mateusz, Sima, Indresh, Arjav, Max, Dana, and Sarah for many fun conversations we have had in the office. Finally, I am especially thankful to Gwen Wilcox for all her kind helps that have effectively solved many difficult problems for us.

I am thankful to my practice school group, Charles, Drew, Jennifer, Kara, Lucky, Sarah, Xiaorui, and Ani. We had good adventures in many places. I learned a lot from these talented and friendly peers, not only about English and American culture, but also about critical thinking and problem solving. I really enjoyed the trips to New Zealand and Australia with these people.

My gratitude extends to my undergraduate research advisor, Prof. Kuo-Lun Tung. I greatly appreciate his treasured support and guidance. He always made me very motivated in doing research. I also want to thank my colleagues at National Taiwan University, Allen Huang and Yi-Rui Chen for many collaborative projects we have had.

Finally, this journey would not have been possible without the support of my family and partner. To my parents and sister, thank you for your unconditional love and support. To Ting-An, thank you for coming into my life and making me a better person.

Table of Contents

List of Figures

List of Tables

Chapter 1 Introduction

1.1 Motivation

Drug development is a prolonged and expensive process. Thousands of drug candidate compounds have to undergo many clinical trials to be tested for their toxicity and potency before one final active pharmaceutical ingredient (or API) is approved by the United States Food and Drug Administration (FDA). This unique active pharmaceutical ingredient then has to be processed with inactive excipients to form final drug products through pharmaceutical formulations. Excipients are introduced for stabilization, building up solid formulations, and controlling release properties. However, advances in drug development have mainly focused on the discovery and synthesis of APIs, and there has been less innovation in the formulation steps.

Among various drug products, oral dosage forms are the most preferred product forms dominating the market because of their wide acceptance.[1,2] However, conventional oral drug formulations typically require inefficient multistep manufacturing (**Figure 1.1**), and poor bioavailability of hydrophobic APIs still remains a persistent challenge in many formulations. It has been reported that 40% of marketed drugs and 90% of drug candidates in the pipeline are hydrophobic.[3] Their poor water-solubility renders the drugs difficult to be absorbed in the gastrointestinal tract, greatly undermining their potency. Nanocrystalline formulations are an attractive route to increase API solubility, but typically require abrasive mechanical milling and several processing steps to create an oral dosage form. Milling can often damage the API or transform it to an undesirable crystal polymorph.[4] Moreover, many inefficient steps are required to process the generated nanocrystals with polymeric excipients into a drug product, and achieving homogenous distribution of API is still difficult.[5] Therefore, it is imperative to develop alternative strategies which are efficient and effective.

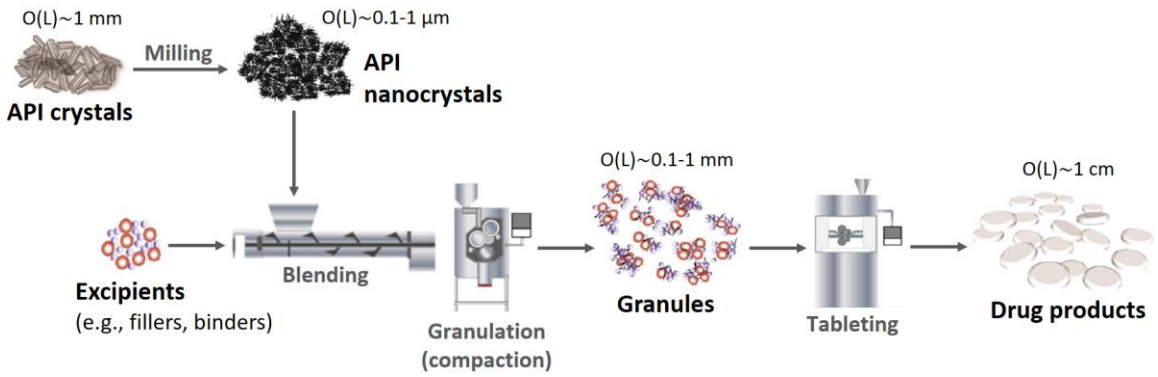

Figure 1.1. Conventional pharmaceutical formulations (adapted from a prior work[6]).

1.2 Nanoemulsions

Nanoemulsions have gained considerable attention in recent years with the increasing need to develop effective delivery systems for hydrophobic active ingredients. Hydrophobic active ingredients are ubiquitous in a wide variety of applications, such as pharmaceuticals,[7–9] cosmetics,[10] and food.[11,12] An oil-in-water nanoemulsion involves dispersed oil droplets with an average size ranging from 20 to 500 nm in a continuous water phase (**Figure 1.2a**).[13] The oil nanodroplets can act as more effective reservoirs for solubilizing various hydrophobic ingredients compared to simple micellar dispersions (**Figure 1.2b**).[14] Nanoemulsions can protect the active ingredients from degradation due to harmful external factors, such as oxidation, pH, or hydrolysis (**Figure 1.2c**).[14] In contrast to conventional macroemulsions, a nanoemulsion has uniformly small nanodroplets, and the strong Brownian motion can oppose flocculation and coalescence.[11] Therefore, a nanoemulsion can be highly stable and have a long shelf life. (**Figure 1.2d**).[10] Because of the small size, an oil-in-water nanoemulsion can be effectively absorbed by human bodies (**Figure 1.2e**).[15] For oral drug delivery, a nanoemulsion loaded with a hydrophobic drug has shown a significant bioavailability improvement compared to the unformulated crystalline drug.[16] Nanoemulsions have also been used to enhance lipid digestibility and the absorption of bioactive ingredients in food products and supplements.[17] Moreover, cosmetic products made with nanoemulsions show improved efficacy, because the oil nanodroplets can easily permeate through a skin.[18]

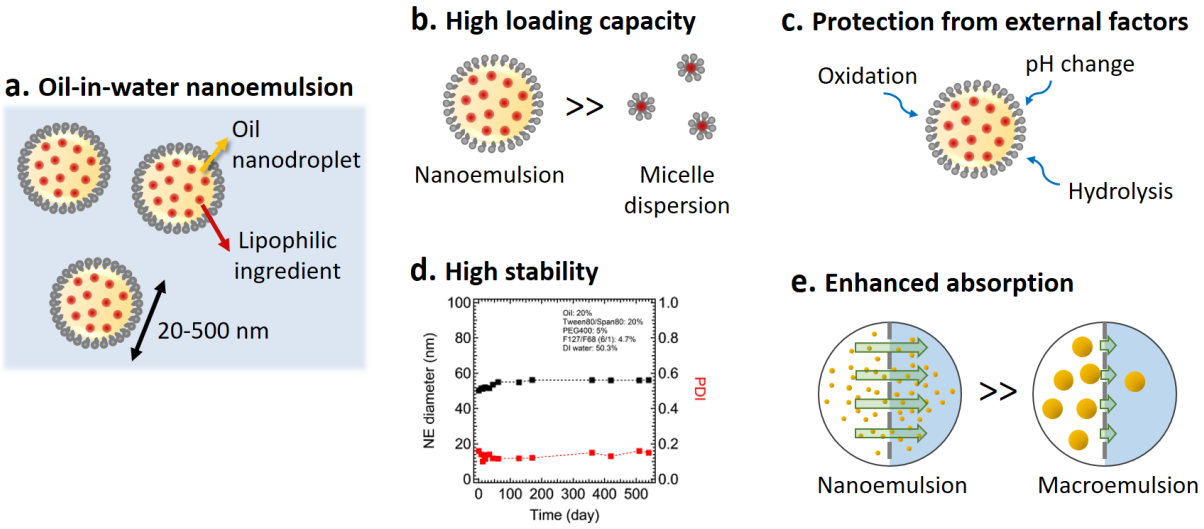

Figure 1.2. Overview of oil-in-water nanoemulsions and their properties. (a) An oil-in-water nanoemulsion system involves oil nanodroplets that are dispersed in the continuous water phase. The nanodroplets are stabilized by a layer of surfactants and have a diameter between 20 and 500 nm. The oil nanodroplets can act as good reservoirs for loading hydrophobic ingredients. (b) Nanoemulsions generally show higher loading capacity compared to micellar dispersions.[10] (c) Nanoemulsions can protect the loaded active ingredients from harmful external factors. (d) Nanoemulsions are stable over a long time. (e) Nanoemulsions show enhanced absorption compared to macroemulsions.

1.2.1 Nanoemulsion Synthesis

Nanoemulsions are formed when two immiscible phases (e.g., oil and water) are mixed with the addition of an emulsifier (e.g., surfactant) that decreases the interfacial tension between the two phases. The free energy required to form a nanoemulsion (ΔG_{NE}) is the difference between the free energy required to increase the oil-water interface ($\gamma \Delta A$) and the free energy associated with increasing the number of possible nanodroplet arrangements ($T\Delta S_{config}$).[19,20]

$$\Delta G_{NE} = \gamma \Delta A - T\Delta S_{config} \quad (1.1)$$

where γ is the interfacial tension, A is the interfacial area, T is the temperature, and S is the entropy. It is noted that the $\gamma \Delta A$ term is always positive, which opposes the formation of nanoemulsions. Generally, the $\gamma \Delta A$ term is greater than the $T\Delta S_{config}$ term, and additional energy input is required to form a nanoemulsion.

Preparation of nanoemulsions can be classified into two categories: high-energy and low-energy methods (**Figure 1.3**). The input energy densities of high-energy and low-energy methods are 10^8-10^{10} and 10^3-10^5 W/kg, respectively. The factors that control the droplet size of a nanoemulsion include energy input, oil volume fraction, surfactant hydrophilic-lipophilic balance (HLB), and surfactant-to-oil ratio (SOR).[21]

1.2.1.1 High-Energy Methods

High-energy methods provide a robust way to prepare nanoemulsions, which are commonly achieved by a homogenizer or an ultrasonicator (**Figure 1.3a**). A homogenizer consists of a high-pressure pump that can generate high shear stresses on a macroemulsion when pushing the macroemulsion through a narrow gap on the order of a few microns. An ultrasonicator can provide high energy shock waves that create turbulence in a macroemulsion. Both the high shear stresses and high energy shock waves can effectively break down the dispersed bulk oil droplets and transform a macroemulsion into a nanoemulsion.

1.2.1.2 Low-Energy Methods

Emulsion inversion point (EIP) and phase inversion temperature (PIT) are two widely used low-energy methods (**Figure 1.3b**). EIP is also called phase inversion composition (PIC). The EIP method involves diluting the dispersed phase/surfactant mixture with the continuous phase of a nanoemulsion, and the PIT method involves cooling an oil/water system that has a thermosensitive surfactant.[22] During the dilution or cooling, the system can pass through an inversion point where the interfacial tension between the oil and water can be as low as 10 μN/m.[23] The low interfacial tension favors the formation of dispersed nanodroplets with low energy requirements. Low-energy methods only require simple stirring, and thus have great potential for large-scale production. Because nanoemulsions are kinetically stable, order of adding each component can affect the final droplet size.[24]

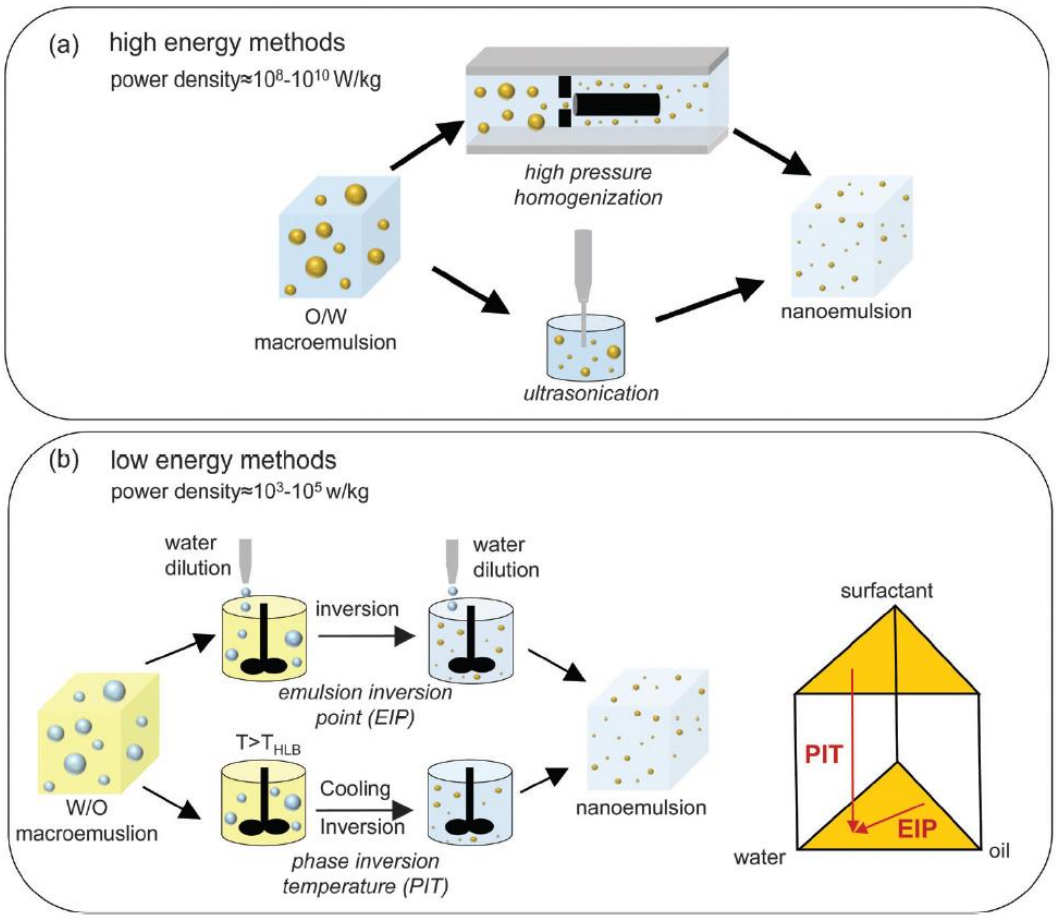

Figure 1.3. Overview of high-energy and low-energy methods for preparing oil-in-water nanoemulsions. (a) High-energy methods include high pressure homogenization and ultrasonication. (b) Low-energy methods include emulsion inversion point (EIP) and phase inversion temperature (PIT).[13]

1.3 Hydrogels

Hydrogels are promising materials to encapsulate active ingredients for more accurate administration,[25] controlled delivery,[26–29] and enhanced stability.[30] They provide versatile delivery platforms for various administration routes, including oral, parenteral, and topical routes.[31] Hydrogels are three-dimensional polymeric networks that can be readily customized and formulated into particles with various sizes and shapes.[31] They can swell under biological conditions, and thus are ideal materials for biomedical applications, such as drug delivery[31] and tissue engineering.[32] Their tunable physical properties facilitate the development of novel drug delivery platforms.[33] However, the hydrophilic nature of hydrogels inherently limits their ability to encapsulate hydrophobic active ingredients. To overcome this limitation, major

research efforts have been focused on incorporating hydrophobic domains into hydrogel matrices by encapsulating nanoparticles,[34] macroemulsions,[35] and nanoemulsions[36] into hydrogel particles.

1.3.1 Alginate

Alginate hydrogels are natural polysaccharides that have gained increasing interest because of their non-toxicity and biocompatibility.[37] They are widely applied in food, pharmaceutical, and biomedical industries.[38] Formation of alginate hydrogels requires ionic crosslinking between alginate and divalent cations (**Figure 1.4**). The divalent cations can bind the guluronate blocks of an alginate chain to the guluronate blocks of an adjacent chain. The binding between the cations and guluronate blocks can form an egg-box structure, which leads to a hydrogel network.[37] Because the gelation process is facile, many production techniques have been developed to form alginate particles with different length scales.[39]

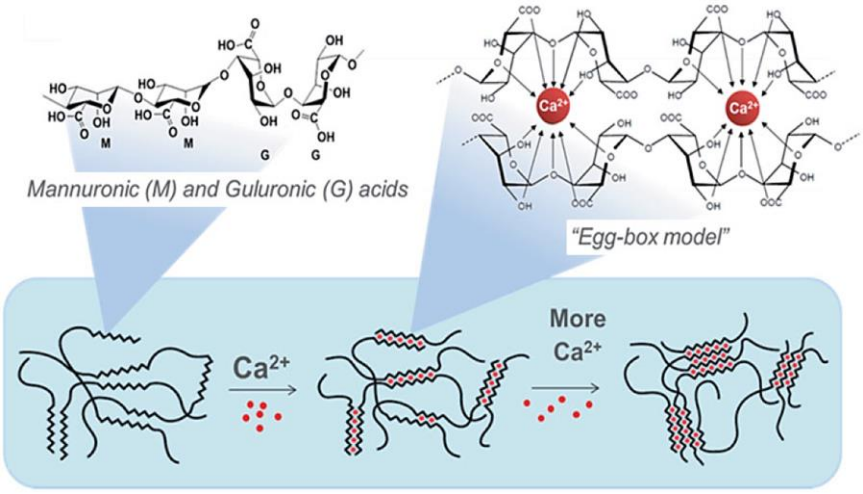

Figure 1.4. Ionic cross-linking of alginate molecules in the presence of calcium ions. The guluronate blocks of alginate molecules are bound together by calcium ions to form egg-box structures.[40]

1.3.2 Methylcellulose (MC) and Hydroxypropyl Methylcellulose (HPMC)

Methylcellulose (MC) and hydroxypropyl methylcellulose (HPMC) are two types of nature-based cellulose ester excipients that have been widely formulated into oral solid dosage forms in food and pharmaceutical applications.[41–43] Their unique swelling and erosion behaviors are

suitable for the design of controlled release systems and for the study of drug delivery models.[44] Upon contact with water, a gel layer can form on the polymer surface due to rapid hydration, which slows down further water penetration into the inner dry polymer core.[45] The non-ionic nature of the cellulose materials ensures reproducible pH-independent drug release profiles in gastrointestinal fluids with varying pH conditions.[43] In addition, drug solubility is a key factor that determines the drug release behavior. For hydrophilic drugs, drug diffusion through the gel layer and matrix erosion both contribute to the drug release. For hydrophobic drugs, drug release is mainly through the erosion of cellulose matrices.[46]

Reversible thermal gelation is a smart property of MC and HPMC that has gained considerable attention in the field of rheology[47,48] and tissue engineering.[49,50] The polymer gels upon heating and returns back to the sol state upon subsequent cooling.[48] This property has been applied to develop many *in situ* gelling materials for drug delivery.[51,52] MC and HPMC belong to thermoresponsive polymers that have a lower critical solution temperature (LCST), which defines the sol-gel transition for a polymer. Because polymers with a LCST have a negative mixing entropy (ΔS_{mix}), increasing temperature leads to an increase in ΔG_{mix} and more unfavorable mixing.

$$\Delta G_{mix} = \Delta H_{mix} - T\Delta S_{mix} \quad (1.2)$$

The sol-gel transition for a MC (or HPMC) solution is schematically shown in **Figure 1.5**. Below the LCST, hydrogel bonds are formed between the water molecules and the hydroxyl groups (-OH) of the cellulose materials. The hydration layers can prevent the hydrophobic methoxy groups (-OCH3) from associating together. Upon heating, the hydrogel bonds are broken. With the loss of the hydration layers, the hydrophobic groups can associate together and form a gel structure.[53]

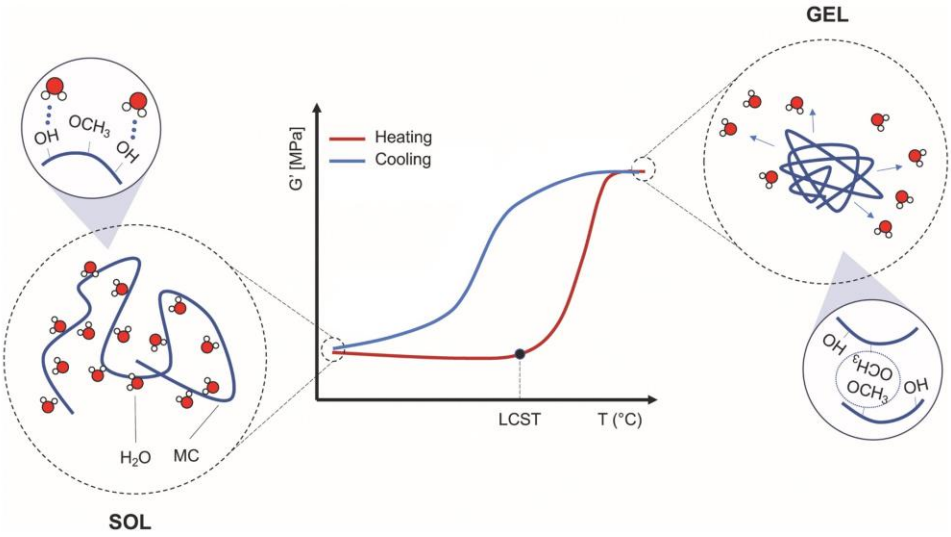

Figure 1.5. Sol-gel transition for a methylcellulose solution: below the LCST, hydrogel bonds are formed between the water molecules and the hydroxyl groups of MC. The hydration layers can prevent the hydrophobic association. Upon heating to T>LCST, hydrogen bonds are broken, and the hydrophobic groups of MC associate together to form hydrophobic junctions that lead to a hdyrogel structure.[53] The same sol-gel transition mechanism is also applied to HPMC.

1.4 Nanoemulsion-Loaded Hydrogels

To generate nanoemulsion-loaded hydrogels for nanoemulsion encapsulation, crosslinkable nanoemulsions have been developed with crosslinking agents loaded in the continuous phase. After the gelation is induced, a hydrogel is formed with immobilized oil nanodroplets embedded in the hydrogel network. The nanoemulsion-loaded hydrogels have been applied for nanoemulsion delivery[10,36] and confined crystallization.[9,54–56]

1.4.1 Thermogelling Nanoemulsions

Our group has designed several thermogelling nanoemulsions in which gelation is triggered by an increase in temperature (**Figure 1.6**).[10,57,58] The thermal gelation can be induced through oligomer bridging the nanodroplets (**Figure 1.6a**),[58] surfactant replacement to lower the repulsion between the nanodroplets (**Figure 1.6b**),[57] and jamming via adsorption of copolymers onto the nanodroplets (**Figure 1.6c**).[10] Temperature is a simple and convenient stimulus that can remotely induce gelation for material processing. However, these thermogelling nanoemulsions are only limited to non-volatile organic solvents as the oil phase

(e.g., silicone oil and isopropyl myristate), which cannot be easily evaporated to induce crystallization.

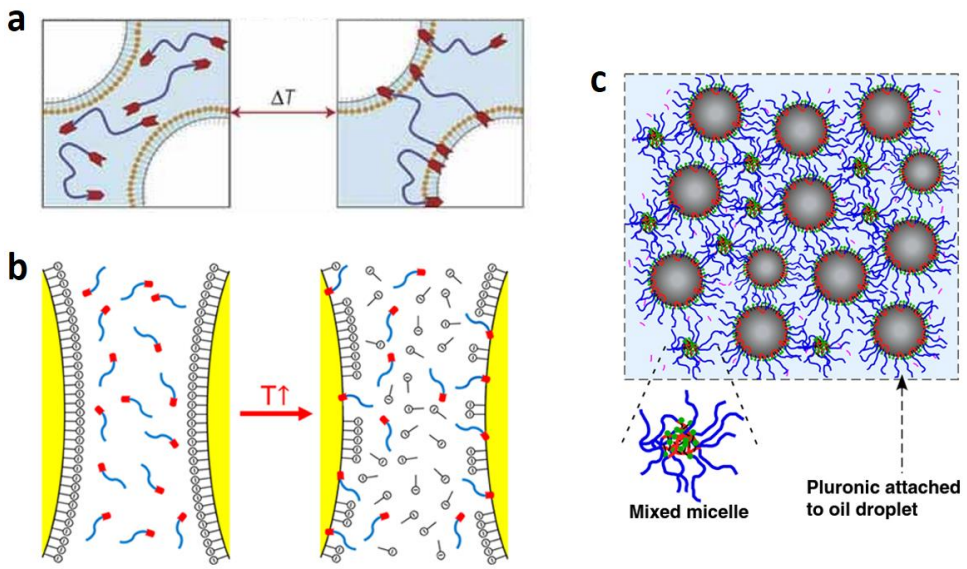

Figure 1.6. Overview of thermogelling nanoemulsions with different thermal gelation mechanisms: (a) oligomer bridging the nanodroplets,[58] (b) surfactant replacement to lower the repulsion between the nanodroplets,[57] and (c) jamming via adsorption of copolymers onto the nanodroplets.[10]

1.4.2 Alginate Nanoemulsions for Confined Crystallization

Our group has developed alginate nanoemulsions for more efficient oral drug formulations (**Figure 6**). The formulations involve ionic crosslinking of alginate molecules and heating to remove the solvents (**Figure 6a**). The ionic crosslinking is achieved by dripping the alginate nanoemulsion into a $CaCl_2$ solution to form crosslinked alginate particles with embedded oil nanodroplets, which then are dried at an elevated temperature.[9,54–56] During the drying, the nanodroplets act as crystallization reactors, and the final nanocrystal size is dictated by the nanoemulsion droplet size. The alginate nanoemulsions can be prepared using high-energy[54,56] and low-energy methods.[9,55] In addition to the simple dripping method driven by gravity, centrifugal forces can also be applied on smaller dispensing tips to form smaller hydrogel particles.[9,55] To incorporate more functionalities, polyvinyl alcohol (PVA) has been introduced into an alginate nanoemulsion.[56] During the drying, the PVA molecules can migrate to the alginate particle surface to form a shell for delayed release (**Figure 1.7b**). By mixing two

nanoemulsions loaded with two different hydrophobic APIs, coformulation is easily achieved with two APIs uniformly distributed in a single alginate particle (**Figure 1.7c**).[9] However, confined crystallization in nanoemulsions is limited to alginate crosslinking mechanism, and it would be desirable to utilize other gelation techniques to immobilize oil nanodroplets for confined crystallization. For example, if confined crystallization can occur in a thermogelling nanoemulsion, we can induce the gelation and crystallization just by heating the nanoemulsion, which would be more efficient than using alginate nanoemulsions which require ionic crosslinking and heating to dry.

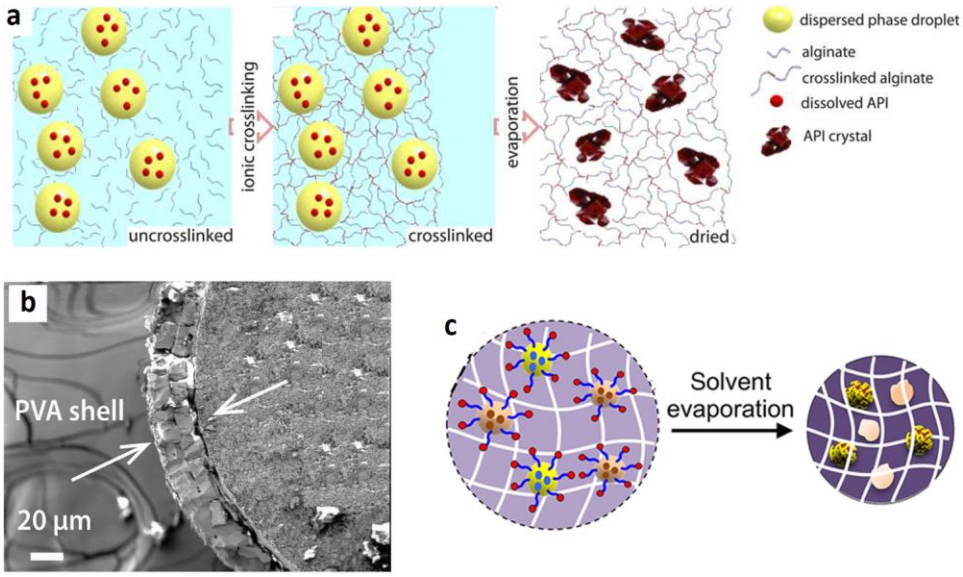

Figure 1.7. (a) Ionic crosslinking of an alginate nanoemulsion, which is then dried to induce API crystals in a dried alginate matrix.[54] (b) SEM image of a PVA shell around an alginate particle.[56] (c) Coformulation of two different hydrophobic APIs.[9]

1.5 Pharmaceutical Nanocrystals

In the pharmaceutical community, nanocrystals have a size between a few nanometers and 1000 nm.[59] Nanocrystals have novel properties (e.g., enhanced dissolution and melting point depression) that are very different from their bulk materials.[4] Therefore, many pharmaceutical formulations have been developed to generate nanocrystals for hydrophobic APIs.[4]

1.5.1 Preparation of Drug Nanocrystals

The preparation of drug nanocrystals can be classified into two categories, top-down and bottom-up methods (**Figure 1.8**).[4] The top-down methods involve mechanical forces to break down larger particles into smaller ones, while the bottom-up methods involve building up nanocrystals from molecules.

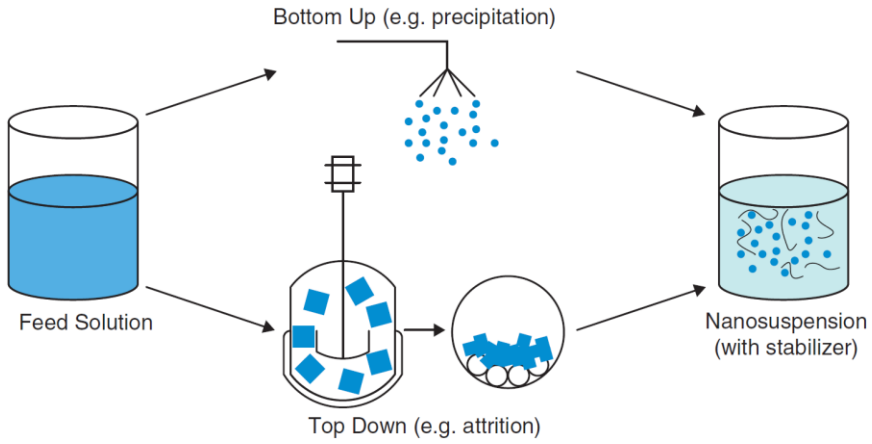

Figure 1.8. Schematic diagram of bottom-up and top-down methods for preparing nanocrystals.[4]

1.5.1.1 Top-Down Methods

Top-down methods include fluid energy milling (or air jet milling), ball milling, wet stirred medial milling, high-pressure homogenization, cryogenic milling. These methods are generally energy-intensive, and the abrasive nature could lead to polymorphic transformation.[4] The fluid energy milling and ball milling belong to dry milling techniques, in which the smallest particle size is limited to a few micrometers.[60] Wet stirred media milling is one of the most extensively used techniques to formulate nanoparticle suspensions, because it is a robust and well-established process that can be applied to many hydrophobic drugs.[61,62] However, it generally involves long milling durations (3-12 h),[63,64] and erosion of milling media may cause severe contamination of drugs.[65,66]

1.5.1.2 Bottom-Up Methods

Bottom-up methods are more energy-efficient, and are also called precipitation methods. The principle is to precipitate drug nanocrystals from a supersaturated solution of a drug. Strategies

to generate supersaturation include solvent evaporation, temperature reduction, and antisolvent addition.[67] Bottom-up methods include supercritical fluid technology, spray drying, freeze drying, antisolvent precipitation, and evaporative precipitation.[67–69] In recent years, crystallization in rigid confinement has also been applied to template the formation of drug nanocrystals.[70–73] Confined crystallization in porous matrices of known size can lead to uniform nanocrystal sizes[70] and better controls over the polymorphic forms.[71,72] However, these methods are limited to certain specifications of porous materials that are generally not ideal excipients, and it is not flexible to simultaneously control the drug crystal size and the drug loading content.

1.5.2 Dissolution Enhancement of Nanocrystals

The dissolution velocity of a drug crystal can be described by the Noyes-Whitney equation.[59]

$$\frac{dC}{dt} = \frac{DA}{h_D}(C_s - C_x) \tag{1.3}$$

where $\frac{dC}{dt}$ is the dissolution velocity, D is the diffusion coefficient, A is the surface area of the particle, h_D is the diffusional distance, C_s is the saturation solubility, C_x is the bulk concentration. The saturation solubility is dependent on the particle size, and the dependence can be described by the Kelvin equation[74] and the Ostwald-Freundlich equation.[75] The Kelvin equation is used to describe the dissolution pressure of a solid particle, which is a function of the particle curvature. Equilibrium exists between dissolving and recrystallizing molecules. Reducing the particle size increases the dissolution pressure, which corresponds to increased saturation solubility.[74]

$$\ln\left(\frac{P_r}{P_\infty}\right) = \frac{2\gamma M_r}{RT\rho r} \tag{1.4}$$

where P_r is the dissolution pressure of a particle with a radius r, P_∞ is the dissolution pressure of an infinitely large particle, γ is the surface tension, M_r is the molecular weight, R is the universal gas constant, T is the absolute temperature, ρ is the particle density, r is the particle radius.

The Ostwald-Freundlich equation correlates the drug saturation solubility and the drug particle size.[75]

$$\log\left(\frac{C_s}{C_\infty}\right) = \frac{2\sigma V}{2.303RT\rho r} \tag{1.5}$$

where C_s is the saturation solubility of a particle with a radius r, C_∞ is the solubility of an infinitely large particle, σ is the interfacial tension between the particle surface and the surrounding medium, V is the molar volume of the drug, R is the universal gas constant, T is the absolute temperature, ρ is the particle density, r is the particle radius.

From the Ostwald-Freundlich and Noyes-Whitney equations, when the particle size is smaller than the critical size of 1-2 μm,[59] the dissolution velocity can be greatly improved for hydrophobic drugs because of the increase in the surface area and the saturation solubility.

1.5.3 Melting Point Depression of Nanocrystals

At the equilibrium of a melting crystal, the Gibbs free energies are the same for the liquid phase and the solid phase.

$$G_{s,bulk} + G_{s,interface} = G_{l,bulk} + G_{l,interface} \tag{1.6}$$

where $G_{s,bulk}$ and $G_{s,interface}$ are the Gibbs free energies of the bulk and surface in the solid phase. $G_{l,bulk}$ and $G_{l,interface}$ are the Gibbs free energies of the bulk and surface in the liquid phase.

With the following definitions,

$$\Delta G_{s-l,bulk} = G_{s,bulk} - G_{l,bulk} \tag{1.7}$$

$$\Delta G_{s-l,interface} = G_{s,interface} - G_{l,bulk} \tag{1.8}$$

we can rewrite **Equation 1.6** into

$$\Delta G_{s-l,bulk} + \Delta G_{s-l,interface} = 0 \tag{1.9}$$

Assuming that the fusion enthalpy is constant, $\Delta G_{s-l,bulk}$ can be expressed by

$$\Delta G_{s-l,bulk} = \Delta H_m - T(r)\Delta S_m = \Delta H_m - T(r)\frac{\Delta H_m}{T_m} \quad (1.10)$$

where ΔH_m is the fusion enthalpy of the bulk phase, ΔS_m is the entropy of the bulk phase, T_m is the melting point of the bulk phase, $T(r)$ is the melting point of particle with a radius r.

For a spherical particle, the $\Delta G_{s-l,interface}$ can be described by the Kelvin equation:

$$\Delta G_{s-l,interface} = \frac{-2\gamma V_m}{r} \quad (1.11)$$

where γ is the surface tension of the solid-liquid interface, V_m is the drug molar volume, and r is the particle radius.

Plugging **Equation 1.10** and **Equation 1.11** into **Equation 1.9** leads to the Gibbs-Thomson equation (**Equation 1.12**),[76] which describes melting point depression of nanocrystals:

$$\Delta T_m = T_m - T(r) = \frac{2\gamma V_m T_m}{r\Delta H_m} \quad (1.12)$$

1.6 Thesis Organization

In this thesis, two promising building blocks, functional nanoemulsions and hydrogels, are simultaneously utilized to design new materials that enable more efficient and effective formulations of oral drug products (e.g., tablets, capsules, particles, nanoparticle suspensions, and oral thin films). The new formulation methods can not only address the current formulation problems, but also ensure high quality drug products with improved dissolution/absorption of hydrophobic drugs, high drug content uniformity, and versatile release controls (e.g., delayed release and tunable fast release).

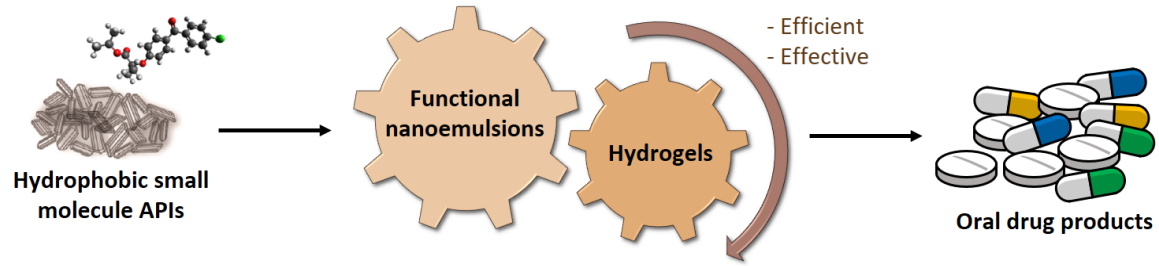

Figure 1.9. Proposed scheme for formulating oral drug products.

The thesis is broken down into several parts. After a brief introduction, different technologies to formulate drug products are presented.

Chapter 1 discusses the motivation and general scope for this work.
Chapter 2 describes a method to encapsulate nanoemulsions in alginate capsules for controlled delivery of lipophilic active ingredients.
Chapter 3 presents a new thermogelling nanoemulsion system that can be easily formulated into composite solid dosage drug products with well-controlled API nanocrystals embedded in a MC matrix.
Chapter 4 presents a thermogelling HPMC nanoemulsions that can directly act as film precursors for casting and provide robust templates to formulate oral films with uniform drug nanoparticles embedded in a dried HPMC matrix.
Chapter 5 summarizes the conclusions from this work and comments on future direction.

Chapter 2 Nanoemulsion-Loaded Capsules for Controlled Delivery of Lipophilic Active Ingredients

Nanoemulsions have become ideal candidates for loading hydrophobic active ingredients and enhancing their bioavailability in the pharmaceutical, food, and cosmetic industries. However, the lack of versatile carrier platforms for nanoemulsions hinders advanced control over their release behavior. In this work, a method is developed to encapsulate nanoemulsions in alginate capsules for the controlled delivery of lipophilic active ingredients. Functional nanoemulsions loaded with active ingredients and calcium ions are first prepared, followed by encapsulation inside alginate shells. The intrinsically high viscosity of the nanoemulsions ensures the formation of spherical capsules and high encapsulation efficiency during the synthesis. Moreover, a facile approach is developed to measure the nanoemulsion release profile from capsules through UV-Vis measurement without an additional extraction step. A quantitative analysis of the release profiles shows that the capsule systems possess a tunable, delayed-burst release. The encapsulation methodology is generalized to other active ingredients, oil phases, nanodroplet sizes, and chemically crosslinked inner hydrogel cores. Overall, the capsule systems provide promising platforms for various functional nanoemulsion formulations.

This chapter has been adapted with permission from L.-H. Chen, L.-C. Cheng, and P. S. Doyle. Nanoemulsion-Loaded Capsules for Controlled Delivery of Lipophilic Active Ingredients. *Advanced Science* (2020): 2001677.[77]

2.1 Introduction

Nanoemulsions have gained considerable attention in recent years because of the increasing need to develop effective delivery systems for lipophilic active ingredients. These lipophilic active ingredients are ubiquitous in a wide variety of applications, such as pharmaceutical manufacturing,[7–9] cosmetic formulations,[10] and food processing.[11,12] In pharmaceutical applications, it is known that 40% of currently marketed drugs and 90% of drugs in development are hydrophobic[3] wherein the low water solubility greatly limits their bioavailability and absorption efficiency. Oil-in-water (O/W) nanoemulsion systems have been extensively pursued for hydrophobic pharmaceutical compounds. These nanoemulsions are

dispersed oil droplets with an average size ranging from 20 to 500 nm in an aqueous continuous phase.[13] The oil nanodroplets can act as effective reservoirs for solubilizing various lipophilic ingredients and protecting them from degradation due to external factors, such as oxidation, pH, or hydrolysis.[14] In contrast to conventional macroemulsions, a nanoemulsion has uniformly small nanodroplets that are more resistant to flocculation and coalescence.[11] Moreover, their improved kinetic stability enables a nanoemulsion to possess a longer shelf life, and their larger active surface area to volume of droplets enables better availability of incorporated active ingredients. For oral drug delivery, the high loading capacity of an O/W nanoemulsion to solubilize a hydrophobic drug has shown a significant improvement of the bioavailability compared to the unformulated crystalline form.[16] O/W nanoemulsions are used to enhance lipid digestibility and the absorption of bioactive ingredients in food products and supplements.[17] The efficacy of cosmetic products can also be greatly improved with oil nanodroplets leading to enhanced permeation of active ingredients into skin.[18]

Advances in encapsulation technologies have facilitated the formulation of active ingredients into versatile dosage forms, in which the active ingredients can be carried for accurate administration,[25] controlled delivery,[26–29] and enhanced stability.[30] Hydrogel encapsulation is one of the most promising routes and has been widely applied to design delivery platforms for various administration routes, including oral, parenteral, and topical routes.[31] Hydrogels are three-dimensional polymeric networks that can be readily customized and formulated into particles with various sizes and shapes.[31] Their tunable physical properties facilitate the development of novel drug delivery platforms.[33] Alginate hydrogels are natural polysaccharides that have gained increasing interest because of their non-toxicity and biocompatibility.[37] In addition, the ionic crosslinking of alginate via divalent cations is facile and gentle on incorporated actives. Thus, alginate hydrogels are widely applied in food, pharmaceutical, and biomedical industries.[38] However, the hydrophilic nature of hydrogels inherently limits their ability to encapsulate hydrophobic active ingredients. To overcome this limitation, major research efforts have been focused on incorporating hydrophobic domains into hydrogel matrices by encapsulating nanoparticles,[34] macroemulsions,[35] and nanoemulsions into hydrogel particles. For example, alginate beads have been used to encapsulate macroemulsions for controlled lipid digestion.[78,79] The encapsulation efficiency of lipid droplets depends on the degree of alginate crosslinking.[80] Recently, our group

encapsulated nanoemulsions inside alginate beads for confined crystallization.[9,54–56] After solvent evaporation, nanocrystals of a lipophilic active pharmaceutical ingredient were formed with the crystal size dictated by the oil droplet size. In addition, nanoemulsion-loaded alginate beads have also been applied for delivering a lipophilic bioactive ingredient in the liquid form.[36] However, the encapsulation of nanoemulsions in alginate beads becomes more challenging as the droplet sizes are reduced to nanoscale.[36] A large number of oil nanodroplets, especially when their sizes are close to the alginate mesh size (~10 nm),[79] could potentially hinder the alginate crosslinking and disrupt the hydrogel structure, leading to significant leakage of the nanoemulsion.

To the best of our knowledge, nanoemulsion encapsulation techniques are limited to monolithic dosage forms.[9,36,54–56,81] Here, we report a new method to encapsulate nanoemulsions in alginate capsules for the controlled delivery of lipophilic active ingredients. After the addition of $CaCl_2$ into nanoemulsions, a simple one-batch inverse gelation technique[82] is applied by dripping the calcium-laden nanoemulsions into an alginate bath. The nanoemulsion suspensions prepared in our work have an intrinsically large viscosity which enables their encapsulation in alginate capsules. In addition, a facile method is proposed to measure the release of nanoemulsions which avoids a tedious extraction step and facilitates automated real-time measurements using a United States Pharmacopeia (USP) dissolution apparatus. We demonstrated that alginate capsules have improved encapsulation efficiency compared to their monolithic bead counterparts. The bursting time of the alginate capsules is related to the shell properties which can be easily engineered by varying the calcium concentration during synthesis. The capsule systems are also generalized to other combinations of active ingredients and oils, and tailored nanodroplet sizes. With the addition of UV-crosslinkable precursors, the inner nanoemulsion liquid cores can be chemically crosslinked into a nanoemulsion-laden hydrogel for the preparation of core-shell hydrogel particles. The proposed capsule systems provide an advanced platform for the encapsulation and controlled release of nanoemulsions.

2.2 Experimental Section

Materials: Sodium alginate (~39% in guluronic acid blocks, Mw ~ 100 kDa), Span 80 (sorbitan monooleate), Tween 80 (polysorbate), isopropyl myristate (≥98%), calcium chloride ($CaCl_2$), sodium chloride (NaCl), Nile red, vitamin E (α-tocopherol, ≥ 99.5%), corn oil, poly(ethylene glycol) diacrylate (PEGDA, Mn = 700 g/mol), silicone oil, photoinitiator 2-hydroxy-2-methyl-1-phenyl-propan-1-one (Darocur 1173) were purchased from Sigma-Aldrich. Ibuprofen (99%, ACROS Organics™) was purchased from Fisher Scientific™ to be used as an active pharmaceutical ingredient (API). Sucrose (ultrapure) was purchased from VWR Life Science.

Nanoemulsion Synthesis: Nanoemulsions were prepared using a low-energy method (phase inversion approach) at ambient temperature. In this study, two nanoemulsion systems (calcium nanoemulsions and alginate nanoemulsions) were developed for the preparation of alginate capsules and alginate beads, respectively. The two systems are composed of the same oil phase and surfactant. The oil (dispersed) phase was isopropyl myristate loaded with ibuprofen (100 mg/mL), and the surfactant was a mixture of Tween 80 and Span 80 with a HLB value of 13. The HLB value for a mixture of Tween 80 and Span 80 is calculated by HLB = $4.3x_w$ + 15(1 − x_w), where x_w is the weight fraction of Span 80 in the mixture. Span 80 and Tween 80 have HLB values of 4.3 and 15, which represent oleophilic and hydrophilic surfactants, respectively. To engineer the nanoemulsion droplet sizes, calcium nanoemulsions were prepared with surfactant mixtures of different HLB values. For the preparation of calcium nanoemulsions, a 3 g sucrose aqueous solution (25 wt.%) was slowly dripped into a mixture of 1 g API-loaded oil and 1 g surfactant at a magnetic stirring rate of 1000 rpm. After stirred for another 10 minutes at the same speed, the nanoemulsion was added with $CaCl_2$ (0.1/0.2/0.3 g). The resulting calcium concentrations (w_{CaCl_2}) are 0.02, 0.04, and 0.06 g/g nanoemulsion, respectively. For the alginate nanoemulsion, a 3 g alginate aqueous solution (1/2/4% w/v) was slowly dripped into a mixture of 1 g API-loaded oil and 1 g surfactant at a magnetic stirring rate of 1000 rpm. After another 10 minutes of stirring at the same speed, the alginate nanoemulsion is obtained.

Dynamic Light Scattering (DLS): The droplet size and polydispersity index (PDI) of a nanoemulsion were measured by DLS (Brookhaven NanoBrook 90Plus PALS) operated at a

fixed scattering angle of 90° and a temperature of 25°C. The sample was prepared by diluting 5 μL of the nanoemulsion solution with 3 mL deionized water in a cuvette. The dilution is performed to eliminate multiple scattering effects and ensure a consistent baseline. For each sample, five sets of one-minute measurements are done to determine the droplet size distribution.

Alginate Capsules for Nanoemulsion Encapsulation: The inverse gelation technique is used to prepare alginate capsules.[82] The gelation bath was a 200 mL 1% w/v alginate solution with 0.1% w/v Tween 80 added to lower the surface tension. For nanoemulsion encapsulation, 3 mL of a calcium nanoemulsion was loaded into a syringe and dripped into the bath at a dripping height of 10 cm. The stirring rate was maintained at 350 rpm to enhance the mass transfer of calcium ions and prevent the capsules in close contact from sticking together due to the fast gelation process. An 18 gauge (18G, Nordson EFD Optimum®, inner diameter = 0.84 mm, outer diameter = 1.27 mm, length = 12.7 mm) stainless steel dispensing tip was used to drip the calcium nanoemulsions with three different calcium concentrations. For the calcium concentration (w_{CaCl_2}) of 0.04 g/g nanoemulsion, 22 gauge (22G, Nordson EFD Optimum®, inner diameter = 0.41 mm, diameter = 0.72 mm, length = 12.7 mm) stainless steel dispensing tip was also used to prepare smaller capsules for comparison. After all the nanoemulsion in the syringe was dripped into the bath, the bath was stirred for another 1.5 hours. Before the capsules were collected, the alginate bath was diluted four-fold by adding 600 mL deionized water to quench the gelation process. The collected capsules were then washed by deionized water briefly and incubated in a 2% w/v $CaCl_2$ solution at a stirring rate of 350 rpm for 15 minutes. Finally, the alginate capsules were rinsed with deionized water again to remove excess $CaCl_2$ and stored in the refrigerator overnight before release tests.

Alginate Beads for Nanoemulsion Encapsulation: The external gelation technique is used to prepare alginate beads.[82] A 3 mL alginate nanoemulsion was loaded into a syringe and dripped into a 200 mL 2% w/v $CaCl_2$ solution (containing 0.1% w/v Tween 80) at a dripping height of 10 cm. The stirring rate was maintained at 100 rpm to enhance the mass transfer of the calcium ions. An 18G stainless steel dispensing tip was used for dripping the alginate nanoemulsion with three different alginate concentrations. After all the nanoemulsion in the syringe was dripped into the bath, the $CaCl_2$ concentration of the bath was increased to 4% w/v by adding

more $CaCl_2$ into the bath, and the beads were stirred for another 2 hours to ensure complete crosslinking. Finally, the alginate beads were rinsed with deionized water to remove excess $CaCl_2$ and stored in the refrigerator overnight before the release test.

Particle Size and Shell Thickness Analyses: The images of the as-prepared nanoemulsion carriers (capsules and beads) were captured from the top view using a digital camera (Canon PowerShot ELPH 190 IS). ImageJ was used as an image processing tool to characterize the area (A) as well as the maximum and minimum Feret diameters (d_{max} and d_{min}). With these parameters, the carrier outer radius ($r_{carrier}$) and sphericity factor (SF) can be calculated as follows:

$$r_{carrier} = \sqrt{A/\pi} \tag{2.1}$$

$$SF = \frac{d_{max} - d_{min}}{d_{max} + d_{min}} \tag{2.2}$$

To further determine the inner core radius and thickness of the alginate capsules, the capsules were cut in half, and their images were analyzed by ImageJ to determine the shell thickness (h_{shell}). Finally, the core radius (r_{core}) was obtained by subtracting the h_{shell} from the $r_{carrier}$. For each condition, ten carriers are used for analyses.

Viscosity Measurement: TA Instruments DHR-3 stress-controlled rotational rheometer was used to measure the viscosity of the API-loaded nanoemulsion and its continuous phase combinations. The rheometer was equipped with an upper-cone geometry (diameter = 60 mm, cone angle = 1.004°, truncated gap = 29 μm). Viscosities were measured by carrying out shear rate sweeps from 0.1 to 1000 s^{-1} at 20°C. The equilibration time and averaging time were set to be 5 and 30 s.

UV-Vis Spectroscopy: UV-Vis spectrophotometer (Thermo Scientific™ NanoDrop™ One) was used to measure the absorbance spectra of two samples: bulk oil phase (100 mg ibuprofen/mL isopropyl myristate) and O/W nanoemulsion prepared from the oil phase. The light wavelength was swept from 150 to 850 nm. Pure isopropyl myristate and deionized water

was used to determine the baseline for the bulk oil phase and the nanoemulsion, respectively. The characteristic absorbance peaks of the two samples were both at 230 nm.

Release Experiment: The *in vitro* release of API-loaded nanoemulsions from the alginate capsules and beads was measured using a USP Dissolution Apparatus II (Agilent Technologies Varian VK 7025). A Cary 50 UV-Vis spectrometer and an *in situ* probe set, which were integrated in the dissolution apparatus, automatically recorded the absorbance at a wavelength of 230 nm every minute. The release medium of 900 mL 0.9% w/v (0.154 M) saline was used to simulate physiological conditions because of the similar osmolarity to human body fluids. The operating temperature and paddle rotational speed were set at 37°C and 75 rpm, respectively. Before release experiments, the UV-Vis spectrometer was first calibrated with an API-loaded nanoemulsion. The nanoemulsion was then added sequentially into the vessel with the addition mass and the corresponding absorbance recorded. For each release experiment, the number of nanoemulsion carriers (capsules or beads) are controlled so that about 500 mg optimal API-loaded nanoemulsion was released from the carriers. The required numbers of carriers prepared from 18G and 22G needles were 40 and 70, respectively. All reported measurements were repeated three times under identical conditions and averaged values are reported.

Determination of Effective Diffusivity for the Early Diffusion (R1) Regime: Assuming a steady-state diffusion in the radial direction through a spherical shell with inner (r_i) and outer (r_o) radii, we get the following mass transfer per time n_A (mol/s):

$$n_A = \frac{4\pi r_i r_o D_{eff}\left(C_{A,in} - C_{A,out}\right)}{r_o - r_i} \tag{2.3}$$

where $C_{A,in}$ and $C_{A,out}$ are the species concentrations of the capsule core and bath, and D_{eff} is the effective diffusivity of the species in the shell. Because the D_{eff} is determined for the early diffusion regime where most of the nanoemulsion still remains in the capsules, the equation is further approximated by setting $C_{A,in}$ and $C_{A,out}$ to be $C_{A,0}$ (initial species concentration of the capsule core) and 0, respectively. Based on the fact that the cumulative release *R* reaches 100% for the complete release, the $C_{A,0}$ can be further represented in the unit of *R* (%):

$$C_{A,0} = \frac{100\%(V_b + n_c V_c)}{n_c V_c} \tag{2.4}$$

where V_b is the bath volume, n_c is the number of carriers (capsules) added into the release vessel, and V_c is the core volume for each capsule. In the early diffusion regime, the *R* increases linearly with time. Therefore, the n_A can be approximated as:

$$n_A = \frac{\frac{\Delta R}{\Delta t} V_b}{n_c} \tag{2.5}$$

where $\Delta R/\Delta t$ is the slope fitted from the *R* (%) in this regime. Combining the above three equations, we obtain an expression for the D_{eff}:

$$D_{eff} = \frac{\frac{\Delta R}{\Delta t} V_b (r_o - r_i)}{4\pi r_i r_o n_c C_{A,0}} \tag{2.6}$$

The diffusivity of the free nanodroplets in the release medium (37°C 0.9% w/v saline solution) can be estimated by the Stokes-Einstein equation (**Equation 2.7**) as an upper bound of the D_{eff}.

$$D_{SE} = \frac{k_B T}{6\pi \eta_w r_{NE}} \tag{2.7}$$

where k_B is Boltzman constant (1.38×10^{-23} J/K), T is bath temperature (310.15 K), η_w is the water viscosity at 37°C (0.69 mPa-s), r_{NE} is the nanoemulsion droplet radius (~29 nm). The corresponding D_{SE} is 1.13×10^{-11} m^2/s.

Retention Rate Estimation: The retention rate of nanoemulsion carriers is estimated from the result of release test. Theoretically, the optimal nanoemulsion mass m_{opt} (for 100% retention) added in the vessel is estimated by:

$$m_{opt} = n_c m_d \tag{2.8}$$

where n_c is the number of carriers (capsules or beads) added into the release vessel, m_d is the mass of each nanoemulsion droplet dripped into the gelation bath through a syringe for encapsulation. After the release experiment, the actual nanoemulsion mass in the release vessel is determined as:

$$m_{act} = I_{sat}/s_{cal} \tag{2.9}$$

where I_{sat} is the absorbance of saturated bath when all the nanoemulsion is released from the carriers, s_{cal} is the slope of the calibration curve (**Figure 2.3c**) for the mass and absorbance. The retention (R_t) is expressed as $R_t = m_{act}/m_{opt}$.

Vitamin E-Loaded Nanoemulsion-Encapsulated Capsule: A 3 g sucrose aqueous solution (25 wt.%) was slowly dripped into a mixture of 1 g vitamin E-loaded corn oil (20 wt.% vitamin E) and 1 g surfactants (HLB = 13) at a magnetic stirring rate of 1000 rpm. After another five minutes of stirring, the resulting pre-emulsion was ultrasonicated at 30% amplitude in an ultrasonicator with a 24 mm diameter horn (from Cole Parmer) at a frequency of 20 kHz for five minutes. Finally, 0.2 g $CaCl_2$ was added into the nanoemulsion. The nanoemulsion was encapsulated in alginate capsules following the same inverse gelation procedure as described above.

Core-Shell Hydrogel with a Nanoemulsion-Laden Solid Core: A 3 g PEGDA700 aqueous solution (25 wt.%) was slowly dripped into a mixture of 1 g silicone oil and 1 g surfactant (HLB = 15, pure Tween 80) at a magnetic stirring rate of 1000 rpm. After another five-minute stirring, the resulting pre-emulsion was ultrasonicated at 20% amplitude in an ultrasonicator with a 24 mm diameter horn (from Cole Parmer) at a frequency of 20 kHz for 15 minutes. Finally, 0.2 g $CaCl_2$ and 50 μL photoinitiator (Darocur 1173) were added into the nanoemulsion. To encapsulate the UV-crosslinkable calcium nanoemulsion, the same inverse gelation technique was applied. The only difference is that the alginate bath was exposed to a UV lamp (365 nm, 1.3 W) for the first 30 minutes of the gelation period.

2.3 Results and Discussion

2.3.1 Preparation of Calcium API-Loaded Nanoemulsions and Their Encapsulation in Alginate Capsules

To encapsulate a nanoemulsion containing an active pharmaceutical ingredient (API) in an alginate capsule, a non-ionic nanoemulsion loaded with an API is first prepared using a low energy phase inversion method,[83] followed by the addition of $CaCl_2$ into the aqueous continuous phase. Ibuprofen is used as a model API because of its poor water solubility (0.021 mg/mL at 25°C)[84] and is dissolved in isopropyl myristate (100 mg/mL) as the oil phase. The water phase containing 25 wt.% sucrose solution is slowly dripped into a mixture of the oil phase and surfactants (a mixture of 81.3 wt.% Tween 80 and 18.7 wt.% Span 80 with a hydrophilic-lipophilic balance (HLB) value of 13) (**Figure 2.1a**). The resulting nanoemulsion has an oil weight fraction of approximately 20 wt.% and a surfactant-to-oil ratio (SOR) of 1. During the dilution process, the system passes through an inversion point where the interfacial tension of the oil-water interface is significantly decreased, and thus small droplets are formed. Sucrose is chosen as a small molecule thickener to slightly increase the nanoemulsion viscosity for the subsequent formation of spherical capsules. Viscosifying the continuous phase has been reported to decrease the nanodroplet size which leads to enhanced long-term nanoemulsion stability by mitigating gravitational separation and droplet coalescence.[17] To enable the capsule gelation process, calcium chloride is added into the nanoemulsion. In this study, nanoemulsion dispersions containing various calcium concentrations are prepared. Because the oil nanodroplets are stabilized by non-ionic surfactants, the introduction of calcium ions into the continuous aqueous phase does not perturb the system. The droplet size for each as-prepared calcium containing nanoemulsion is approximately 50 nm (**Figure 2.1b**). The polydipersity index (PDI) of each calcium nanoemulsion varies between 0.1 and 0.2, which lies in the typical range for nanoemulsion systems.[13] **Figure 2.1c** shows an optical image of an as-prepared calcium nanoemulsion in a glass vial. The nanoemulsion is optically transparent because the small droplets remain colloidally stable and weakly scatter visible light. Capsules are synthesized by dripping the calcium nanoemulsion into an alginate bath (**Figure 2.1d**). When a droplet containing nanoemulsion and calcium ions enters the bath, the calcium ions quickly diffuse out and crosslink the alginate polymers around the droplet into a thin shell. The alginate

shell prepared from 1% w/v sodium alginate solution has a mesh size of about 10 nm[79] and is able to entrap nanodroplets. Excess calcium ions continue diffusing out and the alginate shell grows until the calcium source supplied in the droplet is depleted. During the gelation process, the alginate bath remains clear with no observable signal of the active ingredient detected by the UV-Vis spectrometer. After the gelation, the nanoemulsion inside the capsules is pipetted out for dynamic light scattering (DLS) measurements to determine the droplet size. The nanoemulsion droplet size is observed to increase slightly with a mean droplet size of 55 nm and a PDI still ranging between 0.1 and 0.2 (**Figure 2.1b**). It is noted that the nanoemulsion still remains stable despite the composition change in the continuous phase. This exceptional stability can be attributed to the kinetic stability of nanoemulsions, which enables them to be less sensitive to environmental changes compared to microemulsions.[19]

Although alginate capsules have been extensively applied to encapsulate different materials, forming spherical capsules via droplet dripping still remains difficult because of the high viscosity of an alginate solution which deforms impinging droplets into non-spherical shapes. Therefore, the calcium precursor solutions are generally viscosified with a nongelling polymer.[85,86] The viscosity of an emulsion suspension diverges asymptotically with increasing oil fraction. The droplets become closely packed and their motions are severely constrained.[87,88] Compared to a macroemulsion, a nanoemulsion has a much higher effective volume fraction than its nominal oil volume fraction. The surfactant shell (with the thickness of δ) around the oil core (with the radius of a) can greatly enhance the nominal oil volume fraction by a factor of $(1+\delta/a)^3$.[89] This unique rheological property renders a concentrated nanoemulsion intrinsically highly viscous, and thus only a minor modulation of the continuous phase viscosity is required to produce spherical capsules. In our work, the as-prepared nanoemulsions have a droplet diameter of $2(\delta+a)$ ~50 nm, and the δ for Tween 80 (the main and larger surfactant in the mixture) is ~3 nm.[90] These dimensions render the "effective oil fraction" to be about 1.50-fold higher than the nominal oil fraction. To demonstrate the rheological benefit of the nanoemulsions in the capsule gelation process, we compare the canonical nanoemulsion formulation to three calcium containing precursor solutions prepared from pure water, a 25 wt.% sucrose solution, and a 25 wt.% sucrose solution containing the same surfactants at the concentration used in the nanoemulsions. The viscosity-shear rate flow curves for these fluids are shown in **Figure A.1**. For alginate gelation, when a liquid droplet

penetrates into the gelation bath, it can create a cavity on the bath surface in about 10 ms.[91] With the cavity depth having the same length scale as the droplet diameter,[91] the liquid droplet experiences a shear rate on the order of 100 s^{-1}. Therefore, the reported viscosity values are averaged across shear rates between 10 and 1000 s^{-1}. **Figure 2.1e** shows the viscosity for each calcium precursor solution and the corresponding capsule prepared through the dripping process shown in **Figure 2.1d**. It is noted that the addition of sucrose in water can only increase the viscosity from 0.95 to 2.32 mPa-s, which is still much smaller than the viscosity of the 1% w/v alginate bath (9.85 mPa-s). Therefore, the capsules are severely elongated for these two solutions. For the 3 g sucrose solution (25 wt.%) with added 1 g surfactants (a mixture of 81.3 wt.% Tween 80 and 18.7 wt.% Span 80 with HLB value of 13), the viscosity is about four times higher than that of the alginate bath, and more spherical capsules can be prepared. However, a large proportion of the capsules still have a distorted pear-like appearance. In contrast, the nanoemulsion dispersion has a viscosity of 301 mPa-s which ensures the formation of uniformly spherical capsules (more discussion is in **Appendix A.1**).

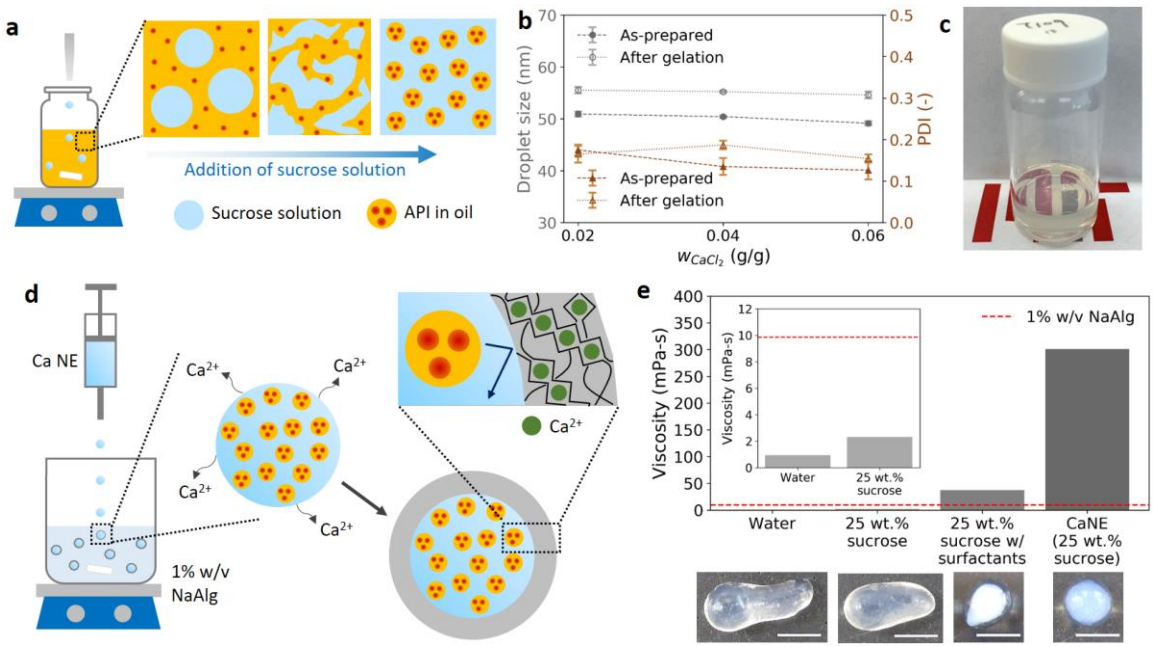

Figure 2.1. Overview of the nanoemulsion and capsule synthesis. (a) Schematic diagram of the low-energy nanoemulsion preparation. Ibuprofen-loaded isopropyl myristate (oil phase) added with surfactants are slowly diluted with 25 wt.% sucrose solution. (b) Droplet size and polydispersity index for the as-prepared and post-gelation calcium-added nanoemulsions containing calcium concentrations w_{CaCl_2} of 0.02, 0.04, 0.06 g/g nanoemulsion. (c) Optical image of an as-prepared calcium-added nanoemulsion in a glass vial. (d) Schematic diagram of the formation of alginate capsules for nanoemulsion encapsulation. The calcium ions diffuse out and ionically crosslink the alginate polymers. (e) Viscosity of the nanoemulsion solution used to produce spherical capsules compared to the viscosity of water, 25 wt.% sucrose and the nanoemulsion continuous phase, each containing 0.2 g $CaCl_2$. The dotted red line represents the viscosity of the 1% w/v alginate bath. Corresponding images for the capsules prepared with each solution are shown below. The scale bar is 5 mm.

2.3.2 Size and Shape Analyses of Capsules Prepared under Different Conditions

With an ideally high viscosity, the nanoemulsion dispersion can be easily encapsulated into uniformly spherical alginate capsules (**Figure 2.2a**). The transparent ring and blue-shining inner regions indicate the alginate shell and the inner API-loaded nanoemulsion, respectively. The nanoemulsion turns blue when the images are taken against a black background (**Figure A.2**). This phenomenon can be attributed to Rayleigh scattering, which happens when the capsules are observed away from the light source and the nanodroplets are much smaller than the wavelength of visible incident light.[92] Blue light of a shorter wavelength is scattered more

strongly than other light of longer wavelengths. **Figure 2.2b-e** show the capsules prepared under the four different conditions (capsules in groups are shown in **Figure A.3**). With the same 18G dispensing tip (**Figure 2.2b, d, e**), the inner cores look similar in size but the shell thickness increases with increasing w_{CaCl_2}. The inner core size can also be tuned by controlling the size of the dispensing tip (**Figure 2.2c, d**). As mentioned before, the alginate mesh size is smaller than the oil nanodroplets. In addition to the optical images that clearly show the two different regions for the inner core and outer shell, a lipophilic dye is also introduced into the oil phase to label the nanodroplets in a capsule. **Figure 2.2f** shows the fluorescence microscopy image of a capsule with dyed nanodroplets. The inner core shows a strong fluorescence while the outer shell still remains black, which again demonstrates the effective encapsulation of nanoemulsions in the capsules with our technique. **Figure 2.2g** further shows the capsule radius, shell thickness, and core radius that are determined using ImageJ image analysis software. The quantitative results match our observation that the core radii are very similar for the same 18G dispensing tip for the different calcium concentrations, however the shell thickness is proportional to the w_{CaCl_2} (**Figure 2.2h**). Previous work also finds a similar trend and explained that a higher calcium concentration across the shell leads to a larger gradient for calcium ions to diffuse out, and thus a thicker shell can be formed.[86] Holding w_{CaCl_2} constant at a value 0.04, dispensing tips with different sizes are utilized to control inner core radii. The relationship between the tip size and inner core size can be described by Tate's law[93] in which the inner core size is proportional to the cube root of the tip size (**Figure A.5**). Sphericity factors are also determined from the maximum and minimum Feret diameters of the capsules. The sphericity factors for all the conditions are lower than a threshold value of 0.05 (**Figure 2.2i**), below which the capsules are considered spherical.[93]

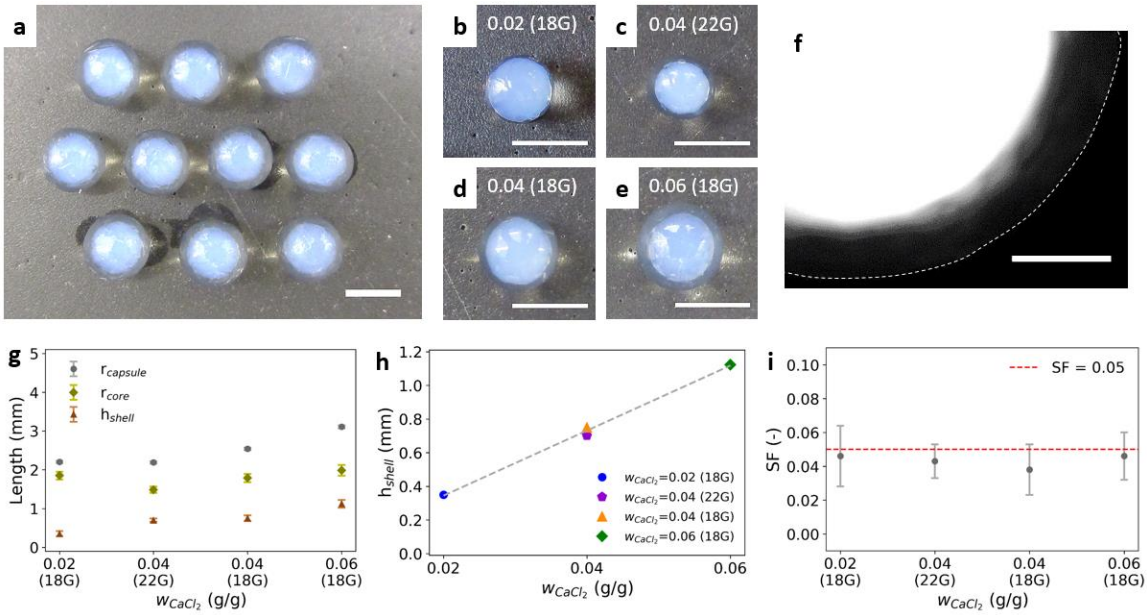

Figure 2.2. Overview of the nanoemulsion-laden capsule dimensions. Weight fraction of calcium chloride w_{CaCl_2} is defined as the calcium chloride mass divided by 5 g nanoemulsion. (a) Optical images of capsules prepared with w_{CaCl_2}= 0.06 and an 18 gauge (18G) dispensing tip. **(**b-e) Zoomed-in optical images of capsules prepared using different preparation conditions: (b) w_{CaCl_2}= 0.02 and 18 gauge dispensing tip, (c) w_{CaCl_2}= 0.04 and 22 gauge dispensing tip, (d) w_{CaCl_2}= 0.04 and 18 gauge dispensing tip, (e) w_{CaCl_2}= 0.06 and 18 gauge dispensing tip. (f) Fluorescence microscopy image of a capsule prepared with a lipophilic dye added into the oil phase to label nanodroplets. The white dotted line is the capsule boundary determined from the bright field microscopy image. (g) Capsule dimensions (outer radius, core radius, and shell thickness) of capsules prepared under different conditions. (h) Linear correlation between shell thickness and w_{CaCl_2}. (i) Sphericity factors (SF) of the capsules for different preparation conditions. Scale bars for (a-e) and (f) are 5 mm and 1 mm, respectively.

2.3.3 Development of Release Tests and Controlled Release for Different Preparation Conditions

Controlled release is a potential benefit provided by encapsulating a nanoemulsion in alginate capsules. A common and straightforward method utilized to monitor release in prior studies is to combine solvent extraction and UV-Vis measurement.[36] However, with this method it is difficult to measure the release in real time in an automated manner. To develop an alternative method, we first compare the UV-Vis spectra of the bulk API-loaded oil phase and the nanoemulsion prepared from only the oil phase (**Figure 2.3a, b**). Both samples have a characteristic peak occurring at 230 nm. In the nanoemulsion, the Tween 80 also shows strong

absorption at this wavelength while the continuous phase materials (sucrose and alginate) have negligible signals (**Figure A.6**). The UV-Vis results indicate that we could possibly apply UV-Vis spectroscopy to directly measure the release of the nanoemulsion droplets (and micelles) that consist of the surfactants and dispersed phase. To demonstrate the applicability of this idea, a calibration curve is developed between the UV-Vis absorbance and the nanoemulsion mass added into the dissolution apparatus (**Figure 2.3c**). A nanoemulsion dispersion with a known mass is added sequentially into the release vessel filled with a 900 mL saline solution, and the corresponding absorbance is recorded. A linear trend is observed for the calibration curve. In our release experiments, the nanoemulsions are substantially diluted in the release vessel and the resulting oil volume fraction is $\sim 10^{-4}$ (v/v), which can minimize the light scattering events resulting from the nanoemulsions.[92] With the linear calibration curve, release tests are conducted to obtain the release profiles of capsules for the four different preparation conditions (**Figure 2.3d**). The four release profiles show a similar trend that can be visually separated into three regions. Based on the observation during the release tests, we separate each release curve into three regimes: early diffusion (*R1*), bursting (*R2*), and post-release (*R3*) regimes. In the early diffusion (*R1*) regime, the nanoemulsion droplets in the capsules (diameter ~58 nm) slowly diffuse out through the shell yielding nanodroplets in the release medium (diameter ~58 nm) detected by DLS. The droplet diffusion through the alginate shell can be explained by the swelling of the alginate hydrogels in a large volume of calcium-free release medium which expands the mesh size.[94] During the *R1* regime, the calcium alginate gel softens and weakens because the calcium ions are gradually displaced by sodium ions.[95] When the alginate gel is weak enough, a crack forms on the shell and the nanoemulsion starts releasing. The onset of a bursting event leads to a transition of the release profile from a flat line into the region of a shaper slope, which indicates the time point at which the release process enters the bursting (*R2*) regime. In this regime, capsules randomly burst with the nanoemulsion cargo then quickly released into solution. For a single bursting event for a capsule, the nanoemulsion cargo can be released in a few minutes, followed by the remaining capsule dissolving completely in another few minutes. After all the bursting events are finished, the release process enters the post-release (*R3*) regime. In the last regime, the absorbance signal reaches a saturated value indicating complete release of the cargo. The proposed release mechanism is also supported by the optical images of the capsules taken at different time points

during a release process (**Figure 2.3e-h**). From **Figure 2.3e** to **Figure 2.3f**, the shell thickness remains similar while the shell contrast decreases as the ion displacement proceeds for a sufficient amount of time. This indicates that the hydrogel degradation process is uniform across the shell and can be characterized as bulk erosion.[96] For the bursting capsule, a crack forms on the shell and the osmotic pressure between the two sides of the capsule drives the nanoemulsion to release out (**Figure 2.3g**). Because of the large viscosity difference, the nanoemulsion is released as a viscous jet and then gradually diffuses away. The empty capsule after the release can exist for a few minutes before complete degradation (**Figure 2.3h**).

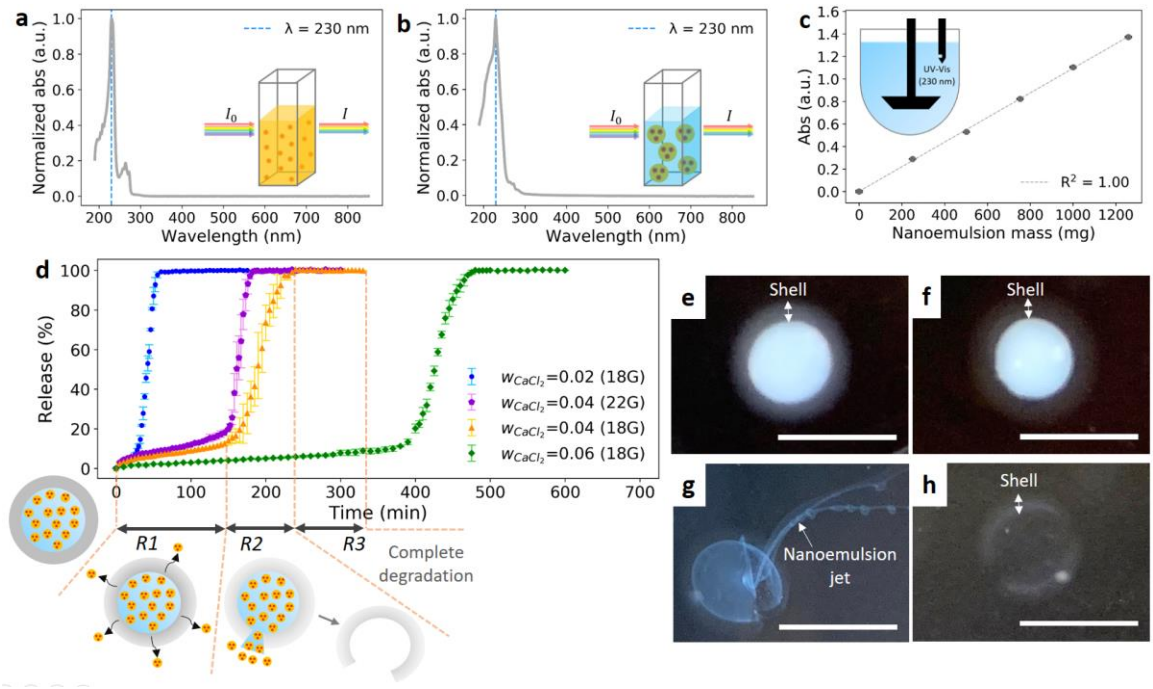

Figure 2.3. Overview of nanoemulsion release experiments. UV-Vis spectra of (a) bulk oil phase (100 mg ibuprofen/mL isopropyl myristate) and (b) nanoemulsion prepared from the bulk oil phase. (c) Calibration curve for absorbance and nanoemulsion mass at λ = 230 nm measured by the UV-Vis spectrometer of the dissolution apparatus. The fitted linear curve has a slope of 1.092×10^{-3}. (d) Release profiles using a USP Dissolution Apparatus II of capsules for different preparation conditions. The schematic images below the release profiles depict the release mechanisms for different regimes corresponding to the w_{CaCl_2} = 0.04 and 18 gauge curve (which also apply to other curves). Regime *R1* is diffusion through the shell. Regime *R2* is the onset of bursting. Regime *R3* is post-release. (e-h) Optical images of capsules (w_{CaCl_2} = 0.04 and 18G dispensing tip) in a 37°C saline bath at different times after being added: (e) *t* = 0 min, (f) in the late *R1* regime (*t* ~140 min), (g) in *R2* regime (t ~ 200 min) when the shell has burst, and (h) in *R2* regime (t ~ 200 min) when the nanoemulsion is depleted. Scale bars are 5 mm.

2.3.4 Quantitative Analyses on the Release Profiles and Stability Tests

The early diffusion (*R1*) regime involves both the diffusion and shell degradation. To deconvolute these two effects, a control experiment with no shell degradation is done in a 37°C deionized water bath (sodium-free environment). The release profile for the control experiment (brown curve in **Figure 2.4a**) closely follows the orange (saline bath) curve in the early diffusion (*R1*) regime, which indicates that the ion displacement process is slow and only begins to have a minor effect on the release in the late *R1* regime. To quantify the *R1* regime, the effective diffusivity (D_{eff}) of the dispersed phase in the alginate shell for each condition is estimated (**Figure 2.4b**, complete results in **Figure A.7a-d**). For typical hydrogels, the D_{eff} is inversely correlated with the crosslinking density.[97] The D_{eff} in **Figure 2.4b** is observed to decrease with increasing w_{CaCl_2}, which can be explained by a more abundant calcium source leading to a higher crosslinking density. To quantitatively identify the bursting (*R2*) regime for a dissolution profile, each regime of the profile is first fitted with a line. The two intersection points between the first two fitted lines (✱) and the last two fitted lines (✚) are defined as the start (t_{start}) and end (t_{end}) bursting time points. The time span between the t_{start} and t_{end} is characterized as the bursting regime in which bursting events can happen randomly in individual capsules to contribute to the increase in nanoemulsion released. The average bursting time (t_{avg}) for the multiple bursting events is then determined by averaging t_{star} and t_{end}. (**Figure 2.4a**, additional data in **Figure A.7e-h**). The release behavior caused by bursting events can be fit by a cumulative distribution function (**Figure A.8**), revealing that the bursting events are statistically random and follow a normal distribution centered at t_{avg}. For the same dispensing tip size, increasing the w_{CaCl_2} leads to a longer average bursting time and a larger standard deviation of the fitted distribution. The longer average bursting time is attributed to the combined effects of the higher crosslinking density and the thicker shell. Because both the crosslinking density and shell thickness increase with the increasing w_{CaCl_2}, we assume a power law function of w_{CaCl_2} to empirically fit t_{avg}. The power-law fitting can approximately describe the trend between w_{CaCl_2} and t_{avg} with an exponent of 2.2 (**Figure 2.4d**), which can be used as the simple design rule for engineering the bursting time of the alginate capsules.

For comparison, we also prepared nanoemulsion-loaded alginate beads by dripping alginate nanoemulsions into a calcium bath (**Figure A.9a**). The alginate nanoemulsion solutions containing alginate but lacking calcium ions and were prepared with the same oil phase, surfactants, and weight fraction as the calcium nanoemulsions. The alginate nanoemulsions with different alginate concentrations show droplet sizes between 50 to 55 nm (**Figure A.9b**), which are very similar to those of the calcium nanoemulsions and allow us to compare the two carrier systems with parity. One of the main differences between the two systems is the retention rates of the nanoemulsion suspension in the formed particles. The capsule gelation bath remains optically clear throughout the gelation process, while in contrast a severe leakage is observed in the bead gelation bath with the transparent bath turning bluish. Because the disparity between the droplet size and alginate mesh size is within an order of magnitude, excessive oil droplets and surfactants are likely to hinder the alginate crosslinking. The severe leakage of the nanoemulsion from the alginate beads is reflected by a low retention rate, which is about 58.8% for the 4% w/v alginate beads and even lower for lower alginate concentrations (**Figure A.10c**). In contrast, the alginate capsules display retention rates higher than 85% for all the conditions (**Figure 2.4e**). For the w_{CaCl_2} higher than 0.04, the retention rates are all above 93%, indicating the effective encapsulation of the nanoemulsion. Detailed calculations for the retention rates of the two carrier systems are tabulated in **Table A.2** and **Table A.3**. **Figure 2.4f** shows the droplet size of the nanoemulsion in capsules over time. The droplet size remains stably around 58 nm over a month with the PDI value lying between 0.1 and 0.2. Because of the uniform distribution and small size, effects of Ostwald ripening, flocculation and coalescence are minimal.

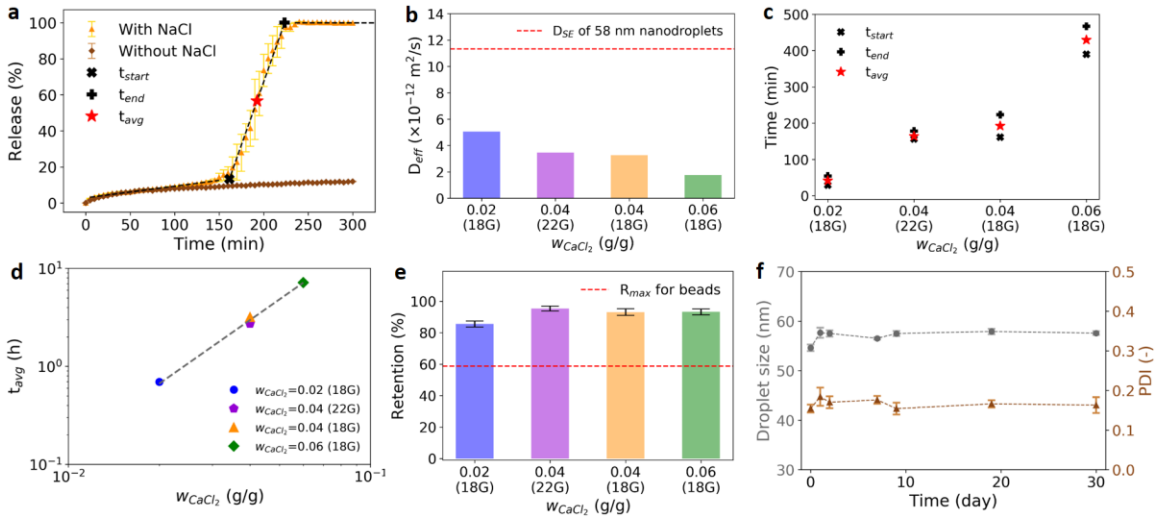

Figure 2.4. Quantitative analysis of release profiles and nanoemulsion stability tests. (a) Comparison of release profiles of capsules (w_{CaCl_2} = 0.04 and 18 gauge dispensing tip) at 37°C in a saline solution (with 0.9 wt.% NaCl) with that in deionized water (without NaCl). Three different regimes of the release profile in the NaCl bath are regressed with linear lines to determine the start (t_{start}), average (t_{avg}), and end (t_{end}) time points in the bursting regime (*R2*). (b) Effective diffusivities (D_{eff}) of the nanoemulsion droplets (and micelles) through the alginate shell in regime *R1* for different preparation conditions. The red dotted line is the diffusivity of free nanodroplets (diameter = 58 nm) in 37°C water determined from the Stokes-Einstein equation. (c) Burst time of capsules for different preparation conditions. (d) Correlation of average burst time with w_{CaCl_2}. (e) Retention of the nanoemulsion suspension in capsules for different preparation conditions. The red dotted line is the highest retention rate achieved in nanoemulsion-loaded alginate beads prepared from the same nanoemulsion. (f) Nanoemulsion stability inside capsules sampled at various times over a month.

2.3.5 Versatility and Extended Applications for Nanoemulsion-Loaded Capsules

To enhance the versatility of the capsule systems, different droplet sizes are engineered by varying the ratio of the two surfactants (**Figure 2.5a**). Decreasing emulsion droplet size has been reported to increase the intestinal absorption of active ingredients.[98] As the surfactant mixture becomes more hydrophilic (increased HLB value), the droplet size decreases. The calcium nanoemulsion of a droplet size of 83 nm is chosen as an example to be encapsulated in alginate capsules for demonstration (**Figure 2.5b**). Because of the larger droplet size, the nanoemulsion liquid core has a bluish-white opacity. In addition to the ibuprofen-loaded isopropyl myristate, the encapsulation technique can also be applied to other combinations of

active ingredients and oils. **Figure 2.5c** shows the encapsulation of a nanoemulsion prepared from a vitamin E-loaded corn oil. The nanoemulsion has a droplet size of 135 nm, thereby leading to an opaque white appearance of the nanoemulsion liquid core due to light scattering. To further extend the applications, core-shell hydrogel particles with nanoemulsion-laden chemically crosslinked hydrogel cores are developed (**Figure 2.5d**). A UV-crosslinkable nanoemulsion is prepared using a 25 wt.% PEGDA700 aqueous solution and a silicone oil. After the addition of $CaCl_2$, the nanoemulsion shows a dual gelation capability for both the alginate and UV light. The alginate thin shell is instantaneously formed when the nanoemulsion is dripped into an alginate bath. The bath is then exposed to a UV light to fully crosslink the nanoemulsion liquid cores into the hydrogels with silicone oil droplets locally locked and embedded in the inner hydrogel matrices. The alginate shell continues growing in the bath until the calcium ions are depleted. The as-prepared core-shell hydrogels are uniform in size (**Figure 2.5e**), and the UV-crosslinked inner core is further examined by cutting the hydrogel in half (**Figure 2.5f**) and by dissolving the alginate shells in an ethylenediaminetetraacetic acid (EDTA) solution (**Figure 2.5g**). The inner core is solid and can be easily detached from the alginate shell, indicating that the UV-crosslinking is effective and the two hydrogel networks are not interpenetrating. Moreover, the shell thickness (0.745±0.051 mm) is almost identical to the canonical condition using the same concentration of $CaCl_2$ (w_{CaCl_2}= 0.04), demonstrating that the shell thickness is not affected by the type of nanoemulsion. In prior studies, introducing additional hydrogel shells around UV-crosslinked hydrogels generally requires multiple steps: first preparing the core particles and encapsulating them in another polymeric shell.[99] The core and shell hydrogels have to be formed separately because the two crosslinkable precursors are miscible. In contrast, our double gelation technique enables the formation of additional alginate shells around UV-crosslinked hydrogels in a single batch. The PEGDA700 molecules are crosslinked shortly after the nanoemulsion is dripped into the bath, minimizing the diffusion of PEGDA700 molecules into the alginate bath and creating a well-defined boundary between the core and shell regions (**Figure 2.5f**). The introduction of additional hydrogel shells around the nanoemulsion-laden hydrogels can find use in various applications, including controlled lipid digestion[78,79] and tunable delayed release for confined crystallization[9,54–56].

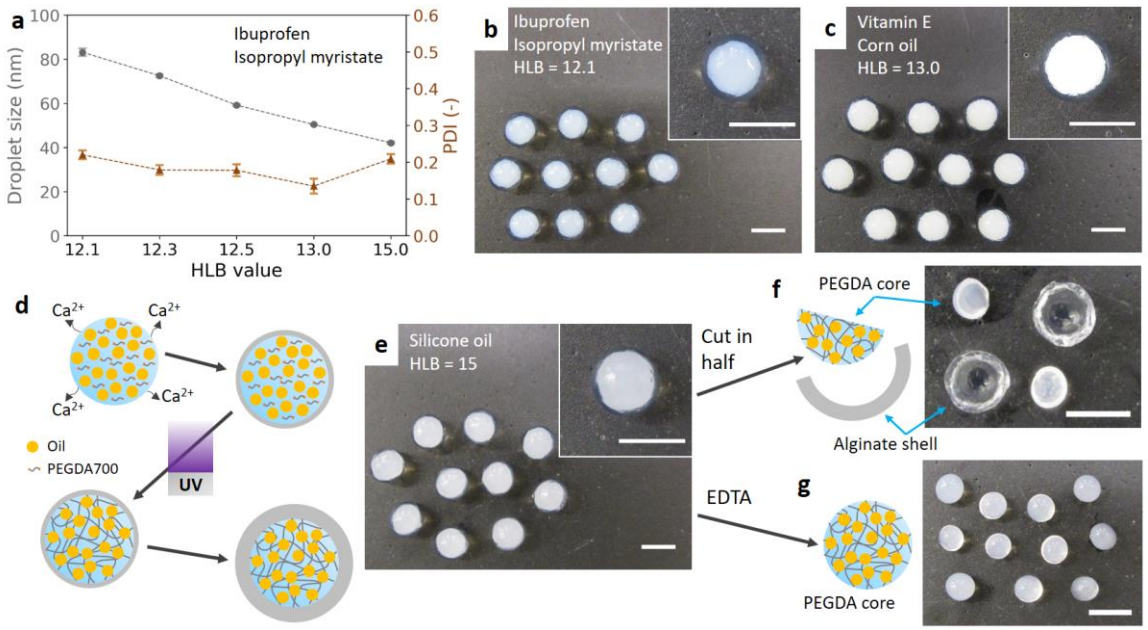

Figure 2.5. Versatility of the approach to prepare capsules with different nanoemulsion sizes, various active chemicals, and chemically crosslinked cores. (a) Relationship between nanoemulsion droplet size and HLB value. The dispersed phase is ibuprofen-loaded isopropyl myristate. (b) Optical image of nanoemulsion-loaded capsules prepared from the calcium nanoemulsion with the HLB value of 12.1 and the dispersed phase of ibuprofen-loaded isopropyl myristate (droplet size = 83.15±1.70 nm). (c) Optical image of nanoemulsion-loaded capsules prepared from the calcium nanoemulsion with the HLB value of 13 and the dispersed phase of vitamin E-loaded corn oil (droplet size = 135.04±1.57 nm). (d) Schematic diagram of the preparation of core-shell hydrogels with a nanoemulsion-laiden, chemically crosslinked PEGDA core. (e) Optical image of the core-shell hydrogels with a nanoemulsion-laden solid core. The nanoemulsion has a HLB value of 15 and the dispersed phase of silicone oil (droplet size = 41.60±0.73 nm). (f) Optical image of core-shell hydrogels after being cut in half and physically extracting the core. (g) Optical image of PEGDA hydrogel cores collected by dissolving alginate shells in an EDTA solution. All capsules in this figure are prepared with w_{CaCl_2} = 0.04 and an 18 gauge dispensing tip. All scale bars are 5 mm.

2.4 Conclusions

We have developed versatile and functional capsule systems for controlled delivery of nanoemulsions that contain lipophilic active ingredients. For the formation of spherical capsules, we leverage the intrinsically high viscosity of the nanoemulsions with only a minor modulation of the viscosity of the continuous aqueous phase through added sucrose. The large viscosity prevents the dripped droplets from deformation due to the drag force exerted by the surrounding alginate solution. The capsule shell thickness and inner core size are easily controlled by varying the calcium concentration and the dispensing tip size, respectively. To investigate the controlled release of the nanoemulsions from the capsules, we developed a facile method to quantify the release of the nanoemulsions through direct UV-Vis measurements in the release vessel. The release profiles of the capsules for different preparation conditions follow a similar trend, and three different release regimes are defined. The nanodroplets first diffuse out slowly through the alginate shell, followed by rapid release due to capsule bursting in a saline solution. The release regimes were quantified to determine the effective nanoemulsion diffusivity through the shell and the bursting time for the capsules. A simple power law equation was developed as a design rule to correlate the bursting time and the calcium concentration. The results show that the bursting time of the capsules can be easily engineered by varying the calcium concentration in the nanoemulsion suspension. The capsules and their contents were very stable, with nanoemulsion droplet size remaining nearly constant over a month of storage. To demonstrate the generality of the approach, nanoemulsion-loaded capsule systems were fabricated with other combinations of active ingredients and oils. In addition, UV-crosslinkable precursors were added into the nanoemulsion solution for the preparation of core-shell hydrogel particles with the oil nanodroplets embedded in the inner chemically crosslinked hydrogel cores. Overall, the versatile capsule systems show great promise for designing carriers with controlled release of functional nanoemulsions, which can find use in a wide range of applications in the food, pharmaceutical, and cosmetic industries.

Chapter 3 Design and Use of a Thermogelling Methylcellulose Nanoemulsion to Formulate Nanocrystalline Oral Dosage Forms

Oral drug products have become indispensable in modern medicine because of their exceptional patient compliance. However, poor bioavailability of ubiquitous low water-soluble active pharmaceutical ingredients (APIs) and lack of efficient oral drug formulations remain as significant challenges. Nanocrystalline formulations are an attractive route to increase API solubility, but typically require abrasive mechanical milling and several processing steps to create an oral dosage form. Utilizing the dual amphiphilic and thermoresponsive properties of methylcellulose (MC), a new thermogelling nanoemulsion and a facile thermal dripping method are developed for efficient formulation of composite particles with the MC matrix embedded with precisely controlled API nanocrystals. Moreover, a fast and tunable release performance is achieved with the combination of a fast-eroding MC matrix and fast-dissolving API nanocrystals. Using the versatile thermal processing approach, the thermogelling nanoemulsion is easily formulated into a wide variety of dosage forms (nanoparticle suspension, drug tablet, and oral thin film) in a manner that avoid nanomilling. Overall, the proposed thermogelling nanoemulsion platform not only broadens the applications of thermoresponsive nanoemulsions, but also shows great promise for more efficient formulation of oral drug products with high quality and tunable fast release.

This chapter has been adapted with permission from L.-H. Chen and P. S. Doyle. Design and Use of a Thermogelling Methylcellulose Nanoemulsion to Formulate Nanocrystalline Oral Dosage Forms. *Advanced Materials* (2021): 2008618.[100]

3.1 Introduction

Pharmaceutical formulation plays an important role in transforming a drug substance into the final drug product taken by a patient. It involves processes that combine an active pharmaceutical ingredient (API) and a mixture of inactive excipients into a final drug product with desired therapeutic effects and physical properties.[101] Among various drug products, oral solid dosage forms are the most preferred product forms dominating the market because of

their high patient compliance and wide acceptance.[1,2] However, conventional oral drug formulations typically require costly multistep manufacturing, and poor bioavailability of hydrophobic APIs still remains a persistent challenge in many formulations. It has been reported that 40% of marketed drugs and 90% of drug candidates in the pipeline are hydrophobic.[3] Their poor water-solubility renders the drugs difficult to be absorbed in the gastrointestinal tract, greatly undermining their potency. Over the past decade, many attempts have been made to develop methods for producing API nanocrystals that possess improved solubility and bioavailability because of their significantly larger specific surface area compared to their bulk counterparts.[59,102,103] However, incorporation of the methods into conventional formulation processes is susceptible to many problems. For example, suitable excipients have to be investigated through tedious trial-and-error experiments,[104–106] and API inhomogeneity raises a potential risk that causes overdosed or ineffective treatment.[5]

Methylcellulose (MC) and hydroxypropyl methylcellulose (HPMC) are two types of natural-based cellulose ester excipients that have been widely formulated into oral solid dosage forms in food and pharmaceutical applications.[41–43] Their unique swelling and erosion behaviors are suitable for the design of controlled release systems and for the study of drug delivery models.[44] Upon contact with water, a gel layer can form on the polymer surface due to rapid hydration, which slows down further water penetration into the inner dry polymer core.[45] In addition, fast release can be easily achieved with the use of MC which shows a much faster matrix erosion than HPMC.[43] Despite these ideal properties, formulations of these cellulose esters and hydrophobic APIs into drug products still lack efficient control over API nanocrystal sizes and heavily depend on multiple blending, sieving, and granulation steps.[107,108] Reversible thermal gelation is another "smart" property of MC and HPMC that has gained considerable attention in the field of rheology[47,48] and tissue engineering.[49,50] The polymer gels upon heating and returns back to the sol state upon subsequent cooling.[48] Although researchers have applied this property to develop *in situ* gelling materials for drug delivery,[51,52] the utility of the thermal gelation property in the formulation of oral solid dosage forms still remains unexplored.

In recent years, hydrogels have been exploited as promising materials for drug product formulations because they can be readily customized into particles with various sizes and shapes.[77,81,109] However, hydrogels are hydrophilic in nature and incompatible with

hydrophobic drugs.[110,111] To address the incompatibility issue and induce API nanocrystalization in the hydrogel matrix, novel technologies have been developed by incorporating hydrophobic nanodomains into hydrophilic hydrogels.[54–56,112,113] The hydrophobic nanodomains, such as oil-in-water nanoemulsions and surfactant micelles, are able to control the formation of API nanocrystals in the hydrogel matrix with tailored drug loading contents. However, hydrogel formation is greatly limited to materials with well-known gelation techniques, such as free radical photopolymerization[113] and ionic-crosslinking.[54,55,112] These materials are generally not the most ideal excipients for oral drug formulation due to their slow release,[113] large release resistance at high drug loadings,[54–56] and potential toxicity.[114] Methylcellulose (MC) is an attractive fast-eroding excipient without the above limitations, though formulation approaches have generally not taken advantage of its gelation properties in forming the drug product. To bridge the gap between the use of fast-eroding MC and the efficiency of oral drug formulation, we report a new thermogelling nanoemulsion system. We develop facile thermal processing methods for the preparation of composite particles and versatile dosage forms with hydrophobic API nanocrystals embedded in the MC matrix.

3.2 Experimental Section

Materials: Methylcellulose (viscosity: 15 cP, molecular weight ~14,000 g/mol), Tween 80 (polysorbate), fenofibrate, anisole, ethyl acetate, sodium chloride (NaCl), ethanol, sodium dodecyl sulfate (SDS) were purchased from Sigma-Aldrich and used without further purification steps.

Synthesis of Thermogelling Nanoemulsions: Prior to nanoemulsion synthesis, the continuous water and dispersed oil phase solutions were first prepared. The continuous water phase was a 5 wt% methylcellulose aqueous solution. The dispersed oil phase was a saturated fenofibrate-in-anisole solution, which was prepared by adding fenofibrate into anisole until excessive fenofibrate crystals settled down in the bottle and could not be further dissolved. To prepare the nanoemulsion, a pre-emulsion was first prepared by vortexing a mixture of the continuous phase, dispersed phase, and Tween 80 in a 50 mL Falcon conical centrifuge tube. The pre-emulsion was then ultrasonicated at 30% amplitude in an ultrasonicator with a 24 mm diameter

horn (from Cole Parmer) at a frequency of 20 kHz for 30 min. The ultrasonicator was kept at 10°C using a cooling circulating water bath. The as-prepared ion-free nanoemulsion was added with 0.1 g NaCl and vortexed for another 30 s. The parameter space for the nanoemulsion synthesis is summarized in **Table B.1**. The droplet size and polydispersity index (PDI) of the nanoemulsion were measured by dynamic light scattering (Brookhaven NanoBrook 90Plus PALS) operated at a fixed scattering angle of 90° and a temperature of 25°C. The sample was prepared by diluting ~5 μL of the nanoemulsion solution with 3 mL deionized water in a cuvette. For each sample, five sets of one-minute measurements were done to determine the droplet size distribution.

Rheological Characterization of Nanoemulsions: Rheological properties of nanoemulsions were characterized using a stress-controlled rheometer (DHR-3, TA instrument) equipped with an upper-cone geometry (diameter = 60 mm, cone angle = 1.004°, and truncated gap = 29 μm) and a temperature-controlled Peltier lower-plate. To minimize the evaporation, a few water drops were added on top of the cone geometry and a solvent trap was used. Before each measurement, a conditioning procedure was performed at 20°C: a pre-shear at a constant rotational speed of 10 rad/s for 60 s, followed by an equilibration duration of 60 s. Temperature ramp measurements were conducted from 20°C to 70°C with a heating rate of 2°C/min, a strain amplitude of 0.1%, and frequency of 20 rad/s. Temperature jump experiments were performed from 20°C to 70°C with a strain amplitude of 0.1% and a frequency of 20 rad/s. Viscosities were measured with the shear rate sweeping from 1 to 1000 s^{-1} at 20°C.

Preparation of Thermogel Particles: Thermogel particles were prepared by a thermal dripping method. The gelation bath was a 300 mL 70°C deionized water added with 0.1% w/v Tween 80 to lower the surface tension. 2-3 mL of the thermogelling nanoemulsion was loaded into a 3 mL syringe and dripped into the bath at a dripping height of 1 cm. The stirring rate was maintained at 150 rpm to enhance the heat transfer. Different dispensing tips were used to vary the particle size: smooth-flow tapered tips (14 gauge, 18 gauge, and 25 gauge) and precision stainless steel tip (30 gauge). After the dripping, the water was removed from the gelation bath until the height of the remaining water was comparable to the particle size. The gelation container carrying the particles and water thin film was quickly transferred to a 70°C oven and

dried for 1 day to evaporate anisole and water. The dried thermogel particles were stored at room temperature before characterization and release tests.

Estimation of Drug Loading Efficiency and Drug Loading Content: Drug loading efficiency (L_E) is estimated as follows:

$$m_{opt} = m_{NE}\psi_{FEN/NE} \tag{3.1}$$

$$\psi_{FEN/NE} = \frac{m_o w_{FEN}}{m_c + m_o + m_{Tw80} + m_{NaCl}} \tag{3.2}$$

$$m_{bath} = C_{bath}V_{bath} \tag{3.3}$$

$$L_E = 1 - \frac{m_{bath}}{m_{opt}} \tag{3.4}$$

where m_{opt} is the optimal fenofibrate mass carried by the as-prepared nanoemulsion, m_{NE} is the mass of nanoemulsion dripped into the heated water bath (with 0.1% w/v Tween 80), $\psi_{FEN/NE}$ is the fenofibrate weight fraction in the as-prepared nanoemulsion, m_o is the oil phase mass, w_{FEN} is the fenofibrate weight fraction in the oil phase (~45 wt%[55]), m_c is the mass of the continuous water phase, m_{Tw80} is the Tween 80 mass, m_{NaCl} is the NaCl mass, m_{bath} is the mass of fenofibrate diffusing into the bath, C_{bath} is the fenofibrate concentration in the bath after the dripping process, V_{bath} is the bath volume.

Drug loading content (ϕ_{FEN}) is estimated by:

$$\phi_{FEN} = \frac{m_o w_{FEN}}{m_c w_{MC} + m_o w_{FEN} + \zeta_{Tw80} m_{Tw80} + \zeta_{NaCl} m_{NaCl}} \tag{3.5}$$

where w_{MC} is the MC weight fraction in the water phase (5 wt%), ζ_{Tw80} is the retention rate of Tween 80 in the dried particles, ζ_{NaCl} is the retention rate of NaCl in the dried particles.

Drug Loading Content Measurement: The drug loading content of the dried particles was determined by a UV-vis spectrophotometer (Thermo Scientific NanoDrop One). A concentration-absorbance calibration curve was first established using fenofibrate-in-ethanol solutions with different concentrations ranging from 0.01 to 0.5 mg/mL. From the UV-vis

absorbance spectra recorded from 150 to 850 nm, the absorbance peak values occurring at 287 nm (due to carbonyl groups of fenofibrate) was used for developing the calibration curve. For drug loading content determination, dried particles were first cut into fine powders using a razor blade. Then, 10 mg fine powders were added with 3 mL ethanol, and the mixture was vortexed for 1 min. After the powders settled down by gravity, the ethanol solution was sampled and diluted ten times for UV-Vis measurements. All measurements were done in triplicate.

X-Ray Diffraction (XRD) Analysis: The crystalline structures of the as-received bulk fenofibrate crystals and the fenofibrate nanocrystals in the dried particles were characterized by XRD using an in reflection mode (Philips PANalytical X'Pert Pro MPD). The samples were ground and placed on a silicon crystal zero diffraction plate. The instrument is operated at 40 kV with an anode current of 40 m with the X-ray source generated using a copper anode (Kα emission wavelength of 1.54 Å). The diffraction angle 2θ was swept from 4 to 40° with a step size of 0.01671° at a scanning rate of 2°/min.

Differential Scanning Calorimetry (DSC) Analysis: The melting points of the as-received bulk fenofibrate crystals and the fenofibrate nanocrystals in the dried particles were determined using a differential scanning calorimeter (TA Instruments Q2000). Inert environment was maintained in the sample chamber using a nitrogen gas flow at 50 mL/min. For each measurement, Tzero pans and lids were used with ~5 mg of ground sample. A temperature ramp was performed from −10 to 150°C at a heating rate of 10°C/min.

Scanning Electron Microscopy (SEM): The fenofibrate nanocrystals in the dried particles were observed with high-resolution scanning electron microscope (Zeiss HRSEM) at 1 kV accelerating voltage and at a magnification of 30,000X. All samples were prepared on SEM specimen stubs with carbon tape. The SEM images were analyzed with ImageJ to estimate the nanocrystal sizes.

Drug Release Experiment: The *in vitro* release of the dried particles was measured using a USP Dissolution Apparatus II (Agilent Technologies Varian VK 7025). A Cary 50 UV-vis spectrometer and an *in situ* probe set, which were integrated in the dissolution apparatus, automatically recorded the absorbance at a wavelength of 287 nm every minute. The release

medium was a 900 mL 25 mM sodium dodecyl sulfate (SDS) aqueous solution. The operating temperature and paddle rotational speed were set at 37°C and 75 rpm, respectively. For each dissolution test, the sample mass was adjusted based on its drug loading content to maintain the final fenofibrate concentration constant at 10 μg/mL. The release experiment for each sample was done in triplicate.

Preparation of Nanoparticle Suspensions: A dispersed oil phase of 0.1 g fenofibrate-in-0.3 g ethyl acetate was first prepared and added with 3 g 5 wt% MC solution and 0.1 g Tween 80 for preparing the nanoemulsion. After the nanoemulsion was gelled at 50°C in a capped vial for 5 min, the vial was uncapped to evaporate ethyl acetate until twice the mass of the added ethyl acetate (~0.6 g) is removed. The still hydrated thermogel was then redispersed into deionized water to form a MC-stabilized nanoparticle suspension. Observations of the nanoparticles were carried out using an FEI Tecnai G2 Spirit TWIN TEM equipped with a LaB6 filament, operating at an accelerating voltage of 120 kV. The nanoparticle suspensions were drop-cast onto carbon film supported copper grids (size 200 mesh), and bright-field microscopy images were taken using a Gatan CCD camera.

Preparation of Drug-Loaded Tablets: A coffee bean silicone mold was first applied with a small amount of cooking oil to prevent sticking. Each slot of the mold was filled with 0.5 mL of the nanoemulsion. Then, the nanoemulsion was gelled and evaporated in the mold at 70°C for one day and drug-loaded tablets were formed.

Preparation of Oral Thin Films: A poly(dimethylsiloxane) (PDMS) fragment (length by width: 1.5 cm by 1 cm) was used as a substrate for thin-film casting. 0.1 mL of the nanoemulsion was used to coat the PDMS top surface. Then, the PDMS substrate carrying the nanoemulsion thin film was transferred to a 55°C air circulating oven with the nanoemulsion gelled and evaporated for one day. After separated from the substrate, an oral thin film was obtained.

3.3 Results and Discussion

3.3.1 Synthesis and Thermal Gelation of Thermogelling MC Nanoemulsions

To synthesize the thermogelling nanoemulsion, we use MC as both an emulsifier and gelling agent because of its dual amphiphilic and thermoresponsive properties. Fenofibrate is chosen as a hydrophobic model API due to its extremely low water solubility (0.3 μg/mL at 37°C).[115] Anisole is used as a solvent to dissolve fenofibrate because it is approved for pharmaceutical formulation and has a high solubility for hydrophobic APIs.[54] The continuous water phase contains a 5 wt% MC and the dispersed oil phase is an anisole solution saturated with fenofibrate. By ultrasonicating a mixture of the water and oil phases, oil nanodroplets are formed with the MC hydrophobic units adsorbing on the droplet surface. The gelling mechanism of the MC-stabilized nanoemulsion is proposed schematically in **Figure 3.1a**. At low temperatures, the nanodroplets are uniformly dispersed and the free MC chains are soluble in the water phase. As the temperature increases, the MC hydrophobic units associate strongly into hydrophobic junctions,[116] forming a gel network with the oil nanodroplets locally immobilized in the gel matrix. The proposed mechanism is supported by the temperature ramp experiment with a gel point of 29°C (**Figure B.1a**). Moreover, nanoemulsions with different formulations (**Table B.1**) are prepared to explore the parameter space for tuning the nanoemulsion properties. Introducing additional Tween 80 surfactant results in a stronger emulsifying ability and thus the formation of smaller nanodroplets (**Figure 3.1b**). The addition of 0.1 g Tween 80 is found to effectively reduce the nanodroplet size to ~175 nm and provide excess Tween 80 for increasing the oil phase in **Figure 3.1c** (see **Appendix B.1**). Because the nanoemulsion is stabilized by the non-ionic emulsifiers (MC and Tween 80), the incorporation of NaCl into the water phase does not perturb the kinetically stable nanoemulsion. The average droplet size and polydispersity index (PDI) remain almost identical after the NaCl addition (**Figure 3.1b, c**). The good stability of the nanoemulsion to NaCl provides another parameter for potential process improvement. Cl^- ions (salt-out ions) can compete with MC molecules for water hydration, which facilitates and strengthens hydrophobic association of MC into a gel network for better material encapsulation.[117] To demonstrate the thermal gelation property, a representative nanoemulsion (3 g MC solution, 0.3 g oil phase, 0.05 g Tween 80, 0.1 g NaCl)

is characterized with the results shown in **Figure 3.1d-f**. The liquid nanoemulsion gels and becomes solid-like in an inverted glass vial at an elevated temperature (**Figure 3.1d**). The apparent gel temperature is determined to be ~31°C in the temperature ramp experiment (**Figure 3.1e**). The effects of each nanoemulsion component on the gel temperature is discussed in **Appendix B.2**, where gel points below 35°C are reported for different nanoemulsion formulations. Furthermore, the nanoemulsion gels quickly in response to an abrupt temperature jump (**Figure 3.1f**). The combination of the low gel point and fast thermoresponsive nature of the nanoemulsion enables the formation of nanoemulsion thermogel with simple thermal processing.

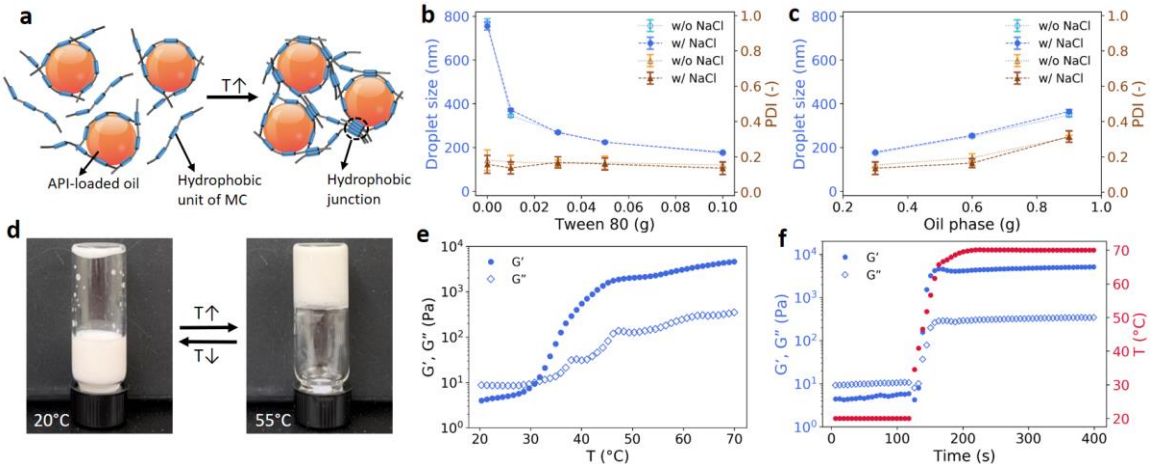

Figure 3.1. Overview of the nanoemulsion properties. (a) Schematic diagram of the thermogelling mechanism. At low temperatures, the nanoemulsion suspension is composed of dispersed MC-stabilized oil nanodroplets and dissolved MC molecules. At elevated temperatures, the hydrophobic groups of MC associate together and a gel network is formed with the oil nanodroplets locally locked inside the thermogel matrix. (b) Average droplet sizes (diameter) and polydispersity indexes (PDIs) for nanoemulsions with different Tween 80 mass (0, 0.01, 0.03, 0.05, 0.1 g) before and after 0.1 g NaCl addition. (c) Average droplet sizes (diameter) and PDIs for nanoemulsions with different oil phase mass (0.3, 0.6, 0.9 g) before and after 0.1 g NaCl addition. d-e) Thermal gelation property of a representative nanoemulsion (3 g MC solution, 0.3 g oil phase, 0.05 g Tween 80, 0.1 g NaCl). (d) Optical images of the nanoemulsion in an inverted glass vial at temperatures of 20 and 55°C. (e) Storage modulus (G') and loss modulus (G'') of the nanoemulsion in the temperature ramp experiment at a heating rate of 2°C/min (0.1% strain, 20 rad/s frequency). Apparent gel point is defined as the cross-over point between G' and G''. (f) Viscoelastic moduli of the nanoemulsion in the temperature jump experiment from a sol state (20°C) to a gel state (70°C) (0.1% strain, 20 rad/s frequency).

3.3.2 Thermal Dripping Process to Formulate API-Loaded Particles

Utilizing the thermal gelation property of the nanoemulsion, a facile process is developed to formulate the nanoemulsion into thermogel particles by dripping the nanoemulsion into a heated water bath. The liquid nanoemulsion gelates into thermogel particles in response to the sudden temperature change when contacting the water bath (**Figure 3.2a**). To prepare spherical particles by dripping a gelling material into a miscible gelation bath, the gelling material has to be sufficiently viscous to overcome the impact and drag forces exerted by the surrounding water.[93] Without any additional thickening agent, the nanoemulsion system can easily achieve a high viscosity by decreasing the droplet size and increasing the oil fraction (**Figure B.2a**). With the addition of 0.05 g Tween 80, the nanoemulsion has a viscosity that facilitates the formation of spherical thermogel particles (see **Appendix B.3**). In this work, we choose 0.1 g surfactant and 0.3 g oil phase (with fixed 5 g MC solution and 0.1 g NaCl) as the canonical condition. **Figure 3.2b** shows the thermogel particles prepared with an 18-gauge dispensing tip using the canonical condition. The particles are nearly spherical with a diameter of 2.72±0.12 mm. Solving for the transient heat transfer in the droplet (see **Appendix B.4**), the droplet surface quickly gels in 10 ms, and the droplet defined by the gelled surface can completely gel in 1.5 s (**Figure B.3**). Fast gelation leads to effective encapsulation with no nanoemulsion leakage detectable by dynamic light scattering. In addition, fenofibrate diffusion from the oil phase to the surrounding water bath is minimal because of the stark difference in fenofibrate solubility. The drug loading efficiencies for all formulations are greater than 99.4 wt%, indicating nearly perfect drug encapsulation (see **Appendix B.5**). The bath water volume is adjusted until the water film thickness is comparable to the particle size, and then the gelation container is directly dried in a 70°C oven without any additional washing step. During the drying, the oil nanodroplets are immobilized in the MC network and define individual crystallization domains, locally inducing API nanocrystals embedded in the dried MC matrix (**Figure 3.2a**). The dried thermogel particles (canonical condition) have a particle size of 1.71±0.10 mm (**Figure 3.2c, d**), corresponding to 75% volume shrinkage of the hydrated particles. The importance of NaCl addition is demonstrated in a control experiment in which the resulting dried particles without NaCl addition buckle due to weak MC hydrophobic association (**Figure B.6**). To observe the confined crystallization enabled by the nanoemulsion templating, SEM imaging is performed on dried API-loaded particles (**Figure 3.2e**) and

pristine MC particles without drug (**Figure 3.2f**). Compared to the pristine MC matrix, the API-loaded particles show clear evidence of embedded nanocrystals in the matrix. The observed nanocrystals have a diameter of 120.6±13.6 nm, which is similar to the predicted nanocrystal diameter (~131.7 nm) based on the oil nanodroplet size and API properties (see **Appendix B.7**). For different nanoemulsion formulations, the observed nanoparticle size in the MC matrix follows the estimated nanocrystal size (**Figure B.7f**), providing evidence of confined crystallization in the nanodroplets. The sizes of the dried particles are also investigated for different formulations (**Figure 3.2g-i**). With the same dispensing tip size, the particle size increases with increasing oil phase mass because a higher oil fraction can create a higher solid content after drying (**Figure 3.2h**). With the same nanoemulsion formulation, the particle size can be effectively controlled by varying the dispensing tip diameter (**Figure 3.2i**), and the correlation can be well described by the Tate's law (**Figure B.8g**).

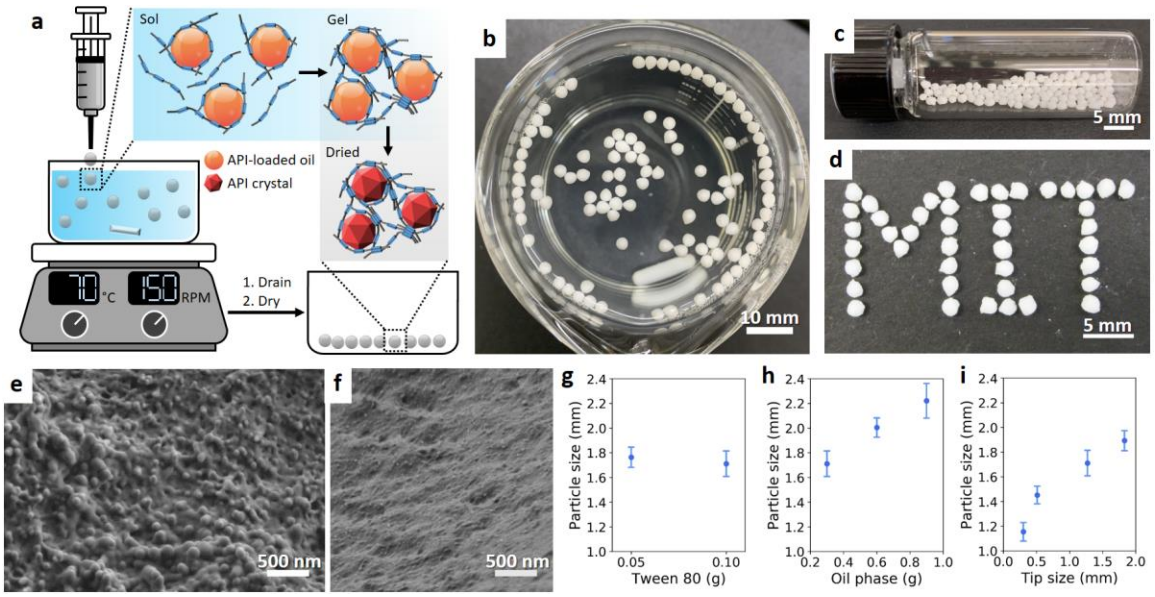

Figure 3.2. Overview of the particle formulation using the thermal dripping process. (a) Schematic diagram of the thermal dripping process. A nanoemulsion at room temperature (~20°C) is dripped into a 70°C water bath stirred at 150 rpm. Once the dripped droplet enters the water bath, the nanoemulsion gelates rapidly in response to the temperature jump. After water removal and solvent evaporation, API nanocrystals are induced locally within the nanodroplets locked within the thermogel network. b-e) Particle formation with the canonical nanoemulsion (3 g MC solution, 0.3 g oil phase, 0.1 g Tween 80, 0.1 g NaCl). (b) Optical image of thermogel particles formed by dripping the nanoemulsion into a 70°C water bath with an 18-gauge dispensing tip. The hydrated particle diameter is 2.72±0.12 mm. (c, d) Optical image of dried particles (c) in a glass vial and (d) on a flat surface. The dried particle diameter is 1.71±0.10 mm. (e) SEM image of the embedded nanocrystals in the dried particles. (f) SEM image of the internal structure of the dried MC particles without drug. (g-i) Correlations between the particle size and various parameters: (g) Tween 80 mass (with an 18-gauge dispensing tip), (h) oil phase mass (with an 18-gauge dispensing tip), (i) dispensing tip outer diameter (with the canonical formulation). Scale bars for (b), (c, d), and (e, f) are 10 mm, 5 mm, and 500 nm, respectively.

3.3.3 Characterization of API Nanocrystals in the API-Loaded Particles

Strategies to increase API loading in a drug product are important because of the great interest to develop smaller drug products for better patient compliance. However, iterative optimization of multiple processing steps are generally required for oral drug formulations with high drug loading contents.[118] **Figure 3.3a** shows the drug loading contents of the dried API-loaded particles as a function of the oil phase mass. The measured drug loading contents lie between the theoretically maximal (blue dashed curve) and minimal (green dash-dotted curve) values, and the loading content curve with 100% and 30% retention for Tween 80 and NaCl (orange dotted curve) is found to well describe the measured drug loading contents (see **Appendix B.9**). With the nanoemulsion system, the drug loading content can be easily scaled up by adding more oil phase without any optimization required of the formulation and process. X-ray diffraction (XRD), Raman spectroscopy, and differential scanning calorimetry (DSC) are used to characterize the polymorphism and crystallinity of the fenofibrate nanocrystals in the particles. The XRD pattern in **Figure 3.3b** confirms the existence of fenofibrate nanocrystals in the particles, with the characteristic peaks aligning with those of crystalline form I fenofibrate at the diffraction angles (2θ) of 12°, 14.5°, 16.2°, 16.8°, and 22.4°.[119] Form I fenofibrate is a desirable form because of its thermodynamic stability compared to the metastable form II and amorphous counterparts. The Raman spectrum also supports that the fenofibrate nanocrystals are form I polymorph (**Figure 3.3c** and **Figure B.11b**).[119,120] Differential scanning calorimetry (DSC) analyses not only suggest the presence of fenofibrate nanocrystals with a single endothermic peak of melting (**Figure 3.3d**) but also show a high degree of crystallinity (~100% in **Figure 3.3e**) approximated with the prior knowledge of decreasing fusion enthalpy for lower melting points[70,113] (see **Appendix B.11**). The Gibbs-Thomson equation predicts that melting point depression becomes more significant for smaller nanocrystals. Compared to the as-received bulk fenofibrate crystals with a melting point of 81.7°C (**Figure B.11c**), the nanocrystal melting point decreases with decreasing nanoemulsion droplet size (**Figure 3.3f**). The melting point depression indicates the effectiveness of nanoemulsion droplets for templating API nanocrystals. Moreover, a linear trend is observed between the melting point and the reciprocal of the droplet size (**Figure 3.3g**). In a prior study, this linear trend was predicted and experimentally realized by carefully confining API crystallization in the nanopores of commercial pore glass.[70] However, unlike the rigid

templates that are limited to certain specifications, "soft" templates enabled by the nanoemulsion provide a flexible approach to simultaneously control the drug crystal size and the drug loading content (i.e., crystal density) for designing a wide range of drug products.

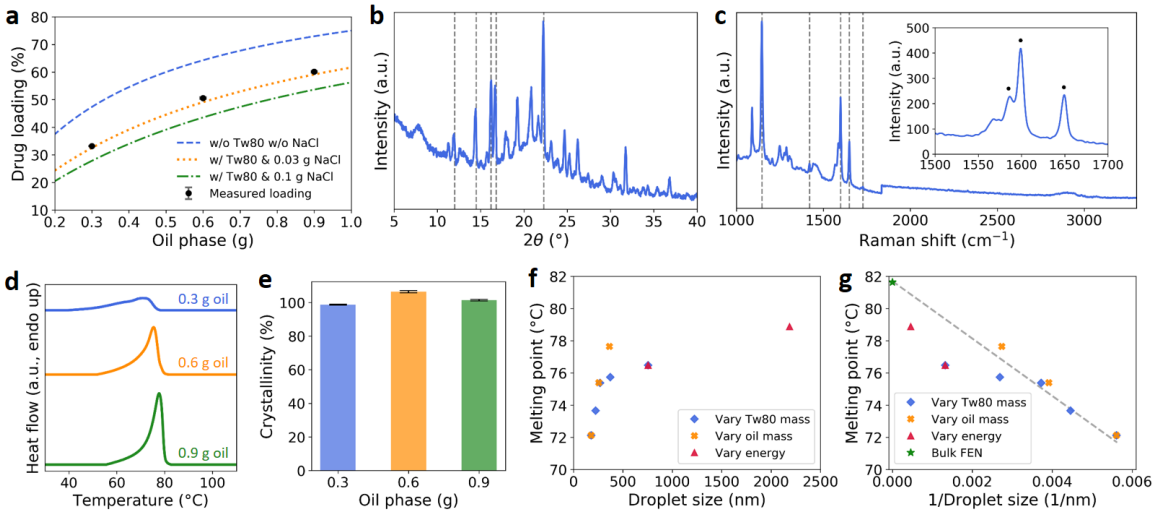

Figure 3.3. Characterization of the fenofibrate nanocrystals in the dried API-loaded particles. (a) Drug loading content of the particles as a function of oil phase mass (fixed 3 g MC solution, 0.1 g Tween 80, 0.1 g NaCl). The blue dashed curve corresponds to **Equation 3.5** with ζ_{Tw80} = 0 and ζ_{NaCl} = 0 (complete removal of Tween 80 and NaCl). The orange dotted curve corresponds to **Equation 3.5** with ζ_{Tw80} = 1 and ζ_{NaCl} = 0.3 (100% and 30% retention for Tween 80 and NaCl). The green dash-dotted curve corresponds to **Equation 3.5** with ζ_{Tw80} = 1 and ζ_{NaCl} = 1 (complete retention of Tween 80 and NaCl). (b) X-ray pattern and (c) Raman spectrum of the fenofibrate nanocrystals in the particles. The inset is the zoomed-in high frequency Raman spectrum. The dashed lines and black dots indicate the characteristic peaks for crystalline form I fenofibrate. (d) DSC thermograms and (e) crystallinity of the fenofibrate nanocrystals in the particles for different oil phase mass. (f) Correlation between the melting point and droplet size. (g) Correlation between the melting point and the reciprocal of droplet size. The bulk fenofibrate is assumed to be templated by an infinitely large droplet (1/droplet size ~ 0).

3.3.4 Release Performance and Analyses of the API-Loaded Particles

Next, the release performance of the API-loaded dried particles was evaluated and compared to that of bulk fenofibrate crystals (**Figure 3.4a** and complete release profile in **Figure B.13a**). The bulk crystals with a size of ~239.6 μm (**Figure B.9a**) are nearly insoluble — it takes 12.1 hours to reach 80% release and another 19.4 hours to reach complete release. As expected, all the nanocrystal-loaded particles show a significantly faster release (**Figure 3.4a, b** and **Figure B.13b**). For different oil phase mass, the release profiles are nearly identical (**Figure 3.4a**),

which is ideal for maintaining the release performance when the drug loading content is increased. In **Figure 3.4b**, varying the particle size for the same nanoemulsion is shown to be an effective approach to engineer the release profile, with the reduction of particle size accelerating the drug release. Furthermore, the crushed particles with the similar size of the bulk fenofibrate crystals show a very fast drug release — 5.4 minutes to reach 80% release and another 8.6 minutes to reach complete release (purple curve in **Figure 3.4b**). The fast release is attributed to the combination of the nano-sized API crystals and fast-eroding MC matrix. **Figure 3.4c** shows the 80% release time (t_{80}) with respect to the drug loading content. The t_{80} can be easily tuned by varying the particle size with the same formulation (vertical change in **Figure 3.4c**) and is maintained nearly constant with increasing drug loading content (horizontal change in **Figure 3.4c**). The constant t_{80} over a wide range of drug loading content can facilitate the design of drug products with a good control over the release performance. Although we have previously shown that alginate hydrogels formulations have fast release that performs very well against the commercial fenofibrate product, the release rate plummets as the drug loading content exceeds 40% (**Figure B.13g**).[55] The release mechanism of alginate hydrogels is through dissolution and diffusion,[112] and above a certain drug loading content threshold the dissolved drug molecules cannot diffuse out effectively for further dissolution. In contrast, the MC particles not only show an even faster release than alginate particles at lower loading contents but also maintain the good performance at high loading contents using both the erosion rate (a/t_{80}) and diffusivity (a^2/t_{80}) metrics (**Figure B.13h, i**). To understand the release mechanism of the particles with the MC matrix, a power law model (**Figure 3.4d** with **Equation B.26**) is used to fit the release profiles.[121] The exponent n values are greater than 1.2 for all cases (**Figure B.14a**), indicating the drug release is strongly erosion-controlled.[122] This finding agrees well with the observation that the drug release occurs with the eroding matrix and is complete once the particles are fully eroded. The synchronous behavior of the drug release and particle erosion implies that nanocrystals dissolve very fast and the drug dissolution is no longer a rate-determining step. To further analyze the release kinetics, an erosion model for an erodible sphere (**Figure 3.4d** with **Equation B.32**) is used to determine the erosion constant and lag time.[123] The lag time is introduced to account for the release suppression due to the initial wetting of the dried particles when they first contact water.[124] The lag time is positively correlated with the particle size (**Figure 3.4e**). The smaller

particles have a larger surface area for faster hydration before the erosion plays an important role. For the crushed particles, the wetting and erosion almost happen simultaneously with the lag time approaching zero. Moreover, the erosion model accounting for the particle size can help explain the convoluted effects on the release profiles. Increasing the oil phase mass corresponds to a larger ratio of the dispersed to continuous phases, and the resulting dried particles have a higher drug loading content and a lower MC polymer content. Therefore, although the particles are larger for more oil phase addition (**Figure 3.2h**), the lower polymer content leads to a faster erosion rate (**Figure 3.4f**). The two factors offset each other and maintain a nearly constant performance when the oil phase is increased (**Figure 3.4a**).

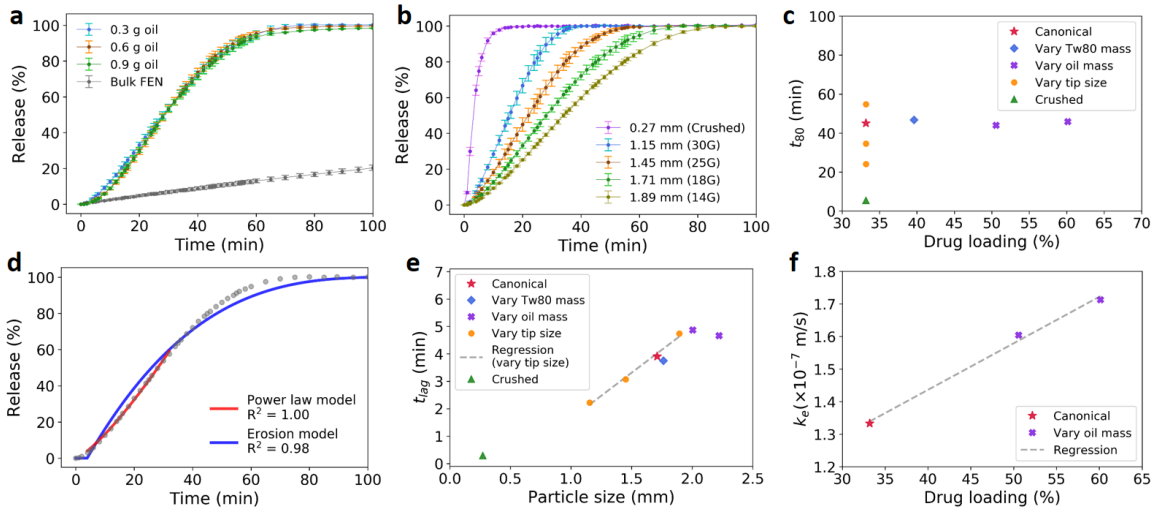

Figure 3.4. Release performance and analyses of the dried API-loaded particles. (a) Cumulative release profiles of the as-received bulk fenofibrate crystals (diameter ~239.6 μm) and the particles with different oil phase addition (fixed 3 g MC solution, 0.1 g Tween 80, 0.1 g NaCl). (b) Cumulative release profiles of particles with different diameters (obtained via crushing and varying dispensing tip size for the canonical formulation). The legend includes the particle diameter and tip specification. (c) Time at 80% drug release (t_{80}) plotted versus the drug loading content for different conditions. (d) Fitting the release profile of the canonical condition with the power law and erosion models. (e) Correlation between the lag time (t_{lag}) and particle size. (f) Correlation between the erosion constant (k_e) and drug loading content.

3.3.5 Versatility of the Thermogelling MC Nanoemulsion to Formulate Various Dosage Forms

In addition to the aforementioned particle formulation, the thermogelling nanoemulsion with "smart" responsiveness to temperature can be easily crafted into versatile dosage forms by simple thermal treatment. For the preparation of nanoparticle suspensions, conventional processes are typically time-consuming and can take more than 10 hours to mill down API crystals to a desirable nanoscale range.[64] In contrast, soft oil droplets can be easily broken up into nanodroplets in five minutes and approach the minimum droplet size in 20 minutes.[125] Ethyl acetate is chosen as a fast-evaporating solvent (boiling point of 77.1°C) to load fenofibrate in order to induce API nanocrystals before the water phase has dried out. With the same water phase (3 g 5 wt% MC) and 0.1 g Tween 80, the oil phase of a 0.1 g fenofibrate-in-0.3 g ethyl acetate solution is used to form a thermogelling nanoemulsion (**Figure 3.5a**). Gelled at 50°C, the nanoemulsion is then evaporated at the same temperature (**Figure 3.5b**) until twice the mass of the added ethyl acetate (~0.6 g) is removed to ensure the complete removal of ethyl acetate. The still hydrated thermogel is redispersed into deionized water to form a polymer-stabilized nanoparticle suspension, and the uniform nanoparticles can be not only detected by dynamic light scattering but also observed by TEM (**Figure 3.5c**). The nanoparticles (~216.7 nm) are found to be larger than the nanoemulsion droplets (~129.5 nm), suggesting that more MC molecules adsorb on the nanocrystals for better stability after redispersion (**Figure B.15**). To demonstrate the utility of the thermogel in producing nanocrystals, a control evaporation test conducted at room temperature (below the gel point) shows undesirable nanoemulsion destabilization (**Figure 3.5d**) and large crystal precipitation (**Figure 3.5e**). Moreover, a thermal molding method is developed to prepare drug tablets (**Figure 3.5f, g**). Instead of relying on the multistep mixing/transport of API crystals and excipient powders as in the conventional manufacturing,[107,108] drug tablets with embedded API nanocrystals can be directly formulated in a facile and powderless manner. Without the issue about stimulus penetrability,[126] heat flux from the environment can easily penetrate through the nanoemulsion in the mold and ensure the complete gelation. The gelled nanoemulsion is then evaporated *in situ* for one day and the drug tablets are formed (**Figure 3.5g**). Lastly, the nanoemulsion can be thermally cast into oral thin films, which are novel dosage forms that have gained considerable attention in recent years because of their exceptional acceptability for geriatric and pediatric patients.[127] The use of the

thermogelling nanoemulsion can avoid dealing with drug crystal agglomeration that is still a common problem in the conventional casting process.[128] By gelling and evaporating a liquid film of the nanoemulsion on a poly(dimethylsiloxane) (PDMS) substrate (**Figure 3.5h-j**), a paper-like oral thin film with a thickness of ~20 μm can be easily prepared (**Figure 3.5k**).

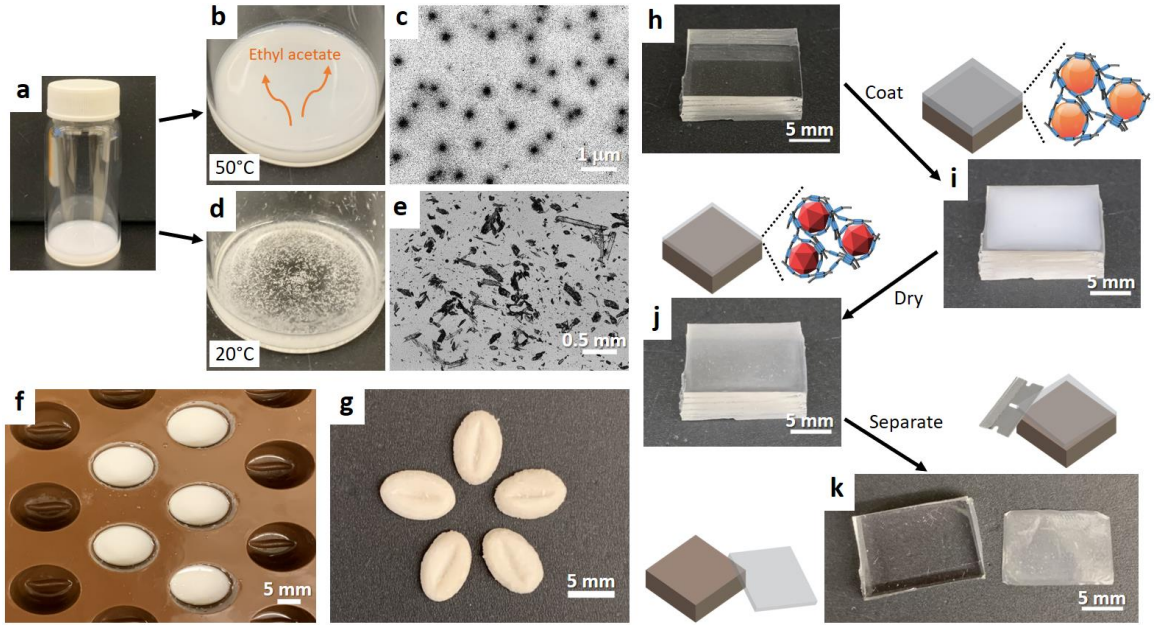

Figure 3.5. Versatility of the thermogelling nanoemulsion in pharmaceutical formulations for various dosage forms. (a) Optical image of the nanoemulsion with the oil phase of a fenofibrate-in-ethyl acetate solution (0.1 g fenofibrate, 0.3 g ethyl acetate). The resulting nanoemulsion has a diameter d_{drop} of 129.5 nm and PDI of 0.195. (b) Optical image of the nanoemulsion thermogel after ethyl acetate is evaporated at 50°C. The redispersed nanoparticle suspension has a diameter of 216.7 nm and PDI of 0.218 (measured by dynamic light scattering). (c) TEM image of the redispersed nanoparticle suspension (diameter 201.4±34.2 nm). (d) Optical image of the nanoemulsion after ethyl acetate is evaporated at room temperature in a circulating fume hood (~20°C). Large fenofibrate crystals precipitate out as droplets are not held in place via a gel network. (e) Bright-field microscopic image of the large crystals from (d). (f) Optical image of a coffee bean mold loaded with the thermogelling nanoemulsion (0.5 mL in one slot). (g) Optical image of the drug tablets in a coffee bean shape after solvent evaporation of the thermogel at 70°C. (h-k) Formulation of oral thin films. (h) Pristine PDMS acts as a platform for thin-film casting. (i) The platform is applied with a nanoemulsion thin film of 0.1 mL. (j) The thin film is gelled and dried at 55°C on the platform. (k) Separated from the platform, an oral thin film with a thickness of ~20 μm is formed. Scale bars for (c), (e), and (f-k) are 1 μm, 0.5 mm, and 5 mm, respectively.

3.4 Conclusions

In summary, we developed a new thermogelling nanoemulsion system that can be easily formulated into composite solid dosage drug products with well-controlled API nanocrystals embedded in the MC matrix. The nanoemulsion suspension has a low gel temperature and fast response to temperature changes which enable the realization of effective particle formulation with a thermal dripping method. The thermally gelled nanoemulsion can be directly dried with the precise formation of API nanocrystals templated by the nanodroplets. The API nanocrystals are characterized to be the most stable polymorph and their presence is validated by SEM, XRD, Raman spectroscopy, and DSC analyses. The significantly improved solubility of the nanocrystals is demonstrated in release tests. The fast drug release is not limited by the dissolution of the API nanocrystals and directly controlled by the fast erosion of the MC matrix. Moreover, the release can be easily tuned by varying the particle size, and fast release is maintained for a wide range of drug loading contents. To demonstrate the versatility of the nanoemulsion formulation, various dosage forms (nanoparticle suspension, drug tablet, and oral thin film) are prepared with a simple and efficient thermal treatment. Overall, the thermogelling nanoemulsion holds significant potential for more efficient formulation of oral drug products with high quality and tunable fast release.

Chapter 4 Thermogelling Hydroxypropyl Methylcellulose (HPMC) Nanoemulsions as Templates to Formulate Poorly Water-Soluble Drugs into Oral Thin Films Containing Drug Nanoparticles

Oral thin films are an emerging solid dosage form for the delivery of poorly water-soluble drugs. Typical thin film formulations require nanomilling of drugs to improve their poor water solubility, followed by incorporating the drug nanoparticles in a polymer solution for casting. However, these formulations are not only inefficient and multistep, but also limited to moderate drug loading capacity and susceptible to irreversible nanoparticle aggregation. Based on a widely used film-forming polymer, hydroxypropyl methylcellulose (HPMC), we developed thermogelling nanoemulsions with drug-loaded oil nanodroplets dispersed in a HPMC-loaded water phase. The nanoemulsions can directly act as film precursors for casting and provide robust templates to formulate oral films with uniform drug nanoparticles embedded in a dried HPMC matrix. The thermally gelled network effectively immobilizes the oil nanodroplets for confined nanoparticle crystallization and avoids potential irreversible nanoparticle aggregation, which enables high drug loading contents up to 63 wt%. The oral films also possess a tunable immediate release because the films have large surface-to-volume ratios and the drug nanoparticles are fast-dissolving. Overall, the thermogelling nanoemulsions show great promise for a more efficient and effective process to formulate HPMC and poorly water-soluble drugs into highly potent oral films with tunable immediate release.

This chapter has been adapted with permission from L.-H. Chen and P.S. Doyle. Thermogelling Hydroxypropyl Methylcellulose (HPMC) Nanoemulsions as Templates to Formulate Poorly Water-Soluble Drugs into Oral Thin Films Containing Drug Nanoparticles. *Chemistry of Materials* (Accepted). Copyright (2022) American Chemical Society.

4.1 Introduction

Solubility of drug molecules is a crucial parameter to consider during the design and formulation of new drug products. Nearly 40% of marketed drugs and 90% of drug candidates in the pipeline are poorly water-soluble (i.e., hydrophobic).[3] The hydrophobic nature makes these drugs difficult to be absorbed in the gastrointestinal tract, resulting in limited bioavailability.[129] Among different strategies to overcome the solubility limitation, particle size reduction has gained the most attention for formulation of poorly water-soluble drugs. By reducing the size of hydrophobic drugs to the nanometer range, the dissolution rate of hydrophobic drugs can be significantly improved compared to their bulk counterparts because of the increased surface area and increased saturation solubility.[59,74] However, nanoparticle suspensions are thermodynamically unstable and susceptible to sedimentation, agglomeration, and crystal growth.[130] Moreover, the suspensions are in a liquid form and should be accurately measured and carefully shaken before administration.[131] Motivated by these issues, tremendous efforts have been made to formulate nanoparticles into oral solid dosage forms that possess improved stability and dosage accuracy,[132] such as tablets and capsules. However, these solid dosage forms are considered difficult to swallow by 37% of the population, which can lead to non-adherence and inappropriate drug modifications.[133]

In the past decade, oral films have emerged as a novel solid dosage form that show great potential over other solid dosage forms for delivery of poorly water-soluble drugs.[127,131,134] Their large surface-area-to-volume ratios enable rapid dissolution and absorption of drugs in the gastrointestinal tract,[131] leading to significantly increased bioavailability.[134] In addition, they are easy to swallow and thus show exceptional acceptability for geriatric, pediatric, and dysphagic patients.[127,131] In a typical film-forming process, a nanosuspension is first prepared and then mixed with a film-forming polymer solution to form a film precursor for casting and drying.[128,135–140] Wet stirred media milling is one of the most extensively used techniques to formulate nanoparticle suspensions, because it is a robust and well-established process that can be applied to many hydrophobic drugs.[61,62] However, it generally involves long milling durations (3-12 h),[63,64] and erosion of milling media may cause severe contamination of drugs.[65,66] In addition, irreversible nanoparticle aggregation during long-time processing and drying is still a common problem that can reduce the dissolution rate of drug nanoparticles and

negatively affect the drug uniformity in oral films.[128,141] The aggregation problem becomes even more prominent when more drug nanoparticles are incorporated in oral films,[141] rendering the oral film technology limited to low drug loading capacity.[131,134] Other film-forming technologies involve the incorporation of amorphous solid dispersions[142–144] and solid lipid nanoparticles,[145–147] both of which provide improved bioavailability of poorly water-soluble drugs. However, amorphous solid dispersions are susceptible to recrystallization that undermines the drug efficacy,[142,148] and the recrystallization becomes more significant with increasing drug loadings.[148] Solid lipid nanoparticles also possess stability issues, such as drug expulsion during storage[149] and polymorphic transformation.[147] Therefore, development of an alternative film-forming technology that addresses the above limitations is imperative.

Hydroxypropyl methylcellulose (HPMC) is one of the most prevalent hydrophilic additives in the food and pharmaceutical industries. HPMC is a naturally sourced biopolymer derived from cellulose[42] and is classified as a safe and non-toxic material by the United States Food and Drug Administration (FDA).[150] The non-ionic nature of HPMC ensures reproducible pH-independent drug release profiles in gastrointestinal fluids with varying pH conditions.[151] With many ideal pharmaceutical features, HPMC has become an excellent film-forming polymer for incorporating hydrophobic drug nanoparticles.[128,135–140] However, formulating HPMC and hydrophobic drugs into oral film products generally requires inefficient and ineffective conventional processes. In addition to inefficient nanoparticle formulations, further mixing of nanoparticle suspensions and a HPMC solution can take another 3-12 h before the mixture is ready for casting.[128,135–139] Moreover, the mixing can dilute the concentration of drug nanoparticles and compromise the drug loading capacity.[152] Therefore, a more effective and efficient film-forming process needs to be developed based on HPMC. From the material fundamentals, HPMC is a well-known emulsifier that has been used to produce oil-in-water emulsions for hair care[153] and eye drop formulation.[154] In addition, it possesses an interesting thermogelling property[155] that has been applied to form injectable gels for drug delivery[156]. Although these two properties have been widely used to develop liquid dosage forms for delivery of drug, they are generally overlooked in oral film formulations that involve incorporating hydrophobic drugs into a HPMC matrix.

In this work, we report a more efficient and effective film-forming formulation that is enabled by thermogelling HPMC nanoemulsions. We leverage the dual emulsifying and thermogelling

properties of HPMC to design the thermogelling nanoemulsions, which provide robust templates to formulate poorly water-soluble drugs into oral films loaded containing drug nanoparticles. HPMC and a surfactant are used to emulsify an oil phase loaded with poorly water-soluble drug for preparing nanoemulsions. The nanoemulsions are thermogelling because the hydrophobic groups of HPMC can associate together to form a gel network upon heating. The thermally gelled nanoemulsions involve drug-loaded oil nanodroplets that are immobilized in a HPMC hydrogel, which ensures confined formation of drug nanoparticles in a HPMC matrix. With the proposed mechanism, the thermogelling nanoemulsions can directly act as film precursors to produce oral films with uniform drug nanoparticles embedded in a dried HPMC matrix. To demonstrate the versatility of the proposed formulation, we develop simple predictive rules and correlations to control the oral film thickness for nanoemulsions with different oil weight fractions, which later correspond to different drug loading contents. The efficacy of the proposed approach is supported by electron microscopy and solid-state characterization techniques. The drug nanoparticles are successfully observed, and the most stable solid-state structure is attained after the oral film formation. Moreover, high drug loading contents of the oral films are achieved by increasing the nanoemulsion volume fraction in the precursor solution without the need to modify any other film formulation steps. We also provide evidence that the drug nanoparticles are uniformly distributed in the oral films without irreversible nanoparticle aggregation. For the release performance, the oral films possess a tunable immediate release that has a strong correlation with the film thickness. We present release models to elucidate the release mechanism of the oral films, and develop a scaling rule for designing their release profiles. Overall, the developed thermogelling nanoemulsions address many limitations that are still common in conventional film-forming processes, such as inefficient formulation steps, low drug loading capacity, and irreversible nanoparticle aggregation.

4.2 Experimental Section

Materials. Hydroxypropyl methylcellulose (HPMC, viscosity of 40-60 cP for 2 wt% in H_2O at 20°C, molecular weight ~22,000 g/mol, methoxyl content of 28-30%, hydroxypropoxyl content of 7-12%), Tween 80 (polysorbate), fenofibrate, anisole, ethanol, sodium dodecyl sulfate (SDS) were purchased from Sigma-Aldrich and used without further purification steps.

Synthesis of Thermogelling HPMC Nanoemulsions. The thermogelling HPMC nanoemulsions consist of a continuous water phase and a dispersed phase oil phase. The continuous water phase was a 4 wt% HPMC aqueous solution. The dispersed oil phase was a saturated fenofibrate-in-anisole solution, which was prepared by adding bulk fenofibrate crystals into anisole until excessive crystals could not be further dissolved and settled down at the bottom. To prepare the nanoemulsions, a pre-emulsion was first prepared by vortexing a mixture of the continuous phase, dispersed phase, and Tween 80 in a 50 mL Falcon conical centrifuge tube. The nanoemulsion compositions for different oil phase mass are summarized in **Table C.1**. The surfactant-to-oil (SOR) ratio was fixed at 1:20 to fix the nanoemulsion droplet size. The pre-emulsion was then ultrasonicated at a 30% amplitude in an ultrasonicator with a 24 mm diameter horn (from Cole Parmer) at a frequency of 20 kHz for 30 min. A cooling circulating water bath was used to keep the ultrasonicator at 10°C.

Dynamic Light Scattering (DLS). The droplet sizes and polydispersity indexes (PDIs) of the nanoemulsions were measured by dynamic light scattering (Brookhaven NanoBrook 90Plus PALS), which was operated at a fixed scattering angle of 90° and a temperature of 25°C. The sample was prepared by diluting 5 μL of the nanoemulsion solution with 3 mL deionized water in a cuvette. The dilution is performed to avoid multiple scattering effects and ensure a consistent baseline. For each sample, five sets of one-minute measurements were done to determine the nanoemulsion size distribution.

Rheological Characterization of Thermogelling Nanoemulsions. The rheological properties of the nanoemulsions were characterized using a stress-controlled rheometer (DHR-3, TA instrument) equipped with a plate geometry (diameter = 40 mm and gap = 500 μm) and a temperature-controlled Peltier lower-plate. To minimize the evaporation, a small amount of water was added on top of the cone geometry, and a solvent trap was used. Before each

measurement, a conditioning procedure was performed: a pre-shear at a constant rotational speed of 10 rad/s for 60 s at 20°C, followed by an equilibration for 60 s at 20°C. Temperature ramp measurements were conducted from 20°C to 70°C with a heating rate of 2°C/min, a strain amplitude of 0.1%, and frequency of 10 rad/s.

Preparation of Oral Films. A microscope slide (plain glass, VWR VistaVision^{TM}) with dimensions of 75×25×1 mm (length×width×height) was used a substrate for oral film formulation. The thermogelling nanoemulsion was poured on a glass slide, and the required nanoemulsion mass for different conditions to achieve the targeted thickness is summarized in **Table C.2**. Then, the glass slide carrying a layer of the nanoemulsion was quickly transferred to a 70°C oven and dried overnight to evaporate anisole and water. After drying, an oral film was detached from the glass slide and stored at room temperature for further characterization and release tests.

Film Thickness Measurement. The thickness of the oral films was measured using a digimatic micrometer (Series No. 293, Mitutoyo) with an accuracy of 0.001 mm. Thickness values were measured at ten different locations across each oral film and were used to calculate the average and standard deviation.

Scanning Electron Microscopy (SEM). The surface and cross-section of the oral films were observed using a high-resolution scanning electron microscope (Zeiss HRSEM) at an accelerating voltage of 1.3 kV. All samples were prepared on SEM specimen stubs with carbon tape. The SEM images were analyzed with ImageJ to estimate the drug nanoparticle size.

Transmission Electron Microscopy (TEM). Observation of the dispersed nanoparticles from the oral films was carried out using an FEI Tecnai G2 Spirit TWIN TEM equipped with a LaB6 filament, operating at an accelerating voltage of 120 kV. The dispersed nanoparticle suspension was drop-cast onto a carbon film supported copper grid (size 200 mesh), and bright-field microscopy images were taken using a Gatan CCD camera.

Drug Loading Measurement. The drug loadings of the oral films were determined using a UV-Vis spectrophotometer (Thermo Scientific NanoDrop One). According to the UV-Vis absorbance spectrum from 150 to 850 nm (**Figure C.7a**), the absorbance peak occurs at λ =

287 nm for the carbonyl groups of fenofibrate. A concentration-absorbance calibration curve was developed using fenofibrate-in-ethanol solutions with different concentrations ranging from 0.01 to 0.5 mg/mL at λ = 287 nm (**Figure C.7b**). For drug loading content measurements, a 10 mg small piece of the oral film was soaked in 3 mL ethanol and vortexed for 1 min. The ethanol solution was sampled and diluted ten times to lie in the range of the calibration curve for UV-Vis measurements. All measurements were done in triplicate.

X-Ray Diffraction (XRD) Analysis. The crystal structures of the as-received bulk fenofibrate crystals and the fenofibrate nanoparticles in the oral films were characterized by XRD using an in reflection mode (Philips PANalytical X'Pert Pro MPD). The oral film was ground and placed on a silicon crystal zero diffraction plate. The X-ray source was generated using a copper anode (Kα emission wavelength of 1.54 Å) at 40 kV and 40 mA. The diffraction angle 2θ was swept from 4 to 40° with a step size of 0.01671° at a scanning rate of 2°/min.

Differential Scanning Calorimetry (DSC) Analysis. The melting points of the as-received bulk fenofibrate crystals and the fenofibrate nanoparticles in the oral films were determined using a differential scanning calorimeter (TA Instruments Q2000). Inert environment was maintained in the sample chamber with nitrogen flowing at 50 mL/min. For each measurement, a set of Tzero pan and lid was used with ~5 mg of the ground oral film. A temperature ramp was performed from −10 to 150°C at a heating rate of 10°C/min.

Raman Spectroscopy. Raman spectroscopy was performed using a Horiba Jobin Yvon LabRAM HR800 system that involves a 633 nm excitation laser, 100× objective lens, and 1800 lines per mm grating. Prior to the measurement, the system was calibrated using the standard 521 cm^{-1} band of Si. The Raman spectra were analyzed using the LabSpec 5 software. The baseline correction of the spectra was implemented using a line with a degree of two. Raman mapping was performed at a step increment of 1 μm in both *x* and *y* directions over 51 μm×51 μm area of the oral film. The Raman mapping was based on the signal at 1650 cm^{-1}.

Tensile Testing. Tensile properties of the oral films were measured using an Instron 8848 MicroTester. Each oral film was first glued onto a hollow cardboard using 5-minute epoxy. The gauge length and width of the thin film were 14 mm and 5 mm, respectively. The cardboard with the oral film was then held between the two clamps, and the connecting parts

of the cardboard were cut. The tensile testing was performed at a constant crosshead displacement rate of 0.005 mm/s until the point of film fracture. A stress-strain curve was obtained for each oral film. The stress (engineering stress) was calculated by normalizing the tensile force over the initial cross-sectional area of the oral film. The strain (engineering strain) was calculated by dividing the difference between the initial and final lengths by the initial length of the oral film. From the stress-strain curve, the tensile strength and the elongation at break were obtained from the maximum stress and the strain corresponding to the maximum stress. The Young's modulus was obtained from the initial elastic deformation region of the stress-strain curve.

Drug Release Experiment. The release profiles of the oral films were measured using a USP Dissolution Apparatus II (Agilent Technologies Varian VK 7025). Integrated in the dissolution apparatus, a Cary 50 UV-vis spectrometer and an *in situ* probe set automatically recorded the absorbance at a wavelength of 287 nm every minute. The release medium was a 900 mL 25 mM sodium dodecyl sulfate (SDS) aqueous solution, which is recommended by the FDA Dissolution Methods Database for fenofibrate dosage forms[157] to simulate *in vivo* solubilization of hydrophobic fenofibrate by biorelevant surfactants.[158,159] Each oral film (15 mm×10 mm) was placed into a USP compliant Japanese Pharmacopoeia sinker basket to decrease the variability of the release results caused by potential floating of the oral films.[160] The operating temperature and paddle rotational speed were set at 37°C and 75 rpm, respectively. The release experiment for each sample was done in triplicate.

4.3 Results and Discussion

4.3.1 Preparation and Thermal Gelation of Thermogelling HPMC Nanoemulsions

Synthesizing the thermogelling HPMC nanoemulsions requires three key elements: continuous water phase, dispersed oil phase, and surfactant. The continuous water phase is a 4 wt% HPMC aqueous solution (**Figure 4.1a**). HPMC molecules are based on a linear polysaccharide cellulose chain with ether-linked methoxy (OCH_3) and hydroxypropyl ($OCH_2CH(OH)CH_3$) side groups. The dispersed oil phase is an anisole solution saturated with fenofibrate. Fenofibrate is selected as a hydrophobic model drug because of its extremely low water

solubility (0.3 μg/mL at 37°C).[115] Anisole is chosen as an organic solvent because it has a high solubility for hydrophobic fenofibrate and is approved for pharmaceutical formulations. In addition to the HPMC molecules in the water phase, a small amount of Tween 80 surfactant (1/20 the mass of the oil phase) is added to help emulsify the oil phase. The mixture of all the above materials is vortexed quickly to form a pre-emulsion, which is then placed in an ultrasonicator kept at 10°C for 30 min. The ultrasonication provides energy to break the large oil droplets into nanoscale droplets. The as-prepared nanoemulsions comprise oil nanodroplets that are uniformly dispersed in the continuous water phase with free HPMC molecules (**Figure 4.1b**). These oil nanodroplets are stabilized by both the HPMC and Tween 80 molecules. The nanoemulsions are thermogelling because of the thermoresponsive nature of HPMC. Upon heating, the hydrophobic methoxy groups of HPMC molecules can associate together to form hydrophobic junctions,[53,161–164] as shown by the red points in **Figure 4.1c**. The hydrophobic association forms a hydrogel network that immobilizes the oil nanodroplets.

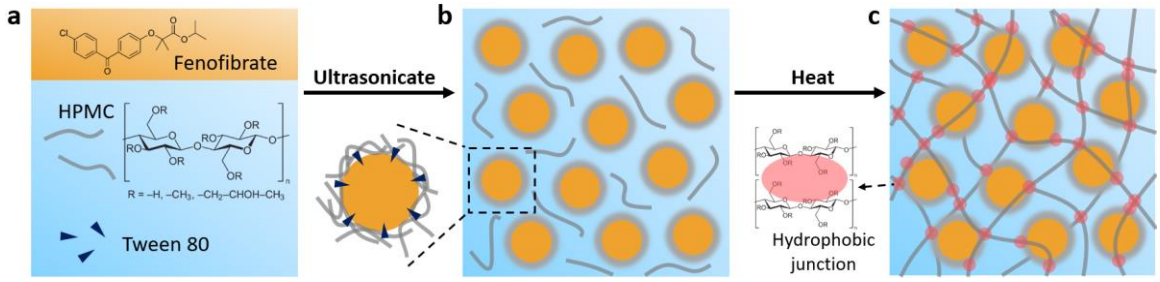

Figure 4.1. Overview of the thermogelling HPMC nanoemulsion preparation. (a) Dispersed oil phase (saturated fenofibrate-in-anisole solution) and continuous water phase (4 wt% HPMC and a small amount of Tween 80 surfactant). The surfactant-to-oil (SOR) ratio is 1:20. (b) As-prepared themogelling nanoemulsion after ultrasonication. The nanoemulsion consists of oil nanodroplets that are stabilized by both the HPMC and Tween 80 molecules, which are illustrated as a diffuse halo around the oil nanodroplets. (c) Gel structure formed by the thermogelling nanoemulsion upon heating. The hydrophobic groups of HPMC associate together to form hydrophobic junctions that lead to a gel structure and immobilize the oil nanodroplets. The hydrophobic junctions are illustrated as red points.

Figure 4.2a shows the average droplet diameters and polydispersity indexes (PDIs) characterized by dynamic light scattering (DLS) for the thermogelling nanoemulsions with different oil phase mass. With the same 3 g continuous water phase, different mass (0.2 g, 0.4 g, 0.6 g) of the dispersed oil phase and a small amount of Tween 80 (1/20 of the oil mass) are added to prepare the nanoemulsions. The surfactant-to-oil ratio (SOR) is fixed at 1:20 to enable

similar nanoemulsion droplet sizes (~350 nm) for different oil mass conditions. The polydispersity indexes (PDIs) of the nanoemulsions vary between 0.1 and 0.2, which lie in the typical range for uniform nanoemulsion droplet sizes.[13,77] To quantify the gel temperatures, temperature ramp experiments are conducted for the pure HPMC and the nanoemulsions (**Figure 4.2b** and **Figure C.1**). In addition, the sol-gel transition is qualitatively demonstrated in a vial inversion test (**Figure 4.2c**). **Figure 4.2d** summarizes the gel temperatures of the pure HPMC and the thermogelling nanoemulsions. Compared to the gel temperature of the pure HPMC (59.4°C), the nanoemulsion with 0.2 g oil has a slightly increased gel temperature (61.3°C). The small change in the gel temperature can be attributed to two competing factors. One is that the oil nanodroplets act as crosslinking points for hydrophobic association upon heating, leading to faster gelation and a lower gel temperature. The other is that amphiphilic Tween 80 molecules can cloak the hydrophobic units of HPMC chains. This cloaking phenomenon delays the gelation and increases the gel temperature, because more energy is required to break away the surfactant molecules and expose the hydrophobic groups for association.[165] With the increasing oil mass from 0.2 g to 0.6 g, the gel temperature of the nanoemulsion decreases. A higher density of the oil nanodroplets provides more crosslinking points that dominate the cloaking effect of surfactant, which facilitates the hydrophobic association and accelerates the gelation upon heating. The elastic moduli and viscous moduli at 70°C of the pure HPMC and the thermogelling nanoemulsions are summarized in **Figure 4.2e, f**. The elastic modulus is higher than the viscous modulus for each condition, indicating solid-like behavior of the gel. The gel becomes stronger with a larger elastic modulus as the oil phase mass increases, because more crosslinking points created by the oil nanodroplets are able to reinforce the gel network.

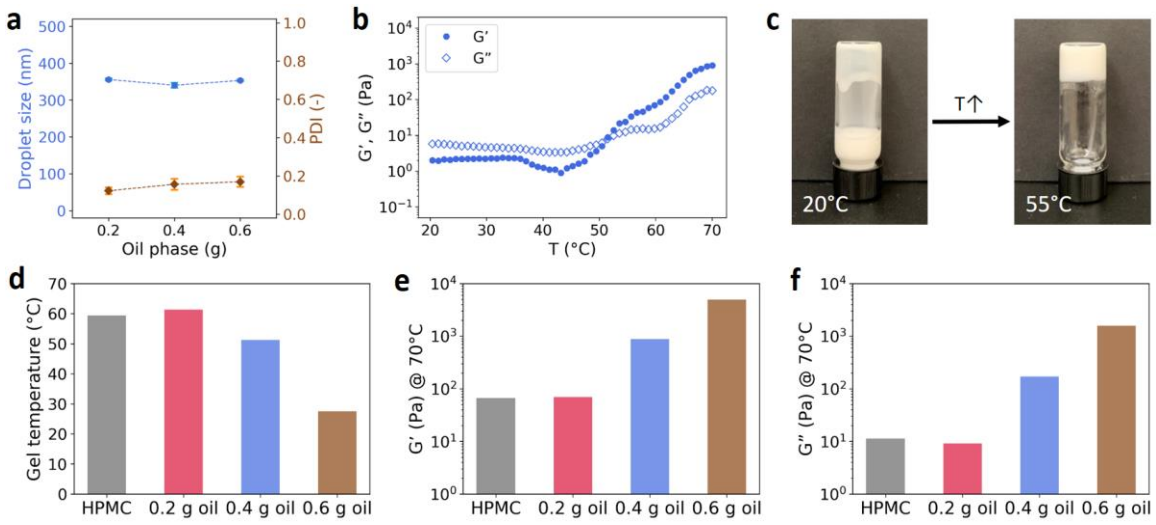

Figure 4.2. Overview of the nanoemulsion properties. (a) Average droplet sizes (hydrodynamic diameters from DLS) and polydispersity indexes (PDIs) for the thermogelling nanoemulsions with different oil phase mass (0.2, 0.4, 0.6 g). (b) Elastic modulus (G') and viscous modulus (G'') of the nanoemulsion (0.4 g) in a temperature ramp experiment at a heating rate of 2°C/min (0.1% strain, 10 rad/s frequency). Apparent gel temperature is defined as the cross-over point between G' and G''. (c) Vial inversion test for the nanoemulsion (0.4 g oil) at temperatures of 20 and 55°C. (d) Gel temperatures of the pure HPMC (gray bar) and the nanoemulsions with different oil mass (red, blue, brown bars). (e) Elastic moduli (G') at 70°C of the pure HPMC (gray bar) and the nanoemulsions with different oil mass (red, blue, brown bars). (f) Viscous moduli (G'') at 70°C of the pure HPMC (gray bar) and the nanoemulsions with different oil mass (red, blue, brown bars).

4.3.2 Preparation of Oral Films with Adjustable Thickness

The proposed film-forming process based on the thermogelling nanoemulsion is shown in **Figure 4.3a-c**. A glass slide is first loaded with a layer of the thermogelling nanoemulsion in the sol state at ~20°C (**Figure 4.3a, d**). The nanoemulsion is then heated to form a gel with immobilized hydrophobic oil nanodroplets (**Figure 4.3b**). The heating temperature is chosen to be 70°C, which is greater than the gel temperatures of the nanoemulsions with different oil phase mass. The drying process then proceeds at the same elevated temperature to evaporate both the water and organic solvent (anisole). During the drying process, the nanoparticles are locally induced within the oil nanodroplets, and the continuous phase hydrogel becomes a dried HPMC matrix (**Figure 4.3c**). Because the thermally gelled network protects the oil nanodroplets from coalescence, each nanodroplet is expected to become a single nanoparticle. Therefore, the dried film (i.e., oral film) involves uniform drug nanoparticles embedded in a dried HPMC matrix. The oral film detached from the glass slide has a white appearance, as shown in **Figure 4.3e, f**. To demonstrate the advantages of the proposed film-forming process, we summarize the conventional methods for preparing oral films that are loaded with fenofibrate microparticles or nanoparticles in **Table 4.1**. The conventional milling methods (wet stirred media milling and fluid energy milling) typically take at least 2 h to mill down solid crystals[128,136–138,140]. Among the conventional methods, fluid energy milling is difficult to reach the desirable nanoscale range (<1 μm).[136,137] Although melt emulsification provides a faster way to form a nanoparticle suspension (~15 min), it requires extreme temperatures (melting at 95°C and sudden cooling to –3°C for fenofibrate), and it can be difficult to avoid irreversible nanoparticle aggregation during cooling.[135] After a nanoparticle suspension is made using the conventional methods, it has to be mixed with a HPMC film-forming polymer solution to form a film precursor for casting. The mixing process is time-consuming (typically 3-12 h)[128,135–139] and can compromise the drug loading content because of the dilution effect.[152] In contrast, the film-forming process enabled by the thermogelling nanoemulsions is more efficient and effective. Because the oil droplets are soft, a thermogelling nanoemulsion can be easily formed in 5 min and reach the minimum droplet size in 20 min.[125] Moreover, the thermogelling nanoemulsion can directly act as a film precursor without further mixing with a film-forming polymer.

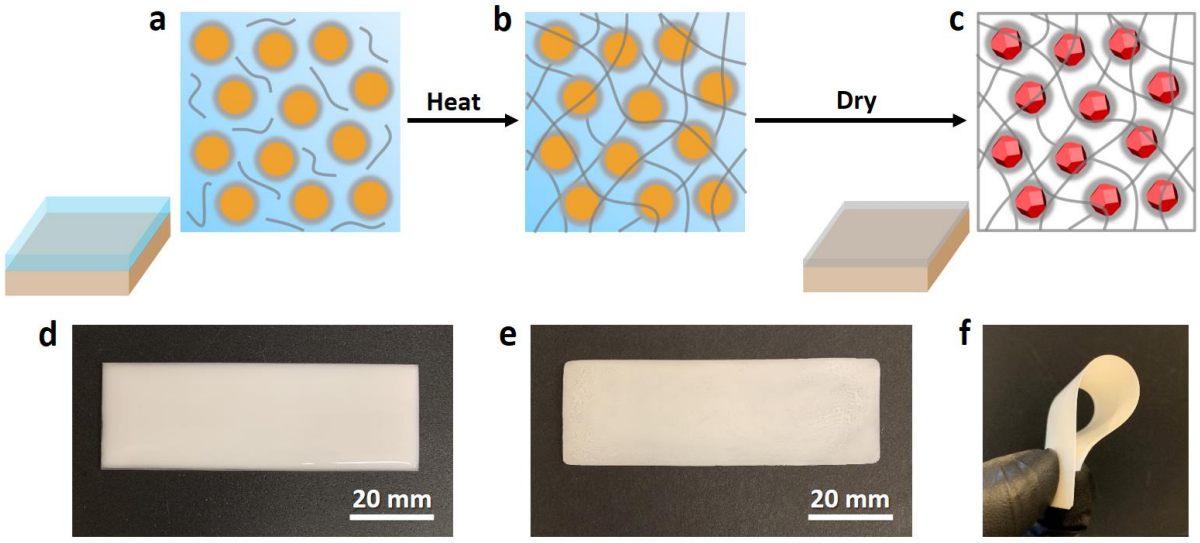

Figure 4.3. Overview of the film-forming process based on the thermogelling nanoemulsion. (a) Thermogelling nanoemulsion loaded on a glass slide at room temperature. (b) Thermogelling nanoemulsion on a glass slide at 70°C. The HPMC moleclules associate together and form a gel network that immobilizes the oil nanodroplets. (c) Oral film on a glass slide after drying at 70°C. Drug nanoparticles are induced locally within the oil nanodroplets during drying and are embedded in a dried HPMC matrix after drying. (d) Optical image of the thermogelling nanoemulsion loaded on a glass slide before drying. The dimensions of the glass slide are 75×25 mm^2. (e, f) Optical images of the oral film detached from the glass slide after drying. The film condition is 0.4 g oil and the thickness is 111.8 μm.

Table 4.1. Previous oral films loaded with fenofibrate microparticles/nanoparticles vs. the oral films loaded with fenofibrate nanoparticles in this work.

Method (before casting & drying)	Demonstrated max drug load	Particle size	Oral film thickness	Reference
Wet stirred media milling (2 h) + mixing with a polymer solution (time not shown)	37.1 wt%	~210 nm	85-165 μm	Kevadiya et al.[140] (2018)
Wet stirred media milling (2 h) + mixing with a polymer solution using a dual-propeller mixer (3 h)	29.3 wt%	~256 nm	20-120 μm	Sievens-Figueroa et al.[128] (2012)
Wet stirred media milling (time not shown) + mixing with a polymer solution dual-propeller mixer (3 h)	26 wt%	Not shown	Not shown	Zhang et al.[139] (2014)
Fluid energy milling (~2 h) + mixing with a polymer solution using a dual-propeller mixer (3 h)	22.8 wt%	~4.53 μm (Large size)	113-148 μm	Zhang et al.[137] (2018)
Wet stirred media milling (2 h) + mixing with a polymer solution using a dual-propeller mixer (6-12 h)	17.0 wt%	~280 nm	93-102 μm	Krull et al.[138] (2015)
Fluid energy milling (~2 h) + mixing with a polymer solution using a dual-propeller mixer (3-6 h)	15.8 wt%	~4.20 μm (Large size)	50-60 μm	Zhang et al.[136] (2018)
Melt emulsification (~15 min with melting at 95°C and sudden cooling to –3°C) + mixing with a polymer solution using a dual-propeller mixer (5 h)	5.0 wt%	~900 nm	65-70 μm	Bhakay et al.[135] (2016)
Thermogelling nanoemulsion synthesis (30 min)	63 wt%	~600 nm	55-150 μm	This work

Because the film formation involves removal of both the water and organic solvent, solid content (w_{solid}) of the nanoemulsion becomes an important parameter to describe the weight fraction of the non-volatile components after drying, which includes HPMC, fenofibrate, and Tween 80. The solid content (w_{solid}) of the nanoemulsion is described by **Equation 4.1**, and the result is shown in **Figure 4.4**.

$$w_{solid} = \frac{m_c w_{HPMC} + m_o w_{FEN} + m_{TW}}{m_c + m_o + m_{TW}} \tag{4.1}$$

where m_c is the mass of the continuous water phase, w_{HPMC} is the HPMC weight fraction in the water phase (4 wt%), m_o is the oil phase mass, w_{FEN} is the fenofibrate weight fraction in the oil phase (≈45 wt%)[55]. Because the oil phase has a high concentration of fenofibrate, a small incremental addition of the oil phase can increase the solid content effectively (≈2.5 wt% increase per 0.2 g oil addition). With the estimated solid content, the oral film mass is predicted from the mass of the nanoemulsion loaded on a glass slide (**Figure 4.4b**). The predicted oral film mass ($m_{dried,p}$) is expressed as follows:

$$m_{dried,p} = m_{NE} w_{solid} \tag{4.2}$$

where m_{NE} is the mass of the nanoemulsion loaded on a glass slide. To compare the oral films made from the nanoemulsions with three different oil phase mass conditions, prediction is made for these nanoemulsions to form the oral films with approximately the same mass (~92 mg). To validate the prediction, the oral film mass is measured and compared with the predicted film mass (**Figure 4.4c**). The measured film mass agrees well with the predicted film mass. In addition, a good correlation (R^2 = 1.00) is observed between the oral film thickness and the measured oral film mass (**Figure 4.4d**). The result suggests that the film thickness is adjustable by varying the mass of the nanoemulsion loaded on the glass slide. The nanoemulsion can be loaded on a glass slide up to 5 g, which corresponds to at least 200 μm for the resulting oral film. The optical images of the resulting oral films for the six conditions are shown in **Figure C.2**.

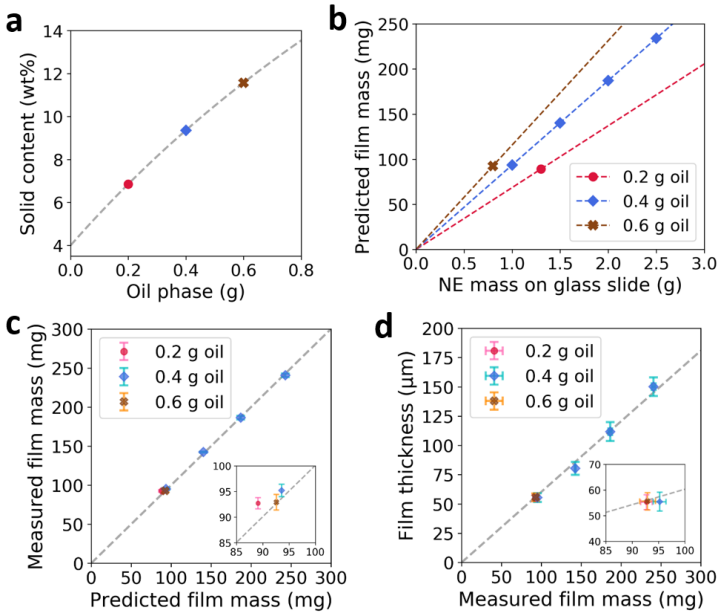

Figure 4.4. (a) Predicted solid contents from mass balance for the nanoemulsions with different oil phase mass (described by **Equation 4.1**). The three markers indicate the three compositions chosen in this work. (b) Predicted oral film mass after drying based on the nanoemulsion (NE) mass loaded on the glass slide. The three lines represent the nanoemulsions with three different oil phase mass conditions (described by **Equation 4.2**). The markers represent the six conditions chosen in this work. (c) Correlation between the predicted oral film mass and the measured oral film mass (R^2 = 0.99). (d) Correlation between the oral film thickness and the measured oral film mass (R^2 = 1.00). From the slope, the densities of the oral films are 0.88 g/cm^3.

4.3.3 Characterization of Drug Nanoparticles in Oral Films

The surface and the cross-section of the oral film are observed using scanning electron microscopy (SEM), as shown in **Figure 4.5**. A drug-free pure HPMC film is prepared as a control for comparison (**Figure C.3**). For the oral film templated by the nanoemulsion, the surface is flat and does not have distinct nanostructures (**Figure 4.5a, b**), which is similar to the case of the pure HPMC film (**Figure C.3a, b**). To observe the cross-section, an oblique cut is applied on the films. The cross-sectional images are very different for the nanoemulsion-templated oral film and the pure HPMC film. The pure HPMC film has a flat and smooth cross-section (**Figure C.3c**), while the nanoemulsion-templated oral film has evident nanoparticles embedded in the porous HPMC matrix (**Figure 4.5c**). The embedded nanoparticles have an average diameter of 599.8±71.6 nm, which is larger than the oil nanoemulsion droplet diameter (~350 nm). The size increase could result from the adsorption of more HPMC molecules to

stabilize the drug nanoparticles. To further investigate the ability of the HPMC polymer to stabilize the drug nanoparticles, the oral film is tested for nanoparticle dispersibility in water. In **Figure 4.5d** (also **Figure C.4**), the dispersed drug nanoparticles can be directly observed using transmission electron microscopy (TEM), and dynamic light scattering (DLS) shows that the dispersed nanoparticles are stable and have a uniform size distribution (**Figure 4.5e**). The average nanoparticle diameter and PDI are 597.7 nm and 0.169, respectively. The above results demonstrate that the thermogelling nanoemulsion can effectively template the formation of uniform drug nanoparticles in the HPMC matrix.

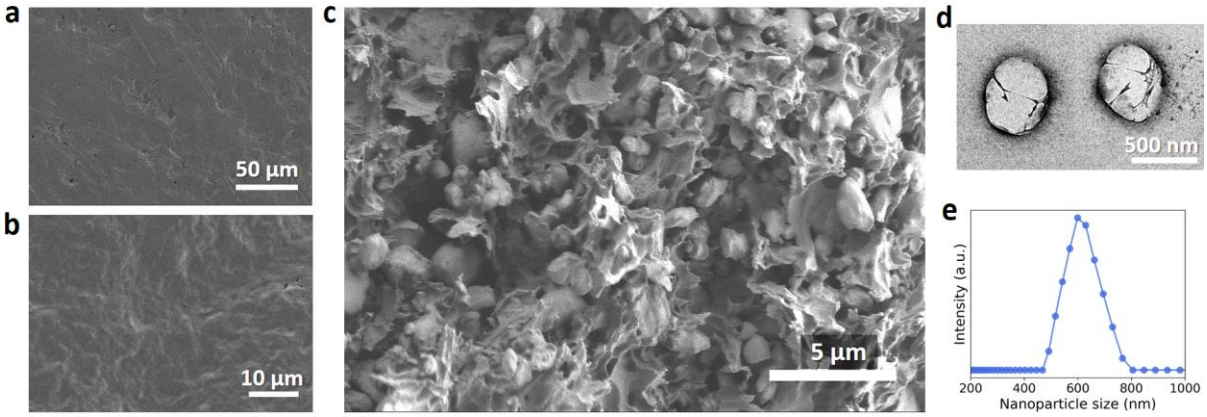

Figure 4.5. (a, b) SEM images of the oral film surface. (c) SEM image of the oral film cross-section (0.4 g oil and 150.2 µm). The embedded drug nanoparticles have an average diameter of 599.8±71.6 nm. (d) TEM image of the dispersed drug nanoparticles. (e) Size distribution (hydrodynamic diameter) of the dispersed drug nanoparticles determined by dynamic light scattering (DLS). The average diameter and PDI are 597.7 nm and 0.169, respectively.

The amount of poorly water-soluble drugs that can be loaded into an oral film is generally limited with conventional film-forming technologies,[131,134] because irreversible aggregation of drug particles can easily occur during processing and drying, especially for oral films with high drug loading contents.[128,141] In contrast, the film-forming process based on the thermogelling nanoemulsion can effectively avoid the aggregation problem, because the thermogelling mechanism ensures confined formation of drug nanoparticles in the immobilized oil nanodroplets. From the aspect of process development, the drug loading content can be easily scaled up by increasing the oil-to-water ratio of the nanoemulsion without any further modifications on the film formulation steps. Adding more oil leads to a higher density of the nanoemulsion droplets, which corresponds to a higher drug nanoparticle density (i.e., higher

drug loading content) after drying. **Figure 4.6a** shows the drug loading contents of the oral films as a function of the oil phase mass. The measured drug loading contents agree well with the estimated drug loading (ϕ_{FEN}) curve that is predicted by **Equation 4.3**.

$$\phi_{FEN} = \frac{m_o w_{FEN}}{m_c w_{HPMC} + m_o w_{FEN} + m_{TW}} \tag{4.3}$$

The high drug loading content is tunable from 40.4 to 63.0 wt% by adding oil from 0.2 g to 0.6 g, which is higher than the highest value (37.1 wt%) demonstrated in the prior studies that used conventional methods to prepare oral films loaded with fenofibrate particles (**Table 4.1**).[140] In order to monitor the fenofibrate crystal structure before and after the formulation, X-ray diffraction (XRD) patterns are measured for the oral film, as-received bulk fenofibrate crystals, and pure HPMC powders (**Figure 4.6b**). The latter two are the starting materials that are dissolved in the dispersed oil and continuous water phases for preparing the nanoemulsions. The nanoparticles in the oral films share the same characteristic peaks of the bulk fenofibrate crystals, which corresponds to crystalline form I fenofibrate at the diffraction angles (2θ) of 12°, 14.5°, 16.2°, 16.8°, and 22.4°. Form I fenofibrate is a desirable form because it has the highest thermodynamic stability compared to the metastable polymorphs and the amorphous form.[166] The high stability can avoid recrystallization under ambient storage conditions and during dissolution.[55,100] In **Figure 4.6c**, differential scanning calorimetry (DSC) identifies a single endothermic peak of melting for the oral films with different oil mass. Compared to the as-received bulk fenofibrate crystals with a melting point of 81.7°C (**Figure C.8a**), the oral films have melting points of ~77.4°C (**Figure 6c**). The melting point depression is a typical feature of nanocrystals compared to bulk crystals, and the phenomenon can be described by the Gibbs-Thomson equation.[167] The similar decreased melting points of the oral films show that crystalline drug nanoparticles are successfully formed with similar sizes for different oil phase mass, which again supports the effectiveness of using the nanoemulsions as templates. Based on the DSC results, drug crystallinity in the oral films can be estimated with the prior data that correlates the fusion enthalpies and melting points of fenofibrate nanocrystals (see **Appendix C.4**).[70,113] The estimation shows that the drug in the oral films has a high degree of crystallinity that is close to complete crystallization for different oil mass conditions (**Figure 4.6d**). The Raman spectra also suggest that the solid-state form of fenofibrate in the oral film

is crystalline form I (**Figure 4.6e, f**). The most prominent peaks occur at 1147, 1599, and 1650 (**Figure 4.6e**), which correspond to C–O stretching, in-plane benzene ring stretching, and C=O stretching, respectively.[168] Moreover, in the CH-stretching region between 2900 and 3100 cm^{-1} (**Figure 4.6f**), there are three peaks between 3050 and 3100, which are fingerprints for crystalline form I fenofibrate.[168]

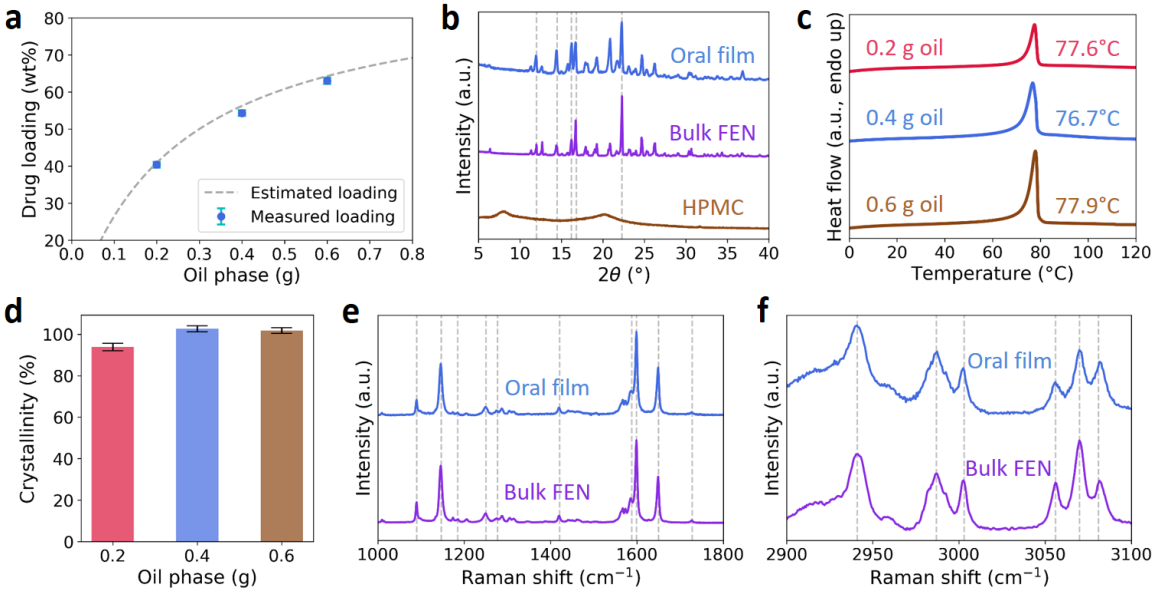

Figure 4.6. Characterization of the fenofibrate nanoparticles in the oral films. (a) Drug loading content of the oral films as a function of oil phase mass. The estimated drug loading content (gray dashed curve) is described by **Equation 4.3**. (b) X-ray diffraction (XRD) patterns of the fenofibrate nanoparticles in the oral films, as-received bulk fenofibrate crystals, and HPMC powders. The gray dashed lines correspond to the XRD characteristic peaks for crystalline form I fenofibrate. (c) DSC thermograms and (d) crystallinity of the fenofibrate nanoparticles in the oral films. (e) Raman spectra of the fenofibrate nanoparticles in the oral films with the spectral range between 1000 and 1800 cm^{-1}. (f) Raman spectra of the fenofibrate nanoparticles in the oral films within the spectral range 2900 to 3100 cm^{-1}. The gray dashed lines in (e) and (f) correspond to the Raman characteristic peaks for crystalline form I fenofibrate.

To investigate the uniformity of the drug nanoparticles in the oral films, Raman mapping images are taken for the oral films with different oil mass (**Figure 4.7a-c**). The Raman intensity becomes higher (i.e., brighter color according to the heat map) as the oil mass increases, which corresponds to a higher density of fenofibrate nanoparticles in the oral film. In addition, no aggregation of pixels (1×1 μm^2) is observed from the Raman mapping images, indicating the fenofibrate nanoparticles are uniformly distributed in the film. **Figure 4.7d** shows the intensity histograms associated with the images in **Figure 4.7a-c**. The average intensity increases with increasing oil mass, and the standard deviation is similar for different oil mass (~15 a.u.). In **Figure 4.7e**, the coefficients of variation (CV) for different oil mass are further calculated, which are 8.5%, 6.4%, and 5.6% for 0.2, 0.4, and 0.6 g oil, respectively. The CV value becomes smaller as the drug loading content increases, which is consistent with a previous finding that increasing the density of nanostructures can enhance the Raman signal uniformity.[169] To set a benchmark, for highly uniform nanostructure arrays reported in previous studies, the CV values of the Raman mapping signals typically lie between 4.3% and 14.8%.[169–171] This quantitatively supports that the oral films templated by the thermogelling nanoemulsions have a high drug content uniformity. The average Raman intensity is roughly proportional to the drug loading content (**Figure 4.7f**), which is consistent with a previous result that the Raman signal of a drug product is linearly correlated with the drug concentration.[172]

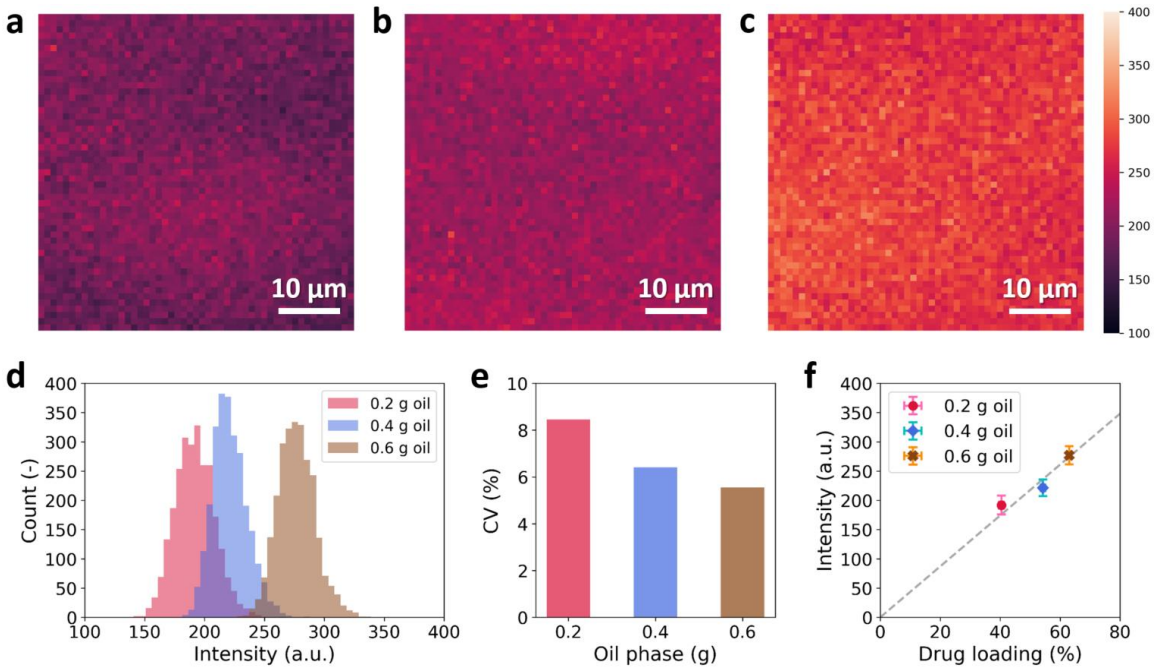

Figure 4.7. Raman mapping images for the oral films with different oil phase mass: (a) 0.2 g oil, (b) 0.4 g oil, (c) 0.6 g oil. Color bar values represent Raman peak intensities at 1650 cm^{-1}. The Raman mapping area is 51×51 μm^2, and each pixel is 1×1 μm^2. (d) Intensity histograms associated with the Raman mapping images in (a-c). (e) Coefficients of variation (CV) determined from the intensity histograms. CV represents the ratio of the standard deviation to the mean. (f) Correlation between the intensity and the drug loading content.

4.3.4 Release Profiles of Oral Films

Fenofibrate belongs to Biopharmaceutics Classification System (BCS) Class II drugs that have high permeability and low solubility.[173] This means that absorption of dissolved fenofibrate is much faster than fenofibrate dissolution, causing sink conditions to prevail *in vivo*. A 25 mM sodium dodecyl sulfate (SDS) aqueous solution recommended by the FDA[157] is used to simulate *in vivo* solubilization by biorelevant surfactants[158,159] and create a sink condition during the dissolution, which provides a good proxy of *in vivo* condition.[158] As suggested in the literature, a sinker basket is used to load and transfer the oral film (**Figure 4.8a**).[160] This can prevent the oral film from floating or sticking to the paddle or the vessel wall. To deconvolute the effects of drug loading content and thickness, we first studied the release profiles for the oral films with the same oil mass (0.4 g) and different thickness. **Figure 4.8b** shows that varying the oral film thickness leads to different release profiles. It takes longer time to finish the release as the oral film thickness increases (**Figure 4.8b**). In contrast to the

as-received bulk fenofibrate crystals (~240 μm), which takes as long as ~12 h to reach the first 80% release (**Figure C.10a**), the oral films exhibit a tunable immediate release (>80% release in 7 min and ~100% release in 11 min for all conditions). The fast release rates are attributed to the large surface-to-volume ratios of the oral films and the successful formation of drug nanoparticles. The surface-to-volume ratios of the oral films can achieve 133 to 361 cm^2/cm^3 for the film thickness range between 55.4 and 150.2 μm, which are much larger than the values of ~10 cm^2/cm^3 for drug tablets.[174,175] Then, the release profiles for the oral films with the same thickness (~55.4 μm) and different oil phase mass are compared (**Figure 4.8c**). The release profiles are nearly identical, indicating that the release does not depend on the drug loading content at the same thickness. In addition, the thin films (~55.4 μm) possess a large surface-to-volume ratio to achieve very fast release rates—3 min to reach 80% release and another 4 min to complete the release. In prior studies, irreversible nanoparticle aggregation can easily lead to a distinct reduction of the release rate,[176,177] because the improved dissolution resulting from the high surface area of the nanoparticles is lost. In this work, the same fast release rates for different oil mass provide evidence that irreversible nanoparticle aggregation is not a problem when the drug loading content is increased. To elucidate the release mechanism of the oral films, a power-law model is first used to fit the release profiles (as the red curve in **Figure 4.8d**):[178]

$$\frac{M_t}{M_\infty} = kt^n \tag{4.4}$$

where M_t and M_∞ are the amount of drug released at time *t* and infinite time, *k* is the kinetic constant (with the unit of t^{-n}), and *n* is the diffusional exponent that indicates the drug release mechanism. From the fitting results (**Figure C.11a-f**), the exponent n values are greater than 1.4 for all the release profiles (**Figure C.11g**), suggesting that the drug release from the oral film is erosion-controlled.[179] Our observations also indicate that the film matrix erodes over time, and the release is complete once the oral film is fully dissolved. The erosion-controlled mechanism indicates that the dissolution of drug nanoparticles is as fast as the film erosion, and poor dissolution of hydrophobic fenofibrate is no longer a rate-limiting barrier for the drug release. To further analyze the release kinetics, an erosion model for a thin film (half thickness

= a) expressed by **Equation 4.5** is used to determine the erosion constant (k_e, with the unit of m/s) and lag time (t_{lag}),[123] as the blue curve in **Figure 4.8d (**see the details in **Appendix C.7**).

$$\frac{M_t}{M_\infty} = \frac{k_e(t - t_{lag})}{a} \tag{4.5}$$

The lag time is introduced to account for release suppression due to the initial wetting of the oral film when it first contacts the release medium.[180] In **Figure 4.8e**, the lag time (t_{lag}) is proportional to the film thickness (2a), which can be explained by the fact that a thinner film has a larger surface-to-volume ratio for faster water hydration before the erosion plays an important role. Because the erosion constants (k_e) are similar for different oral film conditions (**Figure C.12g**) and the lag time is proportional to the film thickness (**Figure 4.8e**), a scaling behavior is found mathematically between the fractional release $\frac{M_t}{M_\infty}$ and the $\frac{t}{a}$ (see **Appendix C.8**). With the scaling rule, the release profiles for various conditions can be collapsed into one master curve (**Figure 4.8f**), which provides a simple design rule for engineering the release profiles of oral films.

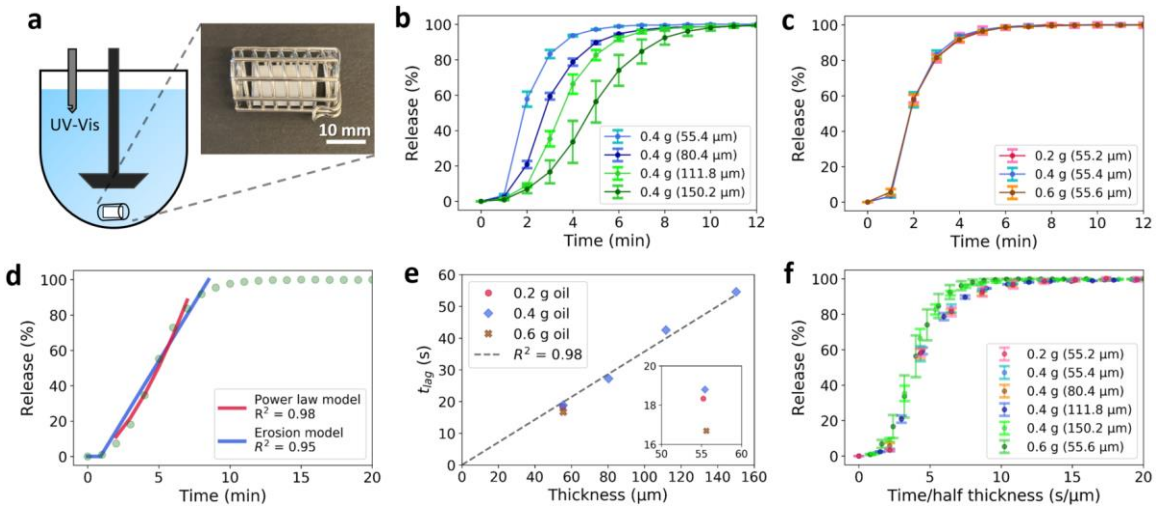

Figure 4.8. Release profiles and analyses of the oral films. (a) Schematic diagram of the United States Pharmacopeia (USP) Dissolution Apparatus II with an automated UV-Vis probe. The inset photo is a USP compliant sinker basket loaded with an oral film (15 mm×10 mm). (b, c) Cumulative release profiles for the oral films with different compositions: (b) varying the oil mass with a constant thickness (~55.4 μm), (c) varying the thickness with a constant oil phase mass (0.4 g oil). (d) Fitting the release profile of the oral film (0.4 g oil and 150.2 μm) with the power-law model (**Equation 4.4**) and erosion model (**Equation 4.5**). (e) Correlation between the lag time (t_{lag}) and the oral film thickness. (f) Rescaling of the release profiles with different compositions onto a universal curve.

4.4 Conclusions

We have developed thermogelling HPMC nanoemulsions as robust templates to formulate poorly water-soluble drugs into oral films containing drug nanoparticles. The thermogelling nanoemulsions are prepared using HPMC and Tween 80 to emulsify saturated fenofibrate-in-anisole solution. The nanoemulsions can gelate upon heating with the hydrophobic groups of HPMC associating together to form hydrophobic junctions, which lead to a hydrogel network with immobilized oil nanodroplets. In contrast to inefficient conventional film-forming processes, the thermogelling nanoemulsions can directly act as film precursors for casting and drying. The thermally gelled nanoemulsions can effectively template the formation of uniform drug nanoparticles in a dried HPMC matrix to produce oral films. The oral film thickness is predictable and adjustable by varying the mass of the nanoemulsion loaded on a glass substrate. The uniform drug nanoparticles (~600 nm) in the oral films have been successfully observed using SEM, TEM, and DLS. The proposed film-forming technology enables a tunable high drug loading content of the oral films up to 63 wt% without any further modifications on the film formulation steps. After the oral film formulation, the most stable crystalline form I fenofibrate is attained as validated by XRD, Raman spectroscopy, and DSC analyses. The melting point depression for the fenofibrate in the oral films demonstrates the formation of crystalline drug nanoparticles. Raman mapping results further show that the oral films have a high drug content uniformity. In the release tests, the oral films display a tunable immediate release because the films have large surface-area-to-volume ratios and the drug nanoparticles are fast-dissolving. Moreover, increasing the drug loading content at the same film thickness does not affect the release profiles, which supports that irreversible nanoparticle aggregation is not a problem even when the high drug loading content is achieved. Finally, we present that the drug release from the oral film is erosion-controlled, indicating the drug dissolution has been significantly improved and is no longer a rate-limiting step. Based on the erosion mechanism, a scaling rule is developed to provide simple design rule for engineering the release profiles of oral films. Overall, the thermogelling nanoemulsions enable a more efficient and effective film-forming process to formulate HPMC and poorly water-soluble drugs into oral films with high drug loading capacity.

Chapter 5 Conclusions and Outlook

In this thesis, we simultaneously utilized two promising building blocks, functional nanoemulsions and hydrogels, to enable more efficient and effective formulations for oral drug products, including tablets, capsules, particles, nanoparticle suspensions, and oral thin films. Moreover, the oral drug products possess improved dissolution and absorption of hydrophobic drugs, high drug content uniformity, and versatile release controls (e.g., delayed release and tunable fast release).

5.1 More Versatile Nanoemulsion Carriers

We developed a method to encapsulate nanoemulsions in alginate capsules for more versatile delivery of lipophilic active ingredients (**Chapter 2**). The intrinsically high viscosity of the nanoemulsions ensures the formation of spherical capsules and high encapsulation efficiency during the synthesis. By carefully analyzing the release profiles, we showed that the capsule systems possess a tunable, delayed-burst release. The proposed encapsulation methodology can be further generalized to other functional nanoemulsions with various active ingredients, oil phases, nanodroplet sizes, and chemically crosslinked inner hydrogel cores. The versatile nanoemulsion-loaded capsules show great promise for delivering lipophilic active ingredients and can find use in a wide range of applications in the food, pharmaceutical, and cosmetic industries.

5.2 More Efficient Oral Drug Formulations

We designed a new thermogelling nanoemulsion system that can be easily formulated into composite solid dosage drug products with well-controlled API nanocrystals embedded in a MC matrix (**Chapter 3**). The nanoemulsion suspension has a low gel temperature and fast response to temperature changes which enable the realization of effective particle formulation with a thermal dripping method. The thermally gelled nanoemulsion can be subsequently dried with the precise formation of stable API nanocrystals templated by the nanodroplets *in situ*. Moreover, a fast and tunable release performance is achieved with the combination of a fast-eroding MC matrix and fast-dissolving API nanocrystals. Using the versatile thermal processing approach, we formulated the thermogelling nanoemulsion into various dosage

forms (nanoparticle suspension, drug tablet, and oral thin film) which all contain stable nanocrystals generated *in situ*.

Because the concept of using thermogelling nanoemulsions is promising for more efficient oral film formulations, and oral films have emerged as a novel dosage form with many advantages, we further developed thermogelling nanoemulsions based on ideal HPMC to formulate oral films (**Chapter 4**). The nanoemulsions that are stabilized by HPMC and Tween 80 can directly act as film precursors for casting and provide robust templates to formulate oral films with uniform drug nanoparticles embedded in a dried HPMC matrix. The nanoemulsions gelate upon heating with immobilized oil nanodroplets that can enable confined nanoparticle crystallization and avoid potential irreversible nanoparticle aggregation even for high drug loading contents. The oral films also possess a tunable immediate release because the films have large surface-to-volume ratios and the drug nanoparticles are fast-dissolving.

5.3 Outlook

5.3.1 From Batch to Continuous Formulations

Continuous formulations are more efficient than batch formulations, because they can provide higher throughput per unit volume and per unit time.[181] In this thesis, the nanoemulsion syntheses and the corresponding gelation methods belong to batch formulations. To enable large-scale production for commercialization, the next step is to develop continuous formulations to produce the same products as in the batch formulations. The nanoemulsion syntheses can be achieved in a continuous manner with high pressure homogenization. Continuous dripping methods can be realized by developing a setup in which a nanoemulsion is dripped by a pump into a flowing channel loaded with a gelation medium (e.g., alginate solution and heated water). For tablet molding and thin film casting, continuous processes can be developed with the use of conveyor belts.

5.3.2 Generalization to Various Hydrophobic Drugs

In this thesis, we used fenofibrate as a hydrophobic model API for confined crystallization. We believe the versatile thermogelling nanoemulsion system can be generalized to various hydrophobic drugs. To find other suitable hydrophobic drug candidates, we can investigate

other well-known hydrophobic APIs have benefitted from nanocrystal technologies, such as danazol, naproxen, ketoprofen, cilostazol, aprepitant, cyclosporine, and itraconazole.[102] For these hydrophobic APIs that can stably exist in their crystalline form, we should be able to find suitable organic solvents to dissolve them and directly generate the API nanocrystals *in situ* in the MC/HPMC matrix using the proposed formulation technology. Our group has done in-depth fundamental studies and proposed general design strategies for nanoemulsion syntheses with different oil phases.[13,83,125] This can help us make informed decisions and broaden the possibility to synthesize a wide variety of API-loaded nanoemulsions for different API/solvent pairs.

5.3.3 More Versatile Release Controls (Delayed Release and Two Release Times)

Tableting coating is critical in food and drug formulations because it can introduce many important functionalities, such as taste-masking, protection layer, delayed release, and different release times in a single dosage form. However, conventional technologies are generally inefficient and require many steps (e.g., milling, blending, granulation, and tableting) to first prepare drug tablets, which then have to undergo a coating process to introduce an additional layer. Motivated by the above limitations, we can combine the nanoemulsion encapsulation technique with the thermogelling nanoemulsion technology to form core-shell composite particles. To realize the idea, we can introduce calcium ions in the thermogelling methylcellulose nanoemulsion. The nanoemulsion with a dual gelation capability can gelate upon heating and ionically crosslink the neighboring alginate molecules when contacting an alginate bath. The dried core-shell particles have an outer shell of alginate matrix and an inner core of methylcellulose matrix that is embedded with drug nanocrystals. The shell is expected to delay the release of the drug that is embedded in the core. In addition, the dual gelation technique can be applied for drug coformulation by encapsulating another drug-loaded nanoemulsion in the alginate shell. In this case, we should be able to have two drugs released at two different times or the same drug released at two different times. The coformulation technology can lower the dosage forms that should be taken by a patient, which can greatly improve patient compliance.

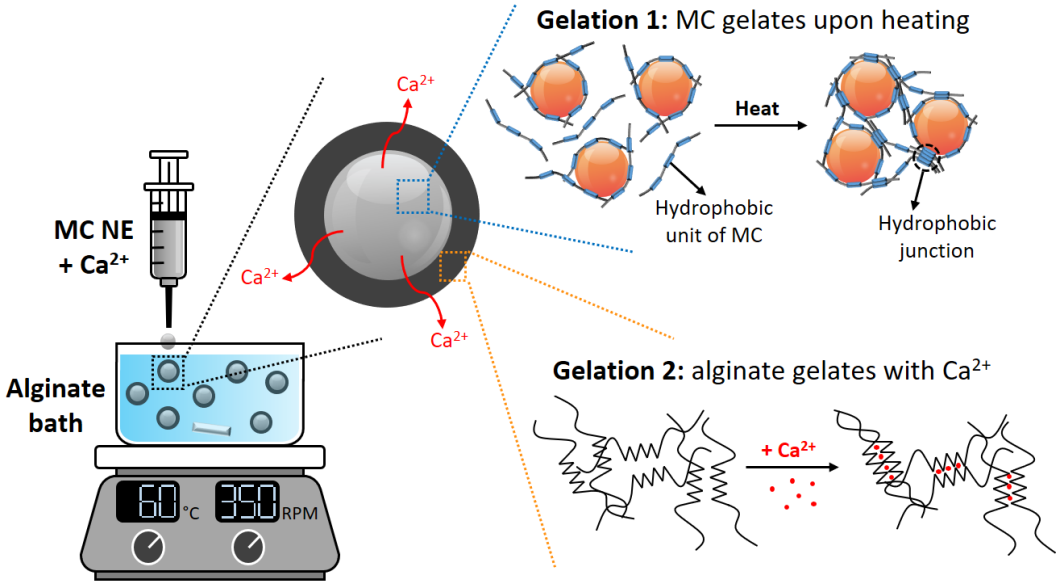

Figure 5.1. Schematic diagram of the dual gelation technique to formulate core-shell particles.

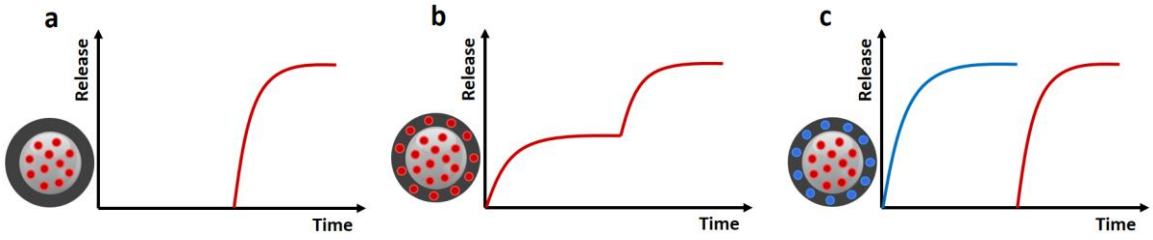

Figure 5.2. Proposed release profiles for core-shell particles with different drug encapsulation schemes: (a) delayed release for one drug, (b) two different release times for one drug, (c) two different release times for two drugs.

5.3.4 Polymorph Controls

Polymorphism of drugs has been widely studied in the pharmaceutical industry, because different drug polymorphs can lead to different drug efficacy, bioavailability, and safety.[182] Different strategies have been proposed to control drug polymorphs, including surfactant addition,[6] solvent choices,[182] and confinement.[182] The thermogelling nanoemulsion system should be generalizable to other surfactants and different organic solvents. Moreover, the nanoemulsion droplet size can be easily adjusted to create different confinement effects. By tuning the composition and the droplet size of the thermogelling nanoemulsion system, we expect to control polymorphs of hydrophobic drugs. For example, we have observed the addition of Tween 80 is crucial for fenofibrate crystallization, and the thermogelling nanoemulsions with and without Tween 80 can lead to crystalline and amorphous oral films, respectively.

Appendix A Supporting Information for Chapter 2

A.1 Conditions for the Formation of Spherical Capsules

When a liquid (calcium precursor) droplet penetrates into a gelation bath, the viscous and surface tension forces have to overcome the impact and drag forces to ensure the formation of spherical capsules. The Ohnesorge number (Oh) can be used to measure the relative importance of inertial, viscous, and surface tension stresses.[93]

$$Oh = \frac{\eta}{\sqrt{\rho d \gamma}} \tag{A.1}$$

where η is the viscosity of the liquid, ρ is the density of the liquid, d is the diameter of the liquid droplet, and γ is the surface tension of the liquid.

For alginate bead formation (dripping an alginate solution into a $CaCl_2$ solution), prior work found that the Oh of alginate solution had to exceed 0.24 (a critical value) to overcome the impact and drag forces for forming spherical beads.[93] However, for alginate capsule formation (dripping a calcium precursor into an alginate bath), the critical value of Oh should be higher than 0.24 because of the large viscosity of the alginate bath. In this work, the calcium nanoemulsion has a high viscosity (301 mPa-s) and a low surface tension (35.7 mN/m). Both of these properties favor a large value of Oh, and the Oh for dripping the nanoemulsion with 18G and 22G dispensing tips are 0.79 and 0.89, respectively (**Table A.1**).

Table A.1. Determination of Oh numbers for dripping the nanoemulsion with 18G and 22G dispensing tips (d_{drop} is approximated by $2r_{core}$).

	η_{NE} (mPa-s)	ρ_{NE} (g/cm^3)	d_{drop} (mm)	γ_{NE} (mN/m)	Oh (-)
18G	301	1.09	3.75	35.7	0.79
22G	301	1.09	2.97	35.7	0.89

A.2 Viscosity-Shear Rate Flow Curves

Figure A.1 shows the viscosity-shear rate flow curves for the different fluids measured in this study. The water, 25 wt.% sucrose solution, and 1% w/v alginate solution are Newtonian over the measured shear rate range. The sucrose-surfactants mixture is a complex fluid and displays minor shear thinning. The calcium nanoemulsion remains Newtonian up to a shear rate of 100 s^{-1} and transitions to a moderate shear thinning region at higher shear rates.

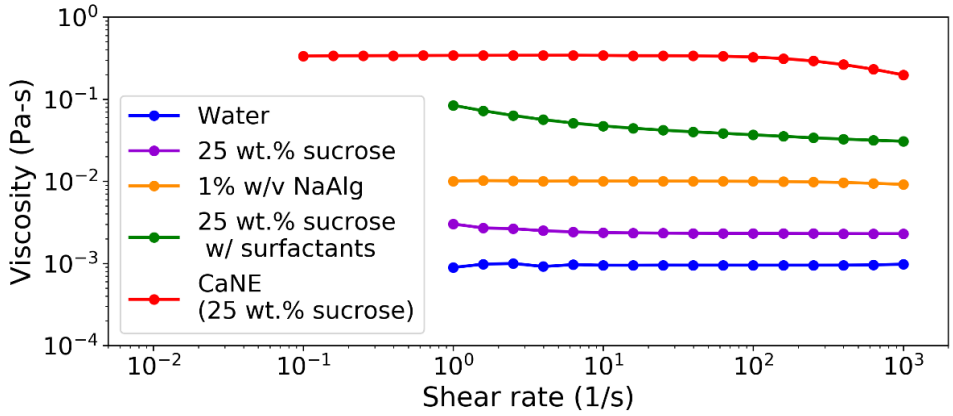

Figure A.1. Viscosity-shear rate flow curves at 20°C for water, 25 wt.% sucrose and 1% w/v alginate solution, 25 wt.% sucrose with surfactants, and calcium nanoemulsion. Experimental details are shown in Chapter 2.

A.3 Optical Image of Nanoemulsion-Loaded Capsules

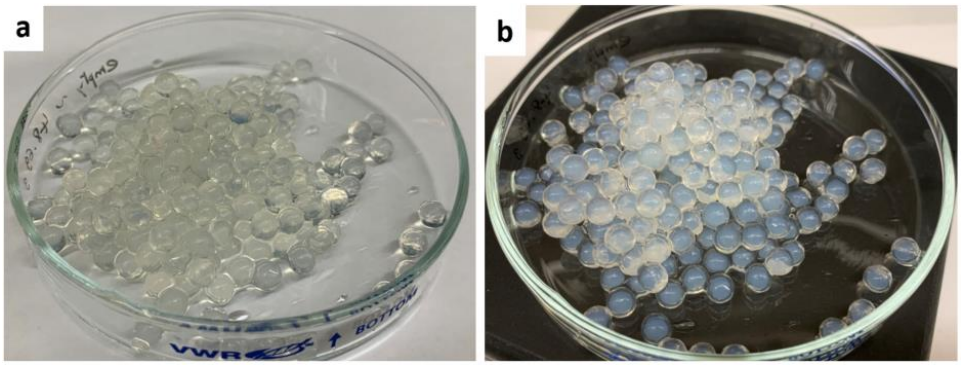

Figure A.2. (a-b) Optical images of capsules against (a) white and (b) black backgrounds.

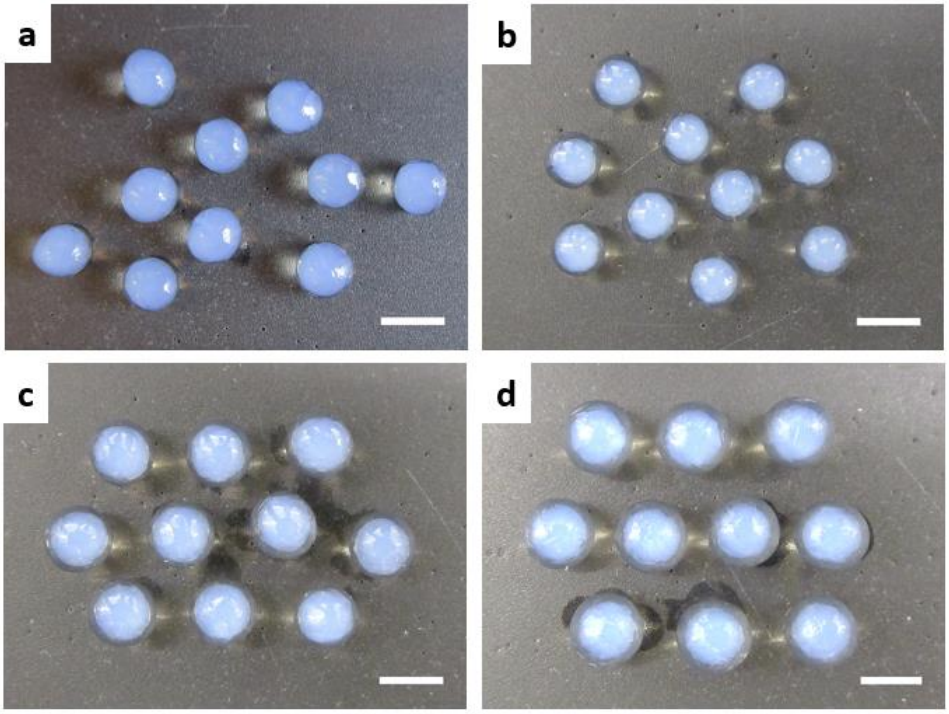

Figure A.3. (a-d) Optical images of capsules for different preparation conditions: (a) w_{CaCl_2}= 0.02 and 18G dispensing tip, (b) w_{CaCl_2}= 0.04 and 22G dispensing tip, (c) w_{CaCl_2}= 0.04 and 18G dispensing tip, (d) w_{CaCl_2}= 0.06 and 18G dispensing tip. Scale bars are 5 mm.

A.4 Design of Capsule Dimensions

The radius of a capsule can be estimated by the sum of the inner core radius and the shell thickness. In this work, the capsule thickness and size are easily controlled by varying the calcium concentration and the dispensing tip size, respectively. As shown in **Figure 2.2h**, the shell thickness is linearly correlated with the calcium concentration. Further extrapolation of this linear correlation (**Figure A.4**) shows that it passes through the origin, which is reasonable because no shell can be formed without $CaCl_2$ being added. For the lower limit, the shell thickness should be further decreased by decreasing the w_{CaCl_2} until the point where the capsules are too fragile to be collected. For the upper limit, the linear correlation is extrapolated up to the point where the continuous phase is saturated with $CaCl_2$ (star symbol). The star symbol corresponds to the theoretically maximum $CaCl_2$ concentration ($w_{CaCl_2,max}$) that can be achieved in the nanoemulsion system. With the solubility of $CaCl_2$ in water (74.5 g/100 mL at 20°C)[183] and the water volume in the continuous phase (3 g sucrose solution × 75 wt.% =

2.25 g water ~ 2.25 mL water), $w_{CaCl_2,max}$ can be approximated as **Equation A.2**. The shell thickness is extrapolated to be 6.44 mm for the $w_{CaCl_2,max}$.

$$w_{CaCl_2,max} = \frac{2.25 \times 0.745}{5} = 0.335 \text{ (g } CaCl_2\text{/g nanoemulsion)} \quad \text{(A.2)}$$

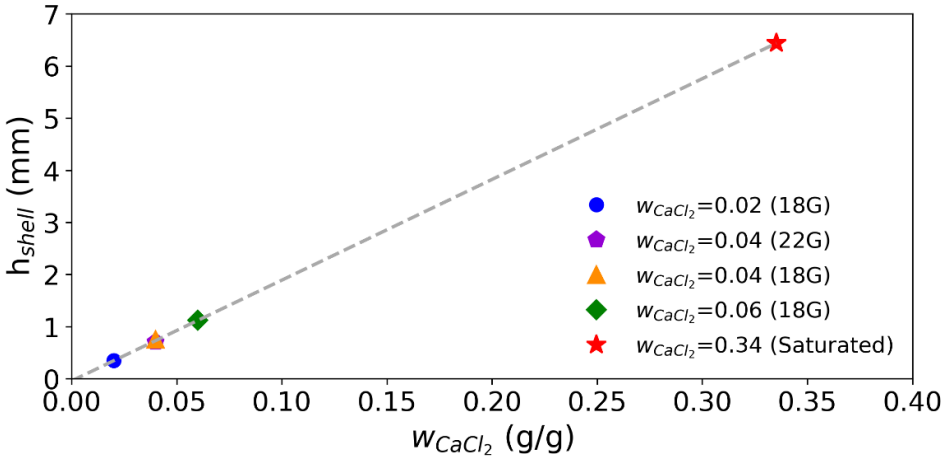

Figure A.4. Linear correlation between shell thickness and w_{CaCl_2} with extrapolation to both saturated conditions and zero w_{CaCl_2}.

Since we use a dripping method to generate droplets, the inner core radius (r_{core}) can be described by Tate's law[93]:

$$r_{core} \propto \left(\frac{d_T \gamma_{NE}}{\rho_{NE} g}\right)^{\frac{1}{3}} \quad \text{(A.3)}$$

where d_T is the outer diameter of the dispensing tip, γ_{NE} is the surface tension of the nanoemulsion, ρ_{NE} is the density of the nanoemulsion, g is the acceleration of gravity (9.8 m^2/s). **Figure A.5** shows the linear correlation for the origin and the four data points (five points in total, R^2 = 0.99). This correlation can provide a criterion for designing the inner core radius of capsules. Alternatively, one could use centrifugal forces to produce even smaller droplets and hence inner cores. We have a previous publication which describes the centrifugal particle generation process in detail.[184]

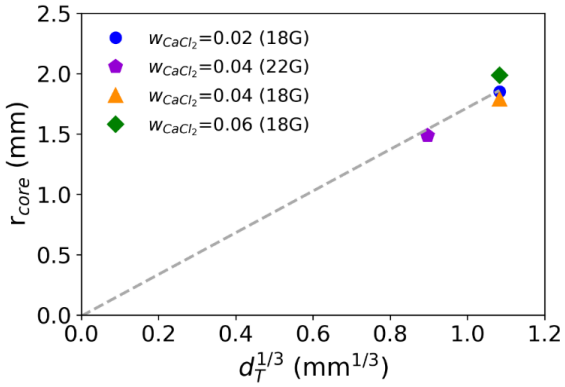

Figure A.5. Linear correlation between core radius (r_{core}) and the cube root of the tip outer diameter ($d_T^{1/3}$).

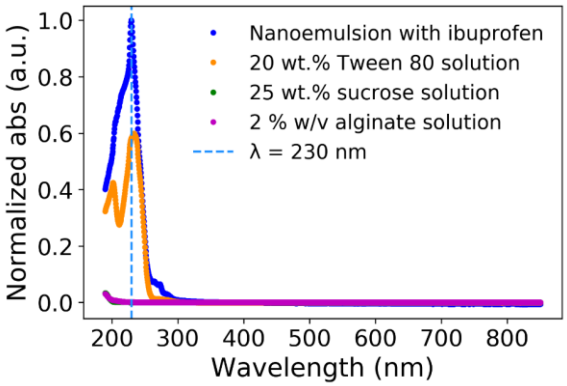

Figure A.6. UV-Vis spectra for the nanoemulsion and its components.

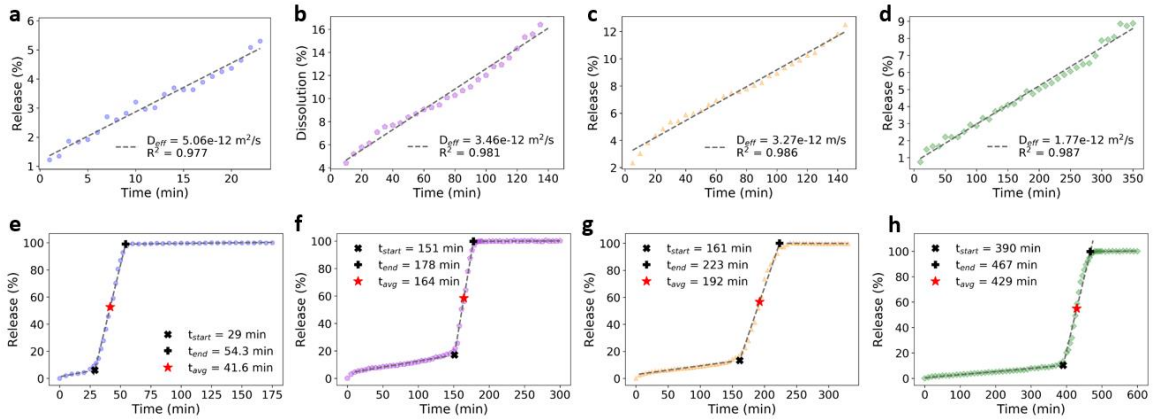

Figure A.7. (a-d) Determination of effective diffusivities (D_{eff}) from the slope in the early diffusion regime (*R1*): (a) w_{CaCl_2}= 0.02 and 18G dispensing tip, (b) w_{CaCl_2}= 0.04 and 22G dispensing tip, (c) w_{CaCl_2}= 0.04 and 18G dispensing tip, (d) w_{CaCl_2}= 0.06 and 18G dispensing tip. (e-h) Determination of bursting time for different preparation conditions: (e) w_{CaCl_2}= 0.02 and 18G dispensing tip, (f) w_{CaCl_2}= 0.04 and 22G dispensing tip, (g) w_{CaCl_2}= 0.04 and 18G dispensing tip, (h) w_{CaCl_2}= 0.06 and 18G dispensing tip.

A.5 Fitting the Bursting Events with Cumulative Distribution Functions

The bursting events occurring in the bursting regime (*R2*) should be statistically random, and the release profile should follow the behavior of a cumulative distribution function (CDF). To fit a CDF to the bursting regime (*R2*) of the release profile, we extracted the release profile $R(t)$ from 10% to 100% (excluding the early diffusion release), and rescaled this 90% release into a CDF $\varphi(t)$ ranging from 0 to 100%. The $\varphi(t)$ represents the cumulative probability of capsule bursting. The $\varphi(t)$ is then transformed into $\varphi(\tau)$ with $\tau = t - t_{avg}$ to shift the distribution mean to $\tau = 0$. With the above setting, the only unknown parameter required to be fitted is the standard deviation σ in the following CDF $\varphi(\tau)$:

$$\varphi(\tau) = \frac{1}{2}\left[1 + \mathrm{erf}\left(\frac{\tau}{\sigma\sqrt{2}}\right)\right] \tag{A.4}$$

The results of the CDF fitting are shown in **Figure A.8a-d**. When the w_{CaCl_2} or the dispensing tip size increases, a larger σ is observed. The fitted CDF can be further transformed into a probability density function $f(\tau)$ (PDF) to represent the release rate in the bursting regime. The $f(\tau)$ is transformed back to $f(t)$, which is further rescaled back to $R(t)$. **Figure A.8e**

shows the release rate profiles of capsules for different preparation conditions. The PDF accurately follows the bursting release rates calculated from the experimental data.

$$f(\tau) = \frac{1}{\sigma\sqrt{2\pi}} \exp\left[-\frac{\tau^2}{2\sigma^2}\right] \tag{A.5}$$

$$\frac{\Delta R(t)}{\Delta t} = f\left(t - t_{avg}\right) \times 90\% \tag{A.6}$$

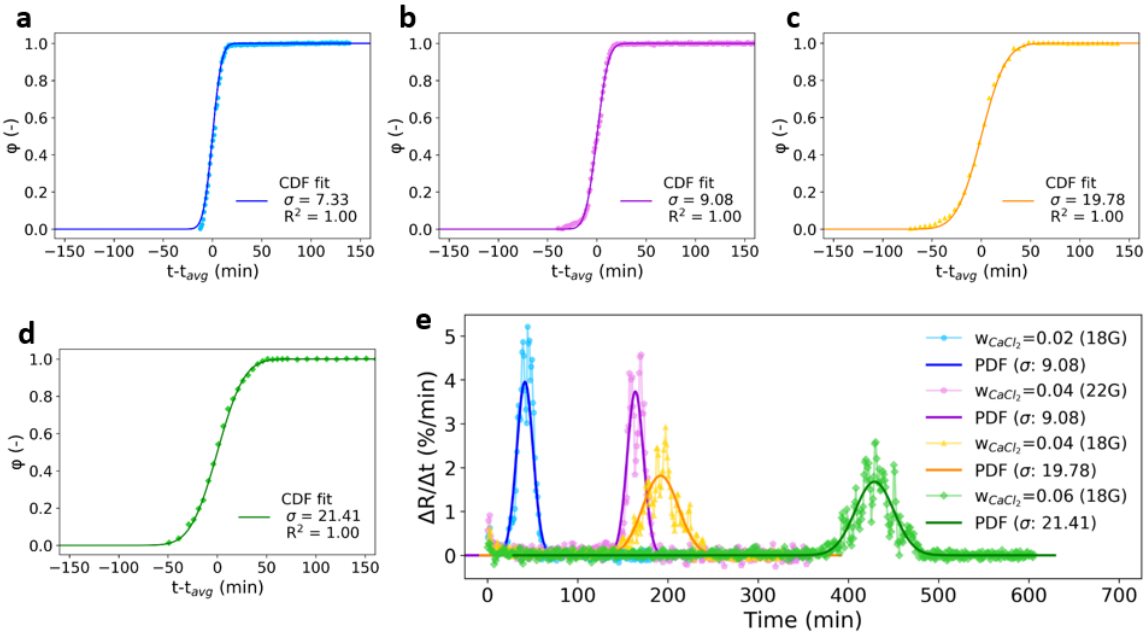

Figure A.8. (a-d) Fitting the bursting regime (*R2*) with a cumulative distribution function (CDF): (a) w_{CaCl_2}= 0.02 and 18G dispensing tip, (b) w_{CaCl_2}= 0.04 and 22G dispensing tip, (c) w_{CaCl_2}= 0.04 and 18G dispensing tip, (d) w_{CaCl_2}= 0.06 and 18G dispensing tip. (e) Release rates ($\Delta R/\Delta t$) of capsules for different preparation conditions: the connected points are calculated from the experimental data, and the solid lines are probability density functions with the standard deviations (σ) obtained from the CDF fitting.

A.6 Preparation of Alginate Beads for Nanoemulsion Encapsulation

Nanoemulsion-loaded alginate beads were prepared by dripping alginate nanoemulsions into a calcium gelation bath (**Figure A.9a**). The alginate nanoemulsions with three different alginate concentrations show droplet sizes between 50 to 55 nm (**Figure A.9b**). The droplet size slightly decreases as the alginate concentration increases, because the continuous phase becomes more viscous, which provides a larger shear to create smaller droplets. The

nanoemulsion-laden alginate beads are shown in **Figure A.9c-e**. The bead radii are similar for different alginate concentrations (**Figure A.9f**). The sphericity factors (SFs) for the three conditions are no greater than a threshold of 0.05 (**Figure A.9g**). The SF slightly decreases with increasing alginate concentration because of a higher viscosity to favor the formation of more spherical alginate beads.

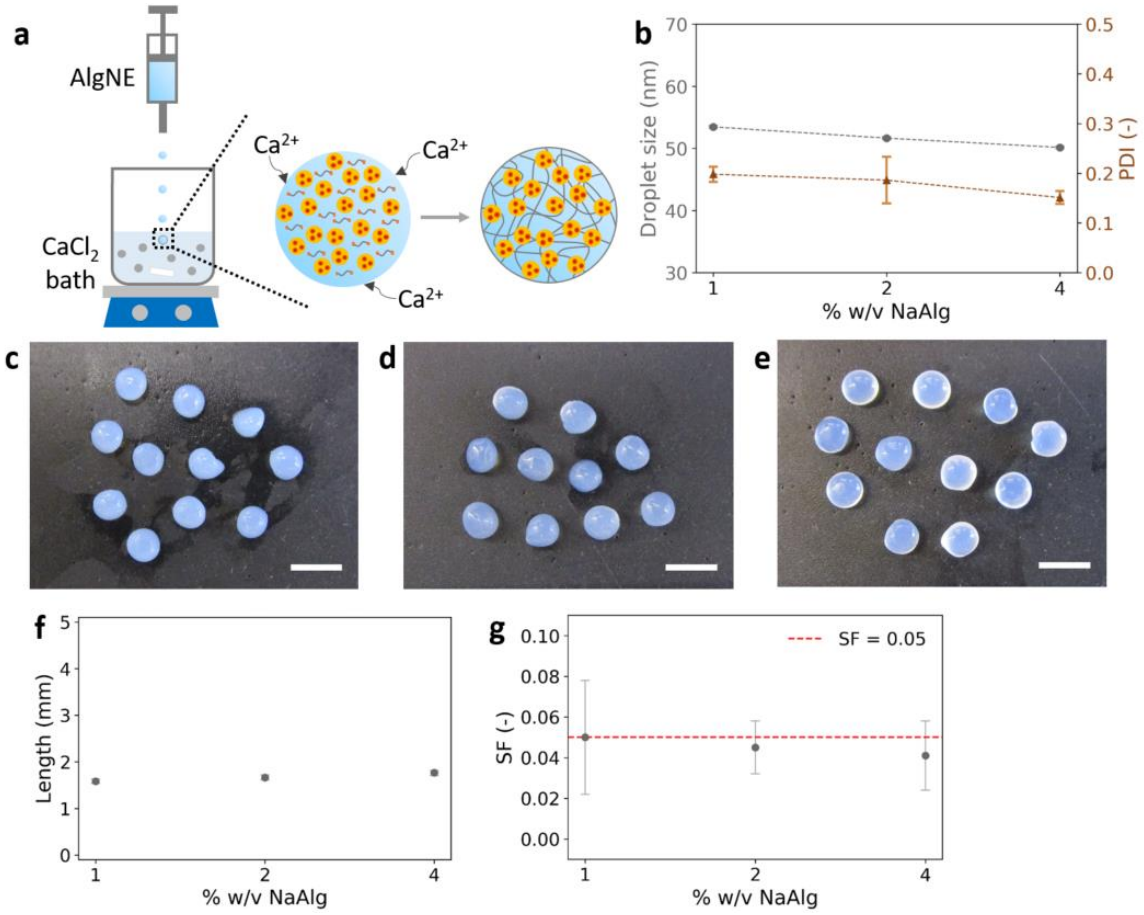

Figure A.9. (a) Schematic diagram of the formation of alginate beads for nanoemulsion encapsulation: the calcium ions diffuse in and ionically crosslink the alginate molecules. (b) Droplet size and polydispersity index for the alginate nanoemulsions prepared with sodium alginate concentrations C_{NaAlg} of 1, 2, and 4% w/v. (c-e) Optical images of beads prepared with an 18G dispensing tip and different sodium alginate concentrations: (c) C_{NaAlg}= 1% w/v, (d) C_{NaAlg} = 2% w/v, and (e) C_{NaAlg} = 4% w/v. f) Bead radii for different preparation conditions. g) Sphericity factors (SF) of the beads for different preparation conditions. All scale bars are 5 mm.

A.7 Release Behavior of Nanoemulsion-Loaded Beads

With the linear calibration curve (**Figure 2.3c**), release tests are conducted to obtain the release profiles of beads for the three different alginate concentrations (**Figure A.10a**). Based on the observation of the release profiles, we separate each release curve into three regimes: diffusion-controlled (*R1*), erosion-controlled (*R2*), and post-release (*R3*) regimes. During the diffusion-controlled (*R1*) regime, no significant bead erosion was observed, and the release profile has a tendency to level off over time. The transition time point (t_{trans}) from the *R1* to *R2* is defined as the point where the slope of the release $R(t)$ stops decreasing and starts to increase again. The t_{trans} is determined to be 15, 30, and 45 s for the C_{NaAlg} of 1, 2, and 4% w/v, respectively. Finally, the release process enters the *R3* as the absorbance signal reaches a saturated value indicating complete release of the cargo. **Figure A.10b** shows the release rates for the three different alginate beads. For each alginate concentration, the release rate increases and develops a peak after the release mechanism transitions to the *R2* regime. In the *R2* regime, the alginate beads degrade significantly, which accelerates the nanoemulsion release. The sharpness of the peaks depends on the crosslinking density of the alginate beads. The alginate beads prepared from a lower alginate concentration possess a lower crosslinking density, which leads to a sharper peak of the release rate. **Figure A.10c** shows the retention of the nanoemulsion suspension in beads for different preparation conditions. The retention rate increases as the alginate concentration increases, and the best retention is about 58.8% for the 4% w/v alginate beads. To further analyze the release profiles, **Equation A.7** and **Equation A.8** based on Peppas power law are used to fit the *R1* and *R2* regimes, respectively.[121]

$$R(\%) = kt^n \tag{A.7}$$

$$R(\%) = k(t - t_{trans})^n + R_{trans}(\%) \tag{A.8}$$

where k is a geometric constant for a hydrogel system, and n is the diffusional exponent representing the release mechanism, $R_{trans}(\%)$ is the $R(\%)$ at t_{trans}. For spherical matrices, the values of $n = 0.43$, $0.43 < n < 0.85$, $n = 0.85$, and $n > 0.85$ represent Fickian diffusion, anomalous (non-Fickian) transport, Case II transport, and Super Case II transport, respectively.[121] The results of the power law fitting are shown in **Figure A.10d-f.** The exponent n values are $0.43 < n < 0.85$ and $n > 0.85$ for the *R1* and *R2* regimes, respectively. This indicates

that the *R1* and *R2* regimes belong to anomalous (non-Fickian) transport and Super Case II transport, respectively. In the *R1* regime, the release is mainly diffusion-controlled with some anomalous behavior due to relaxation and erosion. In contrast, the release is mainly erosion-controlled in the *R2* regime.[185]

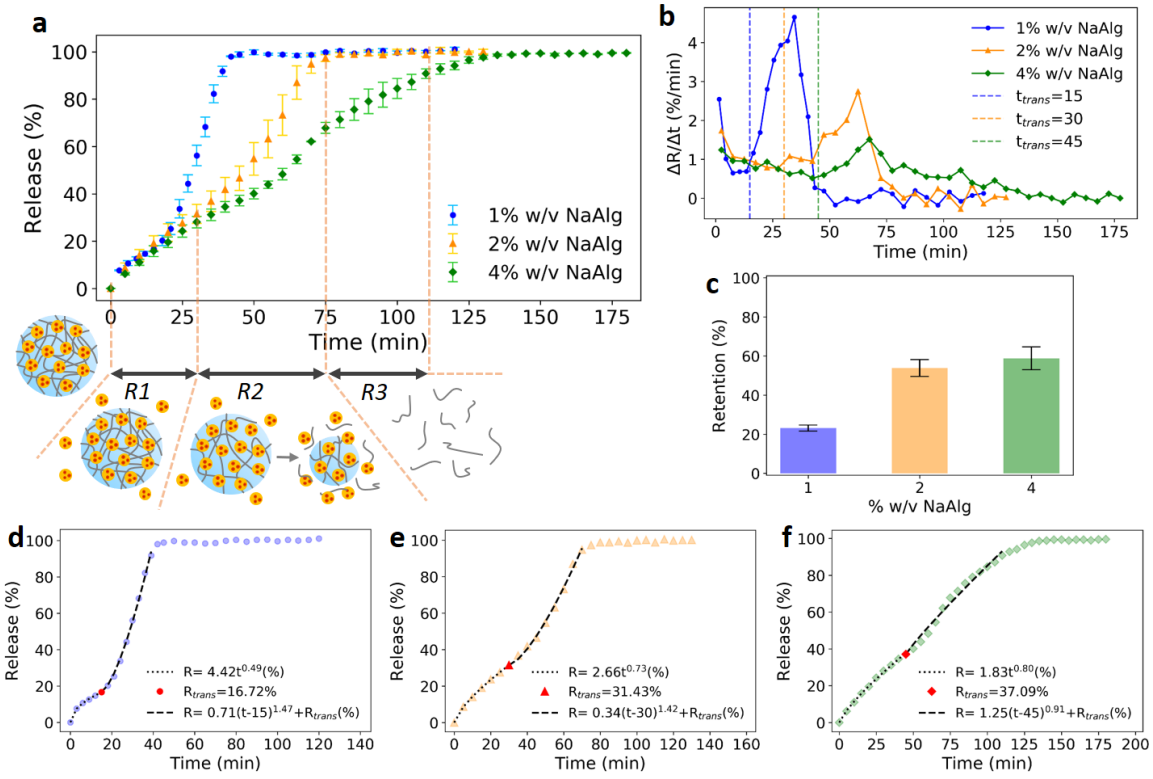

Figure A.10. (a) Release profiles using a USP Dissolution Apparatus II of beads for different preparation conditions. The schematic images below the release profiles depict the release mechanisms for different regimes corresponding to the C_{NaAlg}= 2% w/v (which also apply to other curves). *R1*, *R2*, and *R3* are diffusion-controlled, erosion-controlled, and post-release regimes. (b) Release rates ($\Delta R/\Delta t$) of beads for different preparation conditions. (c) Retention of the nanoemulsion suspension in beads for different preparation conditions. (d-f) Fitting the release profiles with time-dependent power law functions: (d) C_{NaAlg}= 1% w/v, (e) C_{NaAlg}= 2% w/v, and (f) C_{NaAlg}= 4% w/v.

A.8 Tables for Retention Calculation

Table A.2. Retention calculation for alginate capsules.

w_{CaCl_2}(tip size)	0.02 (18G)	0.04 (22G)	0.04 (18G)	0.06 (18G)
n_c	40	70	40	40
m_d (mg)	13.0±0.2	7.0±0.1	12.8±0.3	12.7±0.2
m_{opt} (mg)	518.6±8.8	488.3±5.6	513.1±11.1	506.6±9.8
I_{sat}	0.484±0.007	0.522±0.003	0.508±0.006	0.516±0.004
m_{act} (mg)	443.3±6.4	465.4±5.6	477.5±2.7	472.2±3.4
R_t (%)	85.5±1.9	95.3±1.6	93.1±2.1	93.2±1.9

Table A.3. Retention calculation for alginate beads.

C_{NaAlg} (% w/v)	1	2	4
n_c	40	40	40
m_d (mg)	12.6±0.5	12.6±0.4	12.7±0.3
m_{opt} (mg)	502.4±18.8	502.9±14.5	506.9±14.0
I_{sat}	0.127±0.007	0.296±0.022	0.326±0.031
m_{act} (mg)	116.3±6.7	270.5±20.1	298.1±28.5
R_t (%)	23.1±1.6	53.8±4.3	58.8±5.8

Appendix B Supporting Information for Chapter 3

B.1 Reduction in Nanodroplet Size with Tween 80 Addition

Hydrophilic-lipophilic balance (HLB) of an emulsifier is a critical parameter to control the droplet size of an emulsion. For an anisole-in-water system, it has been reported that larger HLB values favor the formation of smaller droplets.[83] With the prior knowledge that methylcellulose (MC) as an emulsifier has a HLB of 10.5,[186] Tween 80 surfactant with a HLB of 15 is chosen as an additional emulsifier to increase the overall HLB of the nanoemulsion system. The nanodroplet size decreases constantly with increasing addition of Tween 80 (**Figure 3.1b**).

To evaluate the effectiveness of Tween 80 on the dispersed droplet formation, we estimate surface area values occupied by a single Tween 80 for different formulations and compare the results to the theoretical limiting area for a Tween 80 molecule on an interface.[187] Assuming that all the Tween 80 molecules adsorb on the oil nanodroplets in the nanoemulsion, the "effective area" occupied by one Tween 80 molecule ($A_{per\ Tw80}$) can be estimated as follows:

$$N_{drops} = \frac{V_{oil}}{V_{per\ drop}} = \frac{\frac{m_{oil}}{\rho_{oil}}}{\frac{1}{6}\pi d_{drop}^3} = \frac{6m_{oil}}{\rho_{oil}\pi d_{drop}^3} \tag{B.1}$$

$$A_{per\ Tw80} = \frac{N_{drops}A_{per\ drop}}{N_{Tw80}} = \frac{N_{drops}\pi d_{drop}^2}{\frac{m_{Tw80}}{M_{Tw80}}N_A} = \frac{M_{Tw80}N_{drops}\pi d_{drop}^2}{m_{Tw80}N_A} \tag{B.2}$$

where N_{drops} is the number of the oil nanodroplets in the nanoemulsion, $V_{per\ drop}$ is the volume of the oil phase, m_{oil} is the oil phase mass, ρ_{oil} is the density of the oil phase (~1.2 g/mL for a saturated fenofibrate-in-anisole solution), d_{drop} is the nanoemulsion droplet diameter (experimentally determined via dynamic light scattering), $A_{per\ drop}$ is the surface area of one oil nanodroplet, N_{Tw80} is the number of Tween 80 molecules, m_{Tw80} is the Tween 80 mass, M_{Tw80} is the molecular weight of Tween 80 (1,310 g/mol), N_A is the Avogadro constant (6.02×10^{23}).

The calculated effective surface area for a Tween 80 molecule decays quickly with increasing Tween 80 addition (**Figure B.1b**). The effective surface area per Tween 80 value for 0.1 g Tween 80 is below the theoretical limiting area values reported in the literature (gray region),[187] indicating potential excess of free Tween 80 in the system. Therefore, 0.1 g Tween 80 is used to scale up the oil phase mass for a better emulsifying ability. With increasing oil phase mass (fixed 0.1 g Tween 80), the occupied surface area for a Tween 80 increases and levels off at a value close to the lower bound of the theoretical limiting area values (**Figure B.1c**). This indicates the emulsifying limit of Tween 80 could be reached with most Tween 80 molecules adsorbing on the nanodroplets.

Table B.1. Nanoemulsion formulations used in this work. The oil phase is a saturated fenofibrate-in-anisole solution.

	5 wt% MC (g)	Oil phase (g)	Tween 80 (g)	NaCl (g)	Code
	3	0.3	0	0.1	No Tw80
Vary	3	0.3	0.01	0.1	0.01 g Tw80
Tween 80	3	0.3	0.03	0.1	0.03 g Tw80
mass	3	0.3	0.05	0.1	0.05 g Tw80
	3	0.3	0.1	0.1	0.1 g Tw80/0.3 oil/Canonical
Vary	3	0.3	0.1	0.1	0.1 g Tw80/0.3 oil/Canonical
oil phase	3	0.6	0.1	0.1	0.6 g oil
mass	3	0.9	0.1	0.1	0.9 g oil

B.2 Effects of Each Component on Gel Temperature

Figure B.1d summarizes the apparent gel temperature for various nanoemulsions with sequential changes in formulations. Apparent gel point is defined as the cross-over point between G' and G'' at 20 rad/s frequency (0.1% strain) during a temperature ramp experiment at a heating rate of 2°C/min. Compared to the continuous water phase (blue bar), the incorporation of the oil phase (purple bar) results in a lower gel temperature. Oil nanodroplets can be considered as large hydrophobic junctions that already exist at low temperatures. With

the pre-formed hydrophobic junctions that provide a large surface area for further hydrophobic association upon heating, the gelation can complete faster and a lower gel temperature is observed. After Tween 80 is added to the nanoemulsion, the gel temperature slightly increases (from purple to orange bars). The small change in the gel temperature can be attributed to two competing factors. The addition of Tween 80 reduces the nanodroplet size, providing a larger surface area for MC to adsorb and form hydrophobic junctions at low temperatures. This phenomenon should facilitate the gelation and lower the gel temperature. However, amphiphilic Tween 80 molecules can protect the hydrophobic units of MC chains from associating together, which delays the gelation and increases the gel temperature. Lastly, with the surfactant-to-oil (SOR) ratio fixed to have a similar emulsifying ability and droplet size, the addition of more oil phase results in a higher density of oil nanodroplets, providing more hydrophobic junctions that facilitate the gelation and decrease the gel point (from orange to green bars).

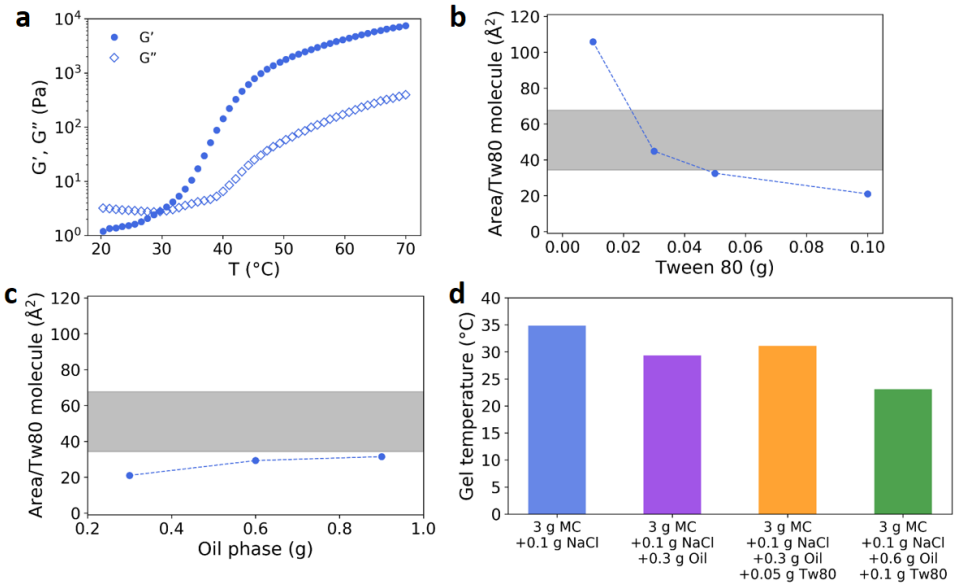

Figure B.1. (a) Storage modulus (G') and loss modulus (G'') of the nanoemulsion (no Tw80) in a temperature ramp experiment at a heating rate of 2°C/min (0.1% strain, 20 rad/s frequency). (b, c) Estimation of the effective surface area occupied by one Tween 80 molecule for nanoemulsions with different formulations: (b) varying Tween 80 mass (0, 0.01, 0.03, 0.05, 0.1 g) and (c) varying oil phase mass (0.3, 0.6, 0.9 g). The gray area indicates the range of theoretical limiting area occupied for one Tween 80 molecule on an interface.[187] (d) Gel temperature of the continuous phase (blue bar) and the nanoemulsions with different formulations (purple, orange, green bars).

B.3 Conditions for Preparing Spherical Thermogel Particles

Figure B.2a shows the viscosity-shear rate flow curves at 20°C for the continuous phase and the nanoemulsions with different formulations. The observed trend for the nanoemulsion system is that decreasing the droplet size (more Tween 80 addition) and increasing the oil fraction result in a higher viscosity and a stronger shear-thinning effect. In contrast to macroemulsion systems, nanoemulsions can easily achieve high viscosities by simple changes in formulations. As the dispersed droplet size reaches the nanoscale, the thickness of the adsorbed surfactant layer (δ) with respect to the droplet radius (r_{drop}) becomes significant, leading to a higher effective dispersed phase concentration than the nominal dispersed phase concentration by a factor of $(1+ \delta/r_{drop})^3$.[89] A prior study shows that a droplet can experience a maximal shear rate of ~290 s^{-1} when it enters a gelation bath.[188] Therefore, the viscosity at 290 s^{-1} for each condition is chosen for comparison (**Figure B.2b**). For the nanoemulsion without the addition of Tween 80 (purple bar), the droplet size is relatively large (~756 nm) and the resulting viscosity is not sufficient to overcome the impact and drag forces exerted by the surrounding water in the gelation bath, as demonstrated by the thermogel particles with a long tail in **Figure B.2c**. In this work, a small addition of 0.05 g Tween 80 is found to facilitate the formation of spherical thermogel particles (**Figure B.2d**). In addition to viscosity, dripping height is also an important parameter for controlling the geometry of gel particles. A prior study showed that for a typical dripping gelation process where a droplet penetrates into a miscible liquid, there is a competition between vortex ring evolution and gelation speed.[188] Mitigating vortex ring evolution and enhancing gelation speed can both favor the formation of spherical gel particles. One simple way to mitigate vortex ring evolution is reducing the momentum of droplet entering the bath. In this work, a dripping height of 1 cm is found to be optimal to prevent the vortex ring evolution (**Figure B.2d**). With increasing dripping height, a larger impact force can be experienced by the droplets, and the thermogel particles gradually evolve from spherical into jellyfish-like shapes (**Figure B.2e, f**).

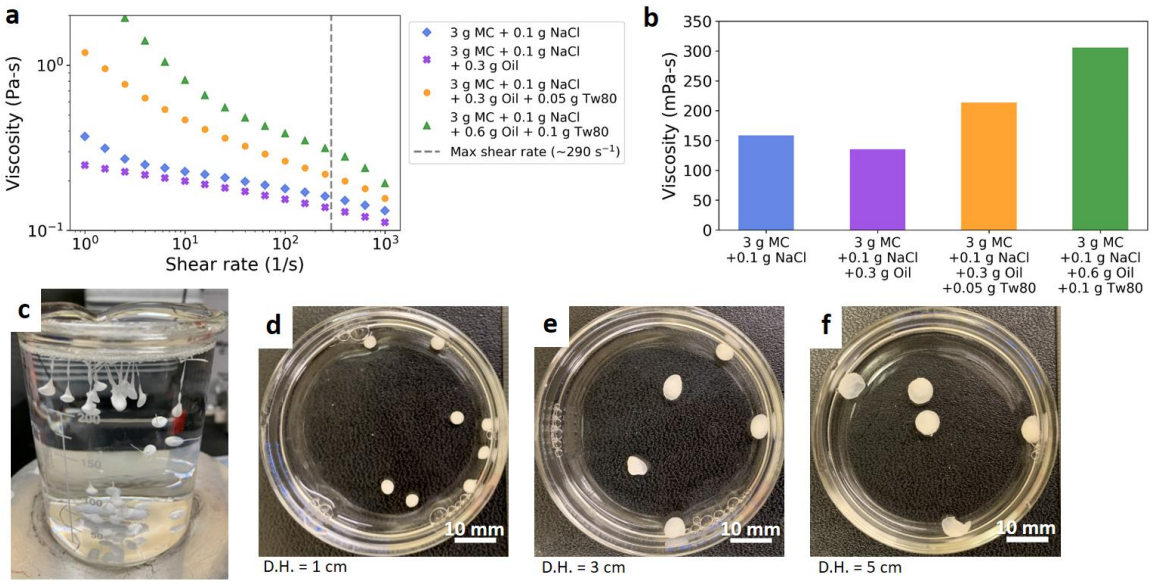

Figure B.2. (a) Viscosity-shear rate flow curves at 20°C for the continuous phase and the nanoemulsions with different formulation conditions. Experimental details are shown in Chapter 3. (b) Viscosity values at a shear rate of 290 s^{-1} for the continuous phase and the nanoemulsions with different formulation conditions. (c) Dangling gel particles with a long tail for the no Tw80 formulation due to the insufficient viscosity to overcome the drag force exerted by the water bath. (d-f) Optical images of the thermogel particles formed with different dripping heights (D.H.): (d) D.H. = 1 cm; (e) D.H. = 3 cm; (f) D.H. = 5 cm. Scale bars are 10 mm.

B.4 Estimation of Time-Dependent Temperature Profiles in a Thermogel Particle

The thermal dripping process can be framed into a one-dimensional transient conduction problem (**Figure B.3a**). A dripped droplet containing the nanoemulsion is initially at T_i = 20°C and enters a water bath with a constant temperature T_∞ = 70°C. The impact velocity (U_0) of a dripped droplet can be calculated using Newton's second law based on air friction and gravitational force.[189]

$$U_0 = \sqrt{\frac{g(1 - e^{-2AH})}{A}} \tag{B.3}$$

$$A = \frac{3C_f \rho_{air}}{\rho_{NE} R} \tag{B.4}$$

where g is the gravitational acceleration (9.8 m/s^2), H is the dripping height (1 cm), C_f is the friction coefficient (~0.7796), ρ_{air} is the air density (~1.225 kg/m^3), ρ_{NE} is the nanoemulsion density (~1.1 g/cm^3), R is the radius of the dripped droplet (1.36 mm for the canonical condition with an 18 gauge dispensing tip).

The thermal diffusivity of the nanoemulsion (α_{NE}) is described by:

$$\alpha_{NE} = \frac{k_{NE}}{\rho_{NE} C_{p,NE}} \tag{B.5}$$

where k_{NE} and $C_{p,NE}$ are the thermal conductivity and specific heat of the nanoemulsion. Because the nanoemulsion is mostly composed of water phase, the k_{NE} and $C_{p,NE}$ are approximated with the properties of 20°C water, which are 0.598 W/m-K and 4.18 kJ/kg-K.

The convective heat transfer coefficient (h) is estimated by the empirical relationship between Nusselt number (Nu), Reynolds number (Re), and Prandtl number (Pr).[190]

$$Nu = \frac{2hR}{k_b} = 0.69 Re^{\frac{1}{2}} Pr^{\frac{1}{3}} \tag{B.6}$$

$$Re = \frac{2\rho_b U_0 R}{\mu_b} \tag{B.7}$$

$$Pr = \frac{C_{p,b}\mu_b}{k_b} \tag{B.8}$$

where ρ_b, μ_b, $C_{p,b}$, and k_b are the density, viscosity, specific heat, and thermal conductivity of the 70°C water bath. Their values are 0.978 g/cm^3, 0.402 mPa-s, 4.19 kJ/kg-K, and 0.660 W/m-K.

The one-dimensional transient conduction problem can be described by the following differential equation in a dimensionless form:

$$\frac{\partial\theta(X,\tau)}{\partial\tau} = \frac{1}{X^2}\frac{\partial}{\partial X}\left[X^2\frac{\partial\theta(X,\tau)}{\partial X}\right] \tag{B.9}$$

where $\theta = \frac{T-T_\infty}{T_i-T_\infty}$, $\tau = \frac{\alpha_{NE}t}{R^2}$, and $X = \frac{r}{R}$ are the dimensionless temperature, time, and distance from the center.

Initial condition is:

$$\theta(X,0) = 1 \tag{B.10}$$

Boundary conditions are:

$$\frac{\partial\theta(X=0,\tau)}{\partial\tau} = 0 \tag{B.11}$$

$$\frac{\partial\theta(X=1,\tau)}{\partial\tau} = -Bi\times\theta \tag{B.12}$$

$$Bi = \frac{hR}{k_{NE}} \tag{B.13}$$

where Bi is Biot number, also known as dimensionless heat transfer coefficient.

The analytical solution to **Equation B.9** can be expressed by the following infinite series:

$$\theta = \sum_{n=1}^{\infty} \frac{4(\sin\lambda_n - \lambda_n \cos\lambda_n)}{2\lambda_n - \sin 2\lambda_n} e^{-\lambda_n^2 \tau} \frac{\sin \lambda_n X}{\lambda_n X} \tag{B.14}$$

where λ_n's are the roots of

$$1 - \lambda_n \cot\lambda_n = Bi \tag{B.15}$$

In this study, the first 100 λ_n's are used to calculate the θ, and the temperature profiles are shown in **Figure B.3b, c**. The important parameters are summarized in **Table B.2**.

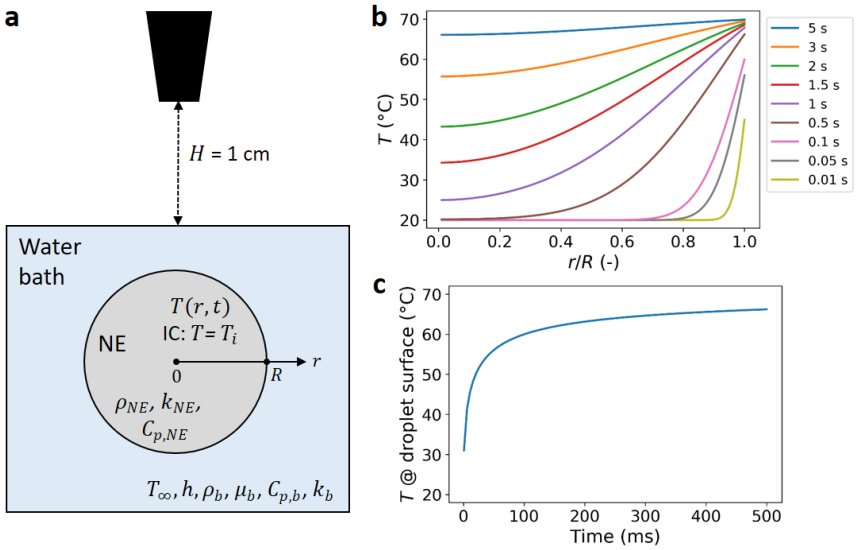

Figure B.3. (a) Schematic diagram of the one-dimensional transient conduction problem with a dripped droplet containing the nanoemulsion in a water bath. (b) Time-dependent temperature profiles across the radius of the droplet from 0.01 to 5 s. (c) Temperature at the droplet surface ($r = R$) within 500 ms.

Table B.2. Summary of important parameters and their values.

Parameter	Value
U_0	0.439 (m/s)
α_{NE}	1.304×10^{-7} (m^2/s)
h	1.231×10^{4} (W/m^2-K)
Bi	28.03 (-)

B.5 Estimation of Drug Loading Efficiency

To determine the drug loading efficiency, m_{NE} (= 3 g) of the nanoemulsion is dripped into the heated water bath (with 1% w/v Tween 80). For this dripping setup, the optimal fenofibrate mass (m_{opt}) carried by the as-prepared nanoemulsion is:

$$m_{opt} = m_{NE}\psi_{FEN/NE} \tag{B.16}$$

$$\psi_{FEN/NE} = \frac{m_o w_{FEN}}{m_c + m_o + m_{Tw80} + m_{NaCl}} \tag{B.17}$$

where $\psi_{FEN/NE}$ is the fenofibrate weight fraction in the as-prepared nanoemulsion, m_o is the oil phase mass, w_{FEN} is the fenofibrate weight fraction in the oil phase (~45 wt%[55]), m_c is the mass of the continuous water phase, m_{Tw80} is the Tween 80 mass, and m_{NaCl} is the NaCl mass.

The drug loss from the gelled nanoemulsion could come from: 1) the leakage of the drug-loaded nanoemulsion from the gelled matrix, and 2) the drug diffusion from the nanoemulsion to the gelation water bath.

Leakage of the drug-loaded nanoemulsion from the gelled matrix

However, for all the formulations used in this work, dynamic light scattering shows that the nanoemulsion is not detectable in the gelation water bath. Instead, only a trace amount of Tween 80 micelles initially in the gelation water bath can be detected with the average size of 11.13±0.85 nm (PDI = 0.144±0.039). The effectiveness of the thermal dripping process is also demonstrated in a turbidity test. An 80 mL clear cold water bath at 20°C (**Figure B.4a**) is sequentially added with the hydrated thermogel particles taken out from the gelation bath. The thermogel particles dissolve quickly in the cold water bath. The cold water bath quickly becomes turbid even though the volume of a single thermogel particle is only 0.01 mL (~10^{-4} of the bath volume). The cold water bath appearances after the sequential addition of 1 to 3 thermogel particles are shown in **Figure B.4b, c, d**. Given that a small thermogel particle can change the turbidity significantly, if the thermal gelation is not effective and there is a small amount of the nanoemulsion leakage, the gelation bath should become turbid easily. The gelation bath water after particle formation is sampled out in a cuvette for comparison as shown

in **Figure B.4e**. The water sample is very clear, demonstrating effective encapsulation of the nanoemulsion in the gelled matrix.

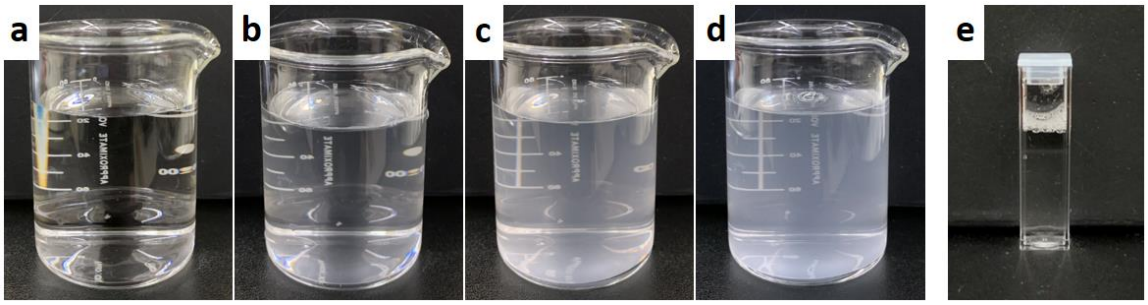

Figure B.4. (a-d) Appearances of a 20°C 80 mL cold water bath with sequential addition of hydrated thermogel particles: (a) clear water bath with no particles dissolved; (b) one particle dissolved; (c) two particles dissolved; (d) three particles dissolved. The volume of one thermogel particle is approximately 0.01 mL. (e) Optical image of the bath water in a cuvette sampled after the gel particles are formed in **Figure 3.2b**.

Drug diffusion from the nanoemulsion to the gelation water bath

To investigate the drug diffusion from the gelled nanoemulsion to the gelation water bath (with 0.1% w/v Tween 80), a concentration-absorbance calibration curve is developed for fenofibrate in a 0.1% w/v Tween 80 aqueous solution (**Figure B.5**). The fenofibrate concentration in the bath (C_{bath}) after the dripping process can be determined from the measured absorbance using the calibration curve (**Figure B.5**). The mass of the fenofibrate (m_{bath}) diffusing into the bath (V_{bath}=300 mL) is estimated by **Equation B.18**, and the drug loading efficiency (L_E) is defined by **Equation B.19**.

$$m_{bath} = C_{bath} V_{bath} \tag{B.18}$$

$$L_E = 1 - \frac{m_{bath}}{m_{opt}} \tag{B.19}$$

Summarized in **Table B.3**, the drug loading efficiencies for different formulations are all greater than 99.4 wt%, indicating minimal drug diffusion to the bath. Compared to anisole that is a good solvent with a high fenofibrate saturation solubility of ~480 mg/mL,[55] the gelation water bath (with 0.1% w/v Tween 80) only has a fenofibrate saturation solubility of ~6.7×10^{-}

^{3} mg/mL.[159] Therefore, it is very unlikely for fenofibrate to partition from the nanoemulsion to the gelation bath.

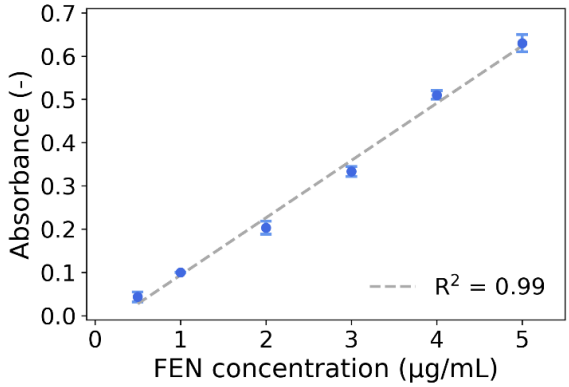

Figure B.5. Concentration-absorbance calibration curve for fenofibrate in a 0.1% w/v Tween 80 solution at λ = 287 nm.

Table B.3. Summary of drug loading efficiency estimation for different formulations.

	Code	$\psi_{FEN/NE}$ (wt%)	m_{opt} (mg)	m_{bath} (mg)	L_E (wt%)
Vary Tween 80 mass	No Tw80	3.97	119.12	0.47±0.03	99.61±0.02
	0.01 g Tw80	3.96	118.77	0.28±0.05	99.76±0.04
	0.03 g Tw80	3.94	118.08	0.54±0.02	99.54±0.02
	0.05 g Tw80	3.91	117.39	0.30±0.01	99.74±0.01
	0.1 g Tw80/0.3 oil/Canonical	3.86	115.71	0.60±0.01	99.48±0.01
Vary oil phase mass	0.1 g Tw80/0.3 oil/Canonical	3.86	115.71	0.60±0.01	99.48±0.01
	0.6 g oil	7.11	213.16	0.65±0.06	99.69±0.03
	0.9 g oil	9.88	296.34	0.90±0.02	99.70±0.01

B.6 Role of NaCl in Particle Formulation

Cl^- ions are salt-out ions that can facilitate and strengthen the hydrophobic association,[117] which is critical for the formation of thermogel particles. The Cl^- ions can compete with MC molecules for water hydration; therefore, the addition of NaCl leads to a poorer solubility of

MC in water and a stronger hydrophobic association. For the salt-free nanoemulsion (canonical condition without NaCl), the resulting dried particles buckle and are flat (**Figure B.6a, b**), suggesting that the hydrophobic interaction is not strong enough.

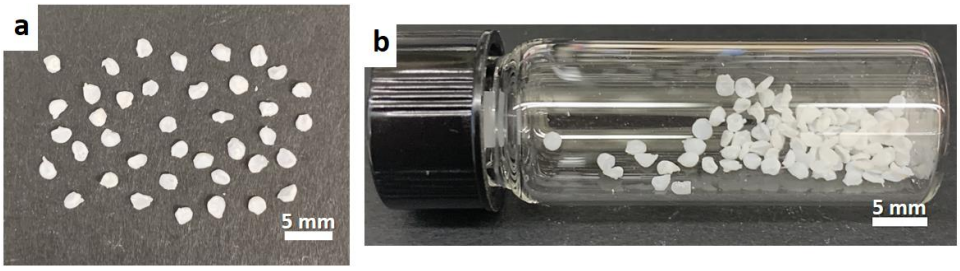

Figure B.6. (a, b) Optical images of the dried API-loaded particles (canonical condition without NaCl addition): (a) on a platform and (b) in a vial. Scale bars are 5 mm.

B.7 Estimation of Nanocrystal Size with Nanodroplet Size

By balancing the fenofibrate mass in a nanodroplet and in a nanocrystal, the size of a nanocrystal can be estimated as follows:

$$d_{c,est} = \left(\frac{C_{fen}}{\rho_c}\right)^{\frac{1}{3}} d_{drop} \tag{B.20}$$

where $d_{c,est}$ is the estimated nanocrystal diameter, C_{fen} is the fenofibrate-in-anisole concentration (~0.48 g/mL[55]), ρ_c is the nanocrystal density (1.2 g/cm^3 = 1.2 g/mL), and d_{drop} is the nanoemulsion droplet diameter.

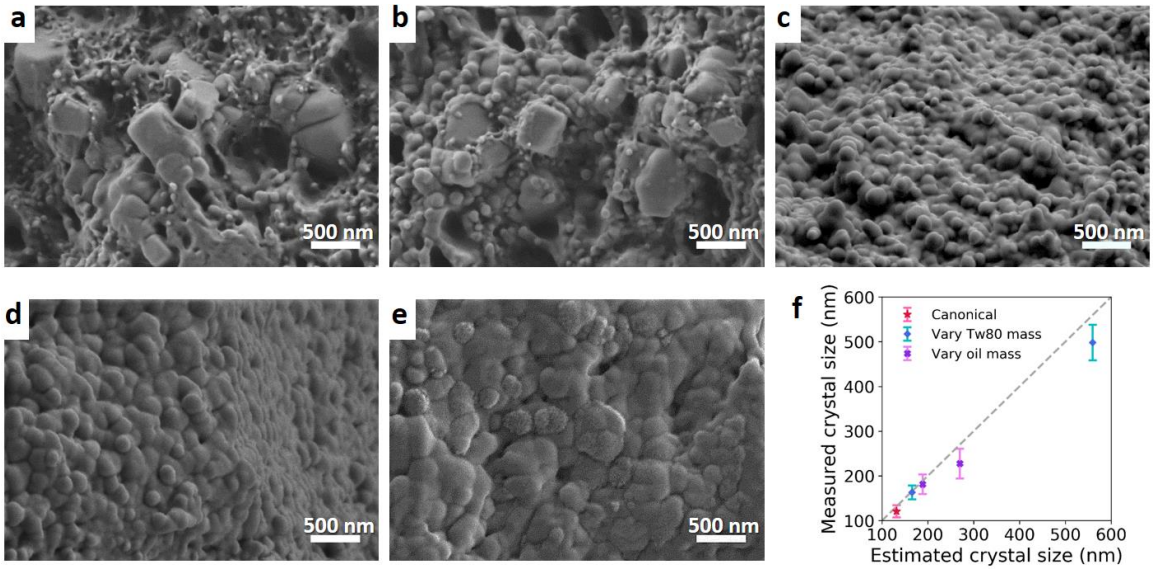

Figure B.7. (a-e) SEM images of the embedded nanocrystals in the dried API-loaded particles for different nanoemulsion formulations: (a, b) no Tw80; (c) 0.05 g Tw80; (d) 0.6 g oil; (e) 0.9 g oil. Scale bars are 500 nm. (f) Comparison between the measured (from the SEM images) and estimated ($d_{c,est}$ in **Equation B.20**) crystal sizes. The accuracy of the measured crystal size is limited by the fact that the nanocrystals are embedded and fused in the MC polymer matrix.

B.8 Tate's Law for Designing Particle Size

The relationship between the dried particle diameter ($d_{particle}$) and the tip outer diameter (d_T) can be described by Tate's law.

$$d_{particle} \propto \left(\frac{d_T \gamma_{NE}}{\rho_{NE} g}\right)^{\frac{1}{3}} \tag{B.21}$$

where γ_{NE} and ρ_{NE} are the surface tension and density of the nanoemulsion, g is the gravitational acceleration (9.8 m/s^2). For the same nanoemulsion formulation, the $d_{particle}$ is proportional to the cube root of the d_T, as shown in **Figure B.8g**.

Table B.4. Specifications of the dispensing tips used in this work. The outer diameter (O.D.) of the smooth-flow tapered tips are measured with a caliper.

Gauge	Type	I.D. (mm)	O.D. (mm)
14	Smooth-flow tapered tip	1.54	1.97
18	Smooth-flow tapered tip	0.84	1.26
25	Smooth-flow tapered tip	0.25	0.68
30	Precision stainless steel tip	0.15	0.30

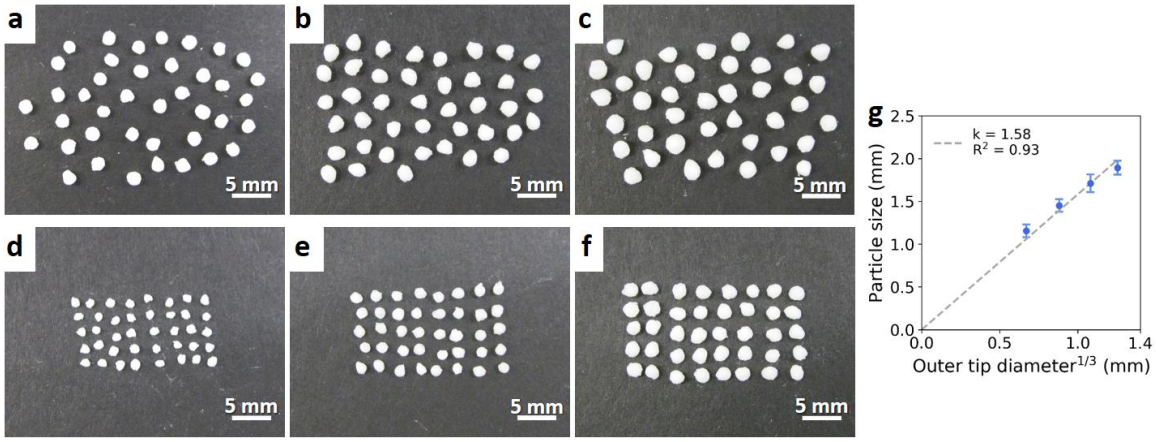

Figure B.8. (a-f) Optical images of the dried API-loaded particles for different conditions: (a) 0.05 g Tw80 with 18-guage tip; (b) 0.6 g oil with 18-guage tip; (c) 0.9 g oil with 18-guage tip; (d) canonical with 30-gauge tip; (e) canonical with 25-gauge tip; (f) canonical with 14-gauge tip. Scale bars are 5 mm. (g) Tate's law correlation between the particle diameter ($d_{particle}$) and the cube root of the tip outer diameter ($d_T^{1/3}$) for the canonical formulation.

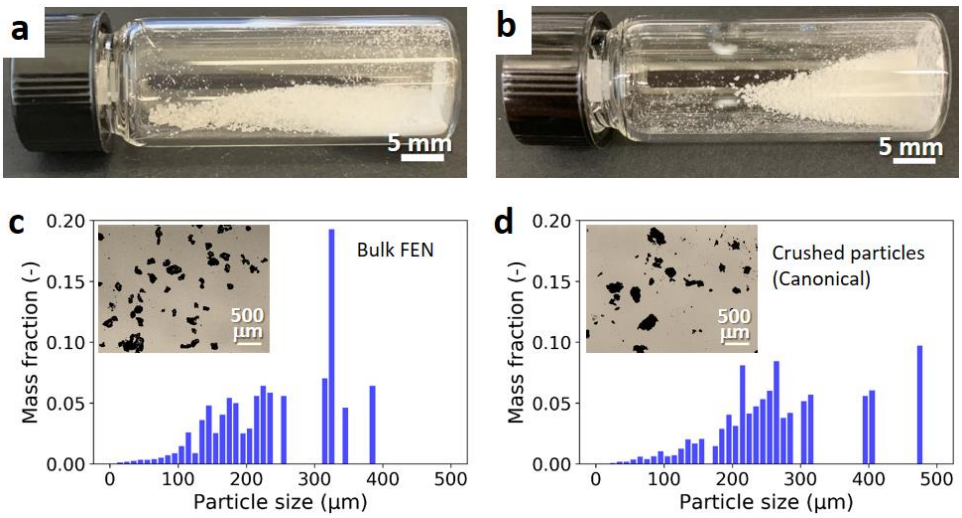

Figure B.9. (a, b) Optical images of the (a) the as-received bulk fenofibrate crystals and (b) the crushed particles (canonical formulation) in a vial. Scale bars are 5 mm. (c, d) Particle size distributions and bright-field microscopy images of (c) the bulk fenofibrate crystals and (d) the crushed particles (canonical formulation). Scale bars in the inset figures are 500 µm.

B.9 Estimation of Drug Loading Content

With the concentration-absorbance calibration curve developed in **Figure B.10b**, the drug loading contents of the dried API-loaded particles can be measured using UV-Vis spectroscopy (**Figure 3.3a** and **Figure B.10c**). In addition, the drug loading contents can be estimated by **Equation B.22** for comparison. Because Tween 80 and NaCl do not form hydrophobic junctions with MC upon heating, they are considered removable and should be able to diffuse out of the thermogel particles in the heated water bath. To account for this, we introduce retention rates for both Tween 80 and NaCl.

$$\phi_{FEN} = \frac{m_o w_{FEN}}{m_c w_{MC} + m_o w_{FEN} + \zeta_{Tw80} m_{Tw80} + \zeta_{NaCl} m_{NaCl}} \tag{B.22}$$

where ϕ_{FEN} is the estimated drug loading content, m_o is the oil phase mass, w_{FEN} is the fenofibrate weight fraction in the oil phase (~45 wt%[55]), m_c is the mass of the continuous water phase, w_{MC} is the MC weight fraction in the water phase (5 wt%), ζ_{Tw80} is the retention rate of Tween 80 in the dried particles, m_{Tw80} is the Tween 80 mass, ζ_{NaCl} is the retention rate of NaCl in the dried particles, and m_{NaCl} is the NaCl mass.

The theoretically maximal (blue dashed curve with ζ_{Tw80} = 0 and ζ_{NaCl} = 0) and minimal (green dash-dotted curve with ζ_{Tw80} = 1 and ζ_{NaCl} = 1) drug loading contents are first determined for complete removal and retention for the two species. As expected, the measured drug loading contents lie in the region between these two curves (**Figure 3.3a** and **Figure B.10c**). To deconvolute the retentions for the two species, we first analyze the retention rate of NaCl for the nanoemulsion without Tween 80 addition (0 g Tween 80 in **Figure B.10c**). A ζ_{NaCl} of ~0.3 is calculated to match the measured drug loading content for this condition. Assuming the effective diffusivity of NaCl is roughly constant for different formulations because the gel matrices are formed with the same continuous phase, a drug loading content curve is plotted with ζ_{Tw80} = 1 and ζ_{NaCl} = 0.3 for different formulations (orange dotted curve), and a good consistency between the measured and estimated drug loading contents is found (**Figure 3.3a** and **Figure B.10c**). The result indicates that most Tween 80 still retains in the dried particles. Compared to small NaCl ions which are freely to move, Tween 80 molecules are mostly anchored on the oil-water interface, preventing them from diffusing out. In addition, the bulky molecular structure of Tween 80 renders the diffusion difficult even if there are free Tween 80 molecules.

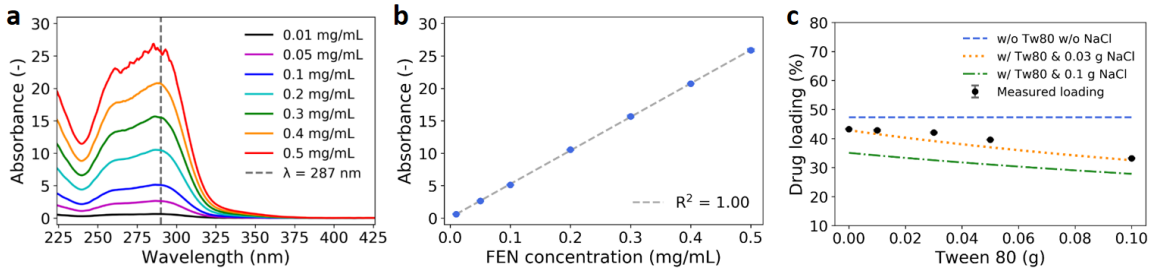

Figure B.10. (a) UV-Vis spectra of fenofibrate-in-ethanol solutions with different concentrations. (b) Concentration-absorbance calibration curve developed with the absorbance values at λ = 287 nm. The curve has a perfect linear relationship with R^2 ~ 1. (c) Drug loading contents of the dried API-loaded particles as a function of Tween 80 mass (fixed 3 g MC solution, 0.3 g oil phase, 0.1 g NaCl). The blue dashed curve corresponds to **Equation B.22** with ζ_{Tw80} = 0 and ζ_{NaCl} = 0 (complete removal of Tween 80 and NaCl). The orange dotted curve corresponds to **Equation B.22** with ζ_{Tw80} = 1 and ζ_{NaCl} = 0.3 (100% and 30% retention of Tween 80 and NaCl). The green dashdotted curve corresponds to **Equation B.22** with ζ_{Tw80} = 1 and ζ_{NaCl} = 1 (complete retention of Tween 80 and NaCl).

B.10 Characterization of Fenofibrate Nanocrystals in Thermogel Particles

The XRD patterns in **Figure B.11a** show that the nanocrystals in the dried particles share the same characteristic peaks of the bulk fenofibrate crystals, which corresponds to crystalline form I.[119] In **Figure B.11b**, the high frequency spectrum (1500 to 1700 cm^{-1}) for the fenofibrate nanocrystals in the dried particles (canonical condition) is compared with the spectra for form I, form II, and amorphous fenofibrate. The solid-state form of the fenofibrate nanocrystals is identified to be crystalline form I by matching the three peaks at 1586, 1599, and 1650 cm^{-1}. The first two wavenumbers correspond to the stretching of in-plane benzene ring, and the 1650 cm^{-1} corresponds to the C=O stretching.[119] DSC is also a powerful tool to identify fenofibrate polymorphs based on their different melting points. The as-received bulk fenofibrate shows a sharp melting point at 81.7°C that corresponds to crystalline form I polymorph (**Figure B.11c**). For all the formulations in this study (**Figure 3.3d** and **Figure B.12a, d**), no exothermic signal is observed for the fenofibrate nanocrystals in the dried particles, indicating no crystallization of amorphous fenofibrate during the measurement.

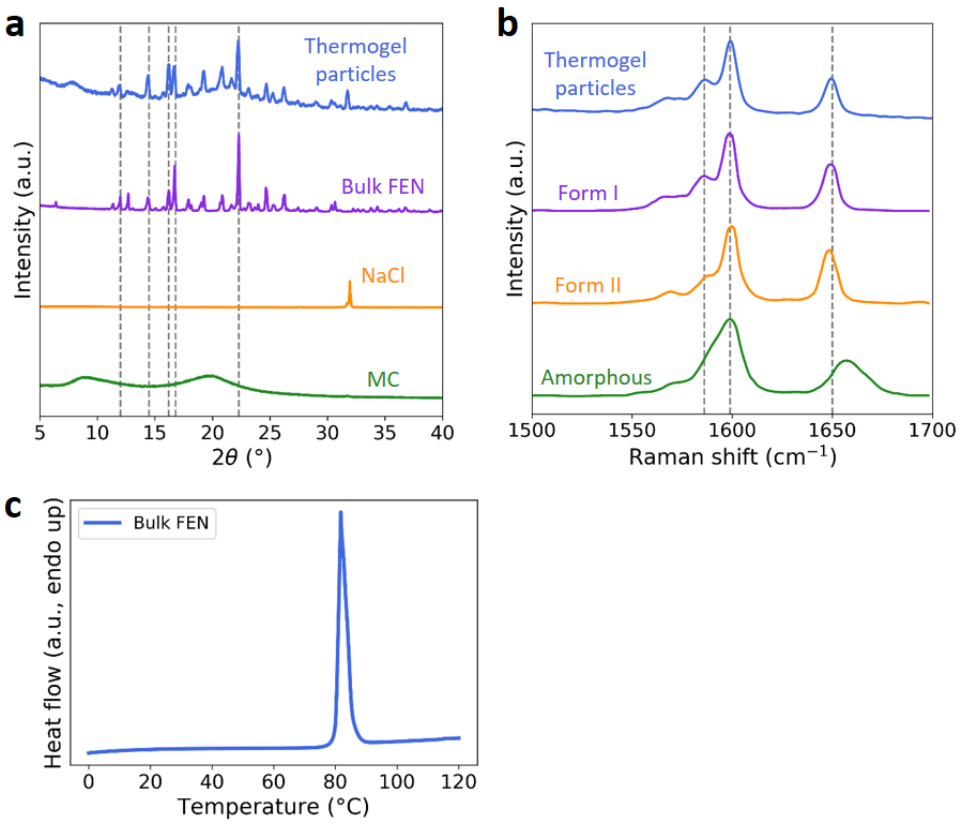

Figure B.11. (a) X-ray patterns of the fenofibrate nanocrystals in the dried API-loaded particles, as-received bulk fenofibrate, NaCl, and methylcellulose. (b) High frequency Raman spectra of the fenofibrate nanocrystals in the dried particles (this work) and three reference solid-state forms of fenofibrate reported in the literature.[120] The dashed lines indicate the characteristic peaks for crystalline form I fenofibrate. (c) DSC thermogram of the as-received bulk fenofibrate crystals.

B.11 Estimation of Crystallinity of Fenofibrate Nanocrystals

Prior studies show that reduction of fenofibrate crystal size leads to decreasing melting point and enthalpy of fusion.[70,113] The correlation between the melting point and enthalpy of fusion data is plotted in **Figure B.12c**. Assuming that each DSC curve represents a melting point (T_{mp}) distribution for a nanocrystal size distribution in the dried particles, the crystallinity (Γ_{FEN}) of the fenofibrate nanocrystals in the dried API-loaded particles is estimated by calculating the ratio of the fenofibrate nanocrystal mass ($m_{FEN,DSC}$) to the optimal fenofibrate mass ($m_{FEN,opt}$).

$$\Gamma_{FEN} = \frac{m_{FEN,DSC}}{m_{FEN,opt}} \times 100\% \tag{B.23}$$

$$m_{FEN,DSC} = \int_{-\infty}^{\infty} \frac{\dot{H} \times m_{sample}}{\dot{T} \times \Delta H_{fusion}} dT_{mp} \tag{B.24}$$

$$m_{FEN,opt} = m_{sample} \times \phi_{FEN} \tag{B.25}$$

where $\dot{H}$ is the specific heat flow (W/g), m_{sample} is the sample mass of the crushed particles for the DSC measurement (g), $\dot{T}$ is the heating rate (°C/s), ΔH_{fusion} is the enthalpy of fusion (J/g), ϕ_{FEN} is the drug loading content determined by UV-Vis spectroscopy. Both the $\dot{H}$ and ΔH_{fusion} are a function of melting point T_{mp}.

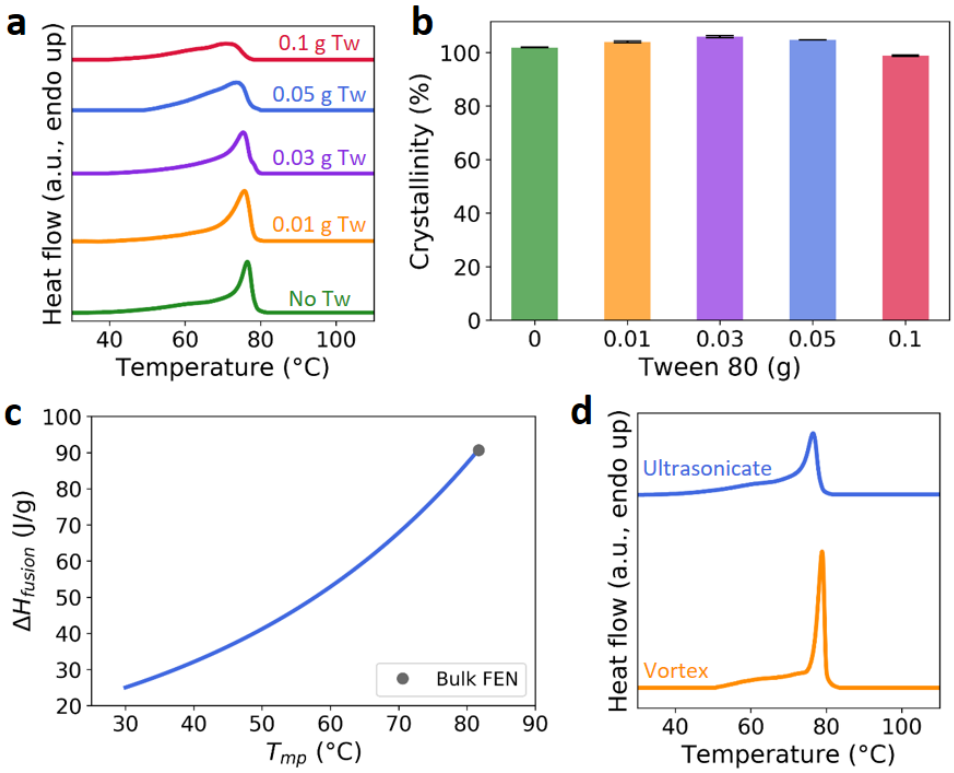

Figure B.12. (a) DSC thermograms and (b) crystallinity of the fenofibrate nanocrystals in the dried API-loaded particles for different Tween 80 mass (fixed 3 g MC solution, 0.3 g oil phase, 0.1 g NaCl). (c) Correlation between the enthalpy of fusion and melting point for fenofibrate nanocrystals. The plot is generated with the data from the previous work.[70,113] (d) DSC thermograms of the fenofibrate nanocrystals in the dried particles prepared with different energy inputs. The nanoemulsion formulation is 3 g MC solution, 0.3 g oil phase, 0.1 g NaCl (no Tw80).

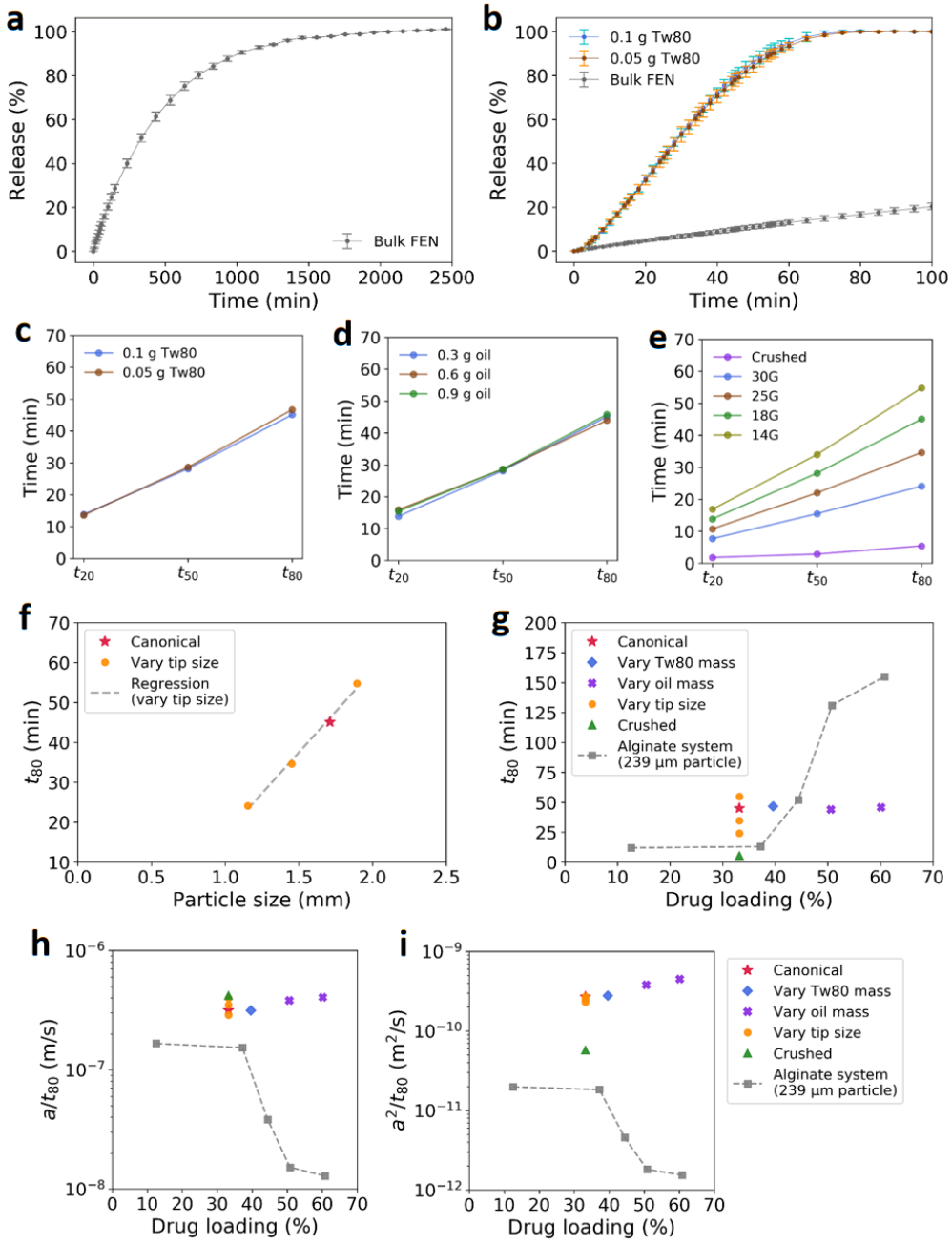

Figure B.13. (a) Cumulative release profiles of the bulk fenofibrate crystals and the dried API-loaded particles with different Tween 80 mass. (b) Complete cumulative release profile of the bulk fenofibrate crystals. (c-e) Time at 20%, 50%, 80% drug release (t_{20}, t_{50}, t_{80}) for various parameters: (c) Tween 80 mass, (d) oil phase mass, (e) dispensing tip size and the crushed particles. (f) Linear correlation between the t_{80} and particle size. (g) Time at 80% drug release (t_{80}) of the dried MC particles and the alginate particles for different drug loading contents. (h) Erosion rate (a/t_{80}) and (i) diffusivity (a^2/t_{80}) comparisons for the dried MC particles and the alginate particles. a is the radius of dried particles. The result for the alginate particles is from our previous work.[55]

B.12 Power Law Model

Power law model[121] is used to describe the fraction of drug release from 3% to 60%:

$$\frac{M_t}{M_\infty} = kt^n \tag{B.26}$$

where M_t and M_∞ are the amount of drug released at time *t* and infinite time, *k* is the kinetic constant (with the unit of t^{-n}), and *n* is the diffusional exponent. The value of *n* is indicative of the drug release mechanism.

B.13 Erosion Model for an Erodible Sphere

A model for an erodible sphere[123] is also used to analyze the release of the dried particles (**Figure B.14c**). Assuming that there exists an erosion constant (k_e, with the unit of m/s) and that volume dissolution rate is proportional to the sphere surface, we get the following differential equation.

$$\frac{dV_t}{dt} = k_e \times 4\pi r^2 \tag{B.27}$$

The volume dissolved (V_t) at time *t* and the volume for complete dissolution (V_∞) are

$$V_t = \frac{4}{3}\pi(a^3 - r^3) \tag{B.28}$$

$$V_\infty = \frac{4}{3}\pi a^3 \tag{B.29}$$

By solving **Equation B.27** and **Equation B.28** simultaneously, we get

$$\frac{V_t}{V_\infty} = 1 - \left[1 - \frac{k_e t}{a}\right]^3 \tag{B.30}$$

Because the well-dispersed nanoemulsion indicates a uniform drug content in the polymer matrix, the fractional mass release should be equivalent to the fractional volume dissolved:

$$\frac{M_t}{M_\infty} = \frac{V_t}{V_\infty} \tag{B.31}$$

To account for the time required to wet the surface of the dried particles, a lag time (t_{lag}) is introduced and the resulting erosion model becomes:

$$\frac{M_t}{M_\infty} = 1 - \left[1 - \frac{k_e(t - t_{lag})}{a}\right]^3 \tag{B.32}$$

For the same nanoemulsion formulation, the k_e gradually decreases as the particle size increases (**Figure B.14d**). The trend could be attributed to the fact that smaller particles provide a larger surface area for water hydration. The water hydration quickly forms a gel layer on the particle surface, which slows down further water penetration into the dry inner cores. When the drug release starts at $t = t_{lag}$, smaller particles are wetted and swollen to a greater extent. In contrast, larger particles still have a larger portion of dry inner cores which require further wetting before erosion. On average, larger particles have a larger volume of dry inner cores that is protected by the gel layer, thereby leading to a smaller k_e.

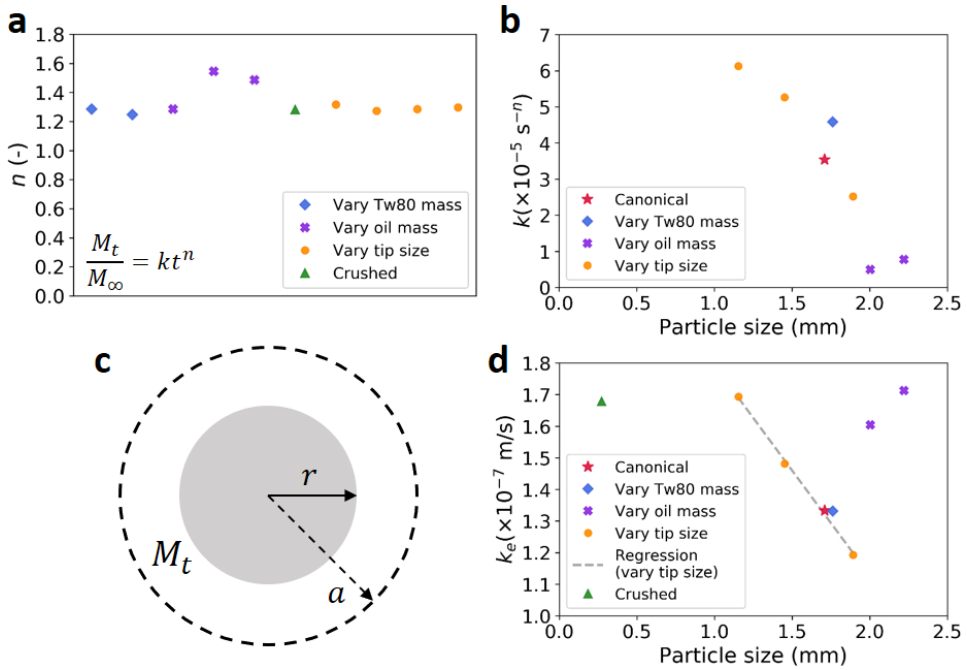

Figure B.14. (a, b) Results for power law fitting. (a) Diffusional exponents n for various conditions. (b) Relationship between the kinetic constant (k) and particle size. (c) Schematic diagram of an erodible sphere which has eroded from its initial radius a to the position r at time t. (d) Relationship between the erosion constant (k_e) and particle size.

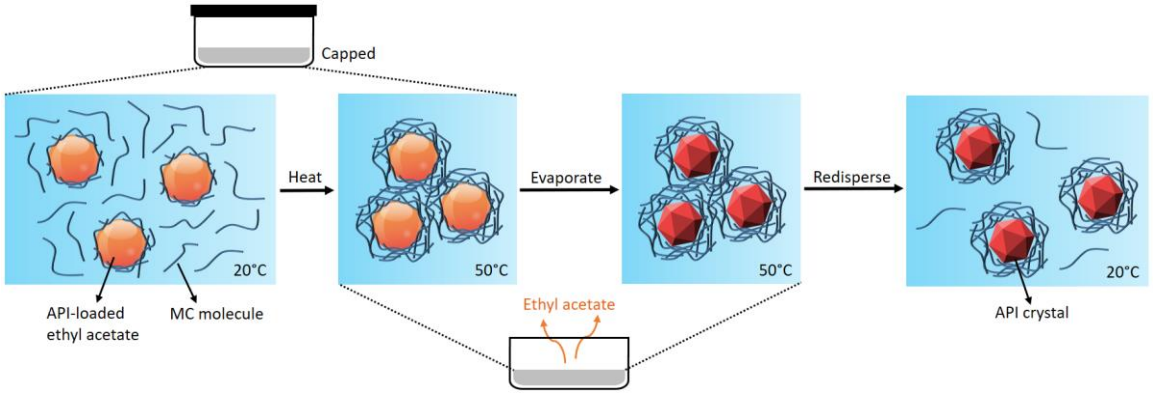

Figure B.15. Procedures for preparing API-loaded nanoparticle suspensions.

B.14 Effects of Dissolution Medium

In this work, a 25 mM sodium dodecyl sulfate (SDS) solution was selected as a dissolution medium. The use of this medium is recommended by the FDA Dissolution Methods Database for fenofibrate dosage forms.[157] Fenofibrate is a hydrophobic API that is practically insoluble in water. Therefore, the addition of SDS surfactant is a valid approach to simulate *in vivo* solubilization done by biorelevant surfactants.[158,159] In addition, fenofibrate belongs to Biopharmaceutics Classification System (BCS) Class II drugs: high permeability and low solubility.[173] This means that absorption of dissolved fenofibrate from solution is much faster than dissolution of fenofibrate, causing sink conditions to prevail *in vivo*. The SDS solution creates a sink condition during the dissolution, which can be a good proxy of *in vivo* conditions.[158]

Fenofibrate is neutral and has no ionizable group, so its solubility is not influenced by changes in medium pH.[191] This explains why pH buffers are not demanded in the FDA Dissolution Methods Database. Moreover, the excipient selected in this study is methylcellulose (MC), which is also neutral and non-ionic. As reported by both Dow Inc. and Colorcon Inc., methylcellulose provides a matrix that exhibits a pH-independent drug release profile when drug solubility is pH-independent.[43,192] To demonstrate the pH-independent property, in addition to a 25 mM SDS solution (pH~6.0), we also prepared a simulated gastric fluid (SGF) and a simulated intestinal fluid (SIF) by tuning the pH value of a 25 mM SDS solution to 2.0 and 6.8 using HCl and phosphate buffered saline (PBS), respectively. As shown in **Figure B.16**, the release profiles of particles with the same preparation condition (0.6 g oil condition) are superimposed, indicating a pH-independent release of the fenofibrate dosage forms prepared in this work.

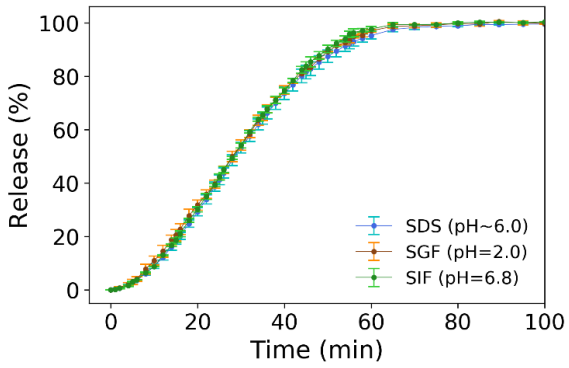

Figure B.16. Cumulative release profiles of particles (0.6 g oil condition) in a 25 mM SDS solution (pH~6.0), a simulated gastric fluid (SGF, pH=2.0), and a simulated intestinal fluid (SIF, pH=6.8). The SGF and SIF are prepared by tuning the pH value of a 25 mM SDS to 2.0 and 6.8 using HCl and phosphate buffered saline (PBS), respectively.

B.15 Stability of Fenofibrate Nanocrystals

Different solvent (ethyl acetate)

In **Figure 3.5c**, a TEM image is taken for the MC-stabilized nanoparticle suspension. Ethyl acetate is chosen as a fast-evaporating solvent (boiling point of 77.1°C) instead of anisole for the design of nanoparticle suspension. To check if the use of ethyl acetate also leads to the crystalline form I fenofibrate as in the anisole system, XRD is applied to characterize the dried nanoparticle suspension. In **Figure B.17**, the XRD patterns for the nanoparticle suspension align well with the characteristic peaks for crystalline form I fenofibrate.[119] This indicates that the use of ethyl acetate also leads to the most stable fenofibrate polymorph.

During the dissolution

To check if the fenofibrate polymorphism changes in the release medium (25 mM SDS), XRD patterns before dissolution and after 50% dissolution are shown in **Figure B.18**. The two XRD patterns both align well with the characteristic peaks for crystalline form I fenofibrate.[119] The agreement is a manifestation that the fenofibrate nanocrystals induced *in situ* in the MC matrix are the most stable solid-state form with the lowest free energy.

Long-term stability

To demonstrate the long-term stability of the fenofibrate nanocrystals in the particles, XRD and DSC analyses are carried out on the particles after six-month storage under the ambient condition (**Figure B.19**). The XRD and DSC results show that the fenofibrate nanocrystals after six-month storage are still the most stable crystalline form I, and the crystallinity is still ~100%.

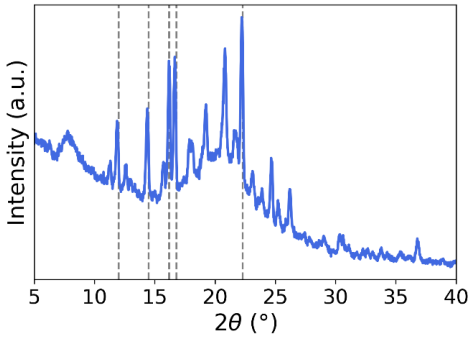

Figure B.17. X-ray pattern of the dried nanoparticle suspension prepared using ethyl acetate as an organic solvent. The dashed lines indicate the characteristic peaks for crystalline form I fenofibrate.

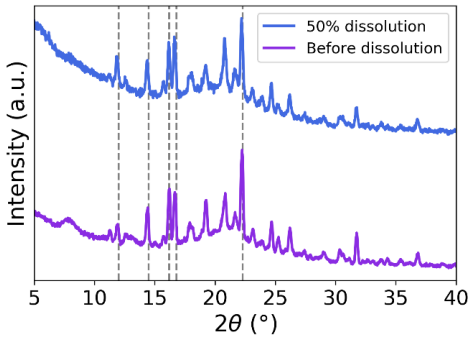

Figure B.18. X-ray patterns of the fenofibrate nanocrystals in the dried particles: before dissolution (purple curve) and after 50% dissolution (blue curve). The dashed lines indicate the characteristic peaks for crystalline form I fenofibrate.

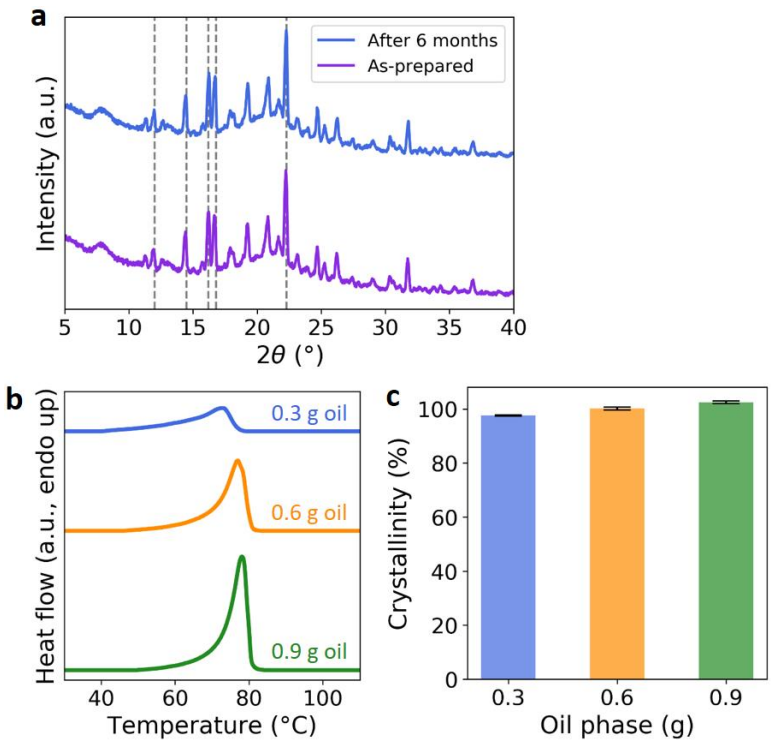

Figure B.19. (a) X-ray patterns of the fenofibrate nanocrystals in the dried particles: as-prepared (purple curve) and after six-month storage (blue curve). The dashed lines indicate the characteristic peaks for crystalline form I fenofibrate. (b) DSC thermograms and (c) crystallinity of the fenofibrate nanocrystals in the particles for different oil phase mass after six-month storage.

B.16 API Candidates for the Proposed Formulation Technology

The proposed formulation technology is targeted for hydrophobic APIs that belong to the Biopharmaceutics Classification System (BCS) Class II and Class IV. In the conventional process, nanocrystal formation of hydrophobic APIs has been proven to greatly enhance the bioavailability compared to their bulk counterparts. Many well-known hydrophobic APIs have been benefitted from the nanocrystal technology, such as danazol, naproxen, fenofibrate, ketoprofen, cilostazol, aprepitant, cyclosporine, and itraconazole.[102] For these hydrophobic APIs that can stably exist in their crystalline form, we should be able to find suitable organic solvents to dissolve them and directly generate the API nanocrystals *in situ* in the MC matrix using the proposed formulation technology. Our group has done in-depth fundamental studies and developed general design strategies for synthesizing nanoemulsions with different oil phases.[13,83,125] This can help us make informed decisions and broaden the possibility to synthesize a wide variety of API-loaded nanoemulsions for different API/solvent pairs.

Appendix C Supporting Information for Chapter 4

C.1 Parameter Space for the Thermogelling Nanoemulsions and Oral Films

Table C.1. Nanoemulsion compositions used in this work. The water phase and oil phase are a 4 wt% HPMC solution and a saturated fenofibrate-in-anisole solution, respectively.

Water phase (g)	Oil phase (g)	Tween 80 (g)	Code
3	0.2	0.01	0.2 g
3	0.4	0.02	0.4 g
3	0.6	0.03	0.6 g

Table C.2. Thickness controls for the nanoemulsions with different oil phase mass.

Oil (g)	NE on glass slide (g)	Predicted film mass (mg)	Measured film mass (mg)	Thickness (μm)	Code
0.2	1.3	89.1	92.7±1.1	55.2±2.9	0.2 g (55.2 μm)
0.4	1.0	93.6	95.2±1.2	55.4±3.7	0.4 g (55.4 μm)
0.4	1.5	140.4	142.5±0.7	80.4±5.4	0.4 g (80.4 μm)
0.4	2.0	187.1	186.4±2.3	111.8±8.1	0.4 g (111.8 μm)
0.4	2.5	243.0	240.7±2.3	150.2±7.9	0.4 g (150.2 μm)
0.6	0.8	92.6	92.9±1.5	55.6±3.3	0.6 g (55.6 μm)

C.2 Supporting Figures for the Thermogelling Nanoemulsions and Oral Films

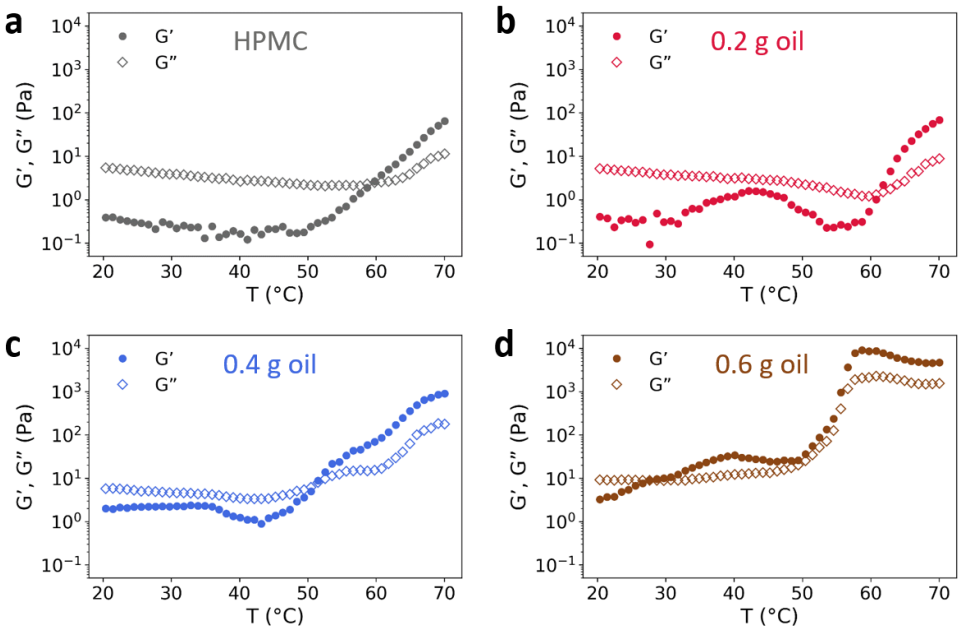

Figure C.1. (a-d) Elastic moduli (G') and viscous moduli (G'') of the pure HPMC and the nanoemulsions in the temperature ramp experiment at a heating rate of 2°C/min (0.1% strain, 10 rad/s frequency): (a) pure HPMC, (b) 0.2 g oil, (c) 0.4 g oil, (d) 0.6 g oil.

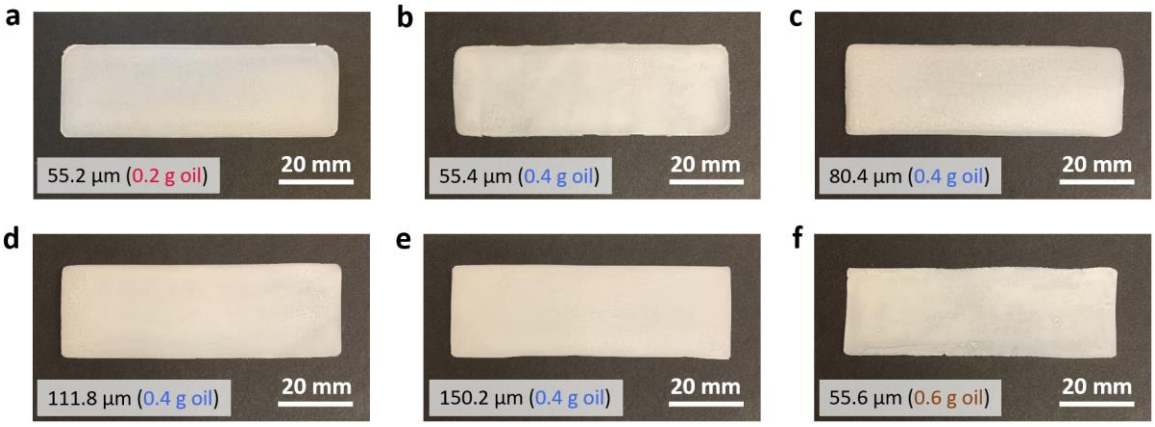

Figure C.2. (a-f) Optical images of the oral films with different conditions: (a) 0.2 g oil (thickness = 55.2 µm), (b) 0.4 g oil (thickness = 55.4 µm), (c) 0.4 g oil (thickness = 80.4 µm), (d) 0.4 g oil (thickness = 111.8 µm), (e) 0.4 g oil (thickness = 150.2 µm), (f) 0.6 g oil (thickness = 55.6 µm).

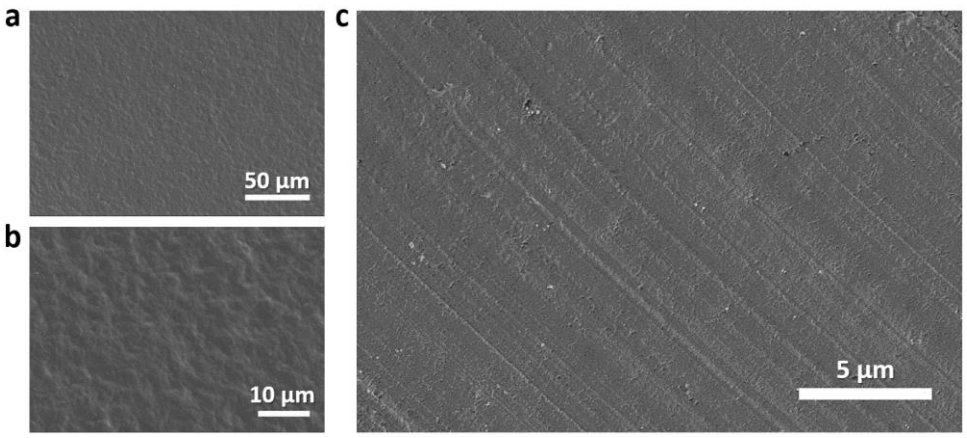

Figure C.3. (a, b) SEM images of the surface of a pure HPMC film without drug. (c) SEM image of the cross-section of a pure HPMC film without drug.

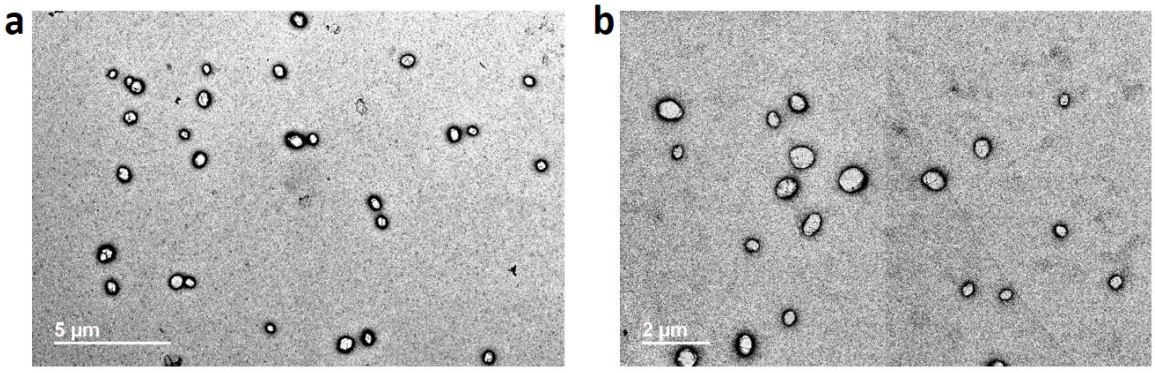

Figure C.4. (a, b) TEM images of the dispersed drug nanoparticles.

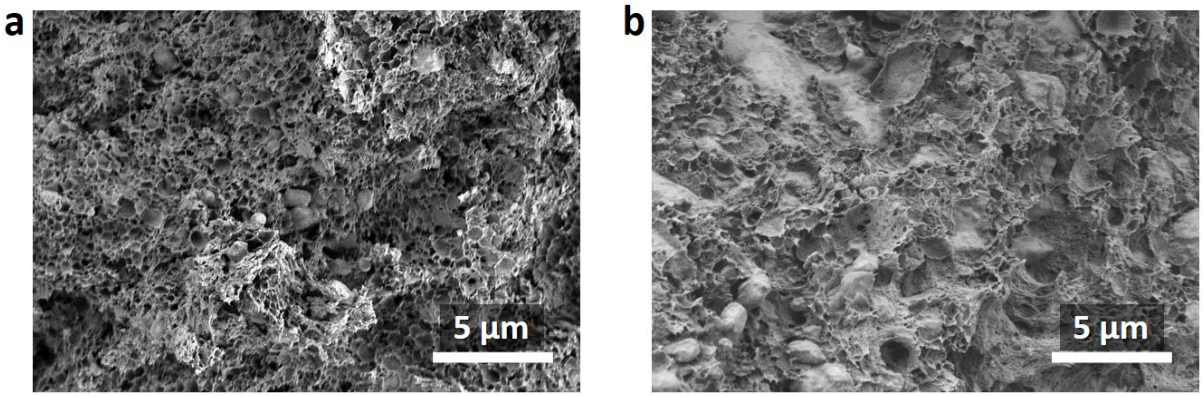

Figure C.5. SEM images of the oral film cross-sections: (a) 0.2 g oil and (b) 0.6 g oil.

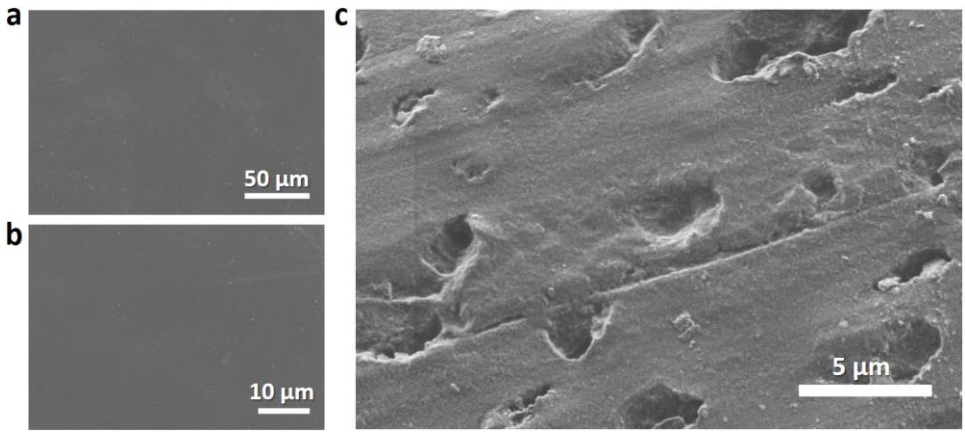

Figure C.6. SEM images of the oral film cross-sections: (a) 0.2 g oil and (b) 0.6 g oil.

C.3 Supporting Drug Loading Data

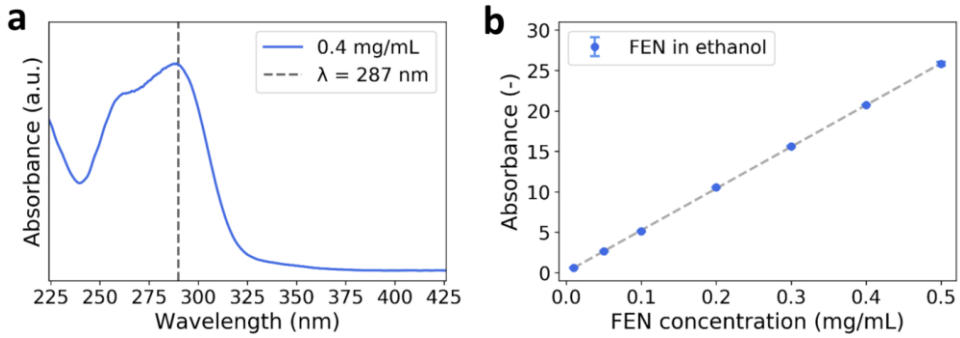

Figure C.7. (a) UV-Vis absorbance spectrum of a 0.4 g mg/mL fenofibrate-in-ethanol solution. The absorption peak occurs at λ = 287 nm. (b) Concentration-absorbance calibration curve developed for different fenofibrate concentrations in ethanol (absorbance values are recorded at λ = 287 nm). The curve has a perfect linear relationship with R^2 ~1.

C.4 Estimation of Fenofibrate Crystallinity in Oral Film

Prior studies show that smaller fenofibrate nanocrystals lead to the decreasing melting point and enthalpy of fusion.[70,113] The prior data is plotted in **Figure C.8b** to build a correlation curve between the melting point and enthalpy of fusion for fenofibrate nanocrystals. Assuming that each DSC curve represents a melting point (T_{mp}) distribution corresponding to different-sized fenofibrate nanocrystals in the oral film. The crystallinity (Γ_{FEN}) of fenofibrate in the oral film can be estimated by taking the ratio of the mass of crystalline fenofibrate ($m_{FEN,cryst}$) to the optimal fenofibrate mass ($m_{FEN,opt}$).

$$\Gamma_{FEN} = \frac{m_{FEN,cryst}}{m_{FEN,opt}} \times 100\% \tag{C.1}$$

$$m_{FEN,cryst} = \int_{-\infty}^{\infty} \frac{\dot{H} \times m_{sample}}{\dot{T} \times \Delta H_{fusion}} dT_{mp} \tag{C.2}$$

$$m_{FEN,opt} = m_{sample} \times \phi_{FEN} \tag{C.3}$$

where $\dot{H}$ is the specific heat flow (W/g), m_{sample} is the sample mass of the oral film for the DSC measurement (g), $\dot{T}$ is the heating rate (°C/s), ΔH_{fusion} is the enthalpy of fusion (J/g), ϕ_{FEN} is the drug loading content determined by UV-Vis spectroscopy. Both the $\dot{H}$ and ΔH_{fusion} are a function of melting point T_{mp}.

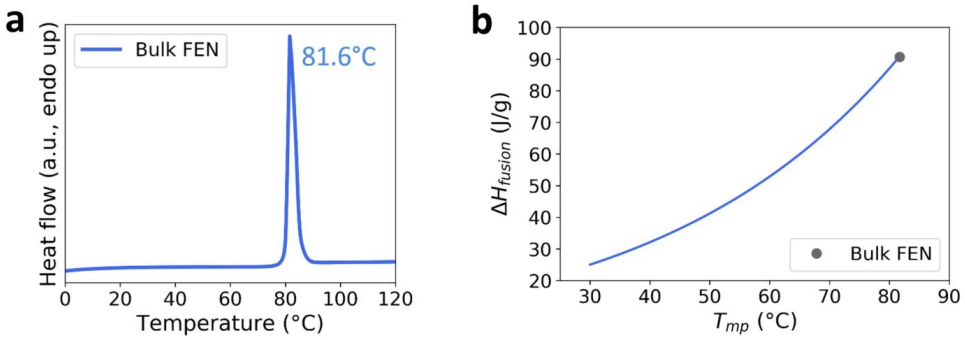

Figure C.8. (a) DSC thermogram of the bulk fenofibrate crystals. (b) Correlation between the enthalpy of fusion and melting point of fenofibrate nanocrystals. The plot is generated with the data obtained from the previous studies.[70,113]

C.5 Tensile Testing

Mechanical properties are important parameters for oral film products; however, there are no official standards about mechanical properties of film products. The rule of thumb is that film products should have good enough mechanical properties so that they can be manufactured and handled without damage or crack.[131] For the oral film images prepared in this work (**Figure C.2**), there is no observable crack on the film surface. Typical mechanical properties include elongation at break, Young's modulus, and tensile strength.[193] The stress-strain curves for the oral films with different conditions are shown in **Figure C.9a**. The films with different conditions have similar Young's moduli (**Figure C.9b**), which lie in the range (0.2 to 3000 MPa) for the fenofibrate-loaded oral films prepared using conventional methods.[128,138] In **Figure C.9c, d**, the tensile strength and elongation at break depend strongly on the drug loading (i.e., oil mass) but weakly on the thickness. Increasing the oil mass leads to a decrease in the tensile strength and elongation at break. This phenomenon could be explained by the fact that more drug nanoparticles decrease the continuity of the polymer matrix.[194] The films have tensile strength values ranging from 6 to 24 MPa, which lie in the range reported in the literature (0.6 to 49 MPa).[128,138] The elongation at break values for the films with 0.2 g and 0.4 g oil lie in the range for marketed thin film products (1.03–6.54%).[193]

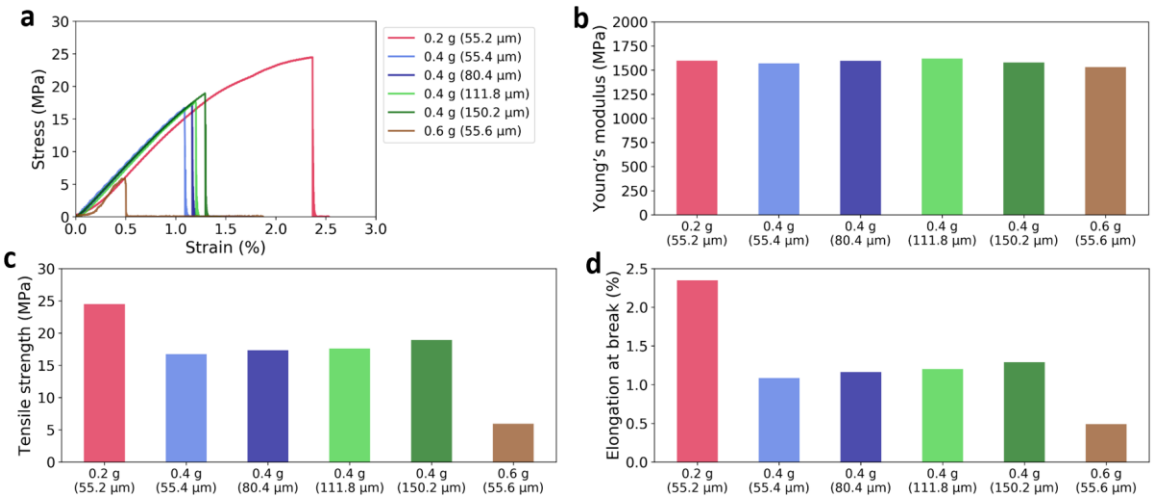

Figure C.9. (a) Stress-strain curves for the oral films with different conditions. (b-d) Tensile properties of the oral films with different conditions: (b) Young's modulus, (c) tensile strength, (d) elongation at break.

C.6 Supporting Release Data

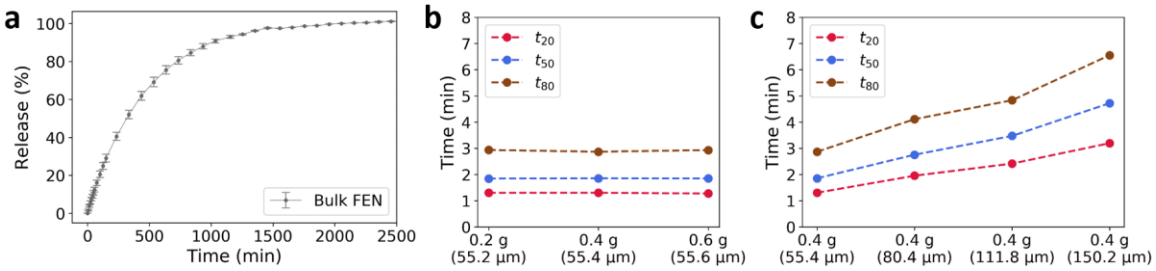

Figure C.10. (a) Cumulative release profile for the bulk fenofibrate crystals. (b-c) Time at 20%, 50%, 80% drug release (t_{20}, t_{50}, t_{80}) for various parameters: (b) varying the oil mass with a constant thickness (~55.4 µm), (c) varying the thickness with the same oil mass (0.4 g oil).

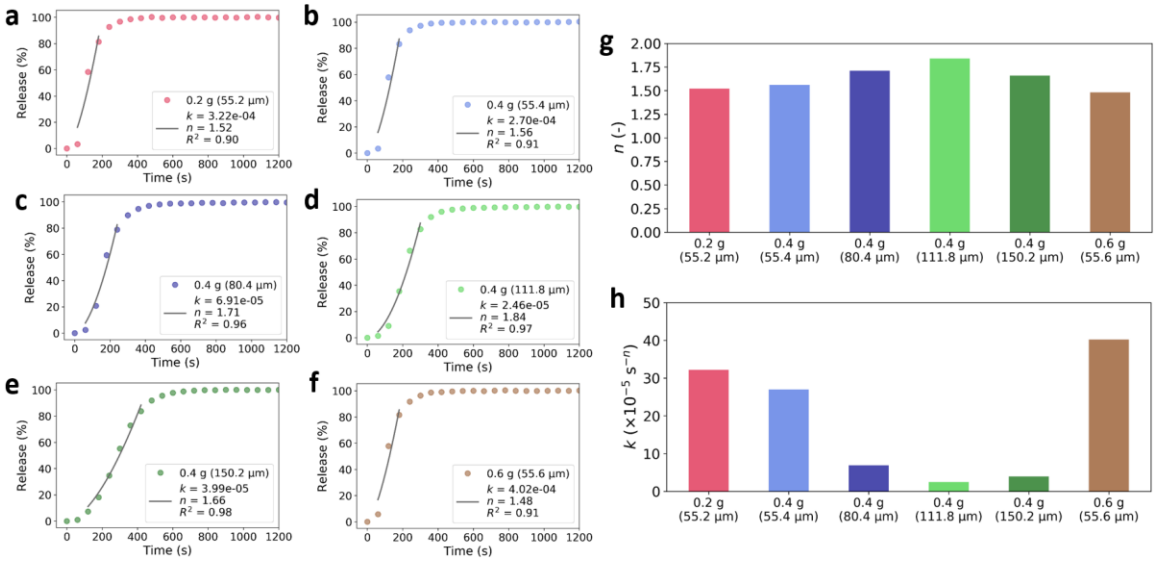

Figure C.11. (a-f) Power-law fitting for the oral films with different conditions: (a) 0.2 g oil (55.2 µm), (b) 0.4 g oil (55.4 µm), (c) 0.4 g oil (80.4 µm), (d) 0.4 g oil (111.8 µm), (e) 0.4 g oil (150.2 µm), (f) 0.6 g oil (55.6 µm). (g-h) Fitting parameters for the oral films with different conditions: (g) diffusional exponent (n), (h) kinetic constant (k).

C.7 Erosion Model for Oral Films

A model for an erodible thin film is used to analyze the drug release from the oral film.[123] Assuming that there exists an erosion constant (k_e, with the unit of m/s) and that volume dissolution rate is proportional to the surface are of the film, we have:

$$V_t = 2k_eAt \tag{C.4}$$

where V_t is the volume dissolved at time t.

With the half thickness of the film to be a, the volume for complete dissolution (V_∞) can be expressed as follows:

$$V_\infty = 2aA \tag{C.5}$$

Because the drug is uniformly distributed in the polymer matrix, the fractional mass release (M_t/M_∞) should be equivalent to the fractional volume dissolved (V_t/V_∞):

$$\frac{M_t}{M_\infty} = \frac{V_t}{V_\infty} = \frac{k_e t}{a} \tag{C.6}$$

where M_t and M_∞ are the amount of drug released at time *t* and infinite time.

To account for the time required to wet the surface of the oral film, a lag time (t_{lag}) is introduced and the erosion model becomes:

$$\frac{M_t}{M_\infty} = \frac{k_e\left(t - t_{lag}\right)}{a} \tag{C.7}$$

C.8 Scaling of Release Profiles

Because the lag time (t_{lag}) is proportional to the film thickness ($2a$), we assume there is a constant (K_{lag}) that relates the t_{lag} and a:

$$t_{lag} = K_{lag}a \tag{C.8}$$

Plugging **Equation C.8** into **Equation C.7**, we get:

$$\frac{M_t}{M_\infty} = k_e\left(\frac{t}{a}\right) - k_e K_{lag} \tag{C.9}$$

As shown in **Figure C.12g**, the k_e values are similar for all conditions. Therefore, according to **Equation C.9**, different release profiles should be collapsed into one master curve by plotting $\frac{M_t}{M_\infty}$ and $\frac{t}{a}$ together.

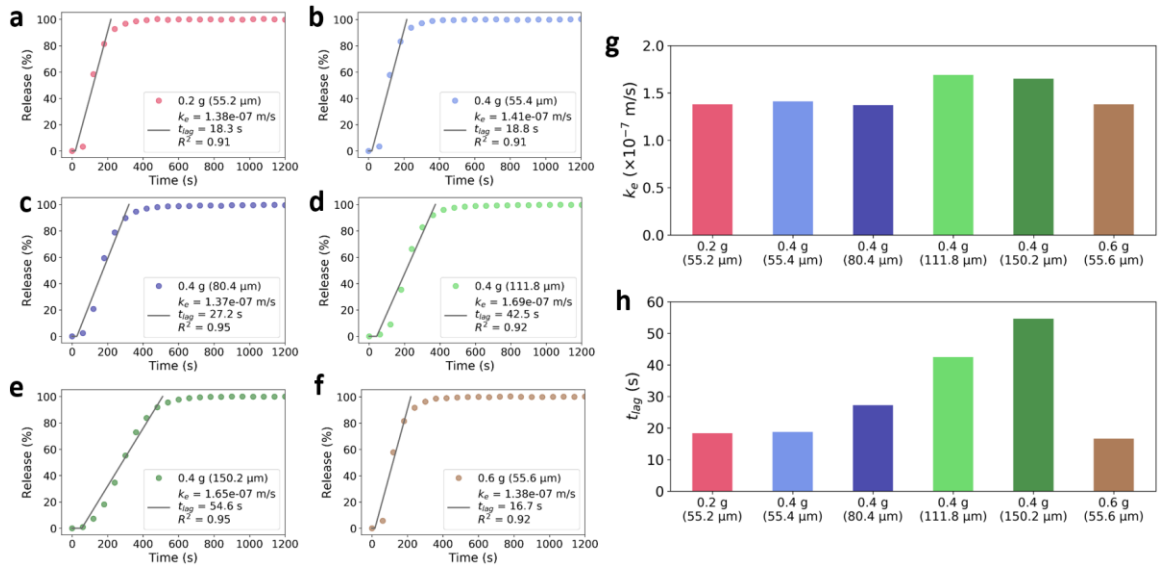

Figure C.12. (a-f) Erosion model fitting for the oral films with different conditions: (a) 0.2 g oil (55.2 μm), (b) 0.4 g oil (55.4 μm), (c) 0.4 g oil (80.4 μm), (d) 0.4 g oil (111.8 μm), (e) 0.4 g oil (150.2 μm), (f) 0.6 g oil (55.6 μm). (g-h) Fitting parameters for the oral films with different conditions: (g) erosion constant (k_e), (h) lag time (t_{lag}).

C.9 Organic Solvent Selection for Fenofibrate

Table C.3 summarizes organic solvents approved by the FDA for drug formulations.[54] There are three critical factors for an organic solvent, which are miscibility with water, density, and solubility of drug. An organic solvent has to be immiscible with water to ensure that the two phases of a nanoemulsion can exist. In addition, a small density difference between an organic solvent and the continuous aqueous phase is preferred to facilitate the formation of nanoemulsions and avoid creaming. Last, high solubility is important to load a high concentration of drug for effective drug products.

Table C.3. Properties of organic solvents approved by the FDA for drug formulations. Green, yellow, and red colors represent good, ok, and bad properties for the preparation of fenofibrate-loaded nanoemulsions.[54]

Solvent	Miscibility with water	Density (g/cm^3)	Fenofibrate solubility (mg/mL)
Acetic acid	Miscible	1.049	200-400
Anisole	Immiscible	0.995	>400
Pentane	Immiscible	0.626	None
Heptane	Immiscible	0.6	<50
Ethyl acetate	Slightly miscible	0.897	>400
Cumene	Immiscible	0.862	None

C.10 Potential Versatility of the Thermogelling HPMC Nanoemulsion

Nanoemulsions are known for their versatility, so we expect that the nanoemulsion droplet size can be effectively tuned by varying the surfactant-to-oil ratio,[13] hydrophilic-lipophilic-balance (HLB) of surfactants,[77] and energy input.[125] Moreover, we expect the thermogelling nanoemulsion can be generalized to other hydrophobic drugs. The potential drug candidates for the thermogelling nanoemulsion system are hydrophobic drugs that have benefitted from conventional nanocrystal technologies, such as danazol, naproxen, ketoprofen, cilostazol, aprepitant, cyclosporine, and itraconazole.[102] For these drugs, we should be able to find suitable organic solvents to dissolve these drugs and directly generate the drug nanocrystals in the HPMC matrix using the thermogelling nanoemulsion. Our group has done in-depth fundamental studies and developed general design strategies for preparing nanoemulsions with different oil phases.[13,83,125] This can provide guidelines to prepare a wide variety of thermogelling HPMC nanoemulsions for different drug/solvent pairs.

C.11 Scale-Up and Sterility of the Thermogelling HPMC Nanoemulsion

Ultrasonic processing has been demonstrated for large-scale production of nanoemulsions.[195] In addition, the scale-up of nanoemulsion production has been achieved with other technologies, including Y-shaped mixer device[196] and phase inversion methods.[22] In terms of sterilization processes, sterile filtration or UV sterilization techniques can be performed prior to the formation of the nanoemulsion (under sterile condition).

Appendix D Preliminary Results for Composite Particles Prepared Using Photocrosslinkable Nanoemulsions and Microfluidics

D.1 Preparation of API-Loaded Photocrosslinkable Nanoemulsions

We used a low-energy direct emulsification method to prepare API-loaded nanoemulsions. For nanoemulsion synthesis, a saturated fenofibrate-in-anisole solution (the dispersed phase) was added dropwise into a 35% v/v PEGDA 700 solution containing a 2% v/v surfactant (HLB=12, a mixture of Span 80 and Tween 80). After the dispersed phase was added, the emulsion precursor was magnetically stirred for 5 min at 1000 rpm to form a nanoemulsion. Then, 1% v/v photoinitiator (Darocur 1173) was introduced to the as-prepared nanoemulsion, followed by vortex mixing for 30 s.

D.2 Contact Flow Lithography

Contact flow lithography was used to prepare hydrogel particles with different oil volume fractions (**Figure D.1**) and shapes (**Figure D.2**). With Nile red (a lipophilic fluorescent dye) introduced in the dispersed phase, effective encapsulation of the nanoemulsions in photocrosslinked hydrogel particles was demonstrated using fluorescence microscopy (**Figure D.1**). In addition, **Figure D.3a** shows the DSC results for bulk fenofibrate and fenofibrate-loaded dried particles. The melting points of fenofibrate in the dried particles are smaller than that of bulk fenofibrate, indicating that fenofibrate nanocrystals are successfully formed in the dried particles. The nanocrystal size distributions (**Figure D.3**) were estimated from the DSC results using the MATLAB fitting algorithm developed in a previous work.[113] **Figure D.3** further shows the dissolution profiles for the dried particles with different oil volume fractions, which correspond to different drug loading contents.

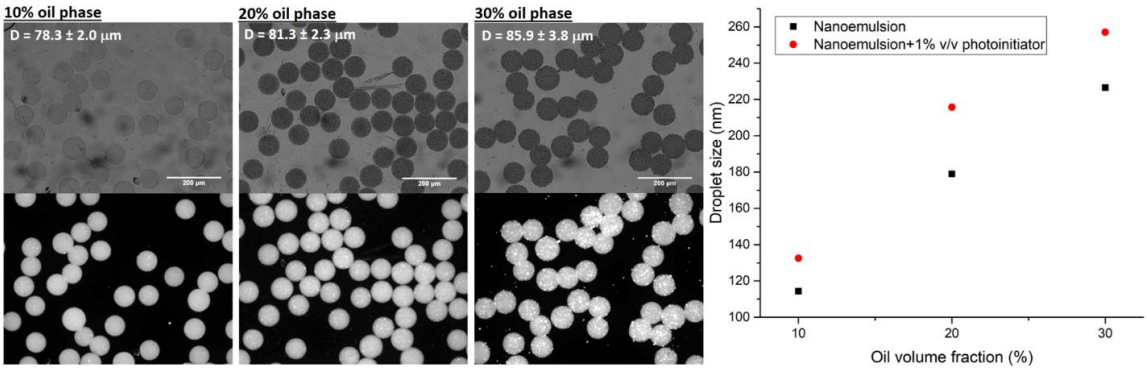

Figure D.1. Cylindrical nanoemulsion-loaded particles with different oil volume fractions prepared using contact flow lithography. The upper row is bright field microscopy images, and the bottom row is the corresponding fluorescence images (Nile red is added as a lipophilic fluorescent dye). The right figure shows the droplet sizes of the nanoemulsions before and after the addition of 1% v/v photoinitiator (Darocur 1173).

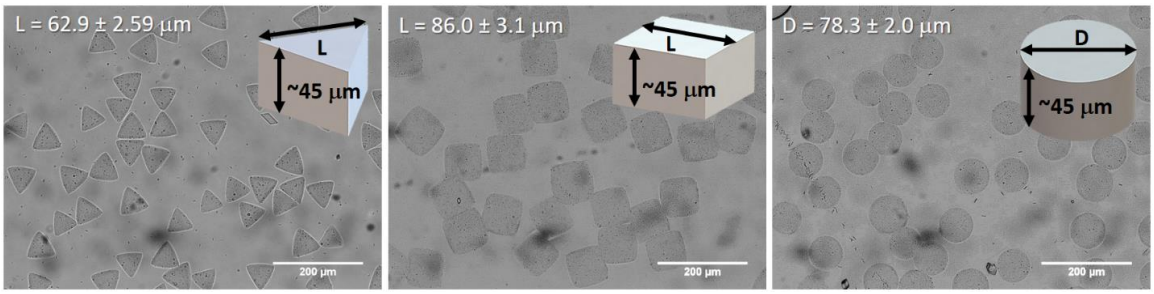

Figure D.2. Nanoemulsion-loaded particles with different shapes prepared using contact flow lithography. The particles with different shapes have a fixed 10% v/v oil volume fraction.

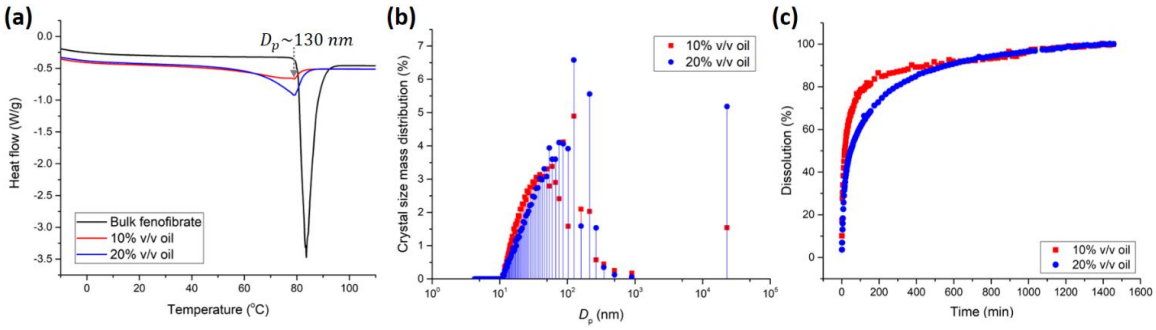

Figure D.3. (a) DSC thermograms, (b) nanocrystal size distributions estimated from the DSC results, and (c) dissolution profiles for the dried cylindrical particles.

D.3 Droplet-Based Microfluidics

Droplet-based microfluidics was used to prepare spherical particles with an average diameter of ~650 μm (**Figure D.4**). **Figure D.4a** shows the microfluidics setup that uses mineral oil for droplet pinch-off. The generated droplets containing the nanoemulsion are then illuminated with UV light to crosslink the droplets into hydrogel particles. The nanoemulsion is effectively encapsulated in the hydrogel particles as demonstrated by fluorescence microscopy (**Figure D.4b**). The dissolution profile of the dried particles is shown in **Figure D.4c**.

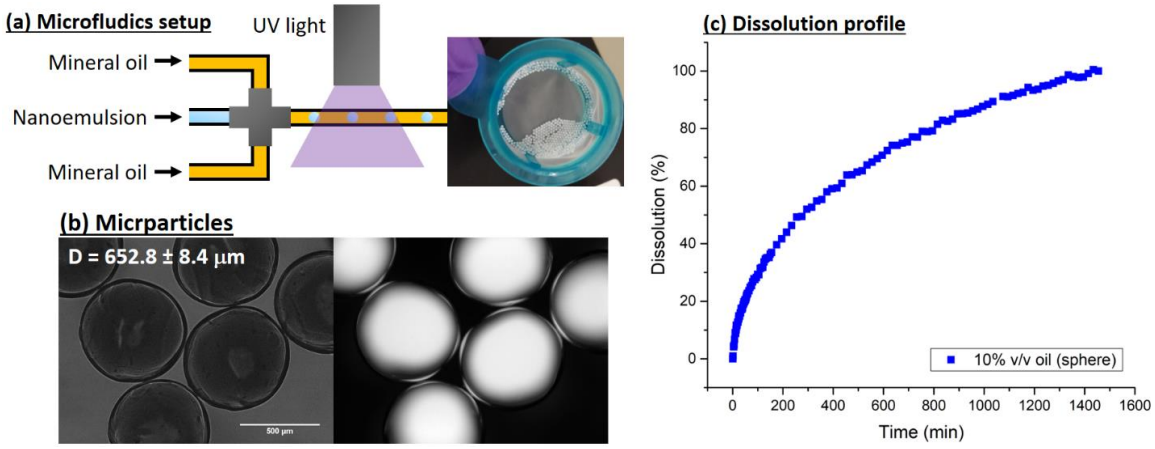

Figure D.4. Spherical nanoemulsion-loaded particles (10% v/v oil volume fraction) prepared using droplet-based microfluidics. (a) Microfluidics setup. (b) Bright field and fluorescence images of the hydrogel particles. (c) Dissolution profile of the dried particles.

D.4 Release Simulation for Particles with Different Aspect Ratios Using COMSOL

Time-dependent transport of 2-D diluted species model in COMSOL was used to estimate the trends of the dissolution profiles for particles with the same area (same drug loading) but different shapes. The particles were in contact with a perfect infinite sink with zero drug concentration. With the same initial uniform concentration in the particles, we found that aspect ratios are an important factor that affects the drug release rates. In **Figure D.5**, the drug release rate increases with the decreasing aspect ratio (a/b).

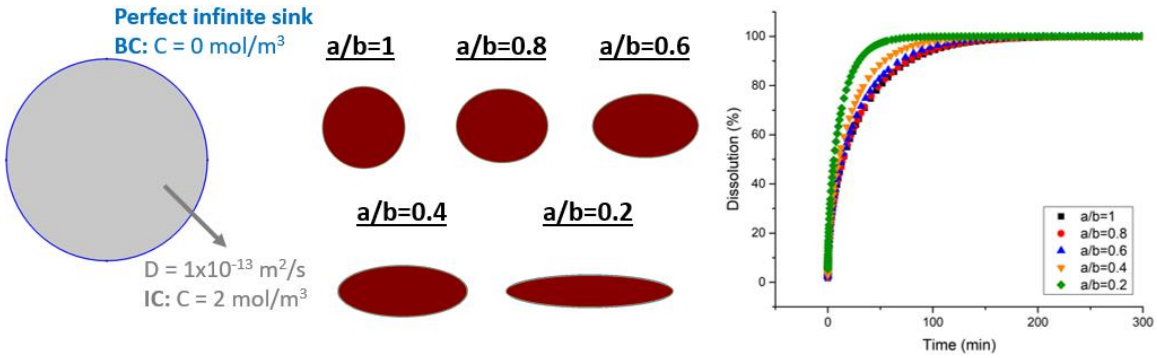

Figure D.5. Simulated dissolution profiles for particles with the same area but different aspect ratios (a/b).

Appendix E Preliminary Results for Molecular Dynamics Simulation of Drug-Polymer Interactions in a HPMC Nanoemulsion System

Molecular dynamics (MD) simulation was applied to explain the two interesting findings in the HPMC nanoemulsion system developed in **Chapter 4**.

1. Without the addition of Tween 80 in the HPMC nanoemulsion, fenofibrate cannot crystallize, and amorphous thin films can be prepared (**Figure E.1**).
2. A small amount of Tween 80 can lead to fenofibrate crystallization.

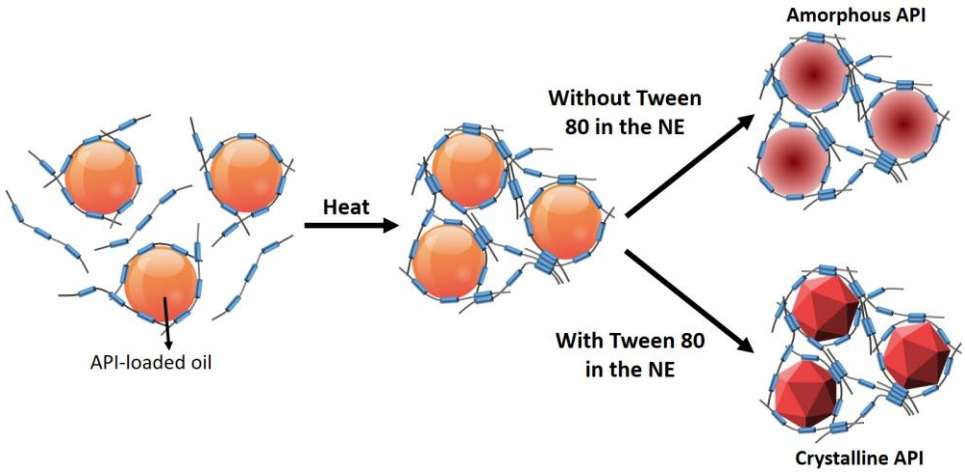

Figure E.1. Schematic illustration of the polymorph control for the HPMC nanoemulsion.

From the literature, cellulose polymers have been used to inhibit crystallization of some hydrophobic APIs for designing amorphous solid dispersions, because cellulose polymers can interact strongly with these hydrophobic APIs. To more effectively understand the interactions between different polymers and drugs, MD simulation has been widely applied.

We established three molecules that exist after evaporating the water and anisole from the HPMC nanoemulsion (**Figure E.2**) and described them with the CHARMM force field (CHARMM36). We then built a simulation box with a centered fenofibrate agglomeration surrounded by Tween 80 and HPMC molecules (**Figure E.3a**). The MD simulation was conducted with the following three steps: 1) energy minimization, 2) NVT at 300 K for 100

ps, and 3) NPT at 1 bar for 100 ps. The resulting configurations after simulation are shown in **Figure E.3b** and **Figure E.3c** for the systems with and without Tween 80, respectively. The interaction energies were obtained for different molecule pairs (**Figure E.3d**). To understand the effect of Tween 80 addition, radial distribution function (RDF) as well as H-bond number between HPMC and fenofibrate for the systems with and without Tween 80 were studied (**Figure E.3e, f**). The results show that Tween 80 molecules can cloak the interaction between HPMC and fenofibrate, which could weaken the ability of HPMC to suppress fenofibrate crystallization.

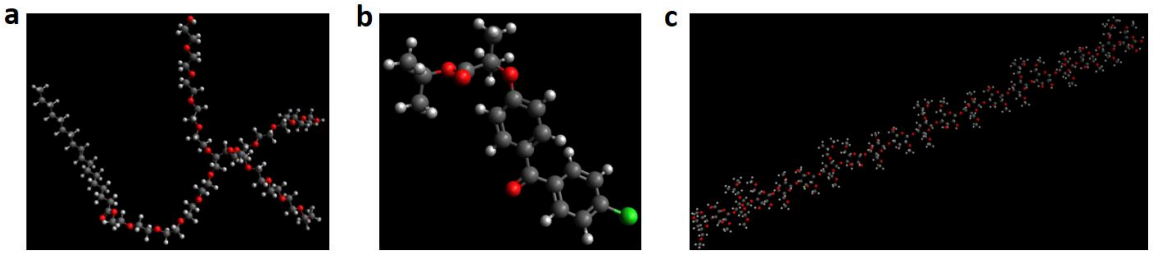

Figure E.2. Molecules that exist in the dried nanoemulsion system: (a) Tween 80, (b) fenofibrate, and (c) HPMC.

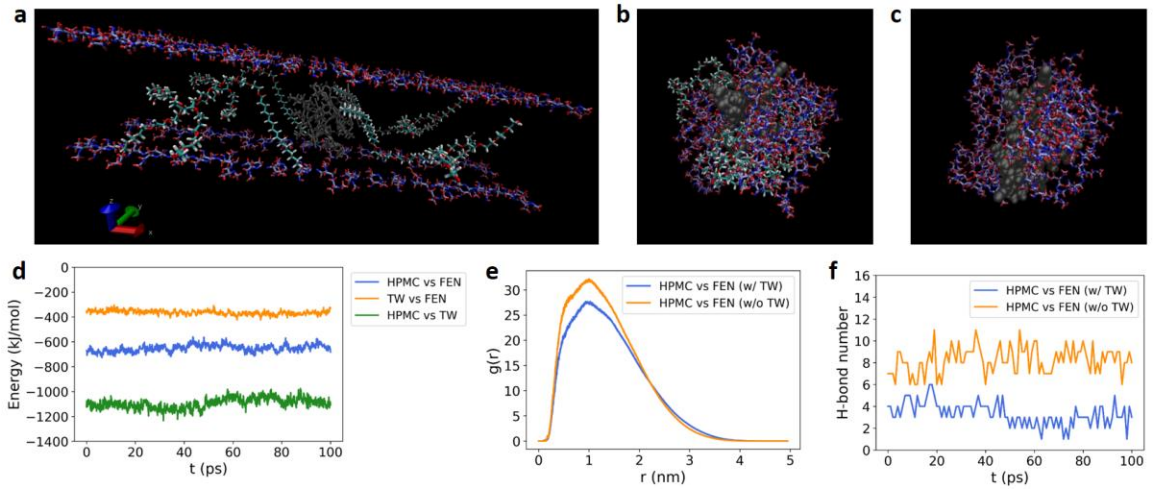

Figure E.3. (a) Initial configuration of molecules in a box (nine fenofibrate, four Tween 80, four HPMC). (b) Molecules with Tween 80 after MD simulation. (c) Molecules without Tween 80 after MD simulation. (d) Interaction energies between molecules for the system with Tween 80. (e) Radial distribution function (RDF) between HPMC and fenofibrate for the systems with and without Tween 80. (f) H-bond number between HPMC and fenofibrate for the systems with and without Tween 80.

Bibliography

(1) Rosen, H.; Abribat, T. The Rise and Rise of Drug Delivery. *Nat. Rev. Drug Discov.* **2005**, *4* (5), 381–385. https://doi.org/10.1038/nrd1721.

(2) Sastry, S. V.; Nyshadham, J. R.; Fix, J. A. Recent Technological Advances in Oral Drug Delivery - A Review. *Pharm. Sci. Technol. Today* **2000**, *3* (4), 138–145. https://doi.org/10.1016/S1461-5347(00)00247-9.

(3) Loftsson, T.; Brewster, M. E. Pharmaceutical Applications of Cyclodextrins: Basic Science and Product Development. *J. Pharm. Pharmacol.* **2010**, *62* (11), 1607–1621. https://doi.org/10.1111/j.2042-7158.2010.01030.x.

(4) Wang, G. D.; Mallet, F. P.; Ricard, F.; Heng, J. Y. Y. Pharmaceutical Nanocrystals. *Curr. Opin. Chem. Eng.* **2012**, *1* (2), 102–107. https://doi.org/10.1016/j.coche.2011.12.001.

(5) Oka, S.; Smrčka, D.; Kataria, A.; Emady, H.; Muzzio, F.; Štěpánek, F.; Ramachandran, R. Analysis of the Origins of Content Non-Uniformity in High-Shear Wet Granulation. *Int. J. Pharm.* **2017**, *528* (1–2), 578–585. https://doi.org/10.1016/j.ijpharm.2017.06.034.

(6) Leon, R. A. L.; Wan, W. Y.; Badruddoza, A. Z. M.; Hatton, T. A.; Khan, S. A. Simultaneous Spherical Crystallization and Co-Formulation of Drug(s) and Excipient from Microfluidic Double Emulsions. *Cryst. Growth Des.* **2014**, *14* (1), 140–146. https://doi.org/10.1021/cg4012982.

(7) Lovelyn, C.; Attama, A. A. Current State of Nanoemulsions in Drug Delivery. *J. Biomater. Nanobiotechnol.* **2011**, *02* (05), 626–639. https://doi.org/10.4236/jbnb.2011.225075.

(8) Chen, H.; Khemtong, C.; Yang, X.; Chang, X.; Gao, J. Nanonization Strategies for Poorly Water-Soluble Drugs. *Drug Discov. Today* **2011**, *16* (7–8), 354–360. https://doi.org/10.1016/j.drudis.2010.02.009.

(9) Badruddoza, A. Z. M.; Gupta, A.; Myerson, A. S.; Trout, B. L.; Doyle, P. S. Low Energy Nanoemulsions as Templates for the Formulation of Hydrophobic Drugs. *Adv. Ther.* **2018**, *1* (1), 1700020. https://doi.org/10.1002/adtp.201700020.

(10) Hashemnejad, S. M.; Badruddoza, A. Z. M.; Zarket, B.; Ricardo Castaneda, C.; Doyle, P. S. Thermoresponsive Nanoemulsion-Based Gel Synthesized through a Low-Energy Process. *Nat. Commun.* **2019**, *10* (1), 1–10. https://doi.org/10.1038/s41467-019-10749-1.

(11) McClements, D. J. Edible Nanoemulsions: Fabrication, Properties, and Functional Performance. *Soft Matter* **2011**, *7* (6), 2297–2316. https://doi.org/10.1039/c0sm00549e.

(12) McClements, D. J.; Rao, J. Food-Grade Nanoemulsions: Formulation, Fabrication, Properties, Performance, Biological Fate, and Potential Toxicity. *Crit. Rev. Food Sci. Nutr.* **2011**, *51* (4), 285–330. https://doi.org/10.1080/10408398.2011.559558.

(13) Gupta, A.; Eral, H. B.; Hatton, T. A.; Doyle, P. S. Nanoemulsions: Formation, Properties and Applications. *Soft Matter* **2016**, *12* (11), 2826–2841. https://doi.org/10.1039/c5sm02958a.

(14) Singh, Y.; Meher, J. G.; Raval, K.; Khan, F. A.; Chaurasia, M.; Jain, N. K.; Chourasia, M. K. Nanoemulsion: Concepts, Development and Applications in Drug Delivery. *J. Control. Release* **2017**, *252*, 28–49. https://doi.org/10.1016/j.jconrel.2017.03.008.

(15) Ashaolu, T. J. Nanoemulsions for Health, Food, and Cosmetics: A Review. *Environ. Chem. Lett.* **2021**, *19* (4), 3381–3395. https://doi.org/10.1007/s10311-021-01216-9.

(16) Yu, H.; Huang, Q. Improving the Oral Bioavailability of Curcumin Using Novel Organogel-Based Nanoemulsions. *J. Agric. Food Chem.* **2012**, *60* (21), 5373–5379. https://doi.org/10.1021/jf300609p.

(17) Salvia-Trujillo, L.; Soliva-Fortuny, R.; Rojas-Graü, M. A.; McClements, D. J.; Martín-Belloso, O. Edible Nanoemulsions as Carriers of Active Ingredients: A Review. *Annu. Rev. Food Sci. Technol.* **2017**, *8* (1), 439–466. https://doi.org/10.1146/annurev-food-030216-025908.

(18) Jafari, S. M.; McClements, D. J. *Nanoemulsions: Formulation, Applications, and Characterization*; Elsevier Inc., 2018.

(19) McClements, D. J. Nanoemulsions versus Microemulsions: Terminology, Differences, and Similarities. *Soft Matter* **2012**, *8* (6), 1719–1729. https://doi.org/10.1039/c2sm06903b.

(20) Komaiko, J. S.; Mcclements, D. J. Formation of Food-Grade Nanoemulsions Using Low-Energy Preparation Methods: A Review of Available Methods. *Compr. Rev. Food Sci. Food Saf.* **2016**, *15* (2), 331–352. https://doi.org/10.1111/1541-4337.12189.

(21) Gupta, A.; Eral, H. B.; Hatton, T. A.; Doyle, P. S. Nanoemulsions: Formation, Properties and Applications. *Soft Matter* **2016**, *12* (11), 2826–2841.

(22) Solans, C.; Solé, I. Nano-Emulsions: Formation by Low-Energy Methods. *Curr. Opin. Colloid Interface Sci.* **2012**, *17* (5), 246–254. https://doi.org/10.1016/j.cocis.2012.07.003.

(23) Forgiarini, A.; Esquena, J.; González, C.; Solans, C. Formation of Nano-Emulsions by Low-Energy Emulsification Methods at Constant Temperature. *Langmuir* **2001**, *17* (7), 2076–2083. https://doi.org/10.1021/la001362n.

(24) Gupta, A.; Badruddoza, A. Z. M.; Doyle, P. S. A General Route for Nanoemulsion Synthesis Using Low-Energy Methods at Constant Temperature. *Langmuir* **2017**, *33*

(28), 7118–7123.

(25) Augsburger, L. L.; Hoag, S. W. *Pharmaceutical Dosage Forms: Capsules*; 2017. https://doi.org/10.1201/b19825.

(26) Amstad, E. Capsules: Their Past and Opportunities for Their Future. *ACS Macro Lett.* **2017**, *6* (8), 841–847. https://doi.org/10.1021/acsmacrolett.7b00472.

(27) Datta, S. S.; Abbaspourrad, A.; Amstad, E.; Fan, J.; Kim, S. H.; Romanowsky, M.; Shum, H. C.; Sun, B.; Utada, A. S.; Windbergs, M.; Zhou, S.; Weitz, D. A. 25th Anniversary Article: Double Emulsion Templated Solid Microcapsules: Mechanics and Controlled Release. *Adv. Mater.* **2014**, *26* (14), 2205–2218. https://doi.org/10.1002/adma.201305119.

(28) Ma, Q.; Song, Y.; Kim, J. W.; Choi, H. S.; Shum, H. C. Affinity Partitioning-Induced Self-Assembly in Aqueous Two-Phase Systems: Templating for Polyelectrolyte Microcapsules. *ACS Macro Lett.* **2016**, *5* (6), 666–670. https://doi.org/10.1021/acsmacrolett.6b00228.

(29) Tangso, K. J.; Patel, H.; Lindberg, S.; Hartley, P. G.; Knott, R.; Spicer, P. T.; Boyd, B. J. Controlling the Mesostructure Formation within the Shell of Novel Cubic/Hexagonal Phase Cetyltrimethylammonium Bromide-Poly(Acrylamide-Acrylic Acid) Capsules for PH Stimulated Release. *ACS Appl. Mater. Interfaces* **2015**, *7* (44), 24501–24509. https://doi.org/10.1021/acsami.5b05821.

(30) Etienne, G.; Ong, I. L. H.; Amstad, E. Bioinspired Viscoelastic Capsules: Delivery Vehicles and Beyond. *Adv. Mater.* **2019**, *31* (27), 1–10. https://doi.org/10.1002/adma.201808233.

(31) Li, J.; Mooney, D. J. Designing Hydrogels for Controlled Drug Delivery. *Nat. Rev. Mater.* **2016**, *1* (12). https://doi.org/10.1038/natrevmats.2016.71.

(32) Zhu, J.; Marchant, R. E. Design Properties of Hydrogel Tissue-Engineering Scaffolds. *Expert Rev. Med. Devices* **2011**, *8* (5), 607–626. https://doi.org/10.1586/erd.11.27.

(33) Lin, C. C.; Metters, A. T. Hydrogels in Controlled Release Formulations: Network Design and Mathematical Modeling. *Adv. Drug Deliv. Rev.* **2006**, *58* (12–13), 1379–1408. https://doi.org/10.1016/j.addr.2006.09.004.

(34) Zhao, F.; Yao, D.; Guo, R.; Deng, L.; Dong, A.; Zhang, J. Composites of Polymer Hydrogels and Nanoparticulate Systems for Biomedical and Pharmaceutical Applications. *Nanomaterials* **2015**, *5* (4), 2054–2130. https://doi.org/10.3390/nano5042054.

(35) Jagadeesan, D.; Nasimova, I.; Gourevich, I.; Starodubtsev, S.; Kumacheva, E. Microgels for the Encapsulation and Stimulus-Responsive Release of Molecules with Distinct Polarities. *Macromol. Biosci.* **2011**, *11* (7), 889–896. https://doi.org/10.1002/mabi.201100045.

(36) Zeeb, B.; Saberi, A. H.; Weiss, J.; McClements, D. J. Formation and Characterization of Filled Hydrogel Beads Based on Calcium Alginate: Factors Influencing Nanoemulsion Retention and Release. *Food Hydrocoll.* **2015**, *50*, 27–36. https://doi.org/10.1016/j.foodhyd.2015.02.041.

(37) Lee, K. Y.; Mooney, D. J. Alginate: Properties and Biomedical Applications. *Prog. Polym. Sci.* **2012**, *37* (1), 106–126. https://doi.org/10.1016/j.progpolymsci.2011.06.003.

(38) Augst, A. D.; Kong, H. J.; Mooney, D. J. Alginate Hydrogels as Biomaterials. *Macromol. Biosci.* **2006**, *6* (8), 623–633. https://doi.org/10.1002/mabi.200600069.

(39) Ching, S. H.; Bansal, N.; Bhandari, B. Alginate Gel Particles–A Review of Production Techniques and Physical Properties. *Crit. Rev. Food Sci. Nutr.* **2017**, *57* (6), 1133–1152. https://doi.org/10.1080/10408398.2014.965773.

(40) Martins, E.; Poncelet, D.; Rodrigues, R. C.; Renard, D. Oil Encapsulation Techniques Using Alginate as Encapsulating Agent: Applications and Drawbacks. *J. Microencapsul.* **2017**, *34* (8), 754–771. https://doi.org/10.1080/02652048.2017.1403495.

(41) Patel, A. R. Functional and Engineered Colloids from Edible Materials for Emerging Applications in Designing the Food of the Future. *Adv. Funct. Mater.* **2020**, *30* (18), 1–34. https://doi.org/10.1002/adfm.201806809.

(42) Cao, Y.; Mezzenga, R. Design Principles of Food Gels. *Nat. Food* **2020**, *1* (2), 106–118. https://doi.org/10.1038/s43016-019-0009-x.

(43) Dow, T. Using Methocel Cellulose Ethers for Controlled Release of Drugs in Hydrophilic Matrix Systems. *Midland, MI Dow Chem. Co.* **2000**.

(44) Siepmann, J.; Peppas, N. A. Modeling of Drug Release from Delivery Systems Based on Hydroxypropyl Methylcellulose (HPMC). *Adv. Drug Deliv. Rev.* **2012**, *64* (SUPPL.), 163–174. https://doi.org/10.1016/j.addr.2012.09.028.

(45) Ju, R. T. C.; Nixon, P. R.; Patel, M. V. Drug Release from Hydrophilic Matrices. 1. New Scaling Laws for Predicting Polymer and Drug Release Based on the Polymer Disentanglement Concentration and the Diffusion Layer. *J. Pharm. Sci.* **1995**, *84* (12), 1455–1463. https://doi.org/10.1002/jps.2600841213.

(46) Ghori, M. U.; Conway, B. R. Hydrophilic Matrices for Oral Control Drug Delivery. *Am. J. Pharmacol. Sci.* **2015**, *3* (5), 103–109. https://doi.org/10.12691/ajps-3-5-1.

(47) Kobayashi, K.; Huang, C. I.; Lodge, T. P. Thermoreversible Gelation of Aqueous Methylcellulose Solutions. *Macromolecules* **1999**, *32* (21), 7070–7077. https://doi.org/10.1021/ma990242n.

(48) Sarkar, N. Thermal Gelation Properties of Methyl and Hydroxypropyl

Methylcellulose. *J. Appl. Polym. Sci.* **1979**, *24* (4), 1073–1087. https://doi.org/10.1002/app.1979.070240420.

(49) Vulic, K.; Shoichet, M. S. Tunable Growth Factor Delivery from Injectable Hydrogels for Tissue Engineering. *J. Am. Chem. Soc.* **2012**, *134* (2), 882–885. https://doi.org/10.1021/ja210638x.

(50) Tate, M. C.; Shear, D. A.; Hoffman, S. W.; Stein, D. G.; LaPlaca, M. C. Biocompatibility of Methylcellulose-Based Constructs Designed for Intracerebral Gelation Following Experimental Traumatic Brain Injury. *Biomaterials* **2001**, *22* (10), 1113–1123. https://doi.org/10.1016/S0142-9612(00)00348-3.

(51) Gupta, D.; Tator, C. H.; Shoichet, M. S. Fast-Gelling Injectable Blend of Hyaluronan and Methylcellulose for Intrathecal, Localized Delivery to the Injured Spinal Cord. *Biomaterials* **2006**, *27* (11), 2370–2379. https://doi.org/10.1016/j.biomaterials.2005.11.015.

(52) Bain, M. K.; Bhowmik, M.; Ghosh, S. N.; Chattopadhyay, D. In Situ Fast Gelling Formulation of Methyl Cellulose for in Vitro Ophthalmic Controlled Delivery of Ketorolac Tromethamine. *J. Appl. Polym. Sci.* **2009**, *113* (2), 1241–1246. https://doi.org/10.1002/app.30040.

(53) Bonetti, L.; De Nardo, L.; Farè, S. Thermo-Responsive Methylcellulose Hydrogels: From Design to Applications as Smart Biomaterials. *Tissue Eng. - Part B Rev.* **2021**, *27* (5), 486–513. https://doi.org/10.1089/ten.teb.2020.0202.

(54) Eral, H. B.; O'Mahony, M.; Shaw, R.; Trout, B. L.; Myerson, A. S.; Doyle, P. S. Composite Hydrogels Laden with Crystalline Active Pharmaceutical Ingredients of Controlled Size and Loading. *Chem. Mater.* **2014**, *26* (21), 6213–6220. https://doi.org/10.1021/cm502834h.

(55) Domenech, T.; Doyle, P. S. High Loading Capacity Nanoencapsulation and Release of Hydrophobic Drug Nanocrystals from Microgel Particles. *Chem. Mater.* **2020**, *32* (1), 498–509. https://doi.org/10.1021/acs.chemmater.9b04241.

(56) Badruddoza, A. Z. M.; Godfrin, P. D.; Myerson, A. S.; Trout, B. L.; Doyle, P. S. Core–Shell Composite Hydrogels for Controlled Nanocrystal Formation and Release of Hydrophobic Active Pharmaceutical Ingredients. *Adv. Healthc. Mater.* **2016**, *5* (15), 1960–1968. https://doi.org/10.1002/adhm.201600266.

(57) Cheng, L. C.; Sherman, Z. M.; Swan, J. W.; Doyle, P. S. Colloidal Gelation through Thermally Triggered Surfactant Displacement. *Langmuir* **2019**, *35* (29), 9464–9473. https://doi.org/10.1021/acs.langmuir.9b00596.

(58) Helgeson, M. E.; Moran, S. E.; An, H. Z.; Doyle, P. S. Mesoporous Organohydrogels from Thermogelling Photocrosslinkable Nanoemulsions. *Nat. Mater.* **2012**, *11* (4), 344–352.

(59) Junghanns, J. U. A. H.; Müller, R. H. Nanocrystal Technology, Drug Delivery and Clinical Applications. *Int. J. Nanomedicine* **2008**, *3* (3), 295–309.

(60) Tozuka, Y.; Imono, M.; Uchiyama, H.; Takeuchi, H. A Novel Application of α-Glucosyl Hesperidin for Nanoparticle Formation of Active Pharmaceutical Ingredients by Dry Grinding. *Eur. J. Pharm. Biopharm.* **2011**, *79* (3), 559–565. https://doi.org/10.1016/j.ejpb.2011.07.006.

(61) Merisko-Liversidge, E.; Liversidge, G. G.; Cooper, E. R. Nanosizing: A Formulation Approach for Poorly-Water-Soluble Compounds. *Eur. J. Pharm. Sci.* **2003**, *18* (2), 113–120. https://doi.org/10.1016/S0928-0987(02)00251-8.

(62) Bhakay, A.; Rahman, M.; Dave, R. N.; Bilgili, E. Bioavailability Enhancement of Poorly Water-Soluble Drugs via Nanocomposites: Formulation–Processing Aspects and Challenges. *Pharmaceutics* **2018**, *10* (3). https://doi.org/10.3390/pharmaceutics10030086.

(63) Loh, Z. H.; Samanta, A. K.; Sia Heng, P. W. Overview of Milling Techniques for Improving the Solubility of Poorly Water-Soluble Drugs. *Asian J. Pharm. Sci.* **2014**, *10* (4), 255–274. https://doi.org/10.1016/j.ajps.2014.12.006.

(64) Shah, D. A.; Murdande, S. B.; Dave, R. H. A Review: Pharmaceutical and Pharmacokinetic Aspect of Nanocrystalline Suspensions. *J. Pharm. Sci.* **2016**, *105* (1), 10–24. https://doi.org/10.1002/jps.24694.

(65) Juhnke, M.; Märtin, D.; John, E. Generation of Wear during the Production of Drug Nanosuspensions by Wet Media Milling. *Eur. J. Pharm. Biopharm.* **2012**, *81* (1), 214–222. https://doi.org/10.1016/j.ejpb.2012.01.005.

(66) Li, M.; Yaragudi, N.; Afolabi, A.; Dave, R.; Bilgili, E. Sub-100nm Drug Particle Suspensions Prepared via Wet Milling with Low Bead Contamination through Novel Process Intensification. *Chem. Eng. Sci.* **2015**, *130*, 207–220. https://doi.org/10.1016/j.ces.2015.03.020.

(67) Sinha, B.; Müller, R. H.; Möschwitzer, J. P. Bottom-up Approaches for Preparing Drug Nanocrystals: Formulations and Factors Affecting Particle Size. *Int. J. Pharm.* **2013**, *453* (1), 126–141. https://doi.org/10.1016/j.ijpharm.2013.01.019.

(68) Hamdallah, S. I.; Zoqlam, R.; Erfle, P.; Blyth, M.; Alkilany, A. M.; Dietzel, A.; Qi, S. Microfluidics for Pharmaceutical Nanoparticle Fabrication: The Truth and the Myth. *Int. J. Pharm.* **2020**, *584* (January). https://doi.org/10.1016/j.ijpharm.2020.119408.

(69) Chan, H. K.; Kwok, P. C. L. Production Methods for Nanodrug Particles Using the Bottom-up Approach. *Adv. Drug Deliv. Rev.* **2011**, *63* (6), 406–416. https://doi.org/10.1016/j.addr.2011.03.011.

(70) Dwyer, L. M.; Michaelis, V. K.; O'Mahony, M.; Griffin, R. G.; Myerson, A. S. Confined Crystallization of Fenofibrate in Nanoporous Silica. *CrystEngComm* **2015**,

17 (41), 7922–7929. https://doi.org/10.1039/c5ce01148e.

(71) Beiner, M.; Rengarajan, G. T.; Pankaj, S.; Enke, D.; Steinhart, M. Manipulating the Crystalline State of Pharmaceuticals by Nanoconfinement. *Nano Lett.* **2007**, *7* (5), 1381–1385. https://doi.org/10.1021/nl0705081.

(72) Ha, J. M.; Wolf, J. H.; Hillmyer, M. A.; Ward, M. D. Polymorph Selectivity under Nanoscopic Confinement. *J. Am. Chem. Soc.* **2004**, *126* (11), 3382–3383. https://doi.org/10.1021/ja049724r.

(73) Azaïs, T.; Tourné-Péteilh, C.; Aussenac, F.; Baccile, N.; Coelho, C.; Devoisselle, J. M.; Babonneau, F. Solid-State NMR Study of Ibuprofen Confined in MCM-41 Material. *Chem. Mater.* **2006**, *18* (26), 6382–6390. https://doi.org/10.1021/cm061551c.

(74) Junyaprasert, V. B.; Morakul, B. Nanocrystals for Enhancement of Oral Bioavailability of Poorly Water-Soluble Drugs. *Asian J. Pharm. Sci.* **2015**, *10* (1), 13–23. https://doi.org/10.1016/j.ajps.2014.08.005.

(75) Kaptay, G. On the Size and Shape Dependence of the Solubility of Nano-Particles in Solutions. *Int. J. Pharm.* **2012**, *430* (1–2), 253–257. https://doi.org/10.1016/j.ijpharm.2012.03.038.

(76) Wu, N.; Lu, X.; An, R.; Ji, X. Thermodynamic Analysis and Modification of Gibbs–Thomson Equation for Melting Point Depression of Metal Nanoparticles. *Chinese J. Chem. Eng.* **2021**, *31*, 198–205. https://doi.org/10.1016/j.cjche.2020.11.035.

(77) Chen, L. H.; Cheng, L. C.; Doyle, P. S. Nanoemulsion-Loaded Capsules for Controlled Delivery of Lipophilic Active Ingredients. *Adv. Sci.* **2020**, *2001677*, 1–11. https://doi.org/10.1002/advs.202001677.

(78) Li, Y.; Hu, M.; Du, Y.; Xiao, H.; McClements, D. J. Control of Lipase Digestibility of Emulsified Lipids by Encapsulation within Calcium Alginate Beads. *Food Hydrocoll.* **2011**, *25* (1), 122–130. https://doi.org/10.1016/j.foodhyd.2010.06.003.

(79) Corstens, M. N.; Berton-Carabin, C. C.; Elichiry-Ortiz, P. T.; Hol, K.; Troost, F. J.; Masclee, A. A. M.; Schroën, K. Emulsion-Alginate Beads Designed to Control in Vitro Intestinal Lipolysis: Towards Appetite Control. *J. Funct. Foods* **2017**, *34* (2017), 319–328. https://doi.org/10.1016/j.jff.2017.05.003.

(80) Chan, E. S. Preparation of Ca-Alginate Beads Containing High Oil Content: Influence of Process Variables on Encapsulation Efficiency and Bead Properties. *Carbohydr. Polym.* **2011**, *84* (4), 1267–1275. https://doi.org/10.1016/j.carbpol.2011.01.015.

(81) An, H. Z.; Helgeson, M. E.; Doyle, P. S. Nanoemulsion Composite Microgels for Orthogonal Encapsulation and Release. *Adv. Mater.* **2012**, *24* (28), 3838–3844. https://doi.org/10.1002/adma.201200214.

(82) Leong, J. Y.; Lam, W. H.; Ho, K. W.; Voo, W. P.; Lee, M. F. X.; Lim, H. P.; Lim, S. L.; Tey, B. T.; Poncelet, D.; Chan, E. S. Advances in Fabricating Spherical Alginate Hydrogels with Controlled Particle Designs by Ionotropic Gelation as Encapsulation Systems. *Particuology* **2016**, *24*, 44–60. https://doi.org/10.1016/j.partic.2015.09.004.

(83) Gupta, A.; Badruddoza, A. Z. M.; Doyle, P. S. A General Route for Nanoemulsion Synthesis Using Low-Energy Methods at Constant Temperature. *Langmuir* **2017**, *33* (28), 7118–7123. https://doi.org/10.1021/acs.langmuir.7b01104.

(84) by Dove Press, published. IJN-99198-Development-of-Ibuprofen-Loaded-Nanostructured-Lipid-Carrier. **2016**, 1201–1212. https://doi.org/10.2147/IJN.S99198.

(85) Blandino, A.; Macías, M.; Cantero, D. Immobilization of Glucose Oxidase within Calcium Alginate Gel Capsules. *Process Biochem.* **2001**, *36* (7), 601–606. https://doi.org/10.1016/S0032-9592(00)00240-5.

(86) Blandino, A.; Macías, M.; Cantero, D. Formation of Calcium Alginate Gel Capsules: Influence of Sodium Alginate and CaCl2 Concentration on Gelation Kinetics. *J. Biosci. Bioeng.* **1999**, *88* (6), 686–689. https://doi.org/10.1016/S1389-1723(00)87103-0.

(87) Brady, J. F. The Rheological Behavior of Concentrated Colloidal Dispersions. *J. Chem. Phys.* **1993**, *99* (1), 567–581. https://doi.org/10.1063/1.465782.

(88) Quemada, D.; Berli, C. *Energy of Interaction in Colloids and Its Implications in Rheological Modeling*; 2002; Vol. 98. https://doi.org/10.1016/S0001-8686(01)00093-8.

(89) Tadros, T. F. Correlation of Viscoelastic Properties of Stable and Flocculated Suspensions with Their Interparticle Interactions. *Adv. Colloid Interface Sci.* **1996**, *68*, 97–200. https://doi.org/10.1016/s0001-8686(96)90047-0.

(90) Amani, A.; York, P.; De Waard, H.; Anwar, J. Molecular Dynamics Simulation of a Polysorbate 80 Micelle in Water. *Soft Matter* **2011**, *7* (6), 2900–2908. https://doi.org/10.1039/c0sm00965b.

(91) Haldar, K.; Chakraborty, S. Effect of Liquid Pool Concentration on Chemically Reactive Drop Impact Gelation Process. *J. Colloid Interface Sci.* **2018**, *528*, 156–165. https://doi.org/10.1016/j.jcis.2018.05.078.

(92) Mason, T. G.; Wilking, J. N.; Meleson, K.; Chang, C. B.; Graves, S. M. Nanoemulsions: Formation, Structure, and Physical Properties. *J. Phys. Condens. Matter* **2006**, *18* (41), 635–666. https://doi.org/10.1088/0953-8984/18/41/R01.

(93) Chan, E. S.; Lee, B. B.; Ravindra, P.; Poncelet, D. Prediction Models for Shape and Size of Ca-Alginate Macrobeads Produced through Extrusion-Dripping Method. *J. Colloid Interface Sci.* **2009**, *338* (1), 63–72. https://doi.org/10.1016/j.jcis.2009.05.027.

(94) Lee, B. H.; Li, B.; Guelcher, S. A. Gel Microstructure Regulates Proliferation and Differentiation of MC3T3-E1 Cells Encapsulated in Alginate Beads. *Acta Biomater.* **2012**, *8* (5), 1693–1702. https://doi.org/10.1016/j.actbio.2012.01.012.

(95) Rolland, L.; Santanach-Carreras, E.; Delmas, T.; Bibette, J.; Bremond, N. Physicochemical Properties of Aqueous Core Hydrogel Capsules. *Soft Matter* **2014**, *10* (48), 9668–9674. https://doi.org/10.1039/c4sm02012j.

(96) Burkersroda, F. Von; Schedl, L.; Göpferich, A. Why Degradable Polymers Undergo Surface Erosion or Bulk Erosion. *Biomaterials* **2002**, *23* (21), 4221–4231. https://doi.org/10.1016/S0142-9612(02)00170-9.

(97) Lin, C. C.; Anseth, K. S. PEG Hydrogels for the Controlled Release of Biomolecules in Regenerative Medicine. *Pharm. Res.* **2009**, *26* (3), 631–643. https://doi.org/10.1007/s11095-008-9801-2.

(98) Tarr, B. D.; Yalkowsky, S. H. Enhanced Intestinal Absorption of Cyclosporine in Rats Through the Reduction of Emulsion Droplet Size. *Pharmaceutical Research: An Official Journal of the American Association of Pharmaceutical Scientists*. 1989, pp 40–43. https://doi.org/10.1023/A:1015843517762.

(99) Seiffert, S.; Thiele, J.; Abate, A. R.; Weitz, D. A. Smart Microgel Capsules from Macromolecular Precursors. *J. Am. Chem. Soc.* **2010**, *132* (18), 6606–6609. https://doi.org/10.1021/ja102156h.

(100) Chen, L. H.; Doyle, P. S. Design and Use of a Thermogelling Methylcellulose Nanoemulsion to Formulate Nanocrystalline Oral Dosage Forms. *Adv. Mater.* **2021**, *33* (29), 1–9. https://doi.org/10.1002/adma.202008618.

(101) Reker, D.; Blum, S. M.; Steiger, C.; Anger, K. E.; Sommer, J. M.; Fanikos, J.; Traverso, G. Inactive Ingredients in Oral Medications. *Sci. Transl. Med.* **2019**, *11* (483), 1–7. https://doi.org/10.1126/scitranslmed.aau6753.

(102) Gao, L.; Liu, G.; Ma, J.; Wang, X.; Zhou, L.; Li, X. Drug Nanocrystals: In Vivo Performances. *J. Control. Release* **2012**, *160* (3), 418–430. https://doi.org/10.1016/j.jconrel.2012.03.013.

(103) Rabinow, B. E. Nanosuspensions in Drug Delivery. *Nat. Rev. Drug Discov.* **2004**, *3* (9), 785–796. https://doi.org/10.1038/nrd1494.

(104) Miwa, A.; Yajima, T.; Itai, S. Prediction of Suitable Amount of Water Addition for Wet Granulation. *Int. J. Pharm.* **2000**, *195* (1–2), 81–92. https://doi.org/10.1016/S0378-5173(99)00376-2.

(105) Willecke, N.; Szepes, A.; Wunderlich, M.; Remon, J. P.; Vervaet, C.; De Beer, T. Identifying Overarching Excipient Properties towards an In-Depth Understanding of Process and Product Performance for Continuous Twin-Screw Wet Granulation. *Int. J. Pharm.* **2017**, *522* (1–2), 234–247. https://doi.org/10.1016/j.ijpharm.2017.02.028.

(106) Willecke, N.; Szepes, A.; Wunderlich, M.; Remon, J. P.; Vervaet, C.; De Beer, T. A Novel Approach to Support Formulation Design on Twin Screw Wet Granulation Technology: Understanding the Impact of Overarching Excipient Properties on Drug Product Quality Attributes. *Int. J. Pharm.* **2018**, *545* (1–2), 128–143. https://doi.org/10.1016/j.ijpharm.2018.04.017.

(107) Kiortsis, S.; Kachrimanis, K.; Broussali, T.; Malamataris, S. Drug Release from Tableted Wet Granulations Comprising Cellulosic (HPMC or HPC) and Hydrophobic Component. *Eur. J. Pharm. Biopharm.* **2005**, *59* (1), 73–83. https://doi.org/10.1016/j.ejpb.2004.05.004.

(108) Ishikawa, T.; Watanabe, Y.; Takayama, K.; Endo, H.; Matsumoto, M. Effect of Hydroxypropylmethylcellulose (HPMC) on the Release Profiles and Bioavailability of a Poorly Water-Soluble Drug from Tablets Prepared Using Macrogol and HPMC. *Int. J. Pharm.* **2000**, *202* (1–2), 173–178. https://doi.org/10.1016/S0378-5173(00)00426-9.

(109) Li, J.; Mooney, D. J. Designing Hydrogels for Controlled Drug Delivery. *Nat. Rev. Mater.* **2016**, *1* (12), 1–17.

(110) Peppas, N. A.; Hilt, J. Z.; Khademhosseini, A.; Langer, R. Hydrogels in Biology and Medicine: From Molecular Principles to Bionanotechnology. *Adv. Mater.* **2006**, *18* (11), 1345–1360. https://doi.org/10.1002/adma.200501612.

(111) Hoare, T. R.; Kohane, D. S. Hydrogels in Drug Delivery: Progress and Challenges. *Polymer (Guildf).* **2008**, *49* (8), 1993–2007.

(112) Badruddoza, A. Z. M.; Gupta, A.; Myerson, A. S.; Trout, B. L.; Doyle, P. S. Low Energy Nanoemulsions as Templates for the Formulation of Hydrophobic Drugs. *Adv. Ther.* **2018**, *1* (1), 1700020. https://doi.org/10.1002/adtp.201700020.

(113) Godfrin, P. D.; Lee, H.; Lee, J. H.; Doyle, P. S. Photopolymerized Micelle-Laden Hydrogels Can Simultaneously Form and Encapsulate Nanocrystals to Improve Drug Substance Solubility and Expedite Drug Product Design. *Small* **2019**, *15* (6), 1–14. https://doi.org/10.1002/smll.201803372.

(114) Moon, H. J.; Ku, M.; Roh, Y. H.; Lee, H. J.; Yang, J.; Bong, K. W. Elimination of Unreacted Acrylate Double Bonds in the Polymer Networks of Microparticles Synthesized via Flow Lithography. *Langmuir* **2020**, *36* (9), 2271–2277. https://doi.org/10.1021/acs.langmuir.9b02737.

(115) Vogt, M.; Kunath, K.; Dressman, J. B. Dissolution Enhancement of Fenofibrate by Micronization, Cogrinding and Spray-Drying: Comparison with Commercial Preparations. *Eur. J. Pharm. Biopharm.* **2008**, *68* (2), 283–288.

(116) Li, L.; Thangamathesvaran, P. M.; Yue, C. Y.; Tam, K. C.; Hu, X.; Lam, Y. C. Gel Network Structure of Methylcellulose in Water. *Langmuir* **2001**, *17* (26), 8062–8068. https://doi.org/10.1021/la010917r.

(117) Xu, Y.; Li, L.; Zheng, P.; Lam, Y. C.; Hu, X. Controllable Gelation of Methylcellulose by a Salt Mixture. *Langmuir* **2004**, *20* (15), 6134–6138. https://doi.org/10.1021/la049907r.

(118) Cai, L.; Farber, L.; Zhang, D.; Li, F.; Farabaugh, J. A New Methodology for High Drug Loading Wet Granulation Formulation Development. *Int. J. Pharm.* **2013**, *441* (1–2), 790–800. https://doi.org/10.1016/j.ijpharm.2012.09.052.

(119) Heinz, A.; Gordon, K. C.; McGoverin, C. M.; Rades, T.; Strachan, C. J. Understanding the Solid-State Forms of Fenofibrate - A Spectroscopic and Computational Study. *Eur. J. Pharm. Biopharm.* **2009**, *71* (1), 100–108. https://doi.org/10.1016/j.ejpb.2008.05.030.

(120) Ying, Y.; Beck, C.; Wu, A.; Dave, R.; Iqbal, Z. Polymorph Formation in Fenofibrate in the Absence and Presence of Polymer Stabilizers: A Low Wavenumber Raman and Differential Scanning Calorimetry Study. *J. Raman Spectrosc.* **2017**, *48* (5), 750–757. https://doi.org/10.1002/jrs.5090.

(121) Ritger, P. L.; Peppas, N. A. A Simple Equation for Description of Solute Release II. Fickian and Anomalous Release from Swellable Devices. *J. Control. Release* **1987**, *5* (1), 37–42. https://doi.org/10.1016/0168-3659(87)90035-6.

(122) Ford, J. L.; Mitchell, K.; Rowe, P.; Armstrong, D. J.; Elliott, P. N. C.; Rostron, C.; Hogan, J. E. Mathematical Modelling of Drug Release from Hydroxypropylmethylcellulose Matrices: Effect of Temperature. *Int. J. Pharm.* **1991**, *71* (1–2), 95–104. https://doi.org/10.1016/0378-5173(91)90071-U.

(123) Hopfenberg, H. B. Controlled Release from Erodible Slabs, Cylinders, and Spheres; ACS Publications, 1976.

(124) Zhang, L.; Alfano, J.; Race, D.; Davé, R. N. Zero-Order Release of Poorly Water-Soluble Drug from Polymeric Films Made via Aqueous Slurry Casting. *Eur. J. Pharm. Sci.* **2018**, *117* (January), 245–254. https://doi.org/10.1016/j.ejps.2018.02.029.

(125) Gupta, A.; Eral, H. B.; Hatton, T. A.; Doyle, P. S. Controlling and Predicting Droplet Size of Nanoemulsions: Scaling Relations with Experimental Validation. *Soft Matter* **2016**, *12* (5), 1452–1458. https://doi.org/10.1039/c5sm02051d.

(126) Suh, S. K.; Bong, K. W.; Hatton, T. A.; Doyle, P. S. Using Stop-Flow Lithography to Produce Opaque Microparticles: Synthesis and Modeling. *Langmuir* **2011**, *27* (22), 13813–13819. https://doi.org/10.1021/la202796b.

(127) Karki, S.; Kim, H.; Na, S. J.; Shin, D.; Jo, K.; Lee, J. Thin Films as an Emerging Platform for Drug Delivery. *Asian J. Pharm. Sci.* **2016**, *11* (5), 559–574. https://doi.org/10.1016/j.ajps.2016.05.004.

(128) Sievens-Figueroa, L.; Bhakay, A.; Jerez-Rozo, J. I.; Pandya, N.; Romañach, R. J.; Michniak-Kohn, B.; Iqbal, Z.; Bilgili, E.; Davé, R. N. Preparation and

Characterization of Hydroxypropyl Methyl Cellulose Films Containing Stable BCS Class II Drug Nanoparticles for Pharmaceutical Applications. *Int. J. Pharm.* **2012**, *423* (2), 496–508. https://doi.org/10.1016/j.ijpharm.2011.12.001.

(129) Kesisoglou, F.; Panmai, S.; Wu, Y. Nanosizing - Oral Formulation Development and Biopharmaceutical Evaluation. *Adv. Drug Deliv. Rev.* **2007**, *59* (7), 631–644. https://doi.org/10.1016/j.addr.2007.05.003.

(130) Wu, L.; Zhang, J.; Watanabe, W. Physical and Chemical Stability of Drug Nanoparticles. *Adv. Drug Deliv. Rev.* **2011**, *63* (6), 456–469. https://doi.org/10.1016/j.addr.2011.02.001.

(131) Borges, A. F.; Silva, C.; Coelho, J. F. J.; Simões, S. Oral Films: Current Status and Future Perspectives: I-Galenical Development and Quality Attributes. *J. Control. Release* **2015**, *206*, 1–19. https://doi.org/10.1016/j.jconrel.2015.03.006.

(132) Scoutaris, N.; Ross, S. A.; Douroumis, D. 3D Printed "Starmix" Drug Loaded Dosage Forms for Paediatric Applications. *Pharm. Res.* **2018**, *35* (2), 1–11. https://doi.org/10.1007/s11095-017-2284-2.

(133) Schiele, J. T.; Quinzler, R.; Klimm, H. D.; Pruszydlo, M. G.; Haefeli, W. E. Difficulties Swallowing Solid Oral Dosage Forms in a General Practice Population: Prevalence, Causes, and Relationship to Dosage Forms. *Eur. J. Clin. Pharmacol.* **2013**, *69* (4), 937–948. https://doi.org/10.1007/s00228-012-1417-0.

(134) Dixit, R. P.; Puthli, S. P. Oral Strip Technology: Overview and Future Potential. *J. Control. Release* **2009**, *139* (2), 94–107. https://doi.org/10.1016/j.jconrel.2009.06.014.

(135) Bhakay, A.; Vizzotti, E.; Li, M.; Davé, R.; Bilgili, E. Incorporation of Fenofibrate Nanoparticles Prepared by Melt Emulsification into Polymeric Films. *J. Pharm. Innov.* **2016**, *11* (1), 53–63. https://doi.org/10.1007/s12247-015-9237-2.

(136) Zhang, L.; Aloia, M.; Pielecha-Safira, B.; Lin, H.; Rajai, P. M.; Kunnath, K.; Davé, R. N. Impact of Superdisintegrants and Film Thickness on Disintegration Time of Strip Films Loaded With Poorly Water-Soluble Drug Microparticles. *J. Pharm. Sci.* **2018**, *107* (8), 2107–2118. https://doi.org/10.1016/j.xphs.2018.04.006.

(137) Zhang, L.; Li, Y.; Abed, M.; Davé, R. N. Incorporation of Surface-Modified Dry Micronized Poorly Water-Soluble Drug Powders into Polymer Strip Films. *Int. J. Pharm.* **2018**, *535* (1–2), 462–472. https://doi.org/10.1016/j.ijpharm.2017.11.040.

(138) Krull, S. M.; Susarla, R.; Afolabi, A.; Li, M.; Ying, Y.; Iqbal, Z.; Bilgili, E.; Davé, R. N. Polymer Strip Films as a Robust, Surfactant-Free Platform for Delivery of BCS Class II Drug Nanoparticles. *Int. J. Pharm.* **2015**, *489* (1–2), 45–57. https://doi.org/10.1016/j.ijpharm.2015.04.034.

(139) Zhang, J.; Ying, Y.; Pielecha-Safira, B.; Bilgili, E.; Ramachandran, R.; Romañach, R.; Davé, R. N.; Iqbal, Z. Raman Spectroscopy for In-Line and off-Line Quantification of

Poorly Soluble Drugs in Strip Films. *Int. J. Pharm.* **2014**, *475* (1), 428–437. https://doi.org/10.1016/j.ijpharm.2014.08.051.

(140) Kevadiya, B. D.; Barvaliya, M.; Zhang, L.; Anovadiya, A.; Brahmbhatt, H.; Paul, P.; Tripathi, C. Fenofibrate Nanocrystals Embedded in Oral Strip-Films for Bioavailability Enhancement. *Bioengineering* **2018**, *5* (1), 1–17. https://doi.org/10.3390/bioengineering5010016.

(141) Krull, S. M.; Moreno, J.; Li, M.; Bilgili, E.; Davé, R. N. Critical Material Attributes (CMAs) of Strip Films Loaded with Poorly Water-Soluble Drug Nanoparticles: III. Impact of Drug Nanoparticle Loading. *Int. J. Pharm.* **2017**, *523* (1), 33–41. https://doi.org/10.1016/j.ijpharm.2017.03.023.

(142) Prodduturi, S.; Manek, R. V.; Kolling, W. M.; Stodghill, S. P.; Repka, M. A. Solid-State Stability and Characterization of Hot-Melt Extruded Poly(Ethylene Oxide) Films. *J. Pharm. Sci.* **2005**, *94* (10), 2232–2245. https://doi.org/10.1002/jps.20437.

(143) Panraksa, P.; Jantrawut, P.; Tipduangta, P.; Jantanasakulwong, K. Formulation of Orally Disintegrating Films as an Amorphous Solid Solution of a Poorly Water-Soluble Drug. *Membranes (Basel).* **2020**, *10* (12), 1–17. https://doi.org/10.3390/membranes10120376.

(144) Weuts, I.; Van Dycke, F.; Voorspoels, J.; De Cort, S.; Stokbroekx, S.; Leemans, R.; Brewster, M. E.; Xu, D.; Segmuller, B.; Turner, Y. T. A. Physicochemical Properties of the Amorphous Drug, Cast Films, and Spray Dried Powders to Predict Formulation Probability of Success for Solid Dispersions: Etravirine. *J. Pharm. Sci.* **2011**, *100* (1), 260–274.

(145) Steiner, D.; Emmendörffer, J. F.; Bunjes, H. Orodispersible Films: A Delivery Platform for Solid Lipid Nanoparticles? *Pharmaceutics* **2021**, *13* (12), 1–17. https://doi.org/10.3390/pharmaceutics13122162.

(146) Jones, E.; Ojewole, E.; Kalhapure, R.; Govender, T. In Vitro Comparative Evaluation of Monolayered Multipolymeric Films Embedded with Didanosine-Loaded Solid Lipid Nanoparticles: A Potential Buccal Drug Delivery System for ARV Therapy. *Drug Dev. Ind. Pharm.* **2014**, *40* (5), 669–679. https://doi.org/10.3109/03639045.2014.892957.

(147) Ghasemiyeh, P.; Mohammadi-Samani, S. Solid Lipid Nanoparticles and Nanostructured Lipid Carriers as Novel Drug Delivery Systems: Applications, Advantages and Disadvantages. *Res. Pharm. Sci.* **2018**, *13* (4), 288–303. https://doi.org/10.4103/1735-5362.235156.

(148) Serajuddln, A. T. M. Solid Dispersion of Poorly Water-Soluble Drugs: Early Promises, Subsequent Problems, and Recent Breakthroughs. *J. Pharm. Sci.* **1999**, *88* (10), 1058–1066. https://doi.org/10.1021/js980403l.

(149) Shirodkar, R. K.; Kumar, L.; Mutalik, S.; Lewis, S. Solid Lipid Nanoparticles and

Nanostructured Lipid Carriers: Emerging Lipid Based Drug Delivery Systems. *Pharm. Chem. J.* **2019**, *53* (5), 440–453. https://doi.org/10.1007/s11094-019-02017-9.

(150) Li, C. L.; Martini, L. G.; Ford, J. L.; Roberts, M. The Use of Hypromellose in Oral Drug Delivery. *J. Pharm. Pharmacol.* **2010**, *57* (5), 533–546. https://doi.org/10.1211/0022357055957.

(151) Asare-Addo, K.; Conway, B. R.; Larhrib, H.; Levina, M.; Rajabi-Siahboomi, A. R.; Tetteh, J.; Boateng, J.; Nokhodchi, A. The Effect of PH and Ionic Strength of Dissolution Media on In-Vitro Release of Two Model Drugs of Different Solubilities from HPMC Matrices. *Colloids Surfaces B Biointerfaces* **2013**, *111*, 384–391. https://doi.org/10.1016/j.colsurfb.2013.06.034.

(152) Steiner, D.; Finke, J. H.; Kwade, A. Efficient Production of Nanoparticle-Loaded Orodispersible Films by Process Integration in a Stirred Media Mill. *Int. J. Pharm.* **2016**, *511* (2), 804–813. https://doi.org/10.1016/j.ijpharm.2016.07.058.

(153) Nazir, H.; Zhang, W.; Liu, Y.; Chen, X.; Wang, L.; Naseer, M. M.; Ma, G. Silicone Oil Emulsions: Strategies to Improve Their Stability and Applications in Hair Care Products. *Int. J. Cosmet. Sci.* **2014**, *36* (2), 124–133. https://doi.org/10.1111/ics.12104.

(154) Schulz, M. B.; Daniels, R. Hydroxypropylmethylcellulose (HPMC) as Emulsifier for Submicron Emulsions: Influence of Molecular Weight and Substitution Type on the Droplet Size after High-Pressure Homogenization. *Eur. J. Pharm. Biopharm.* **2000**, *49* (3), 231–236. https://doi.org/10.1016/S0939-6411(00)00069-2.

(155) Joshi, S. C. Sol-Gel Behavior of Hydroxypropyl Methylcellulose (HPMC) in Ionic Media Including Drug Release. *Materials (Basel).* **2011**, *4* (10), 1861–1905. https://doi.org/10.3390/ma4101861.

(156) Okubo, M.; Iohara, D.; Anraku, M.; Higashi, T.; Uekama, K.; Hirayama, F. A Thermoresponsive Hydrophobically Modified Hydroxypropylmethylcellulose/Cyclodextrin Injectable Hydrogel for the Sustained Release of Drugs. *Int. J. Pharm.* **2020**, *575*, 118845.

(157) U.S. Food and Drug Administration – Dissolution Methods Database https://www.accessdata.fda.gov/scripts/cder/dissolution/dsp_getalldata.cfm.

(158) Amidon, G. L.; Lennernäs, H.; Shah, V. P.; Crison, J. R. A Theoretical Basis for a Biopharmaceutic Drug Classification: The Correlation of in Vitro Drug Product Dissolution and in Vivo Bioavailability. *Pharm. Res.* **1995**, *12* (3), 413–420.

(159) Jamzad, S.; Fassihi, R. Role of Surfactant and PH on Dissolution Properties of Fenofibrate and Glipizide - A Technical Note. *AAPS PharmSciTech* **2006**, *7* (2), 2–7. https://doi.org/10.1208/pt070233.

(160) Preis, M.; Woertz, C.; Schneider, K.; Kukawka, J.; Broscheit, J.; Roewer, N.; Breitkreutz, J. Design and Evaluation of Bilayered Buccal Film Preparations for Local

Administration of Lidocaine Hydrochloride. *Eur. J. Pharm. Biopharm.* **2014**, *86* (3), 552–561. https://doi.org/10.1016/j.ejpb.2013.12.019.

(161) Haque, A.; Morris, E. R. Thermogelation of Methylcellulose. Part I: Molecular Structures and Processes. *Carbohydr. Polym.* **1993**, *22*, 161–173.

(162) Sarkar, N. Thermal Gelation Properties of Methyl and Hydroxypropyl Methylcellulose. *J. Appl. Polym. Sci.* **1979**, *24* (4), 1073–1087. https://doi.org/10.1002/app.1979.070240420.

(163) Nigmatullin, R.; Gabrielli, V.; Muñoz-García, J. C.; Lewandowska, A. E.; Harniman, R.; Khimyak, Y. Z.; Angulo, J.; Eichhorn, S. J. Thermosensitive Supramolecular and Colloidal Hydrogels via Self-Assembly Modulated by Hydrophobized Cellulose Nanocrystals. *Cellulose* **2019**, *26* (1), 529–542. https://doi.org/10.1007/s10570-018-02225-8.

(164) Nasatto, P. L.; Pignon, F.; Silveira, J. L. M.; Duarte, M. E. R.; Noseda, M. D.; Rinaudo, M. Methylcellulose, a Cellulose Derivative with Original Physical Properties and Extended Applications. *Polymers (Basel).* **2015**, *7* (5), 777–803. https://doi.org/10.3390/polym7050777.

(165) Li, N.; Liu, E.; Lim, C. H. Micro-DSC and Rheological Studies of Interactions between Methylcellulose and Surfactants. *J. Phys. Chem. B* **2007**, *111* (23), 6410–6416. https://doi.org/10.1021/jp0712957.

(166) Tipduangta, P.; Takieddin, K.; Fábián, L.; Belton, P.; Qi, S. A New Low Melting-Point Polymorph of Fenofibrate Prepared via Talc Induced Heterogeneous Nucleation. *Cryst. Growth Des.* **2015**, *15* (10), 5011–5020. https://doi.org/10.1021/acs.cgd.5b00956.

(167) Jackson, C. L.; McKenna, G. B. The Melting Behavior of Organic Materials Confined in Porous Solids. *J. Chem. Phys.* **1990**, *93* (12), 9002–9011. https://doi.org/10.1063/1.459240.

(168) Heinz, A.; Gordon, K. C.; McGoverin, C. M.; Rades, T.; Strachan, C. J. Understanding the Solid-State Forms of Fenofibrate - A Spectroscopic and Computational Study. *Eur. J. Pharm. Biopharm.* **2009**, *71* (1), 100–108. https://doi.org/10.1016/j.ejpb.2008.05.030.

(169) Lee, M. K.; Jeon, T. Y.; Mun, C. W.; Kwon, J. D.; Yun, J.; Kim, S. H.; Kim, D. H.; Chang, S. C.; Park, S. G. 3D Multilayered Plasmonic Nanostructures with High Areal Density for SERS. *RSC Adv.* **2017**, *7* (29), 17898–17905. https://doi.org/10.1039/c6ra28150h.

(170) Jeon, T. Y.; Park, S. G.; Kim, D. H.; Kim, S. H. Standing-Wave-Assisted Creation of Nanopillar Arrays with Vertically Integrated Nanogaps for SERS-Active Substrates. *Adv. Funct. Mater.* **2015**, *25* (29), 4681–4688. https://doi.org/10.1002/adfm.201501274.

(171) Chen, H. Y.; Lin, M. H.; Wang, C. Y.; Chang, Y. M.; Gwo, S. Large-Scale Hot Spot Engineering for Quantitative SERS at the Single-Molecule Scale. *J. Am. Chem. Soc.* **2015**, *137* (42), 13698–13705. https://doi.org/10.1021/jacs.5b09111.

(172) Eksi-Kocak, H.; Ilbasmis Tamer, S.; Yilmaz, S.; Eryilmaz, M.; Boyaci, I. H.; Tamer, U. Quantification and Spatial Distribution of Salicylic Acid in Film Tablets Using FT-Raman Mapping with Multivariate Curve Resolution. *Asian J. Pharm. Sci.* **2018**, *13* (2), 155–162. https://doi.org/10.1016/j.ajps.2017.07.010.

(173) Kawabata, Y.; Wada, K.; Nakatani, M.; Yamada, S.; Onoue, S. Formulation Design for Poorly Water-Soluble Drugs Based on Biopharmaceutics Classification System: Basic Approaches and Practical Applications. *Int. J. Pharm.* **2011**, *420* (1), 1–10. https://doi.org/10.1016/j.ijpharm.2011.08.032.

(174) Reynolds, T. D.; Mitchell, S. A.; Balwinski, K. M. Investigation of the Effect of Tablet Surface Area/Volume on Drug Release from Hydroxypropylmethylcellulose Controlled-Release Matrix Tablets. *Drug Dev. Ind. Pharm.* **2002**, *28* (4), 457–466. https://doi.org/10.1081/DDC-120003007.

(175) Goyanes, A.; Robles Martinez, P.; Buanz, A.; Basit, A. W.; Gaisford, S. Effect of Geometry on Drug Release from 3D Printed Tablets. *Int. J. Pharm.* **2015**, *494* (2), 657–663. https://doi.org/10.1016/j.ijpharm.2015.04.069.

(176) Van Eerdenbrugh, B.; Froyen, L.; Van Humbeeck, J.; Martens, J. A.; Augustijns, P.; Van den Mooter, G. Drying of Crystalline Drug Nanosuspensions-The Importance of Surface Hydrophobicity on Dissolution Behavior upon Redispersion. *Eur. J. Pharm. Sci.* **2008**, *35* (1–2), 127–135. https://doi.org/10.1016/j.ejps.2008.06.009.

(177) Mou, D.; Chen, H.; Wan, J.; Xu, H.; Yang, X. Potent Dried Drug Nanosuspensions for Oral Bioavailability Enhancement of Poorly Soluble Drugs with PH-Dependent Solubility. *Int. J. Pharm.* **2011**, *413* (1–2), 237–244. https://doi.org/10.1016/j.ijpharm.2011.04.034.

(178) Ritger, P. L.; Peppas, N. A. A Simple Equation for Description of Solute Release II. Fickian and Anomalous Release from Swellable Devices. *J. Control. release* **1987**, *5* (1), 37–42.

(179) Paarakh, M. P.; Jose, P. A. N. I.; Setty, C. M.; Peter, G. V. Release Kinetics – Concepts and Applications. *Int. J. Pharm. Res. Technol.* **2019**, *8* (1), 12–20. https://doi.org/10.31838/ijprt/08.01.02.

(180) Zhang, L.; Alfano, J.; Race, D.; Davé, R. N. Zero-Order Release of Poorly Water-Soluble Drug from Polymeric Films Made via Aqueous Slurry Casting. *Eur. J. Pharm. Sci.* **2018**, *117* (February), 245–254. https://doi.org/10.1016/j.ejps.2018.02.029.

(181) Lee, S. L.; O'Connor, T. F.; Yang, X.; Cruz, C. N.; Chatterjee, S.; Madurawe, R. D.; Moore, C. M. V.; Yu, L. X.; Woodcock, J. Modernizing Pharmaceutical Manufacturing: From Batch to Continuous Production. *J. Pharm. Innov.* **2015**, *10* (3),

191–199. https://doi.org/10.1007/s12247-015-9215-8.

(182) Llinàs, A.; Goodman, J. M. Polymorph Control: Past, Present and Future. *Drug Discov. Today* **2008**, *13* (5–6), 198–210. https://doi.org/10.1016/j.drudis.2007.11.006.

(183) Lide, D. R. *CRC Handbook of Chemistry and Physics*; CRC press, 2004; Vol. 85.

(184) Eral, H. B.; Safai, E. R.; Keshavarz, B.; Kim, J. J.; Lee, J.; Doyle, P. S. Governing Principles of Alginate Microparticle Synthesis with Centrifugal Forces. *Langmuir* **2016**, *32* (28), 7198–7209. https://doi.org/10.1021/acs.langmuir.6b00806.

(185) Maity, S.; Sa, B. Ca-Carboxymethyl Xanthan Gum Mini-Matrices: Swelling, Erosion and Their Impact on Drug Release Mechanism. *Int. J. Biol. Macromol.* **2014**, *68*, 78–85. https://doi.org/10.1016/j.ijbiomac.2014.04.036.

(186) Melnik, G. M.; Yarnykh, T. G.; Rukhmakova, O. A. Pharmacopaine Aspects of Extemporaneous Technology of Soft Medicines and Suppositories. *J. Adv. Pharm. Educ. Res.* **2020**, *10* (1), 60–65.

(187) Zdziennicka, A.; Krawczyk, J.; Szymczyk, K.; Jańczuk, B. Macroscopic and Microscopic Properties of Some Surfactants and Biosurfactants. *Int. J. Mol. Sci.* **2018**, *19* (7). https://doi.org/10.3390/ijms19071934.

(188) An, D.; Warning, A.; Yancey, K. G.; Chang, C. T.; Kern, V. R.; Datta, A. K.; Steen, P. H.; Luo, D.; Ma, M. Mass Production of Shaped Particles through Vortex Ring Freezing. *Nat. Commun.* **2016**, *7*, 1–10. https://doi.org/10.1038/ncomms12401.

(189) Pregent, S.; Adams, S.; Butler, M. F.; Waigh, T. A. The Impact and Deformation of a Viscoelastic Drop at the Air-Liquid Interface. *J. Colloid Interface Sci.* **2009**, *331* (1), 163–173. https://doi.org/10.1016/j.jcis.2008.11.012.

(190) Beesabathuni, S. N.; Lindberg, S. E.; Caggioni, M.; Wesner, C.; Shen, A. Q. Getting in Shape: Molten Wax Drop Deformation and Solidification at an Immiscible Liquid Interface. *J. Colloid Interface Sci.* **2015**, *445*, 231–242. https://doi.org/10.1016/j.jcis.2014.12.089.

(191) Tsume, Y.; Mudie, D. M.; Langguth, P.; Amidon, G. E.; Amidon, G. L. The Biopharmaceutics Classification System: Subclasses for in Vivo Predictive Dissolution (IPD) Methodology and IVIVC. *Eur. J. Pharm. Sci.* **2014**, *57* (1), 152–163. https://doi.org/10.1016/j.ejps.2014.01.009.

(192) Tiwari, S. B.; Rajabi-Siahboomi, A. R. Modulation of Drug Release from Hydrophilic Matrices. *Pharm. Technol. Eur.* **2008**, *20* (9), 24–32.

(193) Preis, M.; Knop, K.; Breitkreutz, J. Mechanical Strength Test for Orodispersible and Buccal Films. *Int. J. Pharm.* **2014**, *461* (1–2), 22–29. https://doi.org/10.1016/j.ijpharm.2013.11.033.

(194) Centkowska, K.; Ławrecka, E.; Sznitowska, M. Technology of Orodispersible Polymer Films with Micronized Loratadine—Influence of Different Drug Loadings on Film Properties. *Pharmaceutics* **2020**, *12* (3). https://doi.org/10.3390/pharmaceutics12030250.

(195) Leibtag, S.; Peshkovsky, A. Cannabis Extract Nanoemulsions Produced by High-Intensity Ultrasound: Formulation Development and Scale-Up. *J. Drug Deliv. Sci. Technol.* **2020**, *60*, 101953.

(196) Mitri, K.; Vauthier, C.; Huang, N.; Menas, A.; Ringard-Lefebvre, C.; Anselmi, C.; Stambouli, M.; Rosilio, V.; Vachon, J.-J.; Bouchemal, K. Scale-up of Nanoemulsion Produced by Emulsification and Solvent Diffusion. *J. Pharm. Sci.* **2012**, *101* (11), 4240–4247.